



UNIVERSIDADE ESTADUAL DE CAMPINAS
Faculdade de Engenharia Química

JOÃO VICTOR MELO AMARAL

**ANÁLISE DOS EFEITOS GEOMÉTRICOS EM
MICRODISPOSITIVOS NA GERAÇÃO DE
VÓRTICES USANDO FLUIDODINÂMICA
COMPUTACIONAL**

**ANALYSIS OF GEOMETRIC EFFECTS IN
MICRODEVICES TO GENERATE VORTICES
USING COMPUTATIONAL FLUID DYNAMICS**

CAMPINAS - SP

2021

JOÃO VICTOR MELO AMARAL

**ANALYSIS OF GEOMETRIC EFFECTS IN MICRODEVICES TO
GENERATE VORTICES USING COMPUTATIONAL FLUID DYNAMICS**

**ANÁLISE DOS EFEITOS GEOMÉTRICOS EM MICRODISPOSITIVOS
NA GERAÇÃO DE VÓRTICES USANDO FLUIDODINÂMICA
COMPUTACIONAL**

Dissertação apresentada à Faculdade de Engenharia Química da Universidade Estadual de Campinas como parte dos requisitos exigidos para a obtenção do título de Mestre em Engenharia Química

Dissertation presented to the School of Chemical Engineering of the University of Campinas in partial fulfillment of the requirements for the degree of Master in Chemical Engineering

Supervisor: Prof. Dr. Sávio Souza Venâncio Vianna

ESTE TRABALHO CORRESPONDE À VERSÃO FINAL
DA DISSERTAÇÃO DEFENDIDA PELO ALUNO JOÃO
VICTOR MELO AMARAL, ORIENTADO PELO PROF.
DR. SÁVIO SOUZA VENÂNCIO VIANNA

Campinas - SP
2021

Ficha catalográfica
Universidade Estadual de Campinas
Biblioteca da Área de Engenharia e Arquitetura
Rose Meire da Silva - CRB 8/5974

Am13a Amaral, João Víctor Melo, 1996-
Analysys of geometric effects in microdevices to generate vortices using computational fluid dynamics / João Víctor Melo Amaral. – Campinas, SP : [s.n.], 2021.

Orientador: Sávio Souza Venâncio Vianna.
Dissertação (mestrado) – Universidade Estadual de Campinas, Faculdade de Engenharia Química.

1. Microfluídica. 2. Fluidodinâmica computacional. 3. Vórtices. 4. Simulação computacional. 5. Métodos dos volumes finitos. I. Vianna, Sávio Souza Venâncio, 1975-. II. Universidade Estadual de Campinas. Faculdade de Engenharia Química. III. Título.

Informações para Biblioteca Digital

Título em outro idioma: Análise dos efeitos geométricos em microdispositivos na geração de vórtices usando fluidodinâmica computacional

Palavras-chave em inglês:

Microfluidics

Computational fluid dynamics

Vortices

Computational simulation

Finite volume method

Área de concentração: Engenharia Química

Titulação: Mestre em Engenharia Química

Banca examinadora:

Sávio Souza Venâncio Vianna [Orientador]

Lucimara Gaziola de La Torre

Fábio Pereira dos Santos

Data de defesa: 01-03-2021

Programa de Pós-Graduação: Engenharia Química

Identificação e informações acadêmicas do(a) aluno(a)

- ORCID do autor: <https://orcid.org/0000-0003-1107-6193>

- Currículo Lattes do autor: <http://lattes.cnpq.br/0624747483044063>

Folha de Aprovação da Dissertação de Mestrado do aluno João Victor Melo Amaral, e aprovada em 01 de março de 2021 pela comissão examinadora da defesa constituída pelos doutores:

Prof. Dr. Sávio Souza Venâncio Vianna
FEQ / UNICAMP
Videoconferência

Profa. Dra. Lucimara Gaziola de la Torre
FEQ / UNICAMP
Videoconferência

Prof. Dr. Fábio Pereira dos Santos
UFRJ - Escola de Química
Videoconferência

Ata de defesa com as respectivas assinaturas dos membros encontra-se no SIGA/Sistema de Fluxo de Tese e na Secretaria do Programa da Unidade.

To my Mom and Dad.

Acknowledgements

"[...] *The Lord has done great things for me* [...]", Psalms 126:3a

And one of these great things was the opportunity to study a master's degree at the University of Campinas. A new time, a new stage in my life, and with each conquest, I realize that God has prepared a giant future for me, because the victory is of those who have perverted, and, in the certainty that I am at the center of the sovereign will of the Lord, I will be forever I thank God for giving me wisdom, strength, protection in the midst of adversity during these two years. Thank God so much for blessing me, beyond what I deserve!

I would like to gratefully acknowledge my parents Néia and Beto who have always been by my side, trusting on my skills, cheering me up during all my battles, and providing all the comfort and assistance to me.

A very special gratitude to Conselho Nacional de Desenvolvimento Científico e Tecnológico (CNPq) for the financial support of this research during one year (process number 137742/2018-5).

Likewise, I would like to express my gratitude to my advisor/supervisor Prof. Dr. Sávio Vianna for all assistance and confidence in proposing a challenger methodology of a novel topic; and also, for the patience with my not fast enough ability in writing the code and this dissertation.

Last but not least, my sincere thanks goes to the continuous members of the L4R1S4 (Industrial Safety and Risks Analysis Laboratory): Tatiele, Maria Fernanda, Tássia, André, Ana Kássia and Hendrew for sharing all good and bad experiences, and giving many advices during my postgraduate period.

"There are no secrets to success. It is the result of preparation, hard work and learning from failure."

Colin Powell

"Challenges are what make life interesting and overcoming them is what makes life meaningful."

Joshua J. Marine

Resumo

Uma emergente estratégia em estudos de aumento de vorticidade devido a advecção caótica em microcanais tem sido a aplicação de ferramentas computacionais. A fluidodinâmica computacional (CFD) tem sido amplamente utilizada devido às suas vantagens em poder gerar resultados precisos, e em minimizar os custos de testes experimentais nos quais necessitam da fabricação de microdispositivos e do consumo de reagentes. No entanto, a aquisição da licença de um programa de CFD ainda requer elevado investimento econômico. Além disso, em análises de escoamento em microescala, a melhoria na formação de vórtices ainda é um grande empecilho para muitos pesquisadores. Isso pode ser explicado devido ao perfil de escoamento ser predominantemente laminar, prevalecendo assim o transporte por difusão molecular sobre o transporte convectivo, de modo a desfavorecer a geração dos vórtices. Essa pesquisa tem como objetivo desenvolver um código que descreva o escoamento de fluidos ao longo de microcanais, assim como, obter uma intensificação na vorticidade do fluido por meio de pequenas mudanças na geometria de um dispositivo no formato de bocal convergente acoplado à um microcanal com saliências convexas. O código foi programado utilizando linguagem computacional Fortran 95 no qual o domínio espacial e as equações de conservação foram discretizados a partir do Método dos Volumes Finitos (FVM) e do esquema híbrido, respectivamente. Adicionalmente, essas equações foram iteradas até atingir a convergência por meio da implementação do algoritmo SIMPLE co-localizado (Semi-Implicit Method for Pressure-Linked Equations). Por fim, os dados coletados mostram que a largura do microcanal e a inserção de saliências favorecem consideravelmente o aumento da vorticidade e a criação de zonas de recirculação para maiores números de Reynolds, enquanto que a contribuição da posição da alimentação é apenas localizada na entrada dos microdispositivos.

Palavras-chave: Microfluídica, Vorticidade, Microdispositivo com saliências, Microdispositivo de alimentação lateral, Linguagem Fortran, Algoritmo SIMPLE.

Abstract

An increasing strategy to stimulate vorticity due to chaotic advection in microchannels has been involving the use of computational tools. Computational fluid dynamics (CFD) has been widely used due to its advantages in obtaining accurate results, and minimizing the costs of experimental tests, which includes the fabrication of prototypes of microdevices and the consumption of reagents. However, acquiring a CFD software is still expensive. Moreover, in a microfluidic pattern study, the improvement in the formation of vortices still represents a burden for many researchers. The reason is that diffusion transport at molecular level prevails over the convective forces in laminar regimes, contributing to a no chaotic flow performance. The purpose of this study is to develop a code that describes the fluid flow along a microchannel; and also, to propose an improvement of the vortex formation of a fluid by varying slightly the geometry of a converging nozzle coupled to a bumpy microchannel. The code was programmed by employing the Fortran 95 language in which the spatial domain and the derivative conservation equations were discretized by applying the Finite Volume Method (FVM) and the hybrid scheme, respectively. Consequently, these equations were iterated until convergence through the co-located SIMPLE (Semi-Implicit Method for Pressure-Linked Equations) algorithm. Finally, the data collected show that the width of the microchannel and the insertion of bumps considerably favor the increase in vorticity and the creation of recirculation zones for larger numbers of Reynolds, while the contribution of the position of the feed is only located at the entrance of the microdevices.

Keywords: Microfluidics, Vorticity, Bumpy microdevice, Microdevice with lateral feed, Fortran language, SIMPLE algorithm.

List of Figures

| | | |
|-----|---|----|
| 2.1 | Rotation of the particles near the walls caused by the shear stress. | 46 |
| 2.2 | Rotation of the particles caused by the deceleration of the fluid with subsequent positive pressure gradient (Adapted from Kundu and Cohen (2004)). | 47 |
| 2.3 | Cross-sections of channels: (a) circle; (b) ellipse; (c) concentric annulus; (d) rectangle | 50 |
| 3.1 | Representation of a 3-D control volume. | 56 |
| 3.2 | Same grid represented in two different ways. | 62 |
| 3.3 | A control volume around the grid point P. | 63 |
| 3.4 | Example of non-realistic pressure field resulted from the actual discretized method. | 71 |
| 3.5 | Representation of the control volume: (a) at cell W; (b) at the w face from cell P. | 73 |
| 3.6 | Flowchart of the SIMPLE algorithm. | 80 |
| 3.7 | Representation of the control volume adjacent to the wall. | 82 |
| 3.8 | Representation of the control volume adjacent to the feed. | 84 |
| 3.9 | Representation of the control volume adjacent to the outlet. | 85 |
| 4.1 | Flowchart of the code structure. | 91 |
| 4.2 | Representation of the rectangular duct where L_{duct} and D_{duct} are, respectively, 3 mm and 250 μm | 93 |
| 4.3 | Representation of the square lid-driven cavity where L_{cavity} is equal to 1 mm. | 94 |
| 4.4 | Representation of the convergent-nozzle coupled to the bumpy channel with $\alpha=4$ | 95 |

LIST OF FIGURES

| | | |
|------|---|-----|
| 5.1 | Grid dependent test with three meshes where $Re=100$ and $x=0.15$ mm. . . | 97 |
| 5.2 | u -velocity in the x -direction regarding Reynolds numbers resulted from the developed code and from OpenFOAM. | 98 |
| 5.3 | Comparison between the code and the OpenFoam for u -velocity along y -axis at three locations in x -axis where $Re=100$ | 99 |
| 5.4 | Comparison between the kinematic pressure results from code and OpenFOAM along x -axis for $Re=100$ at $y=0.125$ mm. | 99 |
| 5.5 | Representative slices (white lines) for the following analyzes. | 100 |
| 5.6 | Comparison between the different grids for the u -velocity along the x -axis for $Re = 100$ at $y = 0.8$ mm. | 101 |
| 5.7 | Comparison of u -velocity regarding Reynolds number between the code and the OpenFOAM. | 102 |
| 5.8 | Comparison of the u -velocity profile at different heights and Reynolds numbers. | 103 |
| 5.9 | Comparison of v -velocity regarding Reynolds number between the code and the OpenFOAM. | 104 |
| 5.10 | Comparison of the v -velocity profile at different heights and Re | 105 |
| 5.11 | z -Vorticity component at different Reynolds numbers resulted by code. . . | 106 |
| 5.12 | Comparison of the z -vorticity profile at different heights and Re | 106 |
| 5.13 | Stream function at different Reynolds numbers resulted by the code. | 107 |
| 5.14 | Magnitude of velocity regarding Reynolds number where $d=250 \mu m$, $s = 100 \mu m$ and there is no bumps. | 109 |
| 5.15 | Streamlines along the microdevice where $d=250 \mu m$, $s = 100 \mu m$ and there is no bump. | 110 |
| 5.16 | Vorticity field at different Reynolds numbers where $d=250 \mu m$, $s = 100 \mu m$ and there is no bumps. | 111 |
| 5.17 | Representation of the positions selected for the analyses in the following graphics. | 112 |
| 5.18 | u -Velocity regarding Reynolds number and "location of bumps" where $d=250 \mu m$ and there is no bumps. | 113 |

LIST OF FIGURES

5.19 Kinematic pressure regarding Reynolds number "location of bumps" where $d=250 \mu m$ and there is no bumps. 113

5.20 Magnitude of vorticity regarding Reynolds number and the "location of bumps" where $d=250 \mu m$ and there is no bumps. 114

5.21 Mean vorticity and kinematic pressure performances along the device regarding Re for $s = 100 \mu m$, and $d = 250 \mu m$ 114

5.22 Magnitude of velocity regarding the location of the feed where $d=250 \mu m$, $Re = 90$ and there is no bumps (These figures do not have the same data range). 115

5.23 Vorticity field at different locations of the feed where $d=250 \mu m$, and $Re = 90$ (These figures do not have the same data range). 116

5.24 Mean vorticity and kinematic pressure performances along the device regarding s for $Re = 90$, and $d = 250 \mu m$ 117

5.25 Magnitude of velocity regarding Reynolds number where $d=250 \mu m$, $s = 100 \mu m$ and $\alpha = 1$ 118

5.26 Streamlines along the microdevice where $d=250 \mu m$, $s = 100 \mu m$ and $\alpha = 1$. 119

5.27 Vorticity field at different Reynolds numbers where $d=250 \mu m$, $s = 100 \mu m$ and $\alpha = 1$ 120

5.28 Performance of mean vorticity, kinematic pressure and u -velocity along the device regarding Re for $s = 100 \mu m$, and $d = 250 \mu m$ 121

5.29 Comparison between vorticity, pressure and u -velocity along the x -axis for $Re = 90$ and $s = 100 \mu m$ with $d = 250 \mu m$ 121

5.30 Representation of the positions selected for the analyses in the following graphics for when $\alpha = 1$ 121

5.31 u -Velocity regarding Reynolds number and location of bumps where $d=250 \mu m$ and $\alpha = 1$ 122

5.32 Magnitude of vorticity regarding Reynolds number and location of bumps where $d=250 \mu m$ and $\alpha = 1$ 122

5.33 Comparison between pressure and vorticity at three positions (0.83, 1.00 and 1.20 mm) inside the first cavity when $Re = 90$ and $\alpha = 1$ 123

LIST OF FIGURES

| | | |
|------|--|-----|
| 5.34 | Magnitude of velocity regarding the location of the feed where $d=250 \mu m$, $\alpha = 1$ and $Re = 90$ | 124 |
| 5.35 | Stream function with its contours along the microdevice where $d=250 \mu m$, $\alpha = 1$ and $Re = 90$ (These figures do not have the same data range). . . . | 125 |
| 5.36 | Vorticity field at different Reynolds numbers where $d=250 \mu m$, $a = 1$ and $Re = 90$ | 126 |
| 5.37 | Magnitude of vorticity regarding Reynolds number and location of feed before the first throat at $x = 0.58 mm$ | 127 |
| 5.38 | Magnitude of vorticity regarding Reynolds number and location of feed at Bump1 where $d=250 \mu m$ and $\alpha = 1$ | 127 |
| 5.39 | Mean vorticity and kinematic pressure performances along the device re- garding s for $Re = 90$, and $d = 250 \mu m$ when $\alpha = 1$ | 128 |
| 5.40 | Streamlines along the microdevice where $d=250 \mu m$, $s = 100 \mu m$ and $\alpha = 2$. | 129 |
| 5.41 | Vorticity field at different Reynolds numbers where $d=250 \mu m$, $s = 100$ μm and $\alpha = 2$ | 130 |
| 5.42 | Performance of some fluid dynamics parameters along the device regarding Re for $s = 100 \mu m$, $\alpha = 2$ and $d = 250 \mu m$ | 131 |
| 5.43 | Representation of the positions selected for the analyses in the following graphics for when $\alpha = 2$ | 131 |
| 5.44 | Magnitude of vorticity regarding Reynolds number and location of bumps where $d=250 \mu m$ and $\alpha = 2$ | 132 |
| 5.45 | Comparison between pressure and vorticity at three positions (0.83, 1.00 and 1.20 mm) inside the first cavity when $Re = 90$, and $\alpha = 2$ | 133 |
| 5.46 | Magnitude of velocity regarding the location of the feed where $d=250 \mu m$, $\alpha = 2$ and $Re = 90$ | 134 |
| 5.47 | Stream function with its contours along the microdevice where $d=250 \mu m$, $\alpha = 2$ and $Re = 90$.(These figures do not have the same data range) | 135 |
| 5.48 | Vorticity field at different Reynolds numbers where $d=250 \mu m$, $a = 2$ and $Re = 90$ | 136 |
| 5.49 | Magnitude of vorticity regarding Reynolds number and location of feed at Bump0 ($x = 0.58 mm$) and at Bump1 ($x = 1.0 mm$). | 137 |

LIST OF FIGURES

| | | |
|------|---|-----|
| 5.50 | Performances of the vorticity magnitude and the kinematic pressure at $Re = 90$ regarding the curvature of bump α when $s = 100 \mu\text{m}$ and $d = 250 \mu\text{m}$ | 138 |
| 5.51 | u-Velocity regarding Reynolds number and curvature of bumps where $d=250 \mu\text{m}$ and $s = 100 \mu\text{m}$ | 138 |
| 5.52 | Magnitude of vorticity regarding Reynolds number and curvature of the bumps where $d=250 \mu\text{m}$ and $s = 100 \mu\text{m}$ | 139 |
| 5.53 | Kinematic pressure regarding Reynolds number and curvature of the bumps where $d=250 \mu\text{m}$ and $s = 100 \mu\text{m}$ | 139 |
| 5.54 | Pressure drop at different Reynolds numbers (Re) and curvature parameter a when $d=250 \mu\text{m}$ and $s=100 \mu\text{m}$ | 140 |
| 5.55 | Streamlines along the microdevice where $d=200 \mu\text{m}$, $s = 100 \mu\text{m}$ and there is no bumps. | 142 |
| 5.56 | Vorticity performance at different Reynolds numbers (Re) and device's width d when there is no bumps and $s=100 \mu\text{m}$ | 143 |
| 5.57 | Vorticity field at different feed locations where $d=200 \mu\text{m}$, $Re = 40$ and there is no bumps (These figures do not have the same data range). | 144 |
| 5.58 | Magnitude of vorticity regarding Reynolds number and location of feed at $x = 0.6 \text{ mm}$ (Bump0) and $x = 1.0 \text{ mm}$ (Bump1) with $d=200 \mu\text{m}$ and no bumps. | 145 |
| 5.59 | Streamlines along the microdevice where $d=200 \mu\text{m}$, $s = 100 \mu\text{m}$ and $\alpha = 1$ | 146 |
| 5.60 | Vorticity field at different Reynolds numbers where $d=200 \mu\text{m}$, $s = 100 \mu\text{m}$ and $\alpha = 1$ | 147 |
| 5.61 | Fluid dynamics parameters regarding Reynolds numbers at $x = 1 \text{ mm}$ where $d=200 \mu\text{m}$, $s = 100 \mu\text{m}$ and $\alpha = 1$ | 148 |
| 5.62 | Performance of some fluid dynamics parameters along the device regarding Re for $s = 100 \mu\text{m}$, $\alpha = 1$ and $d = 200 \mu\text{m}$ | 148 |
| 5.63 | Stream function with its contours along the microdevice where $d=200 \mu\text{m}$, $a = 1$ and $Re = 40$ | 149 |

LIST OF FIGURES

5.64 Magnitude of vorticity regarding Reynolds number and location of feed s at $x = 0.58$ mm (Bump0) and $x = 1.0$ mm (Bump1) where $d=200 \mu m$ and $\alpha = 1$ 150

5.65 Streamlines along the microdevice where $d=200 \mu m$, $s = 100 \mu m$ and $\alpha = 2$. 151

5.66 Vorticity field at different Reynolds numbers where $d=200 \mu m$, $s = 100 \mu m$ and $a = 2$ 152

5.67 Performance of some fluid dynamics parameters along the device regarding Re for $s = 100 \mu m$, $\alpha = 2$ and $d = 200 \mu m$ 153

5.68 Stream function with its contours along the microdevice where $d=200 \mu m$, $\alpha = 2$ and $Re = 40$ 154

5.69 Magnitude of vorticity regarding Reynolds number and location of feed at $x = 0.6$ mm and at $x = 1.0$ mm with $d=200 \mu m$ and $a = 2$ 155

5.70 Magnitude of vorticity regarding Reynolds number and curvature of the bumps where $d=200 \mu m$ and $s = 100 \mu m$ 156

5.71 Pressure drop at different Reynolds numbers (Re) and curvature α when $d=200 \mu m$ and $s=100 \mu m$ 156

5.72 Magnitude of vorticity regarding Reynolds number and curvature of bumps comparing both values of d when $x = 0.58$ mm. 157

5.73 Magnitude of vorticity regarding Reynolds number and curvature of bumps comparing both values of d when $x = 1.0$ mm. 158

5.74 Vorticity profiles comparing the best results for each device's width d when $s = 100 \mu m$ and $\alpha = 2$ 160

C.1 Magnitude of velocity regarding Reynolds number where $d=250 \mu m$, $s = 100 \mu m$ and there is no bumps. 192

C.2 Magnitude of velocity regarding the location of the feed where $d=250 \mu m$, $Re = 90$, and there is no bumps (These figures do not have the same data range). 193

C.3 Magnitude of velocity regarding Reynolds number where $d=250 \mu m$, $s = 100 \mu m$ and $\alpha = 1$ 194

C.4 Magnitude of velocity regarding the location of the feed where $d=250 \mu m$, $\alpha = 1$ and $Re = 90$ 195

LIST OF FIGURES

| | | |
|------|--|-----|
| C.5 | Magnitude of velocity regarding Reynolds number where $d=250 \mu m$, $s = 100 \mu m$ and $\alpha = 2$ | 196 |
| C.6 | Magnitude of velocity regarding the location of the feed where $d=250 \mu m$, $\alpha = 2$ and $Re = 90$ | 197 |
| C.7 | Magnitude of velocity regarding Reynolds number where $d=250 \mu m$, $s = 100 \mu m$ and $\alpha = 4$ | 198 |
| C.8 | Magnitude of velocity regarding the location of the feed where $d=250 \mu m$, $\alpha = 4$ and $Re = 90$ | 199 |
| C.9 | Magnitude of velocity regarding Reynolds number where $d=200 \mu m$ and $s = 100 \mu m$ | 200 |
| C.10 | Magnitude of velocity regarding the location of the feed where $d=200 \mu m$ and $Re = 40$ | 201 |
| C.11 | Magnitude of velocity regarding Reynolds number where $d=200 \mu m$, $s = 100 \mu m$ and $\alpha = 1$ | 202 |
| C.12 | Magnitude of velocity regarding the location of the feed where $d=200 \mu m$, $\alpha = 1$ and $Re = 40$ | 203 |
| C.13 | Magnitude of velocity regarding Reynolds number where $d=200 \mu m$, $s = 100 \mu m$ and $\alpha = 2$ | 204 |
| C.14 | Magnitude of velocity regarding the location of the feed where $d=200 \mu m$, $\alpha = 2$ and $Re = 40$ | 205 |
| C.15 | Magnitude of velocity regarding Reynolds number where $d=200 \mu m$, $s = 100 \mu m$ and $\alpha = 4$ | 206 |
| C.16 | Magnitude of velocity regarding the location of the feed where $d=200 \mu m$, $\alpha = 4$ and $Re = 40$ | 207 |
| C.17 | Pressure field at different Reynolds numbers where $d=250 \mu m$, and $s = 100 \mu m$ | 208 |
| C.18 | Pressure field at different inlet locations where $d=250 \mu m$, and $Re = 90$ (These figures do not have the same data range). | 209 |
| C.19 | Pressure field at different Reynolds numbers where $d=250 \mu m$, $s = 100 \mu m$ and $\alpha = 1$ | 210 |

LIST OF FIGURES

| | |
|--|-----|
| C.20 Pressure field at different inlet locations where $d=250 \mu m$, $\alpha = 1$ and $Re = 90$ | 211 |
| C.21 Pressure field at different Reynolds numbers where $d=250 \mu m$, $s = 100 \mu m$ and $\alpha = 2$ | 212 |
| C.22 Pressure field at different locations of feed where $d=250 \mu m$, $\alpha = 2$ and $Re = 90$ | 213 |
| C.23 Pressure field at different Reynolds numbers where $d=250 \mu m$, $s = 100 \mu m$ and $\alpha = 4$ | 214 |
| C.24 Pressure field at different locations of feed where $d=250 \mu m$, $\alpha = 4$ and $Re = 90$ | 215 |
| C.25 Pressure field at different Reynolds numbers where $d=200 \mu m$, and $s = 100 \mu m$ | 216 |
| C.26 Pressure field at different locations of feed where $d=200 \mu m$, and $Re = 40$ | 217 |
| C.27 Pressure field at different Reynolds numbers where $d=200 \mu m$, $s = 100 \mu m$ and $\alpha = 1$ | 218 |
| C.28 Pressure field at different locations of feed where $d=200 \mu m$, $\alpha = 1$ and $Re = 40$ | 219 |
| C.29 Pressure field at different Reynolds numbers where $d=200 \mu m$, $s = 100 \mu m$ and $\alpha = 2$ | 220 |
| C.30 Pressure field at different locations of feed where $d=200 \mu m$, $\alpha = 2$ and $Re = 40$ | 221 |
| C.31 Pressure field at different Reynolds numbers where $d=200 \mu m$, $s = 100 \mu m$ and $\alpha = 4$ | 222 |
| C.32 Pressure field at different locations of feed where $d=200 \mu m$, $\alpha = 4$ and $Re = 40$ | 223 |
| C.33 Vorticity field at different Reynolds numbers where $d=250 \mu m$, and $s = 100 \mu m$ | 224 |
| C.34 Vorticity field at different locations of feed where $d=250 \mu m$, and $Re = 90$ (These figures do not have the same data range). | 225 |
| C.35 Vorticity field at different Reynolds numbers where $d=250 \mu m$, $s = 100 \mu m$ and $\alpha = 1$ | 226 |

LIST OF FIGURES

| | |
|---|-----|
| C.36 Vorticity field at different locations of feed where $d=250 \mu m$, $\alpha = 1$ and $Re = 90$ | 227 |
| C.37 Vorticity field at different Reynolds numbers where $d=250 \mu m$, $s = 100 \mu m$ and $\alpha = 2$ | 228 |
| C.38 Vorticity field at different locations of feed where $d=250 \mu m$, $\alpha = 2$ and $Re = 90$ | 229 |
| C.39 Vorticity field at different Reynolds numbers where $d=250 \mu m$, $s = 100 \mu m$ and $\alpha = 4$ | 230 |
| C.40 Vorticity field at different positions of feed where $d=250 \mu m$, $\alpha = 4$ and $Re = 90$ | 231 |
| C.41 Vorticity field at different Reynolds numbers where $d=200 \mu m$, and $s = 100 \mu m$ | 232 |
| C.42 Vorticity field at different locations of feed where $d=200 \mu m$, and $Re = 40$ (These figures do not have the same data range). | 233 |
| C.43 Vorticity field at different Reynolds numbers where $d=200 \mu m$, $s = 100 \mu m$ and $\alpha = 1$ | 234 |
| C.44 Vorticity field at different locations of feed where $d=200 \mu m$, $\alpha = 1$ and $Re = 40$ | 235 |
| C.45 Vorticity field at different Reynolds numbers where $d=200 \mu m$, $s = 100 \mu m$ and $\alpha = 2$ | 236 |
| C.46 Vorticity field at different locations of feed where $d=200 \mu m$, $\alpha = 2$ and $Re = 40$ | 237 |
| C.47 Vorticity field at different Reynolds numbers where $d=200 \mu m$, $s = 100 \mu m$ and $\alpha = 4$ | 238 |
| C.48 Vorticity field at different locations of feed where $d=200 \mu m$, $\alpha = 4$ and $Re = 40$ | 239 |
| C.49 Stream function with its contours along the microdevice regarding Reynolds number where $d=250 \mu m$, and $s = 100 \mu m$ | 240 |
| C.50 Stream function with its contours along the microdevice in terms of the feed position where $d=250 \mu m$, and $Re = 90$ (These figures do not have the same data range). | 241 |

LIST OF FIGURES

C.51 Stream function with its contours along the microdevice regarding Reynolds number where $d=250 \mu m$, $s = 100 \mu m$ and $\alpha = 1$ 242

C.52 Stream function with its contours along the microdevice in terms of the feed position where $d=250 \mu m$, $\alpha = 1$ and $Re = 90$ (These figures do not have the same data range). 243

C.53 Stream function with its contours along the microdevice regarding Reynolds number where $d=250 \mu m$, $s = 100 \mu m$ and $\alpha = 2$ 244

C.54 Stream function with its contours along the microdevice in terms of the feed position where $d=250 \mu m$, $\alpha = 2$ and $Re = 90$ (These figures do not have the same data range). 245

C.55 Stream function with its contours along the microdevice regarding Reynolds number where $d=250 \mu m$, $s = 100 \mu m$ and $\alpha = 4$ 246

C.56 Stream function with its contours along the microdevice in terms of the feed position where $d=250 \mu m$, $\alpha = 4$ and $Re = 90$ (These figures do not have the same data range). 247

C.57 Stream function with its contours along the microdevice regarding Reynolds number where $d=200 \mu m$, and $s = 100 \mu m$ 248

C.58 Stream function with its contours along the microdevice in terms of the feed position where $d=200 \mu m$, and $Re = 40$ (These figures do not have the same data range). 249

C.59 Stream function with its contours along the microdevice regarding Reynolds number where $d=200 \mu m$, $s = 100 \mu m$ and $\alpha = 1$ 250

C.60 Stream function with its contours along the microdevice in terms of the feed position where $d=200 \mu m$, $\alpha = 1$ and $Re = 40$ (These figures do not have the same data range). 251

C.61 Stream function with its contours along the microdevice regarding Reynolds number where $d=200 \mu m$, $s = 100 \mu m$ and $\alpha = 2$ 252

C.62 Stream function with its contours along the microdevice in terms of the feed position where $d=200 \mu m$, $\alpha = 2$ and $Re = 40$ (These figures do not have the same data range). 253

LIST OF FIGURES

| | |
|--|-----|
| C.63 Stream function with its contours along the microdevice regarding Reynolds number where $d=200 \mu m$, $s = 100 \mu m$ and $\alpha = 4$ | 254 |
| C.64 Stream function with its contours along the microdevice in terms of the feed position where $d=200 \mu m$, $\alpha = 4$ and $Re = 40$ (These figures do not have the same data range). | 255 |

List of Tables

| | | |
|-----|--|-----|
| 5.1 | Discretization error (GCI), in percentage, for three grids in different sets of geometry configuration for $Re = 20$ and $s = 100\mu$ m. | 108 |
| 5.2 | Pressure drop (Pa) at different locations of feed and curvature of bumps when $Re = 90$ and $d = 250 \mu m$ | 140 |
| 5.3 | Pressure drop (Pa) for all simulations performed during this work. | 159 |

Nomenclature

Acronyms

CFD Computational Fluid Dynamics

CTS SIMPLE Consistent Time Step - Semi-Implicit Method for Pressure-Linked Equations

FDM Finite Difference Method

FEM Finite Element Method

FIMOSE Fully Implicit Method for Operator-Split Equation

FVM Finite Volume Method

GCI_{fine} fine-Grid Convergence Index

PISO Pressure-Implicit Split Operator

PPE Personal Protective Equipment

PWIM Pressure-Weighted Interpolation Method

QUICK Quadratic Upstream Interpolation For Convective Kinetics

RON Research Octane Number

SIMPLE Semi-Implicit Method for Pressure-Linked Equations

SIMPLEC Semi-Implicit Method for Pressure-Linked Equations Consistent

SIMPLER Semi-Implicit Method for Pressure-Linked Equations Revised

NOMENCLATURE

TDMA Tri-Diagonal Matrix Algorithm

TVD Total Variation Diminishing

Greek Letters

α Curvature of the bump

α_P Pressure under-relaxation factor

α_u u-velocity under-relaxation factor

α_v v-velocity under-relaxation factor

μ Dynamic viscosity of the fluid ($kg.mm^{-1}.s^{-1}$)

ν Kinematic viscosity of the fluid ($mm^2.s^{-1}$)

$\overline{\omega_z}$ Mean vorticity in the z-direction (s^{-1})

$\vec{\omega}$ Vorticity field vector (s^{-1})

ψ Stream function field ($mm^2.s^{-1}$)

ρ Density of the fluid ($kg.mm^{-3}$)

$\vec{\delta}$ Kronecker delta

$\vec{\tau}$ Viscous effects ($kg.mm^{-1}.s^{-2}$)

Latin Letters

$\dot{m}_{imbalance}$ Imbalance of mass ($kg.s^{-1}$)

\bar{u} Mean velocity in x-direction ($mm.s^{-1}$)

\vec{A} Area vector (mm^2)

\vec{f}_e External volume force ($mm.s^{-2}$)

\vec{v} Velocity vector ($mm.s^{-1}$)

A Cross-sectional area (mm^2)

NOMENCLATURE

| | | |
|-----------|--|---------------|
| a | Coefficient from the discretized momentum equations | $(kg.s^{-1})$ |
| a | Length in x -direction for a respective geometry | (mm) |
| a^P | Coefficient from the discretized continuity equation | $(mm.s)$ |
| b | Length in y -direction for a respective geometry | (mm) |
| c | Concentration of reagent | $(g.mm^{-3})$ |
| c^* | Dimensionless concentration | |
| c_0 | Initial concentration of solute | $(g.mm^{-3})$ |
| D | Maximum width of the microdevice | (mm) |
| d | Width of the microchannel | (mm) |
| F | Convective transport rate | $(kg.s^{-1})$ |
| f | Horizontal length of the inlet section | (mm) |
| it | Number of iterations of the code | |
| J | Flux total of species ($F + D'$) | $(kg.s^{-1})$ |
| L | Length of the micromixer | (mm) |
| L_b | Length of a single bump | (mm) |
| L_{ent} | Entrance length | (mm) |
| M | Total mass in the whole domain | (kg) |
| m | Mass of a cell | (kg) |
| N | Number of inlets in a T-shaped | |
| n | Length of the nozzle | (mm) |
| NI | Number of nodes in x -direction | |
| NJ | Number of nodes in y -direction | |

NOMENCLATURE

| | | |
|-------------|--|-----------------------|
| P | Hydrodynamic pressure | $(kg.mm^{-1}.s^{-2})$ |
| P' | Pressure correction field | $(kg.mm^{-1}.s^{-2})$ |
| P_{abs} | Absolute pressure | $(kg.mm^{-1}.s^{-2})$ |
| P_{atm} | Atmospheric pressure | $(kg.mm^{-1}.s^{-2})$ |
| P_{gauge} | Gauge pressure | $(kg.mm^{-1}.s^{-2})$ |
| p_{north} | Position of the bump at the north wall | (μm) |
| p_{south} | Position of the bump in the south wall | (μm) |
| Pe | Dimensionless Peclet number | |
| Re | Dimensionless Reynolds number | |
| S | Source term from the discretized momentum equations | $(kg.mm.s^{-2})$ |
| s | Distance between the largest width and the inlet | (mm) |
| S^P | Source term from the discretized continuity equation | $(kg.s^{-1})$ |
| Sc | Dimensionless Schmidt number | |
| u | Velocity in x-direction | $(mm.s^{-1})$ |
| V | Volume of a cell | (mm^3) |
| v | Velocity in y-direction | $(mm.s^{-1})$ |
| x^* | Dimensionless x -position | |
| y^* | Dimensionless y -position | |
| $D_{A,B}$ | Diffusion coefficient | $(mm^2.s^{-1})$ |
| D' | Diffusive transport rate | $(kg.s^{-1})$ |

Superscripts

' Value from the difference between the realistic value and the guessed one

NOMENCLATURE

lit Value based on the literature

lit Value obtained from the numerical method

u *x*-Momentum equation

*

Value from the previous iteration

Subscripts

cavity Identification for the lid-driven cavity

duct Identification for the rectangular duct

E Nodal point on the east side of the main control volume

e Face on the east side of the main control volume

EE Nodal point two cells to east from the main control volume

in Inlet section

max Maximum value over the whole global control volume

N Nodal point on the north side of the main control volume

n Face on the north side of the main control volume

NN Nodal point two cells to north from the main control volume

out Exit section

P Main control volume

S Nodal point on the south side of the main control volume

s Face on the south side of the main control volume

SS Nodal point two cells to south from the main control volume

sum Sum of all values over the entire global control volume

W Nodal point on the west side of the main control volume

NOMENCLATURE

w Face on the west side of the main control volume

wall Wall section

WW Nodal point two cells to west from the main control volume

x Faces in the x-direction: east or west

y Faces in the y-direction: north or south

Contents

| | | |
|----------|--|-----------|
| 1 | Introduction | 34 |
| 1.1 | Objectives | 36 |
| 1.1.1 | General Objective | 36 |
| 1.1.2 | Specific Objectives | 36 |
| 1.2 | Organization of this Dissertation | 37 |
| 2 | Fundamental Concepts | 38 |
| 2.1 | Introduction to Microfluidics | 38 |
| 2.1.1 | Micromixers | 41 |
| 2.2 | Vorticity Field | 45 |
| 2.3 | Solution Methods | 48 |
| 2.3.1 | Experimental Tests | 48 |
| 2.3.2 | Analytical Solutions | 49 |
| 2.3.3 | Numerical Solutions | 51 |
| 3 | Numerical Modeling | 54 |
| 3.1 | Equation Systems for Fluid Flows | 55 |
| 3.1.1 | Continuity Equation | 55 |
| 3.1.2 | Momentum Equations | 57 |
| 3.1.3 | Vorticity Equation | 59 |
| 3.1.4 | Stream Function Equation | 60 |
| 3.2 | Discretization Process | 61 |
| 3.2.1 | Finite Volume Method (FVM) | 62 |
| 3.2.2 | Discretization of Differential Equations | 63 |
| 3.2.2.1 | Central Differencing Scheme | 64 |

| | | |
|----------|--|-----------|
| 3.2.2.2 | Upwind Scheme | 66 |
| 3.2.2.3 | Hybrid Differencing Scheme | 68 |
| 3.3 | SIMPLE Algorithm | 70 |
| 3.3.1 | Step 1: Storing values to the variables | 72 |
| 3.3.2 | Step 2: Calculating the link coefficients | 72 |
| 3.3.3 | Step 3: Determining the velocity components via TDMA | 72 |
| 3.3.4 | Step 4: Deriving the velocity correction equations | 75 |
| 3.3.5 | Step 5: Obtaining the pressure correction equation | 76 |
| 3.4 | Post-Processing of the Results | 81 |
| 3.5 | Treatment of the Boundary Conditions | 81 |
| 3.5.1 | Walls: no-slip condition | 81 |
| 3.5.2 | Inlet: Constant velocity | 84 |
| 3.5.3 | Outlet: Constant pressure | 85 |
| 4 | Code Development | 88 |
| 4.1 | Code Structure | 88 |
| 4.1.1 | USER's Files | 88 |
| 4.1.2 | CODE File | 90 |
| 4.2 | Case Studies | 92 |
| 4.2.1 | Rectangular Duct | 92 |
| 4.2.2 | Lid-driven Cavity | 93 |
| 4.2.3 | Bumpy Microchannel | 94 |
| 5 | Results | 96 |
| 5.1 | Verification of the Code | 96 |
| 5.1.1 | Case Study in a Rectangular Duct | 97 |
| 5.1.2 | Case Study in a Lid-driven Cavity | 100 |
| 5.2 | Bumpy Microchannel | 107 |
| 5.2.1 | Device's width: $d = 250 \mu\text{m}$ | 108 |
| 5.2.1.1 | Curvature of bumps: No bumps | 108 |
| 5.2.1.2 | Curvature of bumps: $\alpha = 1$ | 117 |
| 5.2.1.3 | Curvature of bumps: $\alpha = 2$ | 128 |

| | | |
|----------|---|------------|
| 5.2.1.4 | Curvature of Bumps: Overall | 137 |
| 5.2.2 | Device's width: $d = 200 \mu\text{m}$ | 140 |
| 5.2.2.1 | Curvature of bumps: No bumps | 141 |
| 5.2.2.2 | Curvature of bumps: $\alpha = 1$ | 145 |
| 5.2.2.3 | Curvature of bumps: $\alpha = 2$ | 150 |
| 5.2.2.4 | Curvature of Bumps: Overall | 155 |
| 6 | Conclusion | 161 |
| | Bibliography | 166 |
| A | Rectangular Duct Case | 173 |
| A.1 | FLOW File | 173 |
| A.2 | GEOM File | 174 |
| B | Lid-Driven Cavity Case | 177 |
| B.1 | FLOW File | 177 |
| B.2 | GEOM File | 178 |
| C | Bumpy Microchannel Case | 180 |
| C.1 | FLOW File | 180 |
| C.2 | GEOM Files | 181 |
| C.2.1 | Curvature of bumps: no bumps | 181 |
| C.2.2 | Curvature of bumps: $\alpha = 1$ | 183 |
| C.2.3 | Curvature of bumps: $\alpha = 2$ | 186 |
| C.2.4 | Curvature of bumps: $\alpha = 4$ | 189 |
| C.3 | Velocity Fields | 192 |
| C.3.1 | Device's width, $d = 250 \mu\text{m}$ | 192 |
| C.3.1.1 | No bumps, $s = 100 \mu\text{m}$ | 192 |
| C.3.1.2 | No bumps, $Re = 90$ | 193 |
| C.3.1.3 | Curvature of bumps $\alpha = 1$, $s = 100 \mu\text{m}$ | 194 |
| C.3.1.4 | Curvature of bumps $\alpha = 1$, $Re = 90$ | 195 |
| C.3.1.5 | Curvature of bumps $\alpha = 2$, $s = 100 \mu\text{m}$ | 196 |
| C.3.1.6 | Curvature of bumps $\alpha = 2$, $Re = 90$ | 197 |

CONTENTS

| | | |
|---------|--|-----|
| C.3.1.7 | Curvature of bumps $\alpha = 4, s = 100 \mu\text{m}$ | 198 |
| C.3.1.8 | Curvature of bumps $\alpha=4, Re = 90$ | 199 |
| C.3.2 | Device's width, $d = 200 \mu\text{m}$ | 200 |
| C.3.2.1 | No bumps, $s = 100 \mu\text{m}$ | 200 |
| C.3.2.2 | No bumps, $Re = 40$ | 201 |
| C.3.2.3 | Curvature of bumps $\alpha = 1, s = 100 \mu\text{m}$ | 202 |
| C.3.2.4 | Curvature of bumps $\alpha = 1, Re = 40$ | 203 |
| C.3.2.5 | Curvature of bumps $\alpha = 2, s = 100 \mu\text{m}$ | 204 |
| C.3.2.6 | Curvature of bumps $\alpha = 2, Re = 40$ | 205 |
| C.3.2.7 | Curvature of bumps $\alpha = 4, s = 100 \mu\text{m}$ | 206 |
| C.3.2.8 | Curvature of bumps $\alpha=4, Re = 40$ | 207 |
| C.4 | Pressure Fields | 208 |
| C.4.1 | Device's width, $d = 250 \mu\text{m}$ | 208 |
| C.4.1.1 | No bumps, $s = 100 \mu\text{m}$ | 208 |
| C.4.1.2 | No bumps, $Re = 90$ | 209 |
| C.4.1.3 | Curvature of bumps $\alpha = 1, s = 100 \mu\text{m}$ | 210 |
| C.4.1.4 | Curvature of bumps $\alpha = 1, Re = 90$ | 211 |
| C.4.1.5 | Curvature of bumps $\alpha = 2, s = 100 \mu\text{m}$ | 212 |
| C.4.1.6 | Curvature of bumps $\alpha = 2, Re = 90$ | 213 |
| C.4.1.7 | Curvature of bumps $\alpha = 4, s = 100 \mu\text{m}$ | 214 |
| C.4.1.8 | Curvature of bumps $\alpha=4, Re = 90$ | 215 |
| C.4.2 | Device's width, $d = 200 \mu\text{m}$ | 216 |
| C.4.2.1 | No bumps, $s = 100 \mu\text{m}$ | 216 |
| C.4.2.2 | No bumps, $Re = 40$ | 217 |
| C.4.2.3 | Curvature of bumps $\alpha = 1, s = 100 \mu\text{m}$ | 218 |
| C.4.2.4 | Curvature of bumps $\alpha = 1, Re = 40$ | 219 |
| C.4.2.5 | Curvature of bumps $\alpha = 2, s = 100 \mu\text{m}$ | 220 |
| C.4.2.6 | Curvature of bumps $\alpha = 2, Re = 40$ | 221 |
| C.4.2.7 | Curvature of bumps $\alpha = 4, s = 100 \mu\text{m}$ | 222 |
| C.4.2.8 | Curvature of bumps $\alpha=4, Re = 40$ | 222 |
| C.5 | Vorticity Fields | 224 |

| | | |
|---------|--|-----|
| C.5.1 | Device's width, $d = 250 \mu\text{m}$ | 224 |
| C.5.1.1 | No bumps, $s = 100 \mu\text{m}$ | 224 |
| C.5.1.2 | No bumps, $Re = 90$ | 225 |
| C.5.1.3 | Curvature of bumps $\alpha = 1, s = 100 \mu\text{m}$ | 226 |
| C.5.1.4 | Curvature of bumps $\alpha = 1, Re = 90$ | 227 |
| C.5.1.5 | Curvature of bumps $\alpha = 2, s = 100 \mu\text{m}$ | 228 |
| C.5.1.6 | Curvature of bumps $\alpha = 2, Re = 90$ | 229 |
| C.5.1.7 | Curvature of bumps $\alpha = 4, s = 100 \mu\text{m}$ | 230 |
| C.5.1.8 | Curvature of bumps $\alpha=4, Re = 90$ | 231 |
| C.5.2 | Device's width, $d = 200 \mu\text{m}$ | 232 |
| C.5.2.1 | No bumps, $s = 100 \mu\text{m}$ | 232 |
| C.5.2.2 | No bumps, $Re = 40$ | 233 |
| C.5.2.3 | Curvature of bumps $\alpha = 1, s = 100 \mu\text{m}$ | 234 |
| C.5.2.4 | Curvature of bumps $\alpha = 1, Re = 40$ | 235 |
| C.5.2.5 | Curvature of bumps $\alpha = 2, s = 100 \mu\text{m}$ | 236 |
| C.5.2.6 | Curvature of bumps $\alpha = 2, Re = 40$ | 237 |
| C.5.2.7 | Curvature of bumps $\alpha = 4, s = 100 \mu\text{m}$ | 238 |
| C.5.2.8 | Curvature of bumps $\alpha=4, Re = 40$ | 239 |
| C.6 | Stream-Function Fields | 240 |
| C.6.1 | Device's width, $d = 250 \mu\text{m}$ | 240 |
| C.6.1.1 | No bumps, $s = 100 \mu\text{m}$ | 240 |
| C.6.1.2 | No bumps, $Re = 90$ | 241 |
| C.6.1.3 | Curvature of bumps $\alpha = 1, s = 100 \mu\text{m}$ | 242 |
| C.6.1.4 | Curvature of bumps $\alpha = 1, Re = 90$ | 243 |
| C.6.1.5 | Curvature of bumps $\alpha = 2, s = 100 \mu\text{m}$ | 244 |
| C.6.1.6 | Curvature of bumps $\alpha = 2, Re = 90$ | 245 |
| C.6.1.7 | Curvature of bumps $\alpha = 4, s = 100 \mu\text{m}$ | 246 |
| C.6.1.8 | Curvature of bumps $\alpha=4, Re = 90$ | 247 |
| C.6.2 | Device's width, $d = 200 \mu\text{m}$ | 248 |
| C.6.2.1 | No bumps, $s = 100 \mu\text{m}$ | 248 |
| C.6.2.2 | No bumps, $Re = 40$ | 249 |

CONTENTS

| | | |
|---------|--|-----|
| C.6.2.3 | Curvature of bumps $\alpha = 1, s = 100 \mu\text{m}$ | 250 |
| C.6.2.4 | Curvature of bumps $\alpha = 1, Re = 40$ | 251 |
| C.6.2.5 | Curvature of bumps $\alpha = 2, s = 100 \mu\text{m}$ | 252 |
| C.6.2.6 | Curvature of bumps $\alpha = 2, Re = 40$ | 253 |
| C.6.2.7 | Curvature of bumps $\alpha = 4, s = 100 \mu\text{m}$ | 254 |
| C.6.2.8 | Curvature of bumps $\alpha=4, Re = 40$ | 255 |

Chapter 1

Introduction

“Advanced technology changes the way we work and the skills we need, but it also boosts productivity and creates new jobs.”

Alain Dehaze

Computational fluid dynamics (CFD) is a useful alternative for modeling and simulating flow fields, providing accurate results regarding the flow parameters (Khan et al., 2018). This computational approach has been applied in many fields of industry, such as aerospace (Spalart and Venkatakrishnan, 2016), metallurgy (Ramasetti et al., 2018), oil and gas (Raynal et al., 2015), biomedical (Bluestein, 2017), and microfluidics (O’Connor et al., 2016); (Chaves et al., 2020).

New studies have been conducted for miniaturizing systems in order to maintain or even obtain improved results (this process is also known as process intensification). The development of innovative equipment and techniques is focused on reducing: energy consumption, equipment/chemical plant sizes, production capacity ratio, and waste generation (Stankiewicz and Moulijn, 2000). Microfluidics has emerged as a technology that leads to these benefits.

Microfluidics is an area of science that studies fluids flow in channels with micrometric dimensions in a range of tens to hundreds of micrometers (Whitesides, 2006). This area offers many advantages, which are related to the requirement of small quan-

tities of reagents, the separation and detection of materials with high resolution, and the analysis performed in a short time. Those advantages have also allowed applications of microfluidics in molecular analysis (Bruijns et al., 2016), (Farshchi and Hasanzadeh, 2021), biodefense (Tian and Finehout, 2008) (Nasseri et al., 2018), and microelectronics (Sochol et al., 2018) (Potrich et al., 2019).

The current pandemic scenario (2020 and 2021), microfluidics has emerged as a facilitator to assist in the diagnosis, the treatment and the prevention of SARS-CoV-2 cases. In fact, rapid detection procedures with low reagent consumption and high sensitivity are required. For instance, in Brazil, the LumiraDx SARS-CoV-2 antigen test was recently approved by Agência Nacional de Vigilância Sanitária (ANVISA), in which nasal samples are analyzed based on microfluidic immunofluorescence for a qualitative detection of nucleocapsid proteins to diagnose a possible infection by Covid-19 (Hoch, 2021). Besides that, other applications can be: the fabrication of mechanical respirators with velocity and air pressure control (Pearce, 2020), as well as the design of Personal Protective Equipment (PPE) with presence of antiviral agents to prevent the spread of/the contamination by the virus via speaking, coughing or sneezing.

Recently, numerous microdevices have been used in microfluidic platforms that require a rapid mixing like in reactions with fast kinetics, precipitation/crystallization processes (Capretto et al., 2011),(Pan et al., 2020), and in biological processes that depend on the mixture degree of reagents for initiation (Nguyen and Wu, 2005),(Liu et al., 2019). However, microchannels' fluid flow behavior has a strong laminar profile because of the small Reynolds number (Re), where viscous forces dominate over inertial, resulting in a no vortex formation. Furthermore, the vorticity is directly related to mixing and stirring performances where a spin advection is required to the flow. Nonetheless, in a microfluidic pattern study, the stirring and mixing operations are restrained by diffusion transport, which has a low mass throughput, and requires therefore long residence time to produce a sufficiently homogeneous mixture.

The application of transport phenomena concepts in a programming language allows understanding how well-known simulators, such as ANSYS and COMSOL, work. Moreover, these simulators require an additional high cost for acquiring their license, and

their frameworks are usually complicated to be understood by researchers, taking weeks to learn their respective features. Thus, writing a code is an alternative route to predict the fluid flow parameters along a microchannel; moreover, academic research can consider the utilization of the code developed in the framework of the current investigation.

This study investigates the fluid dynamics in a microdevice of converging nozzle coupled to a bumpy microchannel, where vortex formation is evaluated. Also, the investigation is conducted by means of computational fluid dynamics using an in house code. Additionally, the width of the bumpiness microchannel, the curvature of these bumps, the location of the feed and the Reynolds number have been studied concerning the magnitude of vorticity and the pressure drop.

1.1 Objectives

1.1.1 General Objective

The general objective of the current research is the development of a computational fluid dynamics code to evaluate the flow field in microdevices.

1.1.2 Specific Objectives

The specific objectives of this study are as follows:

- To simulate the fluid dynamics in a rectangular duct and in a lid-driven cavity by using the code at low Reynolds numbers and compare them qualitatively and quantitatively with OpenFOAM as a verification step;
 - To analyze the influence of Reynolds number in the fluid dynamics of the flow;
 - To assess how the feed position at a converging nozzle affects angular momentum and produces vortices;
 - To evaluate the intensity of the vorticity in terms of the geometry configuration (width and curvature of bump) of the microdevice;
-

- To calculate the pressure drop for each simulation and finally propose the best microdevice geometry.

1.2 Organization of this Dissertation

Each chapter gives a brief overview of the problem stated. Initially, a basic introduction about CFD, microfluidics and the main goals of this study are presented in Chapter 1. A discussion of microfluidics and the main types of equipment, and some definitions about vorticity, the flow regimes and the methods to evaluate microfluidics cases are incorporated in Chapter 2. In Chapter 3, there is a detailed description of the steps in a CFD simulation, which includes: the equations that describe the studied system, the discretization process by the Finite Volume Method, the hybrid scheme applied, the co-located SIMPLE algorithm and its boundary conditions, and finally the post-processing step. Following this, Chapter 4 gives the structure of the code about what each files are meant to do. Also, the description of the geometry and operating conditions of each case study is presented in this chapter. Finally, Chapter 5 shows the results of all case studies. It includes the verification step by analyzing the rectangular duct and the lid-driven cavity cases, and the fluid dynamics study of a new microdevice with convex bumps. The enhancement of vorticity and pressure drop is mainly evaluated along this chapter regarding the geometry and the Reynolds number. Lastly, a final conclusion about a better microdevice, which provides a high magnitude of vorticity with recirculation along with, and a few final considerations are given in Chapter 6.

Chapter 2

Fundamental Concepts

“Modern technology has become a total phenomenon for civilization, the defining force of a new social order in which efficiency is no longer an option but a necessity imposed on all human activity.”

Jacques Ellul

2.1 Introduction to Microfluidics

Many authors are quite cautious about the definition of microfluidics, mainly the range of the hydraulic diameter; so some prefer specifying it while others are more general. According to Colin (2010), microfluidics is related to flows inside microdevices with hydraulic diameter in the order of $1\ \mu m$; while Nouri et al. (2017) prefer defining microfluidics as a technology of designing and manufacturing of systems with small volume of fluid flowing along small channels. Nonetheless, in this work, microfluidics is interpreted as flows inside devices with width in the order of tens to hundreds micrometers (Whitesides, 2006), just like it was introduced in Chapter 1.

The selection of those definitions aforementioned depends on the methodology and the boundary conditions adapted to the case study. The majority of commercial

simulators apply the continuum assumption of fluid flow, and consequently, all constraints must be assessed in this case. Following this idea, the microdevice dimensions should be projected in a range of tens to hundreds of micrometers to prevent significant effects from collisions of individual molecules in a flow.

Santana et al. (2015) studied a transesterification of vegetable oils with alcohols for biodiesel synthesis in three different T-shaped micromixers, whose hydraulic diameter was less than one millimeter. They evaluated this reaction by applying experimental and numerical methods in which are based on the continuum assumption. Their results show that both methodologies present similar fluid flow behaviors, even for the vegetable oil whose structure is composed of long hydrocarbons (around twenty carbon atoms).

Sen et al. (2020) investigated a continuous synthesis of tributyl phosphate in a microreactor analyzing two different micromixers: the T-junction and the split-and-recombine configurations. The diameter of these micromixers is in the range of hundreds of micrometers. Further, they studied this system experimentally and numerically where the momentum, continuity and the mass transfer equations were applied. They concluded that all simulations for both types of geometry have supported qualitatively the results collected from the experimental analysis.

Nevertheless, low stirring/mixing performance is still an issue for many processes in this field. Firstly, the small dimension affects the dimensionless Reynolds number of these channels; and additionally, the viscous forces prevail over the inertial forces resulting in a regime predominantly laminar. Secondly, the fluid flows in parallel layers along the microdevice, providing a flux of low interaction between its streams without producing any eddies. This effect might ease the prediction of the fluid dynamics parameters; however, the lack of stirring reduces not only the vortex formation but also the heat and mass transfers (Colin, 2010).

In microchannels, the ratio between surface area and volume is quite larger when compared to macrochannels; however, mass transfer by diffusion is still weak throughout the device. A precipitate solution is to propose longer microchannels, resulting in a more contact area between the layers of fluid, and thus providing a higher interaction. However, stretching channels is usually not the best solution due to its longer residence

time and its larger dimensions.

New alternatives have been proposed to project microdevices to intend to economize time, space, and money. Likewise, depending on the case, they should contribute to enhancing the selectivity and the yield of a product in a reaction, or even to control other parameters, such as temperature and pressure, more efficiently than in macroscale processes.

Singh et al. (2020) worked on the analysis of propionic acid extraction followed by flash distillation in serpentine microchannels, and compared the total annual cost of this case with a few conventional cases. They concluded that the extraction efficiency (99.6% and 98.4%) and the recovery in the distillation (73% and 98%) of toluene and n-hexane, respectively, for both operations, present high percentages. In addition, they asserted that the total annual cost may reduce in terms of energy and capital costs with the implementation of microchannels.

Current climate control systems have been projected based on heat pumps with air source using finned microchannels in order to heat the interior of the cabin of electric vehicles. This type of device uses the heat generated by the car to prevent ice accumulation on the surfaces of the heat exchangers on cold days to save more energy. Hong et al. (2020) evaluated a new micro heat exchanger with plain-louvered fins to enhance the frosting and defrosting conditions of the heat pumps of air source in electric vehicles based on the higher heat transfer rate produced. Their results show that this micro heat exchanger presents better performance regarding frosting period and peak heating capacity of the heat pump in 102.7% and 14.0% respectively when compared to the corrugated-louvered fin heat exchanger.

Wang et al. (2019) designed a microreactor coupled to a staggered herringbone grooves mixer in order to intensify the Research Octane Number (RON) selectivity from the isobutane/1-butene alkylation process. They compared this reactor with the traditional one (stirring reactor), and they noticed that the microreactor has a better control of temperature (6 °C) while the macro-reactor has a range from 6 to 13 °C. Another point is, the residence time is also ten times superior (45s x 450s); and additionally, the RON yield and the 1-butene conversion for the microreactor are respectively 98.8% and 95.8%,

while for the stirring reactor, they are 96.7% and 89.1%, respectively.

Santana et al. (2016) studied a transesterification of vegetable oils for biodiesel synthesis in a conventional batch reactor and in a microreactor. They concluded that the conventional one produces biodiesel with 94.1% of yield in 180 minutes, while the microreactors has 95.8% of biodiesel yield in a quite shorter time of only one minute.

In this way, several industrial processes demand a better interaction between fluids as, for example, in chemical reactions, extractions and also anti-solvent crystallizations. However, as the molecular diffusion usually prevails in laminar flows in microchannels, its residence time to reach a high percentage of yield tends to be longer, requiring a more extensive microchannel. Thus, micromixers have been extensively investigated in order to intensify this interaction between the fluid streams. There are several types of them, and they will be presented in the next section.

2.1.1 Micromixers

In microflows, two main types of micromixers are recommended to increase the interaction of fluids in a flow: the active and the passive micromixers. Active micromixers require an external energy source to induce a randomly flow of fluid, for example, temperature, periodic pressure, and electromagnetic fields (Khaydarov et al., 2018). Although active micromixers regularly present a fast response with high stirring and mixing performance generating vortices, they usually are expensive and demand space to embed additional elements, represented by the external source or by the addition of a new separation process.

Nouri et al. (2017) studied experimentally and numerically a coupling of a magnetic field (neodymium magnet) on a micromixer. They used a Y-shaped micromixer with two fluids: water and ferrofluid (water with nanoparticles of iron oxide - Fe_3O_4). This system has resulted in an improvement of the mixing index from 8% (without magnetic field) to 90% with a fast response when the magnetization is applied; and besides, there is no source of electricity.

Another active micromixer application was analyzed by Ahmed et al. (2009).

They evaluated a coupling of an acoustic transducer on a Y-shaped micromixer to produce ultrasonic waves. These waves induce a pressure variation in the flow, resulting in an enhance of the mixing performance. Likewise, there is an air bubble trapped in a horse-shoe inside the microchannel, whose objective is to vibrate at its resonance frequency generating perturbation around the membrane. They concluded that their micromixer can provide an excellent homogenized mixing spending seven milliseconds.

On the other hand, passive micromixers depend just the geometric structure, and they can still be divided into two types: laminar (based on increasing the diffusion transport at a molecular level) and convective micromixers (based on proposing a chaotic advection in the flow) (Khaydarov et al., 2018).

The stirring performance in laminar micromixers is limited to the interfacial area between the parallel layers of fluid. Additionally, there are two alternatives to be applied in these microdevices: to stretch their lengths or to decrease their hydraulic diameters (it raises the ratio between interfacial area and volume). These micromixers are commonly represented by T-shaped and Y-shaped mixers (Orsi et al., 2013),(Cortes-Quiroz et al., 2014). Moreover, they are often used as reference to the design of active micromixers. Nouri et al. (2017) and Ahmed et al. (2009) compared the mixing performance with and without magnetization and acoustic waves, respectively; and they concluded that this type of mixer does not contribute to a mixing process at high Re . Thus, straight laminar micromixers are not usually applied to a reaction system due to their slow response and low performance of mixing and stirring.

A convective micromixer produces, in general, vortices that increase the mass transfer during the advection process, enhancing the inertial forces by increasing the Reynolds number. The mixing process in this type of micromixer is influenced by a chaotic advection where fluid streamlines change their directions due to the device's geometry configuration (or due to an external energy source), creating transversal mass transport along with the flow. Some researchers have analyzed many convective micromixers with: curved channels (Alam and Kim, 2012), (Vatankhah and Shamloo, 2018), (Mashaei et al., 2020), a T-shaped modified (Cortes-Quiroz et al., 2014), waviness channels (Chen et al., 2016), (Mondal et al., 2019), a stacking E-shaped (Chen and Shen, 2017), obstacles as

ribs, chambers and staggered herringbone grooves (Borghain et al., 2018), (Wang et al., 2019), and so forth.

A spiral micromixer was proposed by Vatankhah and Shamloo (2018). They evaluated many parameters in the geometry configuration, such as Reynolds number, diffusivity coefficient, initial radius length, rectangular cross sections and mixing angle in the inlet (they applied a Y-shaped in the entrance of the mixer). Their results of mixing performance inside this mixer are around 80% of mixing, and many simulations suggested to stretch the length of this microchannel until over ten millimeters. Besides, the pressure drop is only 12% superior when compared to the straight channel at $Re = 100$. Additionally, Mashaei et al. (2020) also studied how Re , the mixing index, the mixing performance and the pressure drop are influenced in two types of curved T-shaped micromixers with four successive quadrant units in a planar and in a non-planar arrangements. They concluded that the modified curved (non-planar) micromixer generates asymmetrical streamlines along the flow, and also, the narrowing of its channel contributes to a better mixing performance. Likewise, this mixer presents an increase of about 100% and 23% of mixing index and pressure drop, respectively, when compared to the simple curved mixer (the planar one). Lastly, at $Re = 80$, the mixing index and the pressure drop are about 100% and 2.2 kPa, respectively, for the modified device; meanwhile, when $Re \simeq 1$, the mixing index is also approximately 100%.

Cortes-Quiroz et al. (2014) compared the typical T-shaped with a 3-D T-shaped mixer, where the two inlets are set at different z -coordinates. Their results show a fast response of mixing in the 3-D mixer than in the typical T-shaped mixer, while the shear stress is similar in both cases. The best mixing index was around 70% at the outlet of the channel. Moreover, Ortega-Casanova and Lai (2018) analyzed how the mixing efficiency is affected by multiple inlets (from 2 to 7) in a basic T-shaped with a rectangular chamber downstream with two angled bars at low Re and high Schmidt numbers (Sc). They noticed that when $Re = 0.29$ and $Sc = 10.10^3$, the mixing index enhances from 14% to 80% when the number of inlets varies from 2 (traditional T-shaped) to 7 (triple cross-shaped), and after comparing with the other simulations, they concluded that this one - with seven inlets - has the optimal inlet configuration in terms of the mixing efficiency as a micromixer.

Chen et al. (2020) investigated the fluid dynamic along a micromixer based on the fractal-like tree principle at the entrance region using both numerical simulations and experimental analysis. All proposed geometries have microchannels with diameters ranging from 0.25 mm to 1.00 mm, and also, momentum, continuity and mass transfer equations were performed in order to maximize the mixing performance concerning the geometry configuration and operating conditions. They concluded that the increase of the level of the fractal dimension, the angle between the branches, and Reynolds number (when $Re > 10$) contributes to a better mixing efficiency from the numerical and experimental analyzes ($\simeq 96\%$). Besides, the pressure drop at $Re = 100$ present a range from 17.5 to 25.0 kPa in all geometries.

Two different wavy micromixers - called raccoon and serpentine - were analyzed by Mondal et al. (2019). The authors evaluated how the mixing and the pressure drop change for different values of Reynolds numbers (Re), Schmidt number (Sc), and amplitude and wavelength of the waviness in the micromixers. They determined that the serpentine mixer offers a minimum mixing cost in the following conditions: $Re = 100$, $Sc = 25$, amplitude of waviness equal to 0.45, and wavelength of the waviness equal to 12 (mixing index and pressure drop are approximately 60% and 1.5 kPa, respectively); and consequently, this configuration represents the best design of micromixer.

Chen et al. (2016) studied experimentally and numerically six types of serpentine micromixers in a range of Re from 0.1 to 100. They asserted that the three best arrangements in terms of mixing performance are the multi-wave, the zig-zag and the square-wave configurations where this last one has the highest mixing efficiency. They noticed that its sharper turns with long straight paths favor the increase of mixing along the path (95% at $Re=100$). However, this micromixer also has the highest pressure drop (about 6 kPa at $Re=50$) than the other two (approximately 3.5 kPa at $Re=50$) due to its geometry.

Another increasing strategy to provoke this chaotic advection is to couple some obstacles along the flow. Borgohain et al. (2018) investigated a T-shaped micromixer with curved ribs and compared it with another of straight ones. In addition, they conducted some studies about the inlet Re , and the number, the size, and the angle of these ribs.

They affirmed that the micromixer with curved bars generates a better mixing index (61.3% x 47.6%) with lower pressure drop (193.1 Pa x 276.3 Pa) when compared to the device with straight bars at low Re . For $Re = 60$, the maximum mixing index is 85% with a pressure drop equal to about 20 kPa. Besides, the mixing performance is directly influenced by the increase of the number of ribs; meanwhile, the height, and the angle have a no trending performance of their values.

Convective micromixers have been studied due to their simplicity, low-priced, and small portability. Researchers have been proposing geometry configurations that produce rotations in a fluid resulting in a high stirring and mixing performances, and hence, provoking a minimum cost of time, money, and space. All these published works verified an improvement in the mixing performance at high Re (greater than approximately 100) due to the increase of the inertial forces. On the other hand, even when there are insertion of obstacles or asymmetrical arrangements, flows with a low Re do not contribute to the formation of recirculation zones or secondary streams. Thereby, this type of mixer is investigated in this work in order to intensify the rotational motion in a range of Re less than 100.

2.2 Vorticity Field

As presented previously, chaotic advection can be created through obstacles, junctions, curved channels and sharp bends along the flow. However, another factor can also influence the interaction between fluid streams to enhance the mixing/stirring; and, it is the vorticity, which measures the rate of rotation of a solid body about its own center of mass while it is moving through a flow. This parameter can be calculated through the curl of the velocity field, which in 2D cases, comes down to just one component normal to the xy -plane in the z -direction.

In this way, 2D figures are not always able to transmit the regions with strong vorticity since their values are expressed in the z -direction, therefore, there is a necessity to visualize both the vorticity field in the z -component and the streamlines along the xy -plane.

Some factors can influence the rotation of a fluid particle; for example, the viscous boundary layer next to the wall that pulls the fluid making it spin, as shown in Figure 2.1. The non-uniform velocity profile along the y -axis favors the increase of the vorticity in which, as the layer of fluid moves away from the wall, the tendency is its rotational motion also decreases (Davidson, 2004). The particles in the streamlines close to the center-line of the duct flow faster with no effect of rotation, while when they are closer to the wall, they are more affected by the viscous forces and, consequently, their velocity is slower. Another analysis is the rotation directions of the fluid elements are opposed from each wall, so if the particles on the upper wall rotate counterclockwise, then, on the lower wall, they will spin clockwise.

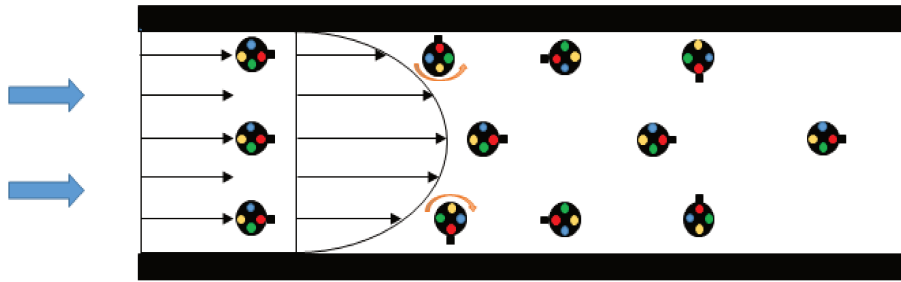


Figure 2.1: Rotation of the particles near the walls caused by the shear stress.

Another parameter that can influence the vorticity is the geometry of the channel. Then, when the flow undergoes a deceleration caused by a constriction (throat), as illustrated in Figure 2.2, the boundary layer is also affected by the addition of a viscous contribution. Thus, the main streamlines tend to follow the main path resulting in an extension of the boundary layer away from the surface immediately after the constriction by both viscous and advective forces. In this way, the abrupt expansion of the boundary layer in decelerated flows, with an increase in the pressure gradient in the flow direction, results in the phenomenon called *separation*, in which the streamlines near the wall change their flow direction. Therefore, for high values of positive pressure gradient, the streamline parallel to the wall tends to flow in the opposite direction, colliding and joining the main flow, thus creating zones of recirculation. Furthermore, at low Reynolds numbers ($Re < 4$), it is noticed that the vorticity is induced by diffusion, while for higher Re ($4 < Re < 200$), the advection starts having its effect in the vorticity right after the

throat (Kundu and Cohen, 2004).

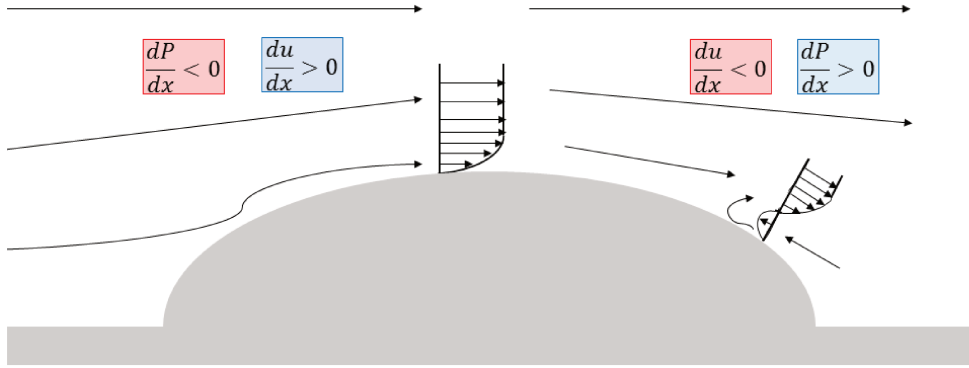


Figure 2.2: Rotation of the particles caused by the deceleration of the fluid with subsequent positive pressure gradient (Adapted from Kundu and Cohen (2004)).

Lastly, the vorticity also depends on the narrowing of the channel where the fluid elements are being stretched, resulting in a variation of their moment of inertia. This case can be exemplified when a large amount of liquid is being drained from a sink, in which it is possible to notice an intense vortex formation upstream of the fluid outlet. However, there is no vortex stretching contribution in flows in 2D because, mathematically, the term referring to the stretch $(\vec{\omega} \cdot \vec{\nabla}) \vec{u}$ is zero (Davidson, 2004).

The geometry of the microdevice and the Reynolds number directly influence the formation of vortices, resulting in an enhancement of the mass transfer rate between the fluid streamlines. In this way, the flow can be identified in three different regimes: stratified, vortex, and engulfment regimes. Thus, the first one is characterized by a flow with lamina of fluid moving side by side being controlled by the molecular diffusion regardless of the geometry. Therefore, this regime presents a low Re and long residence time. In sequence, the vortex regime presents the creation of symmetrical vortices as Re increases, however, diffusion still prevails, and consequently, the higher velocity parallel with a shorter residence time favors a decrease of the mixing performance at the outlet. Ultimately, the engulfment regime shows an improvement of the mixing due to the asymmetry caused by the chaotic advection from the geometry configuration of the channel and the increase of Re . Therefore, the streamlines begin to intertwine, expanding the surface area between them with a shorter time in order to enhance the mixing performance (Dreher et al., 2009), (Galletti et al., 2012), (Mondal et al., 2019).

2.3 Solution Methods

A study of the fluid flow parameters in a micromixer can be performed and determined experimentally, numerically, and analytically. However, there are advantages and disadvantages to the employment of these solution methods. The following subsections presents the description and the main characteristics of these methods.

2.3.1 Experimental Tests

Experimental studies have had a significant impact on the science because thereafter, theories could be validated, resulting in discoveries, and consequently, in the postulation of equations (such as the conservation equations). Basically, Patankar (1980) summaries this effect: "*experiment leads and computation follows*". However, experimental tests continue being widely applied nowadays, even being the oldest solution method. In microfluidics, they can still represent the real behavior of fluid flow parameters inside a microdevice when under the right conditions. Nevertheless, experiments might not be representative in complex cases.

Many parameters may affect the results from experimental tests producing errors, for example, human performance, non-calibrated equipment, unstable boundary conditions, so on. Moreover, this type of method is also limited to the financial investment, the scale, and the complexity of the case study. For instance, drug test for humans is a complicated case related to the correct environment, because the main experimental tools to predict how a drug behaves in a human body are by animal tests and cell in dishes. (Hamilton, 2013).

Most researchers have worked in case studies of simple geometry configurations of micromixers, intending to predict the fluid dynamics parameters experimentally and numerically. Besides, applying the same boundary conditions, it is expected to obtain accurate results from both methodologies like Santana (2016), Nouri et al. (2017), Khaydarov et al. (2018) and Shaha et al. (2019) could achieve on their studies.

2.3.2 Analytical Solutions

In a fluid dynamics pattern study, the governing conservation equations that describe a flow are limited to the continuum assumption. These equations already include non-linear and differential terms (such as convective term in momentum equations), and a time-step term, affecting the complexity of the analytical solution. Consequently, most problems do not have a direct analytical solution, and thus, there is a necessity to set a few assumptions until to achieve the final equation. For example, Jaiswal et al. (2011) and Mojtabi and Deville (2015) solved dispersion and flow problems, respectively, in macroscale; however, despite all assumptions set by them, their analytical solutions should just be applied in fluid moving in one-dimensional with fully developed flow.

In a laminar regime, many researchers take as a starting point the Stokes flow ($Re \ll 1$), whose fluid creeps along the microchannel. This type of flow treats inertial forces as smaller than viscous forces, and thus, this non-linear term may be despised in the momentum equations. The following equation refers to the Stokes flow in x -direction, neglecting the transient term, and the advective and the volumetric forces (gravity or external electric field, for example).

$$\frac{1}{\rho} \frac{dP}{dx} = \nu \left(\frac{\partial^2 u}{\partial y^2} + \frac{\partial^2 u}{\partial z^2} \right), \quad (2.1)$$

Where ρ is the density of the fluid, ν is the kinematic viscosity of the fluid, u is the velocity component flowing in the x -direction, and P is the hydrodynamic pressure. Nguyen (2008) studied the velocity profile in four different cross-sections (Figure 2.3), where the fluid flows at low Re and the flow is governed by the pressure drop under the assumptions of incompressible, viscid, steady, and parallel flow. The boundary conditions are no-slip at the wall and symmetry at the center. Equations (2.2)-(2.5) represent the analytical solution for those four cases:

(a) Circle

$$\bar{u} = \frac{1}{8\mu} \left(-\frac{dP}{dx} \right) r^2, \quad (2.2)$$

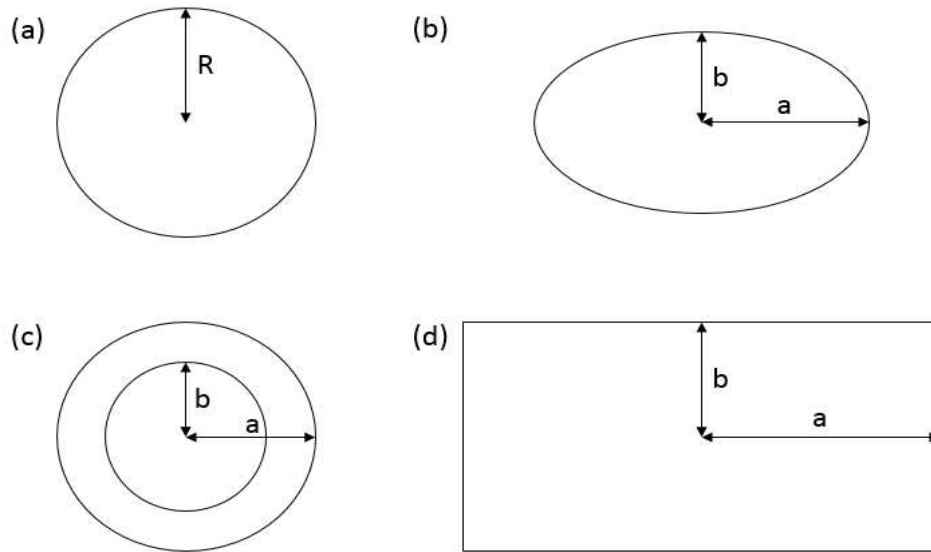


Figure 2.3: Cross-sections of channels: (a) circle; (b) ellipse; (c) concentric annulus; (d) rectangle

Where μ is the dynamic viscosity of the fluid, and \bar{u} is the mean velocity in the channel.

(b) Ellipse

$$\bar{u} = \frac{1}{4\mu} \left(-\frac{dP}{dx} \right) \frac{a^2 b^2}{a^2 + b^2}, \quad (2.3)$$

Where a and b are the semi-major axis and the semi-minor axis of the ellipse, respectively.

(c) Concentric annulus

$$\bar{u} = \frac{1}{8\mu} \left(-\frac{dP}{dx} \right) \left[a^2 + b^2 - \frac{a^2 - b^2}{\ln(a/b)} \right], \quad (2.4)$$

Where a and b are the outer and inner radius respectively of the concentric annulus.

(d) Rectangle

$$\bar{u} = \frac{a^2}{3\mu} \left(-\frac{dP}{dx} \right) \left\{ 1 - \frac{192a}{\pi^5 b} \sum_{n=1}^{\infty} \frac{\tanh[(2n-1)\pi b/2a]}{(2n-1)^5} \right\}, \quad (2.5)$$

Where a and b are the lengths in x-direction and y-direction respectively of the rectangle.

Furthermore, a dimensionless concentration distribution c^* (where $c^* = c/c_0$ being solvent $c = 0$, and solute $c = c_0$) can be derived in laminar micromixers when, for example, a fluid feeds a T-shaped mixer, and flows with many parallel streamlines as laminae along a flat microchannel. Therefore, assuming a uniform velocity u with constant fluid viscosity, according to Nguyen and Wu (2005), the dimensionless concentration c^* is given as:

$$c^*(x^*, y^*) = r + \frac{2}{\pi} \sum_{N=1}^{\infty} \frac{\sin(N\pi r)}{N} \cos(N\pi y^*) \cdot e^{-\frac{2N^2\pi^2}{Pe + \sqrt{Pe^2 + 4N^2\pi^2}} x^*}, \quad (2.6)$$

Where $x^* = x/D$, and $y^* = y/D$ are the dimensionless positions, D is the diameter of the channel, $Pe = uD/D_{A,B}$ is the Peclet number, and $D_{A,B}$ is the diffusion coefficient, and N is the number of inlets. This equation describes the flow in laminar micromixers with no chaotic advection. Therefore, it can be applied to fluid dynamics investigations in micro-scale along with T-shaped mixers as studies of scaling laws, butterfly effect, so forth (Nguyen and Wu, 2005).

As mentioned in section 2.1.1 (Micromixers), convective micromixers are related to stimulating secondary flows inside the device, and thereby increasing the advective forces. In this case, including the convective term in the conservation equations becomes essential. Likewise, it is still a severe study to predict the velocity profile analytically in these mixers where the fluid flows in all directions. In addition, these solutions depend on the cross-section configuration, the boundary conditions, and mainly the assumptions, turning this solution method not appropriate to complex case studies.

2.3.3 Numerical Solutions

The conservation equations, which describe the fluid behavior in channels, do not present an analytical solution in their full form. In contrast to analytical solutions, numerical solutions are proposed to solve these equations with all their physical terms

with assistance of computers, representing, therefore, the fluid dynamics behavior inside a device based on the theoretical model.

Comparing with experimental investigations, numerical solutions usually require low costs to design and to execute a case study; need a short time to perform many analyses; and simulate realistic and ideal scenarios to obtain complete information about all relevant parameters.

In this context, the governing differential equations are discretized by using a numerical scheme approach, while the overall control volume is divided into cells with smaller dimensions. These equations are employed in all small cells from the domain, and they are limited by a few parameters as consistency, stability, and convergence of the numerical scheme chosen (Versteeg and Malalasekera, 2007). Thus, there is the application of a resolution method (a solver) for the systems of equations where the fluid flow parameters are linked each other. Thereafter, the final results can be analyzed by post-processing them in a visualization software. All these steps demand to be defined and developed in a CFD simulation (Hirsch, 2007). The description of each step is better sustained in Chapter 3.

Many numerical schemes can be applied in CFD simulations, such as central differencing, upwind, hybrid, QUICK (Quadratic Upstream Interpolation For Convective Kinetics), TVD (Total Variation Diminishing), so on (Versteeg and Malalasekera, 2007). The selection of the best numerical approach is directly related to the model applied and its boundary conditions. Moreover, there are many pressure-velocity coupling algorithms (iterative methods) that can be employed in steady-state for incompressible fluid; for example, SIMPLE, SIMPLE-Consistent (SIMPLEC), SIMPLE-Revised (SIMPLER), CTS SIMPLE (Consistent Time Step SIMPLE) and FIMOSE (Fully Implicit Method For Operator-Split Equation) (Chao and Ho, 1989); on the other hand, for transient flows, the use of PISO (Pressure-Implicit Split Operator) and PIMPLE (merged PISO-SIMPLE) algorithms are usually applied to the simulation.

In microfluidics, a usual numerical problem is related to the pressure drop. These methods aforementioned based on the pressure-velocity coupling might get lost in numerical precision error when the outlet pressure is in order of 10^5 Pa. The fact is

that cells with micrometers of dimension result in small pressure gradient (less than 1 mPa); and in addition, these values might be registered less than the ninth decimal place. However, to prevent that precision error, the gauge pressure should be inserted into the momentum equations (Mazumder, 2018). Chapter 3 will demonstrate how this parameter is applied to the numerical solution.

Comparing these three analysis methods, numerical simulation by using CFD is a promising alternative to acquiring relevant information about the flow pattern in microchannels, and thus, the possibility to optimize the operating conditions of microfluidic devices (Mott et al., 2009).

Chapter 3

Numerical Modeling

“What distinguishes a mathematical model from, say, a poem, a song, a portrait or any other kind of “model,” is that the mathematical model is an image or picture of reality painted with logical symbols instead of with words, sounds or watercolors.”

John L. Casti

Chapter 2 showed theoretically how the concept of numerical solutions is related to CFD cases. Now, in this chapter, it will be described, in detail, all steps that comprise the study of numerical fluid dynamics. According to Hirsch (2007), a CFD simulation presents four basic components:

1. Mathematical model selection;
2. Discretization process;
3. Resolution step;
4. Post-processing of results.

The code was written following these steps, whose descriptions are present in the next sections.

3.1 Equation Systems for Fluid Flows

The first step is to apply the equations of transport phenomena that describe the flow along the channel. The main conservation equations are:

1. Conservation of mass: continuity equation;
2. Conservation of momentum: Navier-Stokes equation;
3. Conservation of energy.

All these equations are related to three essential parameters of flows: pressure, velocity, and temperature fields. In micromixers, fluids carry one or more species of substances; moreover, these molecules might react resulting in products, and in this case, other equations for the conservation of each species would be required to the equation system (Nguyen, 2008).

In this work, only one fluid flows along the convective microdevice; thus, there is no mixing or chemical reaction. Besides, the thermal effects are neglected, and also, the results are based on a two-dimensional case. Therefore, the governing conservation equations at steady state applied to the code are: continuity equation and momentum equations in x-direction and y-direction. Additionally, two more equations were included: vorticity and stream-function equations in order to measure the rotation and the recirculation of the fluid elements as they flow.

3.1.1 Continuity Equation

The mass conservation is denoted by the variation of mass flux with a given volume (Figure 3.1) due to the quantity of material that is crossing the surface since mass can not be created or destroyed (Hirsch, 2007).

The mass amount m in a single cell from this volume can be represented by the equation:

$$m = \rho V, \tag{3.1}$$

Where ρ is the fluid density; and V is the cell volume. The total mass M in the whole grid can be calculated by integrating the equation (3.1) into the entire control volume:

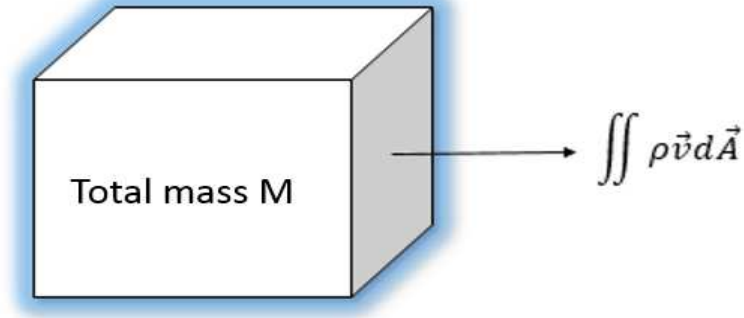


Figure 3.1: Representation of a 3-D control volume.

$$M = \int \rho dV, \quad (3.2)$$

The following equation represents how the variation per unit time of the total mass in Figure 3.1 is related to the mass flux that crosses the borders of each cell. The normal vector on the face of the cells points outward, and thus, it is necessary to introduce the minus sign in the mass flux to contribute to a positive contribution at the inlet and a negative contribution at the outlet.

$$\frac{dM}{dt} = \int \frac{\partial}{\partial t} \rho dV = - \int \rho \vec{v} d\vec{A}, \quad (3.3)$$

$$\int \frac{\partial}{\partial t} \rho dV + \int \rho \vec{v} d\vec{A} = 0, \quad (3.4)$$

Equation (3.4) represents the integral form of the continuity equation. However, another way to present the continuity equation is by its derivative form. Therefore, applying the Gauss divergence theorem to the flow term:

$$\int \frac{\partial}{\partial t} \rho dV + \int \vec{\nabla} \cdot (\rho \vec{v}) dV = 0, \quad (3.5)$$

It can be written by coupling both volume integrals dV into one integral:

$$\int \left[\frac{\partial \rho}{\partial t} + \vec{\nabla} \cdot (\rho \vec{v}) \right] dV = 0, \quad (3.6)$$

Equation (3.6) applies to any volume, in such a way that for the expression to be valid, the integrating needs to be equal to zero, which leads to:

$$\frac{\partial \rho}{\partial t} + \vec{\nabla} \cdot (\rho \vec{v}) = 0, \quad (3.7)$$

Equation (3.7) represents the continuity equation in its differential form.

In this work, a fluid (liquid phase) flows in steady-state along a microchannel. Likewise, the pressure gradient and the temperature do not affect the fluid density, and thus, ρ is constant (incompressible fluid). Moreover, this flow was analyzed in 2-D. Therefore, equation (3.7) can be simplified to:

$$\rho \left(\frac{\partial u}{\partial x} + \frac{\partial v}{\partial y} \right) = 0, \quad (3.8)$$

Equation (3.8) was implemented in the code by applying the SIMPLE algorithm (section 3.3).

3.1.2 Momentum Equations

Similar to mass conservation, the momentum property ($m\vec{v}$) needs to be conserved for any volume. There is also the variation term (accumulation or loss) and the flux contribution through the surface. However, in this case, from Newton's law, some forces influence the variation of momentum in the control volume: external volume forces (\vec{f}_e) and internal forces ($\vec{\tau} - P\vec{\delta}$).

External volume forces are, for example, the action of gravity, electric, or magnetic fields, while internal forces (surface sources) include the viscous effects ($\vec{\tau}$) and the pressure field (P). Thus, based on Hirsch (2007), the momentum equation can be expressed in its integral form based on Figure 3.1 as follows:

$$\int \frac{\partial(\rho \vec{v})}{\partial t} dV + \int \rho \vec{v} (\vec{v} \cdot d\vec{A}) = \int \rho \vec{f}_e dV + \int \vec{\tau} \cdot d\vec{A} - \int P \vec{\delta} \cdot d\vec{A}, \quad (3.9)$$

Where \vec{v} is the velocity vector; and $\vec{\delta}$ is the Kronecker delta. Similarly to continuity equation's demonstration, Gauss divergence theorem was applied to equation (3.9):

$$\int \frac{\partial(\rho\vec{v})}{\partial t} dV + \int \vec{\nabla} \cdot (\rho\vec{v}\vec{v}) dV = \int (\rho\vec{f}_e) dV + \int (\vec{\nabla} \cdot \vec{\tau}) dV - \int (\vec{\nabla} P) dV, \quad (3.10)$$

And, consequently:

$$\frac{\partial(\rho\vec{v})}{\partial t} + \vec{\nabla} \cdot (\rho\vec{v}\vec{v}) = \rho\vec{f}_e + \vec{\nabla} \cdot \vec{\tau} - \vec{\nabla} P, \quad (3.11)$$

Where the first and second terms of the equation (3.11) indicate the variation of momentum flux in time per unit volume and the net flow of momentum out of the fluid element per unit volume, respectively. These terms can be rewritten as:

$$\frac{\partial(\rho\vec{v})}{\partial t} + \vec{\nabla} \cdot (\rho\vec{v}\vec{v}) = \rho \left[\frac{\partial\vec{v}}{\partial t} + \vec{v} \cdot \vec{\nabla}\vec{v} \right] + \vec{v} \left[\frac{\partial\rho}{\partial t} + \vec{\nabla} \cdot (\rho\vec{v}) \right], \quad (3.12)$$

Replacing equation (3.7) into equation (3.12), the differential form of the momentum equation can be expressed:

$$\rho \left[\frac{\partial\vec{v}}{\partial t} + \vec{v} \cdot \vec{\nabla}\vec{v} \right] = \rho\vec{f}_e + \vec{\nabla} \cdot \vec{\tau} - \vec{\nabla} P, \quad (3.13)$$

The demonstration for the viscous shear stress tensor ($\vec{\tau}$) was presented by Hirsch (2007) in the following equation:

$$\vec{\tau} = \mu \left[\left(\frac{\partial v_j}{\partial x_1} + \frac{\partial v_i}{\partial x_j} \right) - \frac{2}{3} (\vec{\nabla} \cdot \vec{v}) \vec{\delta} \right], \quad (3.14)$$

The case study analyzed in this work has evaluated an incompressible fluid flowing ($(\vec{\nabla} \cdot \vec{v}) = 0$ from the continuity equation) in 2-D in a steady-state, with no action of external volume forces. Therefore, equation (3.13) is expressed by:

$$\rho \vec{v} \cdot \vec{\nabla} \vec{v} = \vec{\nabla} \cdot \left(\frac{\partial v_j}{\partial x_1} + \frac{\partial v_i}{\partial x_j} \right) - \vec{\nabla} P, \quad (3.15)$$

And, finally, equation (3.15) can generate two equations for the x -direction (u -velocity), and for the y -direction (v -velocity) as follows:

(a) Momentum equation in x -direction:

$$\rho \left(u \frac{\partial u}{\partial x} + v \frac{\partial u}{\partial y} \right) = -\frac{dP}{dx} + \mu \left(\frac{\partial^2 u}{\partial x^2} + \frac{\partial^2 u}{\partial y^2} \right), \quad (3.16)$$

(b) Momentum equation in y -direction:

$$\rho \left(u \frac{\partial v}{\partial x} + v \frac{\partial v}{\partial y} \right) = -\frac{dP}{dy} + \mu \left(\frac{\partial^2 v}{\partial x^2} + \frac{\partial^2 v}{\partial y^2} \right), \quad (3.17)$$

Continuity and momentum equations were discretized before being included in the SIMPLE algorithm.

3.1.3 Vorticity Equation

Particles of fluid may rotate along a flow in three-dimensional field due to a velocity gradient. The vector for the particle rotation can be represented by equation 3.18:

$$\vec{\omega} = \omega_x \cdot \hat{i} + \omega_y \cdot \hat{j} + \omega_z \cdot \hat{k}, \quad (3.18)$$

Where ω_x is the rotation in the x -direction, ω_y is in the y -direction and ω_z is in the z -direction. Besides, each component can be determined by calculating the curl of the velocity vector as follows:

$$\vec{\omega} = \nabla \times \vec{v} = \begin{bmatrix} \hat{i} & \hat{j} & \hat{k} \\ \frac{\partial}{\partial x} & \frac{\partial}{\partial y} & \frac{\partial}{\partial z} \\ u & v & w \end{bmatrix} = \left(\frac{\partial w}{\partial y} - \frac{\partial v}{\partial z} \right) \hat{i} + \left(\frac{\partial u}{\partial z} - \frac{\partial w}{\partial x} \right) \hat{j} + \left(\frac{\partial v}{\partial x} - \frac{\partial u}{\partial y} \right) \hat{k}, \quad (3.19)$$

Since these analyzes have been performed in 2-D, the derivative in terms of the z is vanished ($\frac{\partial f(x)}{\partial z} = 0$), and also velocity vector \vec{v} can be summarized to only $\vec{v} = (u, v, 0)$. Thereby, the equation 3.19 can be simplified to:

$$\vec{\omega} = \left(\frac{\partial v}{\partial x} - \frac{\partial u}{\partial y} \right) \hat{k} = \omega_z, \quad (3.20)$$

Thus, the code has been based on the discretized form of the equation 3.20, and the implementation of this equation is shown in the following sections.

3.1.4 Stream Function Equation

The last equation inserted into the code was the stream function equation. This scalar parameter ψ helps to study the rotation for the flow where its contours represent the streamlines. Moreover, this scalar can be represented by the velocity components as shown below (Fox et al., 2011):

$$u = \frac{\partial \psi}{\partial y}, \quad (3.21)$$

$$v = -\frac{\partial \psi}{\partial x}, \quad (3.22)$$

These equations show that the variation of two streamlines is equal to the velocity component times its respective cross-sectional area in a 2-D situation ($\partial\psi = u\partial y$ and $-\partial\psi = v\partial x$), resulting in the volume flow passing through the contours of these streamlines.

In addition, the velocity components from the continuity equation (equation 3.8) can be replaced by the stream function by using the equations 3.21 and 3.22:

$$\left[\frac{\partial}{\partial x} \left(\frac{\partial \psi}{\partial y} \right) + \frac{\partial}{\partial y} \left(-\frac{\partial \psi}{\partial x} \right) \right] = 0, \quad (3.23)$$

Therefore, the mass conservation can also be satisfied in terms of ψ via equation 3.23, and consequently, it can be a parameter to verify whether the convergence for the stream function field is satisfactory or not. Furthermore, this scalar can also be written

with respect to vorticity ω_z by replacing the velocity components in equation 3.20 by equations 3.21 and 3.22 as follows:

$$\left(\frac{\partial^2\psi}{\partial x^2} + \frac{\partial^2\psi}{\partial y^2}\right) = -\omega_z, \quad (3.24)$$

Equation 3.24 was discretized and implemented in the code right after the convergence of the equation for ω_z . The next section shows the procedure applied to discretize both space and equations.

3.2 Discretization Process

The discretization process is divided into two steps: space and equation discretizations. The discretization of the global volume is basically the grid generation where the flow domain is divided into small cells, distributing points over the whole space. The accuracy of a numerical solution is influenced by the number of cells in the grid, and how smaller they are. Furthermore, the fluid dynamics parameters are set in these grid points. The most common grid discretization methods are the Finite Difference Method (FDM), the Finite Element Method (FEM) and the Finite Volume Method (FVM) (Hirsch, 2007). The last one is inserted into the discretization process in this study.

The second step includes the discretization of the mathematical models that were presented in section 3.1. Once the grid is generated, and the fluid dynamic parameters are stored in the nodal points, a linkage between these points is necessary by the application of the conservation equations. However, these equations are in the differential form, and an approximation needs to be considered. Therefore, all mathematical operators require to be transformed into arithmetic operations on each control volume (Hirsch, 2007). The code was implemented using a numerical scheme named hybrid differencing scheme.

The discretization process on micro-scale behaves similarly to systems on macro-scale. Nevertheless, the main challenges are related to the approximation that comes from the non-linearity of the momentum equation (convective term) (Colin, 2010), and the calculation of the pressure field (Mazumder, 2018).

3.2.1 Finite Volume Method (FVM)

The FVM associates a control volume (refined cell) to a nodal point, and consequently, applies the conservation equations to this volume. In other words, a small cell is related to a mesh point located, for example, in its center. Likewise, the FVM directly adjusts the conservation equations by discretizing the previous equations in the integral form to any volume. In addition, this technique still can be applied in structured and unstructured grids. Therefore, all these factors with FVM conceptual simplicity make this method to be widely implemented in most simulators (Hirsch, 2007).

According to Blazek (2015), there are two basic approaches to define the shape and the position of each control volume in a grid. These schemes are:

- **cell-centered approach:** unknown fluid dynamic parameters are stored in the center of each cell, while the grid lines represent the finite volumes (three-dimensional cases) and surfaces (2-D cases) (Figure 3.2(a));
- **cell-vertex approach:** unknowns variables are at the corners of each cell, and thus, a grid point can be associated to four cells (2-D cases) conform is illustrated in Figure 3.2(b).

The code has generated grids following the cell-centered approach due to this arrangement to be better adjusted for the SIMPLE algorithm implementation. Besides,

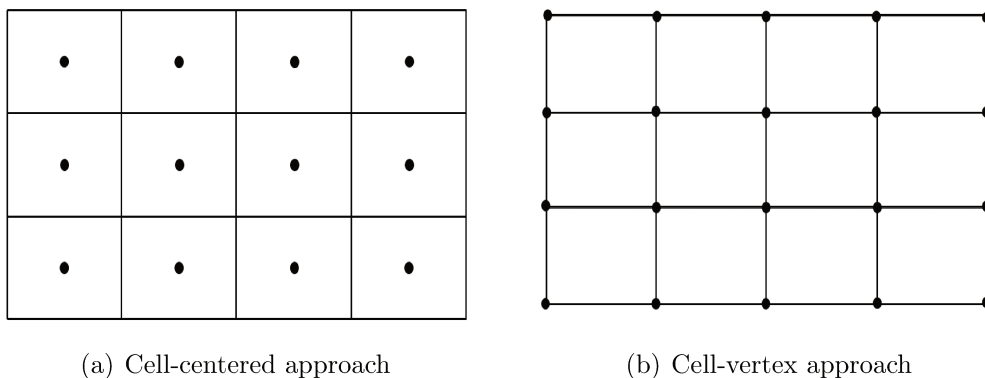


Figure 3.2: Same grid represented in two different ways.

there are additional nodal points at the extremities (usually already known) to represent the boundary conditions.

According to Hirsch (2007), the insertion of the FVM in the discretization process requires a few conditions:

- all small volumes must cover the whole space domain;
- the control volume surfaces should appear as part of an even number of different control volumes (common surfaces between the control volumes);
- the fluxes that cross a cell surface must be computed by the conservation equations independently of the cell shaped.

Therefore, after discretizing the whole domain with all surfaces coupling as an even number, the discretization of the mathematical models is required. For that, a numerical scheme needs to be applied. There are many schemes such as was cited in the last chapter; however, just the Hybrid Differencing Scheme, which bases on the combination between the Central Differencing Scheme and the Upwind Scheme, is implemented in this work.

3.2.2 Discretization of Differential Equations

Continuity equation can be discretized by integrating the equation (3.8) over the control volume in Figure 3.3 (limited by the red color).

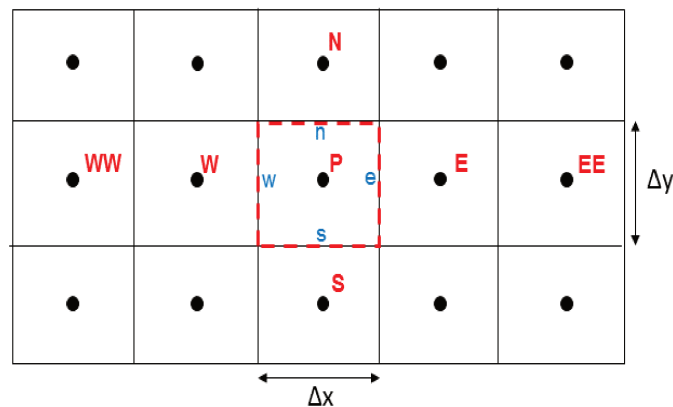


Figure 3.3: A control volume around the grid point P.

$$\left(\rho \frac{\partial u}{\partial x} + \rho \frac{\partial v}{\partial y} \right) = [(\rho u A)_e - (\rho u A)_w] + [(\rho v A)_n - (\rho v A)_s] = 0, \quad (3.25)$$

Where the cross-sectional areas A_e and A_w in a 2D system refer to Δy in the faces east e and west w , respectively, in the control volume. Similarly, A_n and A_s refer to Δx in the faces north n and south s , respectively.

3.2.2.1 Central Differencing Scheme

The Central Differencing Scheme is based on the piecewise-linear profile for the variable. Thus, by integrating the momentum equation (equation (3.16)) in the x -direction over the control volume shown in Figure 3.3, it gives:

$$\begin{aligned} & [(\rho A u u)_e - (\rho A u u)_w] + [(\rho A v u)_n - (\rho A v u)_s] = -((A.P)_e - (A.P)_w) + \\ & + \left[\left(\mu A \frac{\partial u}{\partial x} \right)_e - \left(\mu A \frac{\partial u}{\partial x} \right)_w \right] + \left[\left(\mu A \frac{\partial u}{\partial y} \right)_n - \left(\mu A \frac{\partial u}{\partial y} \right)_s \right], \end{aligned} \quad (3.26)$$

Nonetheless, there is no store of variables on the surface of the cell (represented by lower case letters), therefore, a special treatment to evaluate them must be introduced. Indeed, in this work this parameter is determined by the Pressure-Weighted Interpolation Method (PWIM) proposed by Rhie and Chow (1983), and corroborated by Miller and Schmidt (1988). This methodology is gonna be described in section 3.3.

Since a uniform structured grid is established, and all nodal points are equidistant at a same level, the central differencing scheme is applied in equation (3.26). For instance, for the convective term (left hand side), this scheme gives:

$$\begin{aligned} & [(\rho A u u)_e - (\rho A u u)_w] + [(\rho A v u)_n - (\rho A v u)_s] = \\ & \left[(\rho A u)_e \left(\frac{u_E + u_P}{2} \right) - (\rho A u)_w \left(\frac{u_P + u_W}{2} \right) \right] + \\ & + \left[(\rho A v)_n \left(\frac{u_N + u_P}{2} \right) - (\rho A v)_s \left(\frac{u_P + u_S}{2} \right) \right], \end{aligned} \quad (3.27)$$

Basically, in equation (3.27), a interpolation was performed following that all

interfaces are in the midway between the nodal points. Equations (3.28) and (3.29) represent the same procedure applied in the pressure gradient and diffusive terms, respectively, in the right hand side:

$$-((A.P)_e - (A.P)_w) = -A_e \frac{(P_E + P_P)}{2} + A_w \frac{(P_P + P_W)}{2} = -A \frac{(P_E - P_W)}{2}, \quad (3.28)$$

$$\begin{aligned} & \left[\left(\mu A \frac{\partial u}{\partial x} \right)_e - \left(\mu A \frac{\partial u}{\partial x} \right)_w \right] + \left[\left(\mu A \frac{\partial u}{\partial y} \right)_n - \left(\mu A \frac{\partial u}{\partial y} \right)_s \right] = \\ & \left[\mu_e A_e \frac{(u_E - u_P)}{\Delta x_e} - \mu_w A_w \frac{(u_P - u_W)}{\Delta x_w} \right] + \left[\mu_n A_n \frac{(u_N - u_P)}{\Delta y_n} - \mu_s A_s \frac{(u_P - u_S)}{\Delta y_s} \right], \end{aligned} \quad (3.29)$$

The pressure at the grid point P is vanished in the final result in equation (3.28) when the cross-sectional area $A_e = A_w$, and it might thus cause some problems (instability or non-realistic values) in the resolution phase; however, this issue will also be more detailed and solved by the PWIM in section 3.3. For now, the pressure term will not be the focus.

In equation (3.29), the length Δx_e , for example, denotes the distance between the grid points E and P; while Δx_w refers to the distance between the points W and P. Δy values with a subscript in lower case letter follow the same logic.

The following variables F and D' represent, respectively, the convective and diffusive transport rates. Besides, the dimensionless Peclet number (Pe), which measures the relative importance between advection and diffusion, can be determined from the ratio of F and D' values. They are replaced in the previous equations to ease the next calculations:

$$F_x = (\rho A u)_x \quad \text{or} \quad F_y = (\rho A v)_y, \quad (3.30)$$

$$D'_x = \left(\frac{\mu A}{\Delta x} \right)_x \quad \text{or} \quad D'_y = \left(\frac{\mu A}{\Delta y} \right)_y, \quad (3.31)$$

$$Pe_x = \frac{\rho u \Delta x}{\mu} = \frac{F_x}{D'_x} \quad \text{or} \quad Pe_y = \frac{\rho v \Delta y}{\mu} = \frac{F_y}{D'_y}, \quad (3.32)$$

Where x refers to east (e) and west (w) boundaries, while y refers to north (n) and south (s) boundaries. Moreover, F value can take either positive and negative signs only depending on the flow direction, while D' value always has a positive sign.

Likewise, equations (3.27), (3.28), and (3.29) can be replaced in equation (3.26), and thus, a new expression can be formulated, representing the discretized form for the momentum equation in the x -direction following the central differencing scheme in its second-order accurate:

$$a_P u_P = a_E u_E + a_W u_W + a_N u_N + a_S u_S + P_x, \quad (3.33)$$

Where:

$$a_E = D'_e - \frac{F_e}{2}, \quad (3.34)$$

$$a_W = D'_w + \frac{F_w}{2}, \quad (3.35)$$

$$a_N = D'_n - \frac{F_n}{2}, \quad (3.36)$$

$$a_S = D'_s + \frac{F_s}{2}, \quad (3.37)$$

$$a_P = a_E + a_W + a_N + a_S + (F_e - F_w + F_n - F_s), \quad (3.38)$$

$$P_x = -A \frac{(P_E - P_W)}{2}, \quad (3.39)$$

However, this numerical scheme can provide non-realistic data for $F > 2D'$ (resulting in negative signs to a_E and a_N coefficients), because the grid point P is directly related to its neighbors. Consequently, if a neighbor has a sudden growth, all nodal points around should also increase. Therefore, all coefficients from the discretized equation must take the same sign (Patankar, 1980).

This scheme is recommended to cases where the Reynolds number is low, and then, the diffusion prevails over the convective forces following the expression: $F \leq 2D'$. However, although microflows have a regime strongly laminar, this work has focused on proposing a chaotic advection to increase the vorticity, and consequently, a better numerical scheme taking into account both convective and diffusive forces in any range needs to be studied.

3.2.2.2 Upwind Scheme

According to Patankar (1980), the upwind scheme emerged to solve the issue from the central differencing scheme about the negative coefficients. This methodology

hypothesizes that the calculation of the parameter u_w , for example, by interpolating u_W and u_P is not appropriated. Thus, this scheme in its first-order accurate proposes a new formulation for the convective term F :

$$\begin{cases} u_w = u_W & \text{if } F_w > 0, \\ u_w = u_P & \text{if } F_w < 0, \end{cases}$$

The values of u_e , u_n and u_s (or to v -velocity) follow the same idea. Therefore, the velocity in the interface is taken as the upstream point value, being governed by the flow direction. For instance, basing on these conditions, the convective term of the momentum equation (equation (3.27)) in the x -direction for the face w can be rewritten as:

$$F_w u_w = u_W \cdot \text{Max}[[F_w, 0]] - u_P \cdot \text{Max}[[-F_w, 0]], \quad (3.40)$$

Where Max indicates the expression in brackets with the highest value. For that reason, the coefficients from equation (3.33) in its discretized form will be replaced by:

$$a_E = D'_e + \text{Max}[[-F_e, 0]], \quad (3.41)$$

$$a_W = D'_w + \text{Max}[[F_w, 0]], \quad (3.42)$$

$$a_N = D'_n + \text{Max}[[-F_n, 0]], \quad (3.43)$$

$$a_S = D'_s + \text{Max}[[F_s, 0]], \quad (3.44)$$

$$a_P = a_E + a_W + a_N + a_S + (F_e - F_w + F_n - F_s), \quad (3.45)$$

$$P_x = -A \frac{(P_E - P_W)}{2}, \quad (3.46)$$

Therefore, for the upwind scheme, the coefficients are never negative and the results are always physically realistic. Likewise, Spalding (1972) developed a numerical scheme (named Hybrid Differencing Scheme) where he combined the accuracy of the central differencing scheme with the stability of the upwind scheme.

3.2.2.3 Hybrid Differencing Scheme

Spalding (1972) formulated a high resolution methodology to calculate the coefficients of the discretized equation. For the cases where $-2 \leq Pe \leq 2$, the central scheme should be applied, meanwhile for $Pe > 2$ and $Pe < -2$, the upwind scheme is required, i.e.:

$$\begin{cases} a_W = 0 & \text{if } Pe_w < -2, \\ a_W = D'_w + 0.5F_w & \text{if } -2 \leq Pe_w \leq 2, \\ a_W = F_w & \text{if } Pe_w > 2, \end{cases}$$

The other coefficients follow the same logic. It can be noticed that the diffusion term for when $|Pe| > 2$ (upwind scheme) is neglected due to the greater contribution of convection. Therefore, based on equation (3.33) and on the hybrid scheme, the link coefficients for a 2D case can be rewritten as:

$$a_E = Max \left[-F_e, D'_e - \frac{F_e}{2}, 0 \right], \quad (3.47)$$

$$a_W = Max \left[F_w, D'_w + \frac{F_w}{2}, 0 \right], \quad (3.48)$$

$$a_N = Max \left[-F_n, D'_n - \frac{F_n}{2}, 0 \right], \quad (3.49)$$

$$a_S = Max \left[F_s, D'_s + \frac{F_s}{2}, 0 \right], \quad (3.50)$$

$$a_P = a_E + a_W + a_N + a_S + (F_e - F_w + F_n - F_s), \quad (3.51)$$

$$P_x = -A \frac{(P_E - P_W)}{2}, \quad (3.52)$$

Hence, this numerical scheme covers all values of Pe , avoiding any issue from the stability of the discretized equation. For instance, when diffusion transport prevails in the flow, the term referring to central scheme is chosen, while for cases where $F \gg D'$, the rate of diffusion is set to zero, and the upwind scheme is applied.

According to Versteeg and Malalasekera (2007), this scheme also produces realist data and its stability can be compared with higher-order schemes such as the QUICK

scheme. Additionally, after applying the approaches in the conservation equations, an iterative method needs to be inserted in the code until achieving the convergence of the process where all fluid dynamic parameters calculated (u , v , P , ψ , ω) get constant values.

The discretized form for the momentum equation in the y -direction has a similar profile, just changing the source term (pressure gradient) presented in equation (3.54).

$$a_P v_P = a_E v_E + a_W v_W + a_N v_N + a_S v_S + P_y, \quad (3.53)$$

Where:

$$P_y = -A \frac{(P_N - P_S)}{2}, \quad (3.54)$$

The vorticity equation (equation 3.20) can be discretized after the momentum and continuity equations achieve their convergence once it only depends on the velocity field. Therefore, the discretized form for the vorticity equation can be obtained by integrating this formula over the control volume in Figure 3.3:

$$(\Delta x \Delta y \Delta z) \overline{\omega_z} = (\Delta y \Delta z)(v_e - v_w) + (\Delta x \Delta z)(u_s - u_n), \quad (3.55)$$

Where $\overline{\omega_z}$ is the average value of ω_z over each single volume. Thereby, this mean vorticity can be calculated as:

$$\overline{\omega_z} = \frac{v_e}{\Delta x} - \frac{v_w}{\Delta x} - \frac{u_n}{\Delta y} + \frac{u_s}{\Delta y}, \quad (3.56)$$

And finally, the discretized equation for the stream-function (equation 3.24) can be presented by also integrating Figure 3.3 over the control volume as follows:

$$-(\Delta x \Delta y) \overline{\omega_z} = \left(\Delta y \frac{\partial \psi}{\partial x} \right)_e - \left(\Delta y \frac{\partial \psi}{\partial x} \right)_w + \left(\Delta x \frac{\partial \psi}{\partial y} \right)_n - \left(\Delta x \frac{\partial \psi}{\partial y} \right)_s, \quad (3.57)$$

Following the same approach applied to the diffusive term in the momentum equations, the gradient of ψ can be expressed by a linear approximation (central differencing scheme) as gives:

$$-(\Delta x \Delta y) \overline{\omega_z} = \left(\Delta y \frac{\psi_E - \psi_P}{\Delta x} \right)_e - \left(\Delta y \frac{\psi_P - \psi_W}{\Delta x} \right)_w + \left(\Delta x \frac{\psi_N - \psi_P}{\Delta y} \right)_n - \left(\Delta x \frac{\psi_P - \psi_S}{\Delta y} \right)_s, \quad (3.58)$$

The equation can be rearranged letting only the terms referred to the central node in the left hand side of the discretized equation, while its neighbors nodes with the source term are distributed to the right hand side as follows:

$$a_P \psi_P = a_E \psi_E + a_W \psi_W + a_N \psi_N + a_S \psi_S + S_\psi, \quad (3.59)$$

Where:

$$a_E = \frac{\Delta y_e}{\Delta x_e}, \quad (3.60)$$

$$a_W = \frac{\Delta y_w}{\Delta x_w}, \quad (3.61)$$

$$a_N = \frac{\Delta x_n}{\Delta y_n}, \quad (3.62)$$

$$a_S = \frac{\Delta x_s}{\Delta y_s}, \quad (3.63)$$

$$a_P = a_E + a_W + a_N + a_S, \quad (3.64)$$

$$S_\psi = (\Delta x \Delta y) \overline{\omega_z}, \quad (3.65)$$

Unlike the discretized vorticity equation, the stream-function equation requires an iterative solver to converge. However, its values only depends on the vorticity field, and therefore, it is the last equation to be performed in the code.

3.3 SIMPLE Algorithm

The resolution of the system of equations aforementioned is the next step in a CFD simulation in order to obtain finally the grid point values of the fluid dynamic parameters (Versteeg and Malalasekera, 2007). The type of flow (time-dependent or steady), the discretization method (FVM, FEM or FDM), and the numerical scheme are factors that affect the decision for the appropriate solution algorithm.

In the solution of the momentum equations, the unknown velocity fields are presented in both convective (for example, the non-linear term ρAu^2 in equation (3.26)) and diffusive terms. Another point is, there is no explicit equation to solve the pressure term that appears in both momentum expressions. These problems can be treated in an iterative solution process, that was proposed by Patankar and Spalding (1972), where the SIMPLE iterative algorithm is applied until the process converges in a residual difference between each consecutive iteration. In addition, the choice of the SIMPLE algorithm is supported by the fact that it is strongly indicated for cases with a laminar flow without turbulence.

The discretization process, that was presented in section 3.2, proposes the store of all parameters (pressure, velocity components, density, viscosity, vorticity and stream-function) in the grid points shown before in Figure 3.3. However, as was demonstrated in equation (3.28), this arrangement might still result in a non-uniform pressure field behaving like a uniform field (Figure 3.4) once the expression does not include the nodal point P. Hence, since that nodal points in the east (E) and west (W) boundaries have equal values, the expression will provide a conclusion that the fluid is static in the x -direction (pressure gradient equals to zero). Similarly, this idea can be applied to y -direction for neighbors in the north (N) and south (S) nodes.

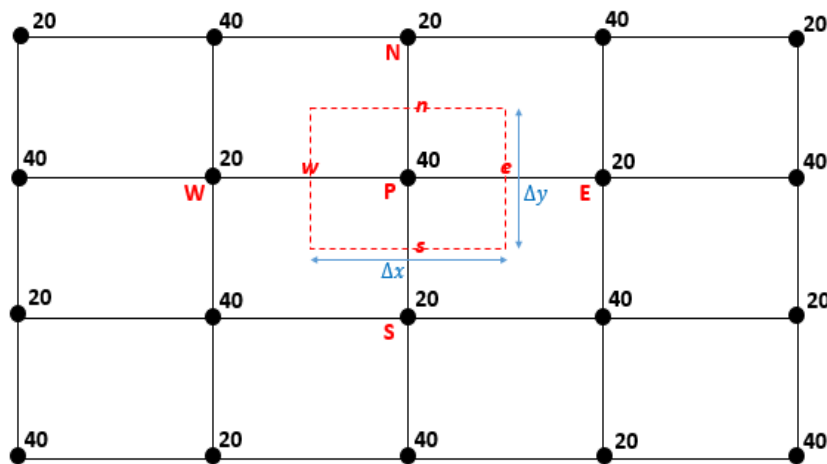


Figure 3.4: Example of non-realistic pressure field resulted from the actual discretized method.

$$\begin{cases} A \frac{(P_E - P_W)}{2}, & \text{in x-direction,} \\ A \frac{(P_N - P_S)}{2}, & \text{in y-direction,} \end{cases}$$

Harlow and Welch (1965) suggested a solution to this problem: to stagger the mesh for the velocity components. Nevertheless, working with a staggered mesh may bring some issues: different arrangements of grids for each velocity component and for the scalar variables; high complexity to perform non-uniform/unstructured meshes; and each boundary condition for each specific arrangement has a different treatment. Thereby, a co-located mesh by applying the Pressure-Weighted Interpolation Method (PWIM) emerged to solve these difficulties (Miller and Schmidt, 1988). Therefore, the following steps describe how the SIMPLE algorithm works with the insertion of the PWIM.

3.3.1 Step 1: Storing values to the variables

The first step is to guess values for the unknown parameters (u , v , P , ω , and ψ) at the nodal points in all cell centers. Besides, the known parameters (ρ and μ) are also fulfilled in this step. Moreover, in order to apply the PWIM, the velocity at all cell faces (represented by lower case letters) needs to be calculated, so, for the first iteration, this value come from a distance-weighted interpolation. Consequently, this step is run once immediately before the code opens the biggest loop.

3.3.2 Step 2: Calculating the link coefficients

The biggest loop starts by calculating the link coefficients from the momentum equation by applying the hybrid scheme (equation 3.47-3.52, 3.54) in terms of the guessed values. In addition, the variables F and D' at the cell faces are obtained through the equations (3.30) and (3.31) for each of the faces e , w , n and s .

3.3.3 Step 3: Determining the velocity components via TDMA

Some numerical iterative methods are usually implemented to solve a system of algebraic equations, such as the Gauss-Seidel method and the Tri-Diagonal Matrix Algorithm (TDMA) (being this one inserted in the code). Consequently, the equations

(3.33) and (3.53) provide a new velocity field of u and v from the old values of pressure and velocity. These results will satisfy only the momentum because the pressure field may still be incorrect. Therefore, a new equation is necessary to be developed in order to obtain the pressure field. Furthermore, the mass conservation also needs to be implemented in the code. Therefore, the SIMPLE algorithm has emerged to link these demands, allowing the continuity equation to calculate the pressure field.

Basically, the equations for the velocity components that only satisfy the conservation of momentum and not mass (in this condition represented by \dot{u} and \dot{v}) can be expressed as follows:

$$\dot{u}_P = \frac{1}{a_P} [(a_E \dot{u}_E) + (a_W \dot{u}_W) + (a_N \dot{u}_N) + (a_S \dot{u}_S)] + \left[\frac{\Delta y}{2a_P} (P_W^* - P_E^*) \right], \quad (3.66)$$

$$\dot{v}_P = \frac{1}{a_P} [(a_E \dot{v}_E) + (a_W \dot{v}_W) + (a_N \dot{v}_N) + (a_S \dot{v}_S)] + \left[\frac{\Delta x}{2a_P} (P_S^* - P_N^*) \right], \quad (3.67)$$

Moreover, it is requested to measure the velocity at each face from all control volumes in order to evaluate the conservation of mass. Therefore, the PWIM need to be derived in order to obtain the cell faces velocities. Thereby, as strategy, the momentum equation regarding the cell W can be represented by the equation below based on Figure 3.5(a):

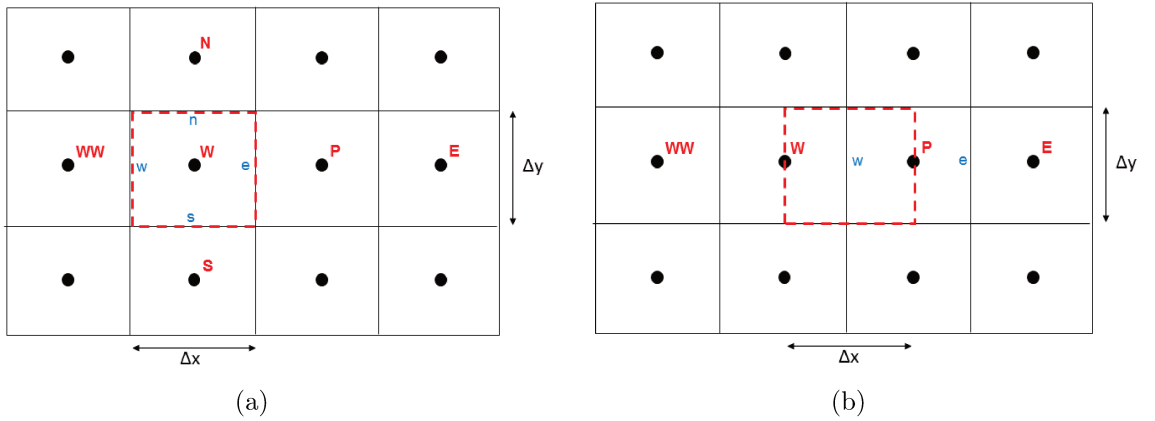


Figure 3.5: Representation of the control volume: (a) at cell W; (b) at the w face from cell P.

$$\dot{u}_W = \frac{1}{a_W} [(a_{WW}\dot{u}_{WW}) + (a_P\dot{u}_P) + (a_N\dot{u}_N) + (a_S\dot{u}_S)] + \left[\frac{\Delta y}{2a_W}(P_{WW}^* - P_P^*) \right], \quad (3.68)$$

And, following the same idea, for a supposed control volume at interface w (Figure 3.5(b)), the momentum equation can also be written as gives:

$$\dot{u}_w = \frac{1}{a_w} [(a_{ww}\dot{u}_{ww}) + (a_p\dot{u}_p) + (a_n\dot{u}_n) + (a_s\dot{u}_s)] + \left[\frac{\Delta y}{a_w}(P_W^* - P_P^*) \right], \quad (3.69)$$

From equation 3.69, the pressure gradient includes both neighbor nodes allowing non-oscillatory performance as shown before in Figure 3.4. However, the link coefficients from this equation are unknown, requiring a standard distance weighted interpolation between the values obtained from the cells W and P :

$$\begin{aligned} & \frac{1}{a_w} [(a_{ww}\dot{u}_{ww}) + (a_p\dot{u}_p) + (a_n\dot{u}_n) + (a_s\dot{u}_s)] = \\ & \frac{1}{2} \left[\frac{1}{a_W} [(a_{WW}\dot{u}_{WW}) + (a_P\dot{u}_P) + (a_N\dot{u}_N) + (a_S\dot{u}_S)] \right] + \\ & + \frac{1}{2} \left[\frac{1}{a_P} [(a_{PW}\dot{u}_{PW}) + (a_E\dot{u}_E) + (a_N\dot{u}_N) + (a_S\dot{u}_S)] \right], \end{aligned} \quad (3.70)$$

$$\frac{1}{a_w} = \frac{1}{2} \left(\frac{1}{a_W} + \frac{1}{a_P} \right), \quad (3.71)$$

Replacing the term referring to the contribution of the four neighboring nodes from equations 3.66 and 3.68 in equation 3.70, and, in sequence, substituting equations 3.70 and 3.71 in 3.69, the cell face velocity at interface w results in:

$$\dot{u}_w = \frac{1}{2} \left[\dot{u}_W - \frac{\Delta y}{2a_W}(P_{WW}^* - P_P^*) \right] + \frac{1}{2} \left[\dot{u}_P - \frac{\Delta y}{2a_P}(P_W^* - P_E^*) \right] + \frac{\Delta y}{2} \left(\frac{1}{a_W} + \frac{1}{a_P} \right) (P_W^* - P_P^*), \quad (3.72)$$

Rearranging the equation above, the cell face velocity in its discreet form regarding the PWIM can be expressed as:

$$\dot{u}_w = \frac{\dot{u}_W + \dot{u}_P}{2} + \frac{\Delta y(P_P^* - P_{WW}^*)}{4a_W} + \frac{\Delta y(P_E^* - P_W^*)}{4a_P} - \left[\frac{1}{a_W} + \frac{1}{a_P} \right] \frac{\Delta y(P_P^* - P_W^*)}{2}, \quad (3.73)$$

Similarly, for the v -velocity, the cell face velocity at interface s can be formulated as follow:

$$\dot{v}_s = \frac{\dot{v}_S + \dot{v}_P}{2} + \frac{\Delta x(P_P^* - P_{SS}^*)}{4a_S} + \frac{\Delta x(P_N^* - P_S^*)}{4a_P} - \left[\frac{1}{a_S} + \frac{1}{a_P} \right] \frac{\Delta x(P_P^* - P_S^*)}{2}, \quad (3.74)$$

Equations 3.73 and 3.74 demonstrate that the cell face velocity is not only the standard distance between the neighboring nodes, but also there is a contribution coming from additional terms involving the pressure gradient where includes four cells in total.

3.3.4 Step 4: Deriving the velocity correction equations

The cell and face velocities aforementioned need to be corrected at each iteration. The cell velocity correction u'_P , for example, can be measured by the difference between its new and the old values (\ddot{u}_P and \dot{u}_P , respectively) from the momentum equations:

$$u'_P = \ddot{u}_P - \dot{u}_P = \frac{1}{a_P} [(a_E u'_E) + (a_W u'_W) + (a_N u'_N) + (a_S u'_S)] + \left[\frac{\Delta y}{2a_P} (P'_W - P'_E) \right], \quad (3.75)$$

The main approach that comes with this algorithm is that the sum of the contribution from the neighboring cells goes to zero at convergence, thus it is plausible to vanish this term. Therefore, equation 3.75 comes down to:

$$u'_P = \ddot{u}_P - \dot{u}_P = \left[\frac{\Delta y}{2a_P} (P'_W - P'_E) \right], \quad (3.76)$$

Similarly, for v_P , its correction can be expressed by:

$$v'_P = \ddot{v}_P - \dot{v}_P = \left[\frac{\Delta x}{2a_P} (P'_S - P'_N) \right], \quad (3.77)$$

For the cell face velocities in the x -direction, it is applied the same strategy to provide the face velocity correction by differencing both new and old values from the expression 3.72. It gives:

$$u'_w = \frac{1}{2} \left[u'_W - \frac{\Delta y}{2a_W} (P'_{WW} - P'_P) \right] + \frac{1}{2} \left[u'_P - \frac{\Delta y}{2a_P} (P'_W - P'_E) \right] + \frac{\Delta y}{2} \left(\frac{1}{a_W} + \frac{1}{a_P} \right) (P'_W - P'_P), \quad (3.78)$$

Where u'_W and u'_P are replaced by equation 3.76 in terms of the correct subscript. Thereby, this equation is summed up to just:

$$u'_w = \frac{\Delta y}{2} \left(\frac{1}{a_W} + \frac{1}{a_P} \right) (P'_W - P'_P), \quad (3.79)$$

Similarly, the face velocity correction for v -velocity is:

$$v'_s = \frac{\Delta x}{2} \left(\frac{1}{a_S} + \frac{1}{a_P} \right) (P'_S - P'_P), \quad (3.80)$$

Equations 3.76, 3.77, 3.79 and 3.80 are implemented in the code, and they need to be requested right after the momentum and the pressure correction equations are solved. Therefore, it is demanded to derive an equation that provides a solution for the pressure field and also expresses the conservation of mass.

3.3.5 Step 5: Obtaining the pressure correction equation

The continuity equation aims to determine the correction of the pressure field herein the SIMPLE algorithm. However, this equation just depends on the velocity field. Therefore, a few replacements are applied in order to let this equation in terms of pressure. Thus, basing on the cell P in Figure 3.3 and applying equation 3.8, the mass balance gives:

$$(\rho_e \ddot{u}_e - \rho_w \ddot{u}_w) \Delta y + (\rho_n \ddot{v}_n - \rho_s \ddot{v}_s) \Delta x = 0, \quad (3.81)$$

Where \ddot{u}_e , \ddot{u}_w , \ddot{v}_n , and \ddot{v}_s are resulted from the momentum equation and, for equation above, they also satisfy the continuity equation. Then, applying the corrections of the velocity $\ddot{u} = u' + \dot{u}$ and $\ddot{v} = v' + \dot{v}$ in the equation 3.81, and knowing that it may have an imbalance of mass $\dot{m}_{imbalance}$ during the iterative process, it gives:

$$(\rho_e u'_e - \rho_w u'_w) \Delta y + (\rho_n v'_n - \rho_s v'_s) \Delta x + (\rho_e \dot{u}_e - \rho_w \dot{u}_w) \Delta y + (\rho_n \dot{v}_n - \rho_s \dot{v}_s) \Delta x = -\dot{m}_{imbalance}, \quad (3.82)$$

Where the terms regarding the velocity corrections can be replaced by equations 3.79 and 3.80; and consequently, a discretized form can be provided similarly to what was done in equations 3.33 and 3.53. The following equations present the discretized form for the pressure correction equation and its link coefficients:

$$a_P^P P'_P = a_E^P P'_E + a_W^P P'_W + a_N^P P'_N + a_S^P P'_S + S^P, \quad (3.83)$$

Where:

$$a_E^P = \frac{\rho_e \Delta y^2}{2} \left(\frac{1}{a_E} + \frac{1}{a_P} \right), \quad (3.84)$$

$$a_W^P = \frac{\rho_w \Delta y^2}{2} \left(\frac{1}{a_W} + \frac{1}{a_P} \right), \quad (3.85)$$

$$a_N^P = \frac{\rho_n \Delta x^2}{2} \left(\frac{1}{a_N} + \frac{1}{a_P} \right), \quad (3.86)$$

$$a_S^P = \frac{\rho_s \Delta x^2}{2} \left(\frac{1}{a_S} + \frac{1}{a_P} \right), \quad (3.87)$$

$$S^P = -\dot{m}_{imbalance} = -[(\rho_e \dot{u}_e - \rho_w \dot{u}_w) \Delta y + (\rho_n \dot{v}_n - \rho_s \dot{v}_s) \Delta x], \quad (3.88)$$

$$a_P^P = a_E^P + a_W^P + a_N^P + a_S^P, \quad (3.89)$$

The equation (3.83) represents the discretized continuity equation to solve the pressure correction field P' . The parameter S^P describes the continuity imbalance due to the velocity components. When this value is near zero, the velocity field satisfies the continuity, because the pressure field reached the convergence.

Patankar (1980) analyzed the implications of that approximation from SIM-

PLE algorithm presented in equation (3.76) and (3.77), and he noticed that it has no effect on the converged solution (when $u' = 0$; $\dot{u} = \ddot{u}$ and $\dot{v} = \ddot{v}$). In this case, the parameter S^P in equation (3.83) will be zero, and thus, the pressure correction field P' will also be nearly to zero. Nonetheless, an under-relaxation is recommended to prevent cases of divergence during the iterations in the pressure correction due to those approximations. Moreover, the pressure correction affects directly the velocity field, and hence, this factor is employed in the momentum equations. This factor should take a value from 0 to 1, and it is applied in the following equations, proposed by Miller and Schmidt (1988) and Mazumder (2018), to the pressure, and to the components of velocity u and v in the cell centers, respectively:

$$P = P^* + \alpha_P P', \quad (3.90)$$

$$\ddot{u}_P = \dot{u}_P + \alpha_u u'_P \Rightarrow \ddot{u}_P = \dot{u}_P + \alpha_u \left[\frac{(P'_W - P'_E)\Delta y}{2a_P} \right], \quad (3.91)$$

$$\ddot{v}_P = \dot{v}_P + \alpha_v v'_P \Rightarrow \ddot{v}_P = \dot{v}_P + \alpha_v \left[\frac{(P'_S - P'_N)\Delta x}{2a_P} \right], \quad (3.92)$$

Where α_P , α_u and α_v are the pressure, u -velocity, and v -velocity under-relaxations factors, respectively; \dot{u} and \dot{v} are the cell center velocity components obtained from the momentum equations; and \ddot{u} and \ddot{v} are the new values after applying the correction. Nevertheless, the cell face velocities also needs to be corrected, then:

$$\ddot{u}_w = \dot{u}_w + \alpha_u u'_w \Rightarrow \ddot{u}_w = \dot{u}_w + \alpha_u \frac{\Delta y}{2} \left(\frac{1}{a_W} + \frac{1}{a_P} \right) (P'_W - P'_P), \quad (3.93)$$

$$\ddot{v}_s = \dot{v}_s + \alpha_v v'_s \Rightarrow \ddot{v}_s = \dot{v}_s + \alpha_v \frac{\Delta x}{2} \left(\frac{1}{a_S} + \frac{1}{a_P} \right) (P'_S - P'_P), \quad (3.94)$$

The choice of appropriate values of these under-relaxation factors is essential for the convergence of the iteration. If these values are too large, they may provide strong oscillations and get non-realistic results due to the divergence, while for small values of under-relaxation, the simulation would achieve the convergence slowly. Patankar (1980) suggests $\alpha_P = 0.8$, $\alpha_u = 0.5$, and $\alpha_v = 0.5$.

Another important point is to discuss the relative nature of pressure in pro-

cesses at steady-state with incompressible fluid. The main governing equations contain only derivatives terms of the dependent variable; and for instance, if velocity v is the dependent variable, the functions v and $v + C$ (where C is an arbitrary constant) should satisfy the solution of this equation. This statement can also be applied in discretized equations (Patankar, 1980). Hence, the equation (3.83) may remain valid when the pressure correction field P' and its neighboring cells are affected by a constant. From this requirement comes the equation (3.89), where the coefficient related to the grid point P at the scalar-control volume is equal to the sum of the neighbor coefficients. Therefore, the center point value is an average of the neighboring values.

The value of fluid dynamics parameters are usually smaller in microchannels when compared to macrochannels. For example, pressure drop might achieve an order of the ninth decimal place. According to Patankar (1980), the absolute value of pressure P is not relevant for the simulation; only differences in pressure are meaningful. Mazumder (2018) suggested to replace the absolute pressure in the momentum equation for the gauge pressure in incompressible flows because:

$$-\frac{dP_{abs}}{dx} = -\frac{d(P_{atm} + P_{gauge})}{dx} = -\frac{dP_{gauge}}{dx}, \quad (3.95)$$

$$-\frac{dP_{abs}}{dy} = -\frac{d(P_{atm} + P_{gauge})}{dy} = -\frac{dP_{gauge}}{dy}, \quad (3.96)$$

Where P_{abs} , P_{atm} , and P_{gauge} are the absolute, atmospheric (constant value) and gauge pressures. This substitution may prevent round-off errors that comes in calculating the difference of pressure in the equations (3.91)-(3.94), for example. Basing on that, all pressure correction points P' are related to the gauge pressure.

After correcting the pressure field and velocities in the centers and on the faces of the cells, the link coefficients are calculated again, starting the loop until the $\dot{m}_{imbalance}$ reduces to zero. On the other hand, after reaching convergence, the other equations (vorticity and stream-function) are explicitly solved. Firstly, the vorticity equation is solved directly from the velocity field, while the stream-function equation needs the iterative TDMA. Finally, a file is generated to be read by a visualization software.

Since many steps from the SIMPLE algorithm were described before, a flowchart

can summarize this method (Figure 3.6), indicating the sequence of equations, and the value of convergence factor (S^P) implemented in the code.

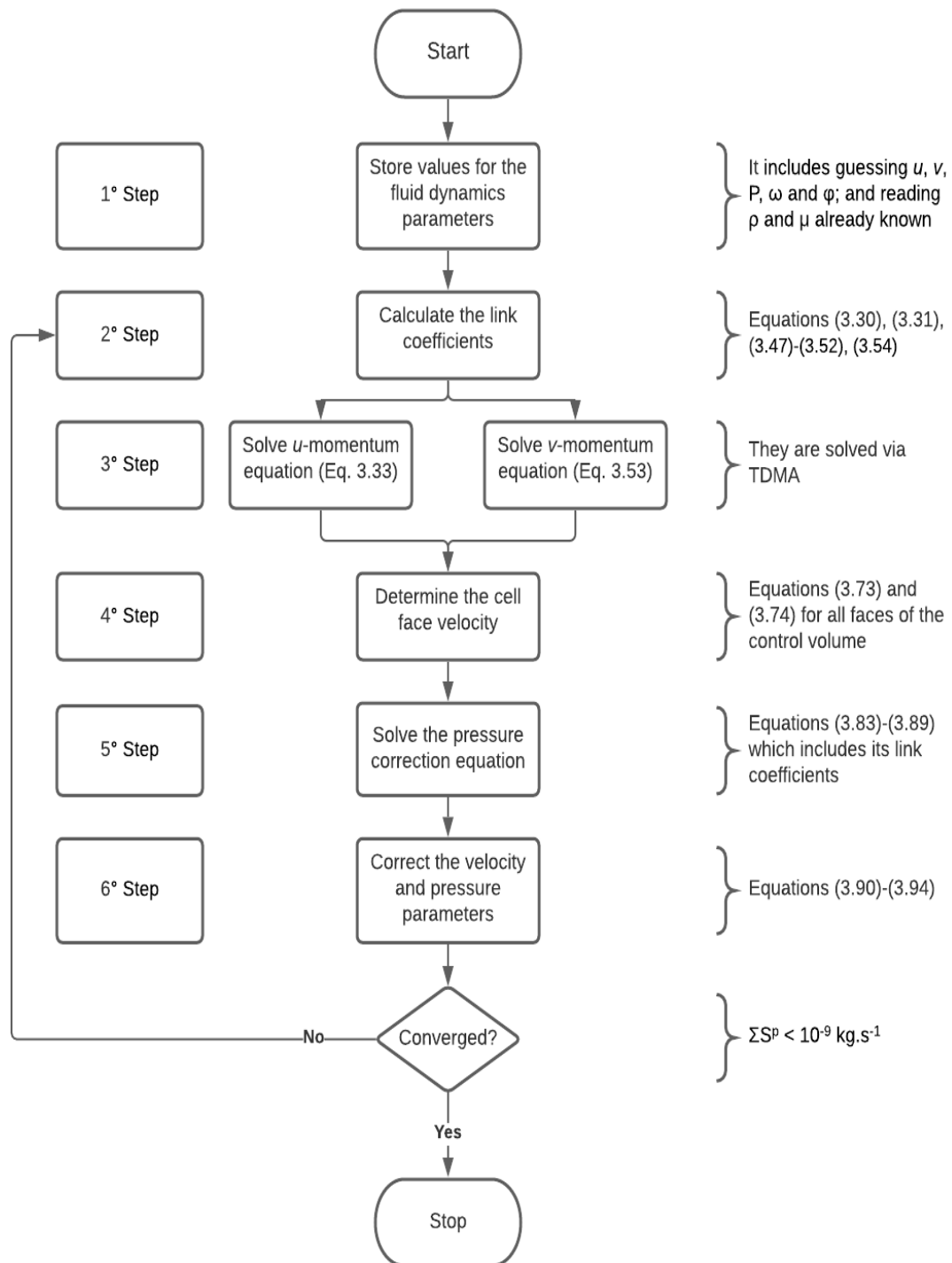


Figure 3.6: Flowchart of the SIMPLE algorithm.

3.4 Post-Processing of the Results

Once the solution is converged, these results are presented by plotting graphics and colour contours that include the magnitude of the velocity (in x - and y -directions), the gauge pressure, the vorticity and the stream-function fields, and also the streamlines, through using the ParaView visualization software. However, the code needs to create a file in *.vtk* format where all final data are stored in order to be read by the software.

The vortex formation in the microdevice is evaluated in order to provide more fluid stirring via qualitatively analysis of the streamlines and quantitatively data from the vorticity field. Then, for that reason, a few parameters might be analyzed: the Reynolds number (Re), the curvature of bumps, the location of feed and the width of the microchannel.

3.5 Treatment of the Boundary Conditions

An important parameter to analyze in a simulation is the insertion of an appropriate boundary condition. Most errors in iterative processes are in considering factors not applicable in a specific case study. For this code, no-slip condition is assumed to the walls; a fixed velocity is set for the feed, while the outlet pressure is constant and equal to zero.

3.5.1 Walls: no-slip condition

It is logical to think that in cases with the application of the no-slip condition, it is only necessary to set the velocity on the walls to zero ($u_{wall} = 0$). However, there are also a few extra contributions to the source term in the boundaries. For instance, analyzing the momentum equation for the u -velocity in the cell highlighted in red in Figure 3.7, it gives:

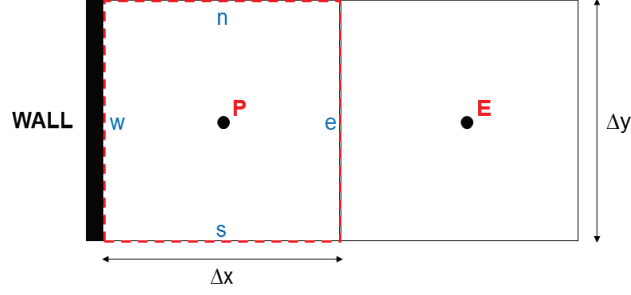


Figure 3.7: Representation of the control volume adjacent to the wall.

$$(J_e^u - J_w^u) \Delta y + (J_n^v - J_s^v) \Delta x = -(P_e - P_w) \Delta y, \quad (3.97)$$

Where:

$$J_w^u = \rho_w u_w u_w - \mu_w \left(\frac{\partial u}{\partial x} \right)_w, \quad (3.98)$$

Consequently, the flow of species in the cell next to the w -interface (J_w^u) comes down to just one contribution from the diffusive term once $u_w = u_{wall} = 0$. Moreover, the derivative term of velocity at w can be obtained by applying the 2 Point Taylor Series Expansion (second order accurate), as follows:

$$u_P = u_w + \frac{\Delta x}{2} \left(\frac{\partial u}{\partial x} \right)_w, \quad (3.99)$$

$$u_E = u_w + \frac{3\Delta x}{2} \left(\frac{\partial u}{\partial x} \right)_w, \quad (3.100)$$

Therefore, multiplying the equation (3.99) by 9, and differencing it by equation (3.100), it gives a value for the u -velocity gradient:

$$\left(\frac{\partial u}{\partial x} \right)_w = \frac{9u_P - 8u_w - u_E}{3\Delta x} = \frac{9u_P - u_E}{3\Delta x}, \quad (3.101)$$

And then,

$$J_w^u = -\mu_w \left[\left(\frac{3\Delta y}{\Delta x} \right) u_P - \left(\frac{\Delta y}{3\Delta x} \right) u_E \right], \quad (3.102)$$

Thereby, there are one extra term for a_P , and another for a_E basing on equation (3.102) when the x -momentum equation is solved. Therefore, the link coefficients will be:

$$a_E = a_E + \mu_w \frac{\Delta y}{3\Delta x}, \quad (3.103)$$

$$a_W = 0, \quad (3.104)$$

$$a_P = a_P + \mu_w \frac{3\Delta y}{\Delta x}, \quad (3.105)$$

A similar analysis can be applied when the momentum equation in the y -direction is aimed. However, regarding the pressure field, the values on the wall are unknown, therefore the pressure in this case is assumed to be its neighbor normal to the surface (first order accurate) basing on the boundary layer approximation where the pressure gradient along the surface is considerably higher over the normal to the surface (Fox et al., 2011)(Mazumder, 2019). Thus, the source term based on Figure 3.7 and the x -momentum equation is:

$$S^u = (P_w - P_e) \Delta y \xrightarrow{P_w = P_P} S^u = \left(P_P - \frac{P_P + P_E}{2} \right) \Delta y = \left(\frac{P_P - P_E}{2} \right) \Delta y, \quad (3.106)$$

Regarding the boundary conditions to solve the pressure correction equation, the starting point is the continuity equation (3.81) where $u_w = 0$ as follows:

$$(\rho_e \ddot{u}_e) \Delta y + (\rho_n \ddot{v}_n - \rho_s \ddot{v}_s) \Delta x = 0, \quad (3.107)$$

Thus, for a no-slip condition, there are no additional terms, so it is only necessary to vanish the link coefficient referring to the position of the wall (in this case, $a_W^P = 0$), and therefore the source term will be:

$$S^P = - [(\rho_e \dot{u}_e) \Delta y + (\rho_n \dot{v}_n - \rho_s \dot{v}_s) \Delta x], \quad (3.108)$$

3.5.2 Inlet: Constant velocity

Unlike the wall condition, in the feed the velocity is not zero allowing to have convective and diffusive influences in the additional terms. Based on Figure 3.8 and the equations 3.98 and 3.101, the flow of species in the feed is:

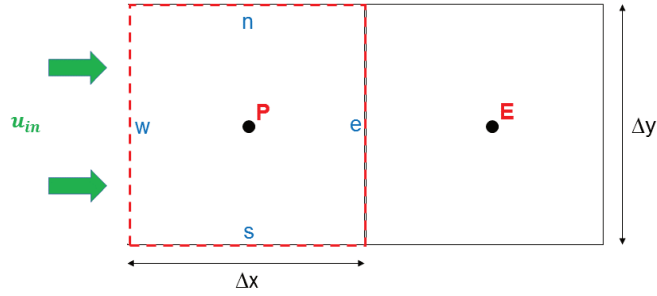


Figure 3.8: Representation of the control volume adjacent to the feed.

$$J_w^u = \rho_w u_{in} u_{in} - \left(\mu_w \frac{3\Delta y}{\Delta x} \right) u_P - \left(-\mu_w \frac{\Delta y}{3\Delta x} \right) u_E - \left(-\mu_w \frac{8\Delta y}{3\Delta x} \right) u_{in}, \quad (3.109)$$

Consequently, some link coefficients are modified from these additional terms to compensate the effect of the boundary ($a_W = 0$).

$$a_E = a_E + \mu_w \frac{\Delta y}{3\Delta x}, \quad (3.110)$$

$$a_W = 0, \quad (3.111)$$

$$a_P = a_P + \mu_w \frac{3\Delta y}{\Delta x}, \quad (3.112)$$

$$S^u = \left[\left(\frac{P_P - P_E}{2} \right) + \rho_w u_{in} u_{in} + \left(\mu_w \frac{8\Delta y}{3\Delta x} \right) u_{in} \right] \Delta y, \quad (3.113)$$

Comparing these previous two types of boundaries, the link coefficients for a_E , a_W and a_P are equivalent, with the only difference being the addition of two extra terms

to the source term due to the non-zero velocity. Moreover, the pressure in the feed is assumed to be equal to the value of its downstream neighbor.

Again, in terms of the pressure correction equation, the analysis of the boundary condition in the feed is similar to the wall previously seen where $a_W^P = 0$ (based on Figure 3.8). However, instead of the velocity being zero in the source term, now it has a quantity: $u_w = u_{in}$.

$$S^P = - [(\rho_e \dot{u}_e - \rho_{in} \dot{u}_{in}) \Delta y + (\rho_n \dot{v}_n - \rho_s \dot{v}_s) \Delta x], \quad (3.114)$$

3.5.3 Outlet: Constant pressure

The outlet pressure is considered constant and equal to zero at the beginning of the calculations. Consequently, the resulting pressure field will have the outlet as a reference point. It is important to point out that for this assumption to be true, the outlet position must not have wall or turbulence effects making the flow get undeveloped. Therefore, a strategy to avoid this inconsistency is to extend the domain at the outlet resulting in a fully developed flow. Thereby, basing on the Figure 3.9, the flux of species that crosses interface e can be represented by:

$$J_e^u = \rho_e u_e u_e - \mu_e \left(\frac{\partial u}{\partial x} \right)_e, \quad (3.115)$$

Where the velocity at the outlet is assumed to be the velocity just upstream: $u_e = u_P$. Moreover, when the flow is fully developed, the viscous effects are despised once there is no u -velocity gradient along the x -axis, then: $\left(\frac{\partial u}{\partial x} \right)_e \simeq 0$. Thus, it gives:

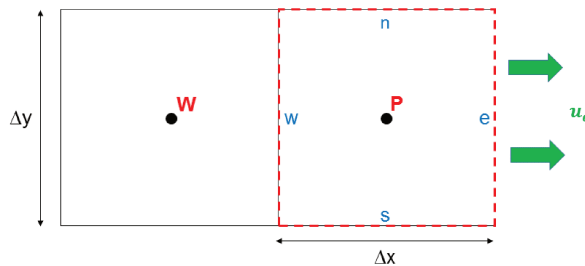


Figure 3.9: Representation of the control volume adjacent to the outlet.

$$J_e^u = (\rho_e u_P) u_P, \quad (3.116)$$

Consequently, in this case, the link coefficients are:

$$a_E = 0, \quad (3.117)$$

$$a_P = a_P + (\rho_e u_P \Delta y), \quad (3.118)$$

$$S^u = (P_w - P_e) \Delta y \xrightarrow{P_e=0} S^u = \left(\frac{P_W + P_P}{2} - 0 \right) \Delta y = \left(\frac{P_W + P_P}{2} \right) \Delta y, \quad (3.119)$$

Finally, the link coefficients for the pressure correction must be analyzed more carefully at the outlet when the pressure is set constant. In this case, $\ddot{u}_e = \ddot{u}_P$ and $P_e = 0$; then, replacing \ddot{u} by $\dot{u} + u'$, and applying the equations for the cell center and cell face velocities (equations 3.76, 3.79, and 3.80, respectively) it gives:

$$a_E^P = 0, \quad (3.120)$$

$$a_W^P = \frac{\rho_w \Delta y^2}{2} \left(\frac{1}{a_W} + \frac{1}{a_P} \right) - \frac{\rho_e \Delta y^2}{2a_P}, \quad (3.121)$$

$$a_P^P = a_N^P + a_S^P + \frac{\rho_w \Delta y^2}{2} \left(\frac{1}{a_W} + \frac{1}{a_P} \right) + \frac{\rho_e \Delta y^2}{2a_P}, \quad (3.122)$$

$$S^P = -[(\rho_e \dot{u}_P - \rho_w \dot{u}_w) \Delta y + (\rho_n \dot{v}_n - \rho_s \dot{v}_s) \Delta x], \quad (3.123)$$

The link coefficients a_N^P and a_S^P stay the same when the outlet is set as illustrated in Figure 3.9.

The boundary conditions for the vorticity field are strictly related to the velocity field, and once it has already generated, the equation 3.56 can provide the boundaries for the vorticity field. Additionally, for the stream-function equation, the boundaries are

set being equal to their closest neighbor inside the domain (first order of accuracy).

All these boundaries conditions are inserted in the code. Obviously, they may change depending on the position of the walls, inlet and outlet. However, these changes follow the same logic as what was presented previously. It is important to emphasize that all case studies presented in this research have only one inlet and one outlet in a two-dimensional perspective although this code is already extended to more than one inlet.

Chapter 4

Code Development

“The price of success is hard work, dedication to the job at hand, and the determination that whether we win or lose, we have applied the best of ourselves to the task at hand.”

Vince Lombardi

This chapter aims to present how the code was developed. In addition, there will also be the inclusion of the necessary adaptations for each specific case study. Finally, a flowchart will summarize how each subroutine from the code is interconnected.

4.1 Code Structure

The numerical code has been developed in FORTRAN 95 language by linking three different files named: FLOW, GEOM, and CODE. Furthermore, some parameters can be easily changed in the first two files by the user, while CODE file represents the implementation of the iterative method with the discretization process and the numerical solution.

4.1.1 USER's Files

Some parameters are related to the main code, and they should be provided by the user. These values have been recorded in two files, in plain-text format, named:

FLOW and GEOM. The FLOW file (Appendix A.1) includes:

- **Line 1:** the number of cells in x- and y-directions (NI and NJ , respectively);
- **Line 2:** the fluid properties: viscosity μ [$\text{kg}\cdot\text{mm}^{-1}\cdot\text{s}^{-1}$] and density ρ [$\text{kg}\cdot\text{mm}^{-3}$];
- **Line 3:** the velocity inlet u_{in} [$\text{mm}\cdot\text{s}^{-1}$] and the gauge pressure outlet P_{out} [$\text{mm}^2\cdot\text{s}^{-2}$];
- **Line 4:** the velocity under-relaxations factors (α_u and α_v), and the pressure under-relaxation factor (α_P);
- **Line 5:** the number of iterations (it).

Thus, from the first line of the FLOW file, it is possible to simulate different meshes for each case. However, there is a memory usage limit to process these meshes by the computational machine. Therefore, the most refined mesh achieved in these simulations was 7,200 cells. It is important to point out that the computer has an Intel CPU, Core i5-7400, with 256 kB of L2 cache, with four processing cores and 64-bit architecture.

Water is the fluid, whose density (ρ) and dynamic viscosity (μ) are $9.97 \times 10^{-7} \text{ kg}\cdot\text{mm}^{-3}$ and $8.935 \times 10^{-7} \text{ kg}\cdot\text{mm}^{-1}\cdot\text{s}^{-1}$, respectively, that flows through all devices proposed in this research. Besides, the outlet boundary condition is set as zero pressure (gauge pressure), and also, the velocity inlet (u_{in}) is set by the user, and in this work, it is based on Re. The process analysis assumes isotherm flow (constant fluid properties), steady state regime and incompressible fluid. Equation 4.1 shows how to calculate the velocity inlet once that Reynolds number in the feed (Re_{in}), ρ and μ are known by the user; and the inlet area (A_{in}) is the length of each cell times the number of cells that fills the proposed feed size:

$$u_{in} = \frac{\mu Re_{in}}{\rho A_{in}}, \quad (4.1)$$

In addition, the unit of length used as an input, and subsequently applied to the solver, is on the mili scale in order to avoid iterations with very small or large values. However, the output of the results is provided in the unit of meters due to a conversion subroutine, which is the case of the results for the pressure [$\text{m}^2\cdot\text{s}^{-2}$], velocity [$\text{m}\cdot\text{s}^{-1}$] and stream-function [$\text{m}^2\cdot\text{s}^{-1}$] fields.

The under-relaxation factors range from zero to one depending mainly on what are the case study and the Reynolds number. Therefore, most of the simulations were performed starting from random values for these constants in order to find a range of values that was better suited to the case study.

Lastly, the number of iterations is directly influenced by Re and the case study again. For instance, the lid-driven cavity case needs only approximately 2,200 iterations (about three minutes) to reach the convergence at $Re = 800$, while 100,000 iterations (about five hours) are required for the residual to approach zero in a rectangular duct case with $Re = 100$. Besides, as Re increases, the chance of oscillations during the process also increases, and the user needs to compensate this in the under-relaxation factors by further dampening the contribution of the applied approximations (parameters with the prime symbol), implying an increase in the number of iterations.

In addition to the file related to the degree of refinement, the properties of the fluid, the boundary conditions and the constant of the algorithm; there is another file aimed at creating the mesh. Indeed, the GEOM file presents all boundary points in the superior and inferior walls along the channel. Therefore, the first and second columns represent the position in x- and y-direction, respectively, in the lower wall, while the third and fourth columns indicate the location in both directions for the topper wall. Appendix A.2 shows an example for the case of a rectangular duct (3 mm x 0.25 mm) with 80 cells in the x-direction (81 equidistant nodal points along x-axis). It is important to note that the number of lines in the GEOM file is equal to $NI+2$, since the first line is the name of the device while the following lines represent the positions of the x -faces on the north and south walls.

4.1.2 CODE File

The third file represents the connection between all steps of a CFD simulation as is proposed by Hirsch (2007) and detailed in Chapter 3. Therefore, the flowchart in Figure 4.1 shows how the CODE file operates by linking the additional files with the discretized process.

The first step includes reading the values set in the FLOW file, and subse-

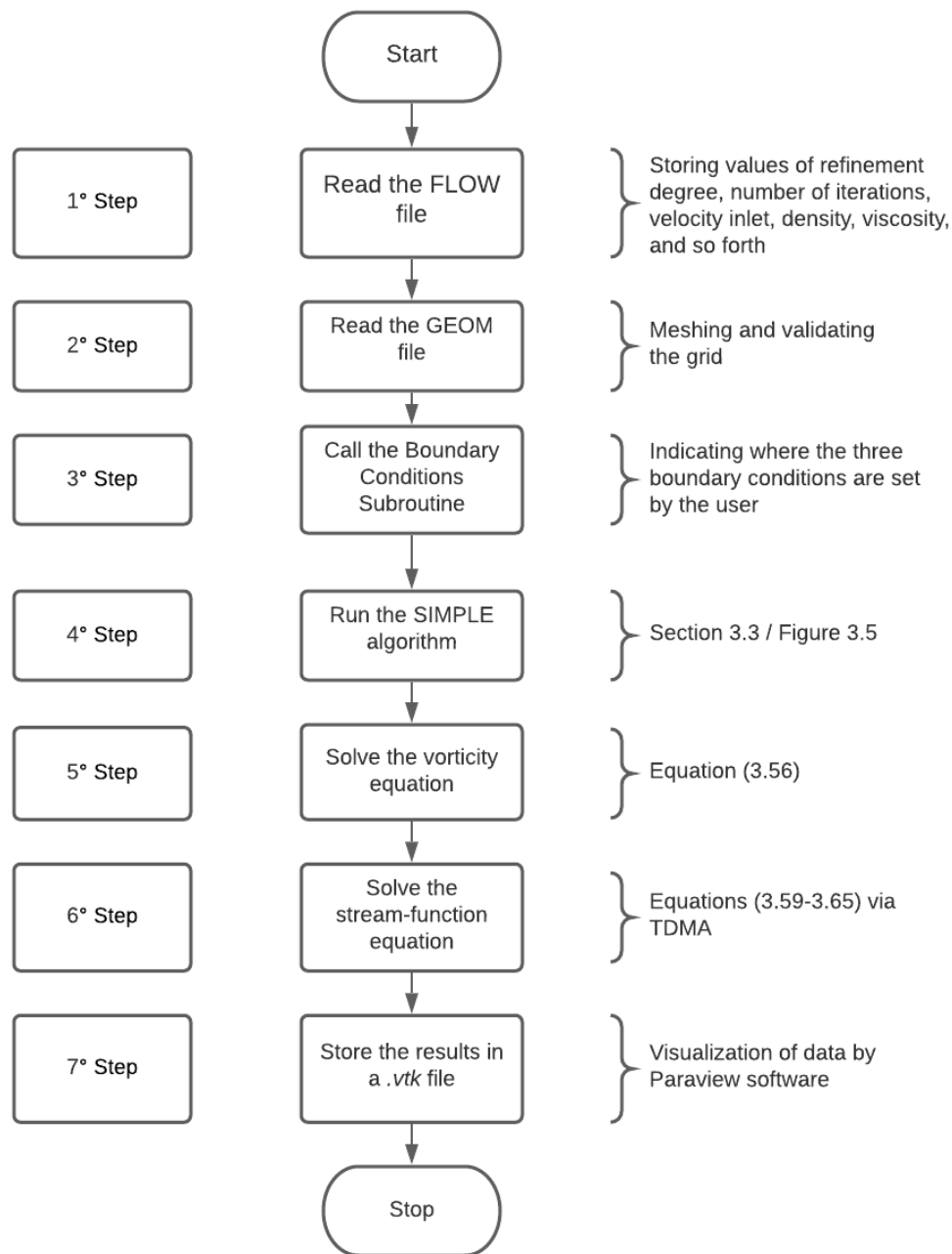


Figure 4.1: Flowchart of the code structure.

quently, creating matrices with dimensions of $NI+2$ and $NJ+2$. The matrix order is based on the number of cell-centered nodes (NI and NJ) added to the boundary condition nodes (2 nodes in each direction). In addition, the next part is the reading of the boundary points from the GEOM file. Hence, the grid is discretized in the whole domain and validated following the three conditions previously presented in section 3.2.1. Before the SIMPLE algorithm is executed, it is necessary to read the subroutine of boundary

conditions. In this way, the user needs to set the location of: the walls, the entrance(s) and the exit, and in sequence, assign the corresponding values for each one. Then, the iterative process is started as presented in section 3.3 until reaching convergence for the velocity and pressure fields. Sequentially, subroutines are called to solve the vorticity field, and finally, the stream-function field.

In addition, at each iteration, the code prints and stores the maximum imbalance of mass S_{max}^P and the sum of all S^P values along the mesh (S_{sum}^P). In this way, the user is able to follow the progress of convergence in terms of S^P by plotting graphs of S_{sum}^P as a function of the number of iterations.

After finalizing of the iterative method by obtaining the converged results for the fluid dynamic variables, the units of length of the pressure, velocity and stream-function fields are converted to meters in another subroutine. Lastly, the final step is related to the writing of the *.vtk* file format in order to fulfill the demands for the Paraview software and provide a discussion about the results, by plotting the fluid dynamics variables in color graphs, and visualizing the streamlines along the microchannel.

4.2 Case Studies

Three different devices in 2D have been analyzed during this work: a rectangular duct, a lid-driven cavity, and a convergent-nozzle coupled with a bumpy channel. However, some adaptations and changes were made to the code for each scenario. The next subsections present these variations in addition to the design of each device.

4.2.1 Rectangular Duct

The first two cases were studied to verify the accuracy of the results obtained by the code when compared with OpenFOAM version 7. Firstly, the length and the width of the duct are, respectively, 3 mm and 250 μm , and they are presented in Figure 4.2. Moreover, water flows in this devices at three values of Re: 100, 200 and 250. All simulations have been at steady state and constant temperature.

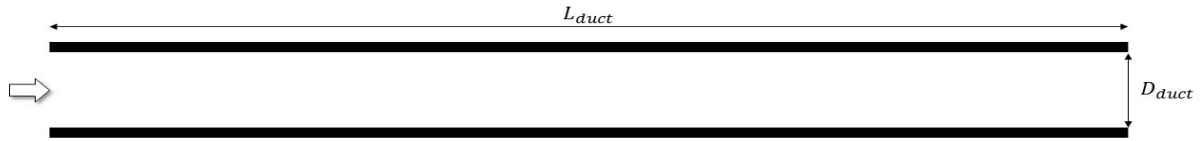


Figure 4.2: Representation of the rectangular duct where L_{duct} and D_{duct} are, respectively, 3 mm and 250 μm .

Further, for the rectangular duct, just the pressure and the velocity field were analyzed, and consequently, compared with OpenFOAM and equations from the literature. Thus, when the flow is fully developed in a rectangular duct, the maximum velocity V_{max}^{lit} can be calculated through the equation 4.2 proposed by Fox et al. (2011):

$$V_{max}^{lit} = \frac{3}{2}\bar{u}, \quad (4.2)$$

Where \bar{u} is the mean velocity of the fluid at a given x in a fully-developed flow; and also, this value can be considered equal to the uniform value set at the inlet. Moreover, the u -velocity along the y -axis has also an analytical solution, and consequently, it can be compared quantitatively with the results from the code and from OpenFOAM:

$$u = \frac{D_{duct}^2}{2\mu} \left(\frac{\partial P}{\partial x} \right) \left[\left(\frac{y}{D_{duct}} \right)^2 - \left(\frac{y}{D_{duct}} \right) \right], \quad (4.3)$$

Lastly, the pressure drop can also be analyzed quantitatively and compared with OpenFOAM once it is constant when the flow is fully developed.

4.2.2 Lid-driven Cavity

The second case evaluated herein this work was the square lid-driven cavity where water flows adjacent to the upper opened boundary. Figure 4.3 shows its dimension being L_{cavity} equal to 1 mm in all boundaries. Unlike the case of the rectangular duct, all discretized equations are solved here and, consequently, the pressure, velocity, vorticity and stream-function fields are generated by Paraview, and compared with OpenFOAM. Lastly, the fluid dynamic parameters were analyzed in terms of Re equal to 100, 200 and 400 where again the fluid properties are constant and the flow is at steady state.

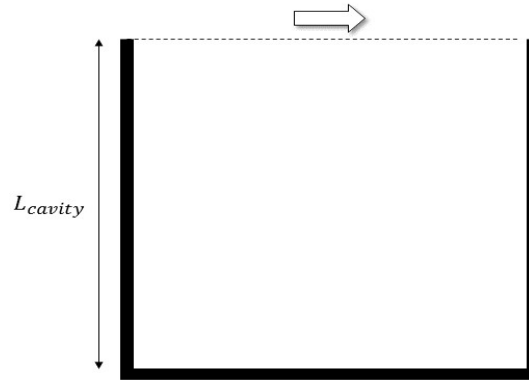


Figure 4.3: Representation of the square lid-driven cavity where L_{cavity} is equal to 1 mm.

The boundary condition for the inlet (top boundary) is set as the cell face velocity in the x -direction, so velocities u_e and u_w are known at this location. Further, v_n is assumed to be zero once the fluid is flowing adjacent to the top boundary. On the other hand, the gauge pressure at the outlet was not included in this simulation because its assumption is not valid. The fact is that the outlet section is the same as the inlet, and therefore the flow tends to develop itself and thus it presents considerable gradient values, not assuming a constant value at the exit.

4.2.3 Bumpy Microchannel

Many recent studies have suggested microdevices where the chaotic advection is caused by embedding obstacles and implementing waviness walls. In this research, the vorticity performance is evaluated not only by a waviness wall, but also by a lateral entrance.

The final case comprises all fluid dynamics parameters studied in this research where its geometry configuration is illustrated in Figure 4.4. The dimensions are presented as follows: d ($200 \mu m$) and D ($600 \mu m$) are the smallest and the largest width of the microdevice, respectively; L ($3,000 \mu m$), n ($600 \mu m$) and f ($200 \mu m$) are the horizontal lengths of the entire microdevice, the nozzle, and the inlet respectively; s ($300 \mu m$) indicates the feed position by measuring the distance between the largest width D and the feed f ; and L_b ($420 \mu m$) is the length of a single bump. Lastly, the number of bumps along the bumpiness channel is considered being equal to five convex bumps at both top

and bottom walls, and the position of each bump is parameterized, in micrometers, by the following equations for the south and the north walls, respectively:

$$p_{south}(x) = \frac{D-d}{2} + \left[75 \left(\sin \left(\frac{\pi(x-1)}{0.65} \right) \right)^{\alpha} \right], \quad (4.4)$$

$$p_{north}(x) = \frac{D+d}{2} - \left[75 \left(\sin \left(\frac{\pi(x-1)}{0.65} \right) \right)^{\alpha} \right], \quad (4.5)$$

Where α from the exponent in these equations dictates the curvature of the bump, and then, as α increases, the convex bump inside the channel gets sharper.

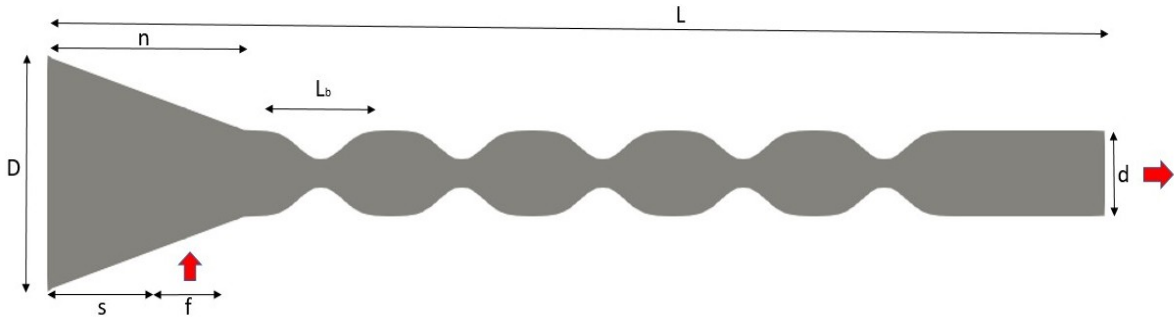


Figure 4.4: Representation of the convergent-nozzle coupled to the bumpy channel with $\alpha=4$.

This study evaluates the fluid dynamics parameters inside this microdevice by setting simulations changing the following variables:

- Device's width d : 200 μm and 250 μm ;
- Reynolds numbers: from 1 to 90;
- Curvature of the bumps α : 1, 2 and 4, and no bumps;
- Distance s from the inlet location to the left wall: 0 μm , 100 μm and 300 μm .

Firstly, it is studied how those fluid dynamics parameters behave as the curvature of the bumps (α) changes. Consequently, at each subsection related to α , the operating conditions (Reynolds number, Re) and the location of the inlet (s) are analyzed. Lastly, this procedure is performed again but evaluating a narrower channel based on d and comparing it with the results collected from the previous subsection.

Chapter 5

Results

“Success is no accident. It is hard work, perseverance, learning, studying, sacrifice and most of all, love of what you are doing or learning to do.”

Pelé

This chapter presents all results, and their respective analyzes and discussion. It is divided into two main sections: the first part shows the numerical results from selected benchmark cases, and the second one includes the study of the fluid dynamics in the new geometry in terms of vorticity and pressure drop.

5.1 Verification of the Code

The results provided from this code were compared qualitatively and quantitatively with the CFD software OpenFOAM (version 7) for two cases: rectangular duct and lid-driven cavity. In both scenarios were analyzed the fluid dynamic performance, which includes velocity, pressure, stream-function, and vorticity fields (these two last parameters were measured only at the lid-driven cavity case). Furthermore, the operating conditions were studied by varying the Reynolds number at the inlet in both cases.

5.1.1 Case Study in a Rectangular Duct

Firstly, three set of grids (40x20, 80x40 and 120x60 cells) were analyzed for the axial velocity profile along y -axis with axial location set at $x = 0.15$ mm - where the flow was still developing - and with $Re = 100$ (Figure 5.1). These grids were generated by changing the first line of the FLOW file (Appendix A.1 for 80x40 cells) and also the GEOM file in terms of the number of cells proposed (Appendix A.2 for 80x40 cells).

All analyzes for the discretization error estimation presented herein are based on the fine-Grid Convergence Index (GCI_{fine}) by collecting 10 points for the error estimation. In this case, although 20% of the points present an oscillatory convergence; the maximum discretization uncertainty is only 4.94%, and consequently, the grid with 3,200 cells was examined. Likewise, based on the Figure 5.1, it is also possible to notice that both simulations with 3,200 and 7,200 cells present similar performance for u -velocity under the proposed conditions.

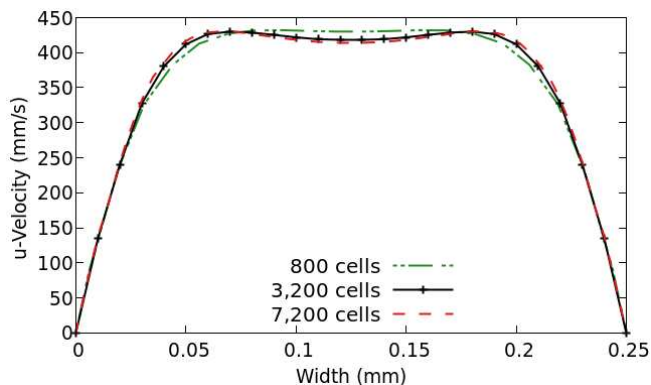


Figure 5.1: Grid dependent test with three meshes where $Re=100$ and $x=0.15$ mm.

After the mesh test, simulations were conducted regarding Re , which was based on the velocity inlet set in the FLOW file. Three Reynolds numbers were performed by using both programs and Figure 5.2 shows qualitatively how similar are their profiles. It is clear that the axial velocity increases as Re increases, and as the fluid elements move away from the wall due to the viscous effects. In addition, the flow develops along the x -axis, and according to Fox et al. (2011), the entrance length L_{ent} can be determined by: $L_{ent} = 0.06ReD_{duct}$, and therefore, L_{ent} is equal to 1.5 mm when $Re=100$.

Furthermore, three different locations along the x -axis were selected in Figure

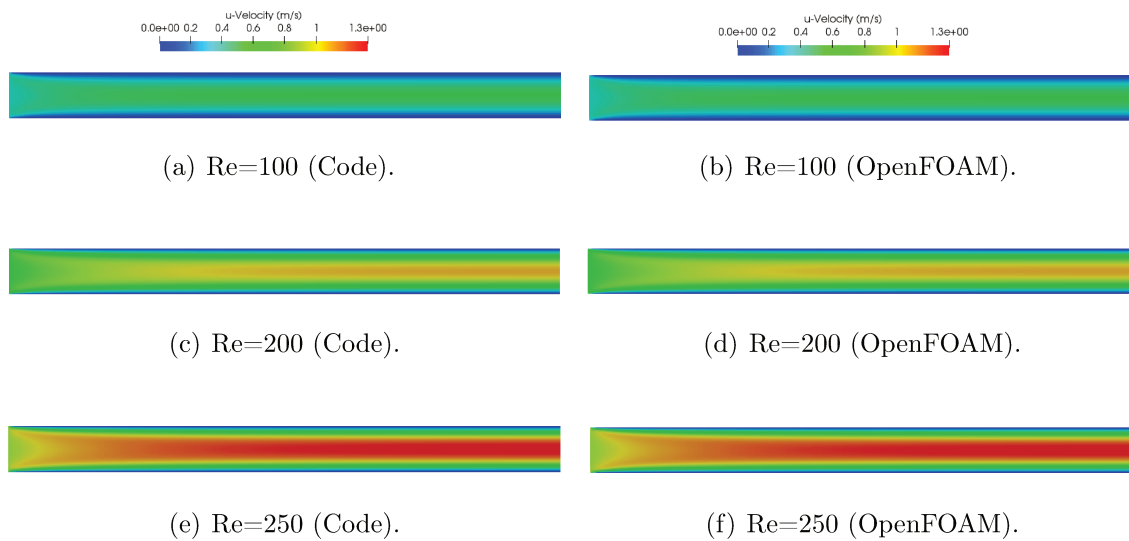


Figure 5.2: u -velocity in the x -direction regarding Reynolds numbers resulted from the developed code and from OpenFOAM.

5.3 in order to plot a few graphs in terms of u -velocity. When $x=0.15$ mm, the flow is abruptly affected by the action of the wall boundary condition, while $x=1$ and $x=2.5$ mm are the regions just before and just after the flow becomes fully-developed. Both programs have provided similar results, and also, the fully-developed flow condition allows to apply the analytical equation 4.3 as an additional way to compare the results as seen in Figure 5.3(d). Thereby, the maximum relative error for the u -velocity values obtained by the code and by the analytical solution was 5.20% near the wall; while the average relative error was 1.45%, allowing to conclude that the code gives great results by following the proposed conditions.

Likewise, the maximum velocity can be measured from the programs and from the equation 4.2. Therefore, V_{max}^{num} resulted from the code and from OpenFOAM are 537.1 mm/s, and 537.0 mm/s, respectively, while basing on the literature, it is equal to $V_{max}^l = 537.7$ mm/s, thus allowing this code to simulate results very close to the literature and OpenFOAM.

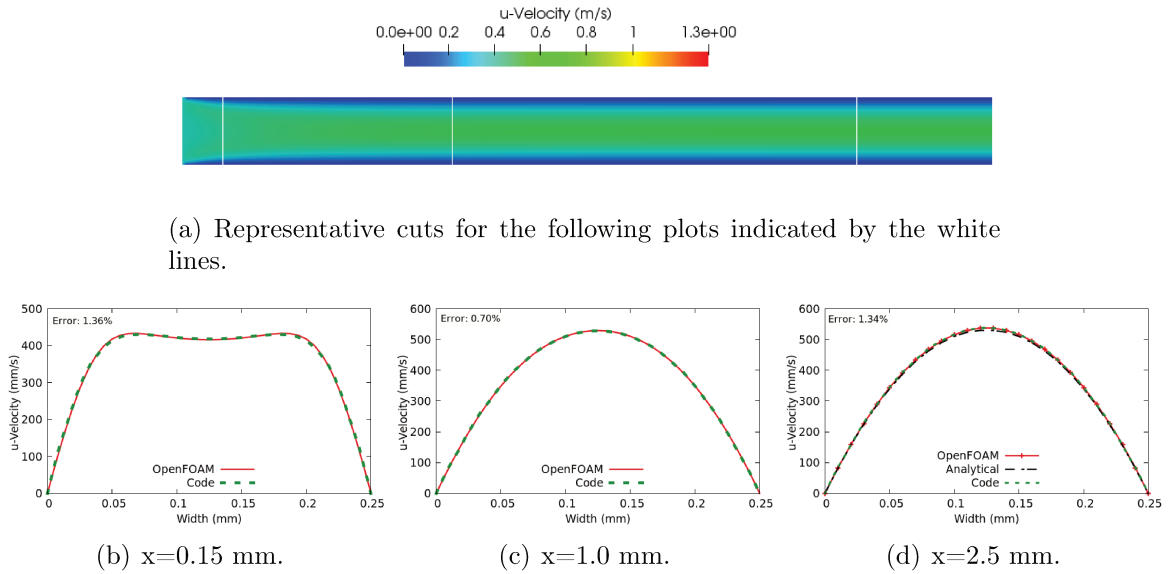


Figure 5.3: Comparison between the code and the OpenFOAM for u-velocity along y-axis at three locations in x-axis where $Re=100$.

Finally, the pressure field could be obtained and compared between the code and OpenFOAM. The Figure 5.4 illustrates how the kinematic pressure varies along the center line ($y=0.125$ mm) when $Re=100$. Based on these results, it is noticed that when the flow is fully developed, the pressure drop becomes constant as the velocity no longer changes.

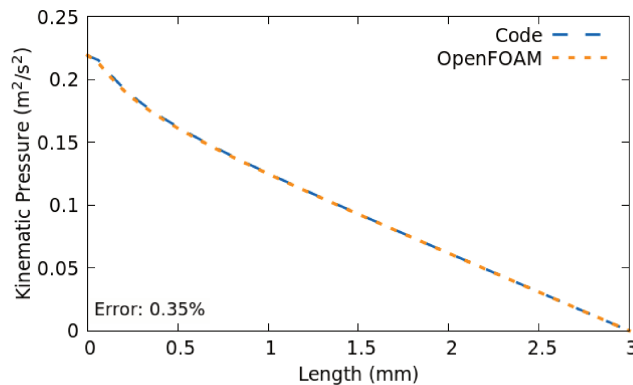


Figure 5.4: Comparison between the kinematic pressure results from code and OpenFOAM along x-axis for $Re=100$ at $y=0.125$ mm.

In parallel, the shear stress in a flow of a Newtonian fluid can be obtained in terms of the derivative of the axial velocity (equation 4.3) in y (Fox et al., 2011):

$$\tau = \mu \frac{\partial u}{\partial y}, \quad (5.1)$$

Thus, the shear stress gets dependent on the pressure gradient and the position of the fluid element on the y -axis:

$$\tau(y) = \frac{\partial P}{\partial x} \left(y - \frac{D_{duct}}{2} \right), \quad (5.2)$$

However, once the pressure gradient is constant, the shear stress reaches its apex when $y = D_{duct}$ or $y = 0$, and then, slowing down the fluid. In contrast, it is negligible when $y = 0.5D_{duct}$, allowing the u -velocity to speed up at this position.

5.1.2 Case Study in a Lid-driven Cavity

The second case was performed at three Reynolds numbers: 100, 200, and 400 by changing the velocity inlet in the FLOW file; afterwards, all results were compared with OpenFOAM version 7. Moreover, the evaluation of the two components of velocity, the stream-function and the vorticity are presented in this section. However, a grid study was firstly investigated herein by following the GCI_{fine} again: three set of grids (40x40, 60x60 and 80x80 cells) were analyzed for the u -velocity profile along x -axis at $y = 0.2$ mm, $y = 0.5$ mm and $y = 0.8$ mm. Figure 5.5 shows these positions in y -axis.

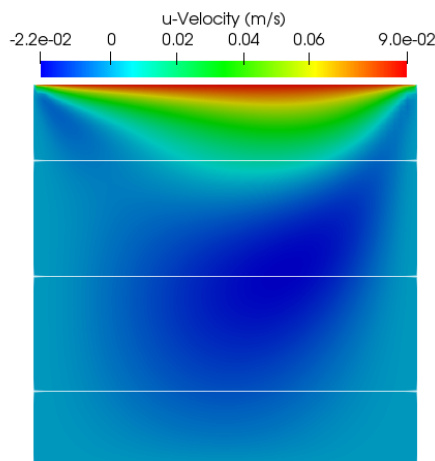


Figure 5.5: Representative slices (white lines) for the following analyzes.

For these three analyses, there were no point with oscillatory convergence and the maximum discretization uncertainty was 7.94% with an average value equal to 2.80% for when $y = 0.8$ mm. Moreover, the convergence in this case study is achieved

quickly, requiring about 3,000 iterations that, in time, means approximately five minutes to converge (case with 3,600 cells).

Figure 5.6 illustrates the u -velocity profile concerning the closest slice to the feed where the maximum discretization uncertainty was determined previously. From this figure, it is possible to see that all grids have good agreement at each other, and supported by its high speed at convergence, the grid with 3,600 cells was selected (Appendices B.1 and B.2 list the set up and the geometry, respectively, regarding this grid with $Re = 100$).

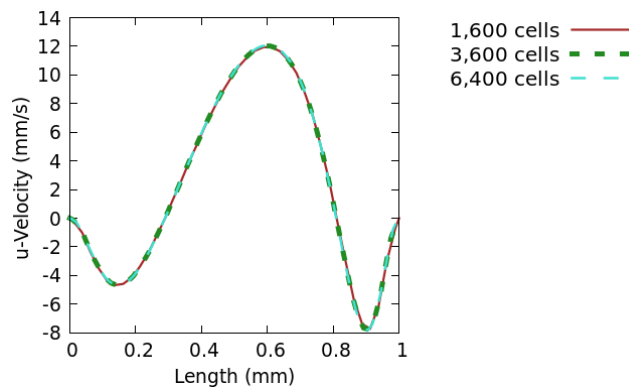


Figure 5.6: Comparison between the different grids for the u -velocity along the x -axis for $Re = 100$ at $y = 0.8$ mm.

The velocity field in the x -direction was also obtained and compared with OpenFOAM conform is illustrated in Figure 5.7 in terms of Re . A low value of Re induces a more diffusive than convective flow, and therefore, the flow with $Re = 100$ shown in Figures 5.7(a) and (b) is partially symmetrical on the y -axis. However, as Re increases, there is a greater intensity in the streamlines hitting the wall, favoring the occurrence of asymmetry in the conditions of $Re = 200$ and $Re = 400$. In addition, qualitatively, both softwares give similar results, and thus, Figure 5.8 comes with graphs in terms of Re in the three values of y previously established to evaluate quantitatively.

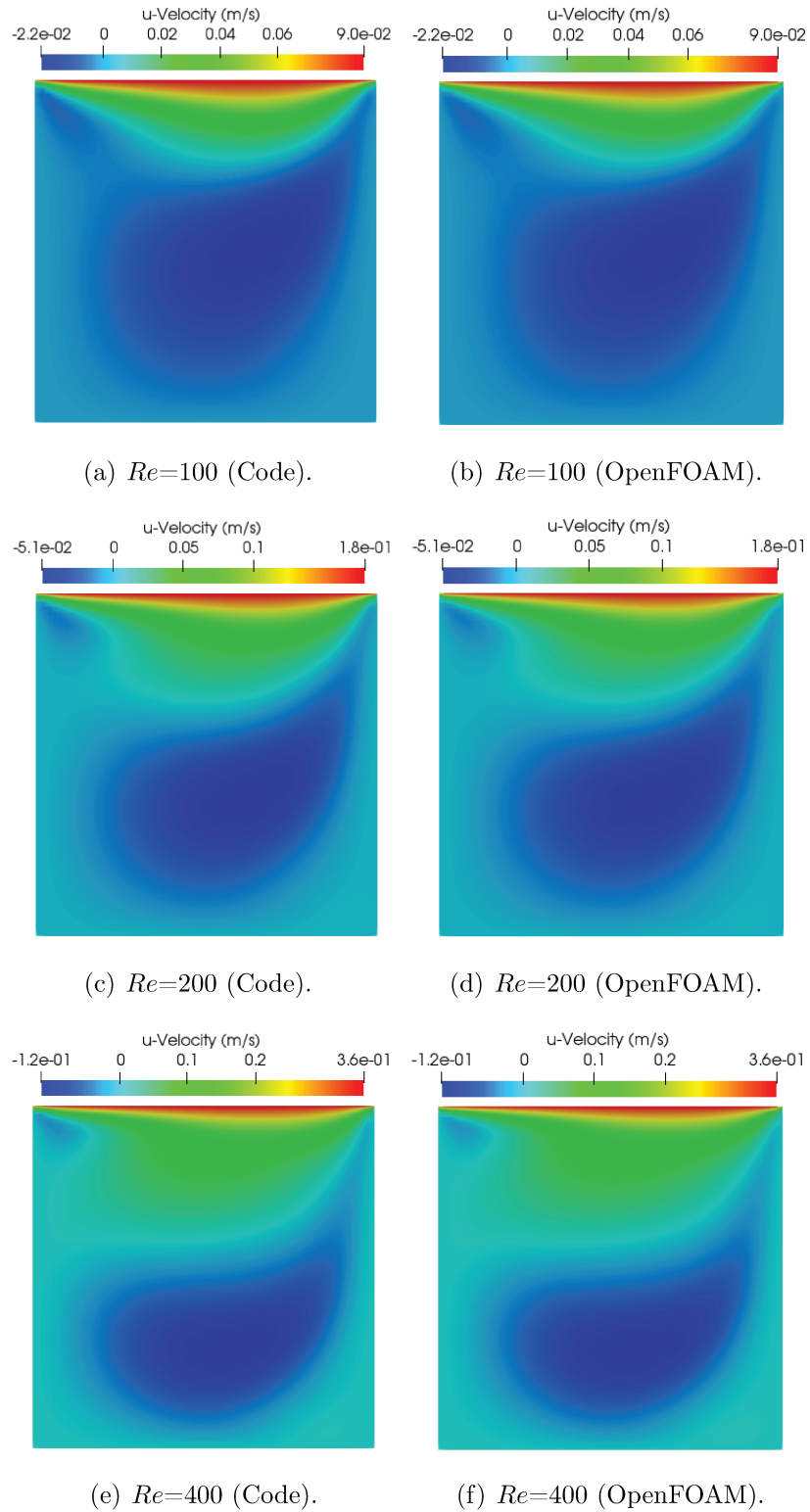


Figure 5.7: Comparison of u -velocity regarding Reynolds number between the code and the OpenFOAM.

The graphs in Figure 5.8 show that the velocity field for the component x calculated by the code showed excellent agreement with OpenFOAM once the biggest

relative average percentage error was 5.50% at $y = 0.8$ mm with $Re = 400$. This fact can be explained due to not only the increase in the intensity of the convective effects by Re , but also the plotting of the curve at $y = 0.8$ mm to be closer to the feed contour condition in which the non-zero value u_{in} is set. These contributions generate higher gradients in the velocity and pressure fields because of the zero values in the other borders due to for no-slip condition on the walls.

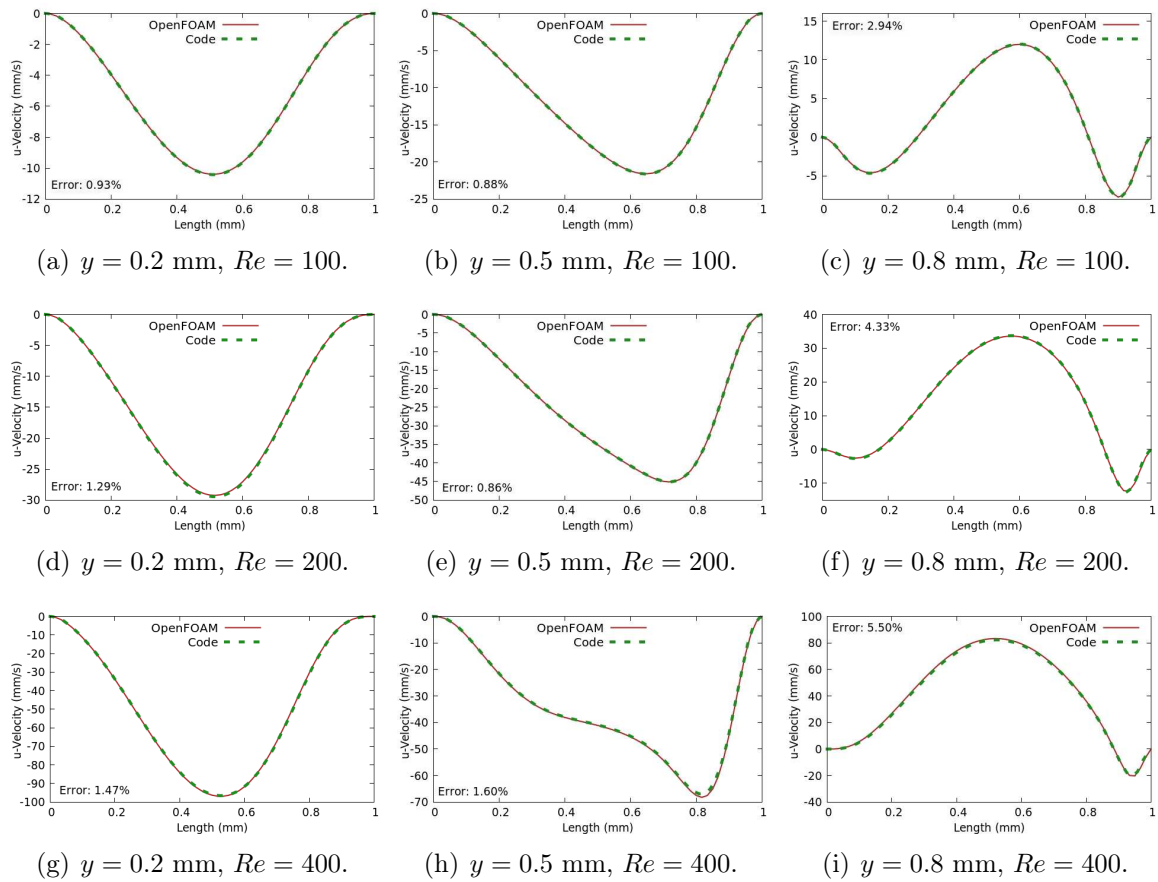


Figure 5.8: Comparison of the u -velocity profile at different heights and Reynolds numbers.

The velocity field in the y -direction was also analyzed under the same conditions and Figure 5.9 illustrates qualitatively the results obtained by the code and by OpenFOAM at the three Re values. According to this figure, it is noted that a large recirculation zone is created, caused by the boundary condition in the feed where fluid descends adjacent to the east wall and rises close to the west wall. Besides, the velocity fields are qualitatively similar again in terms of the softwares and due to this, some graphs are plotted in Figure 5.10 comparing them regarding Re at three positions in y -axis.

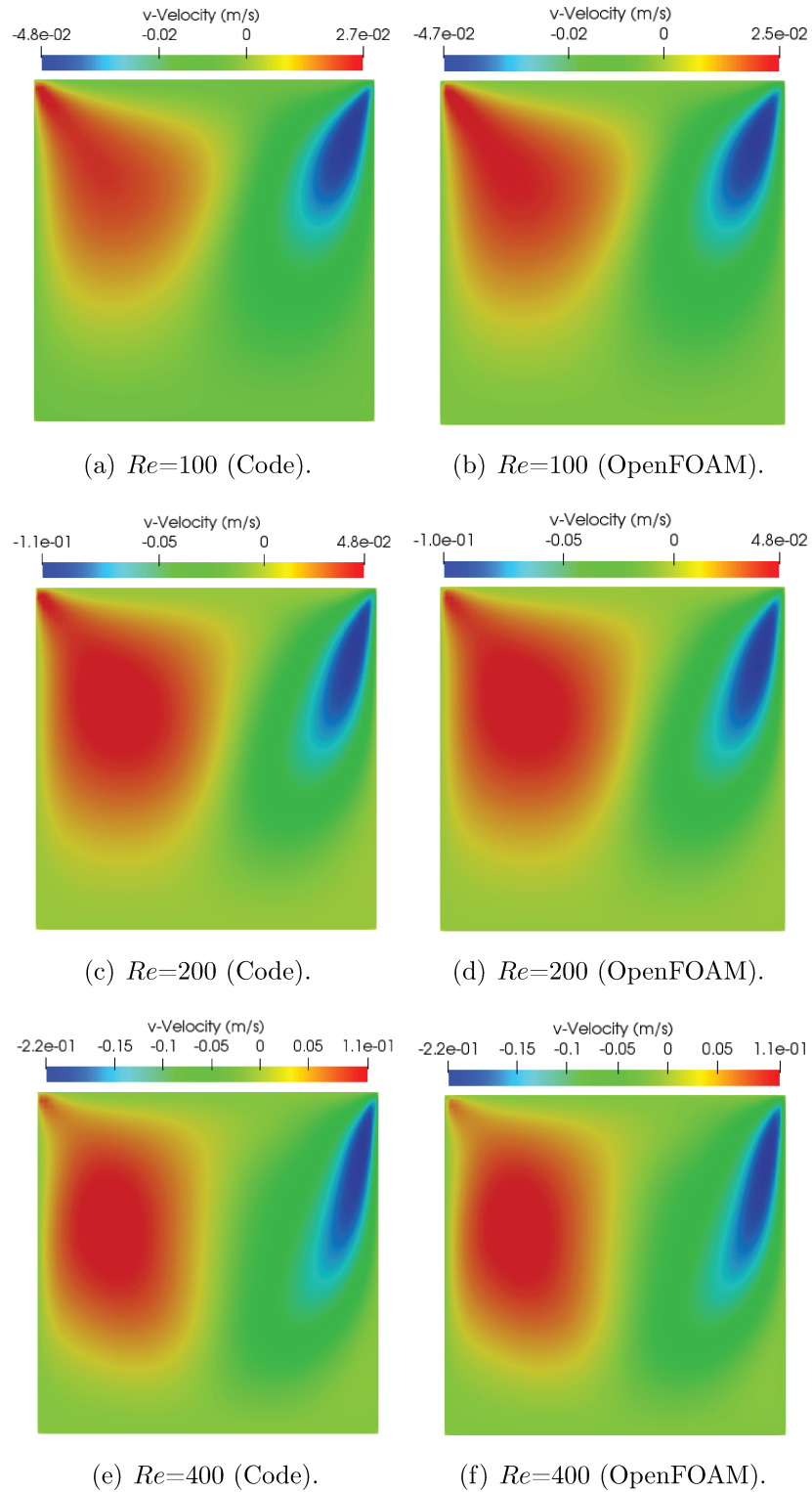


Figure 5.9: Comparison of v -velocity regarding Reynolds number between the code and the OpenFOAM.

Based on Figure 5.10, the highest mean relative error was only 2.98% for v -velocity when $Re = 400$ at $y = 0.2$ mm which means that both code and OpenFOAM can perform this case study and generate similar results in terms of v -velocity as well.

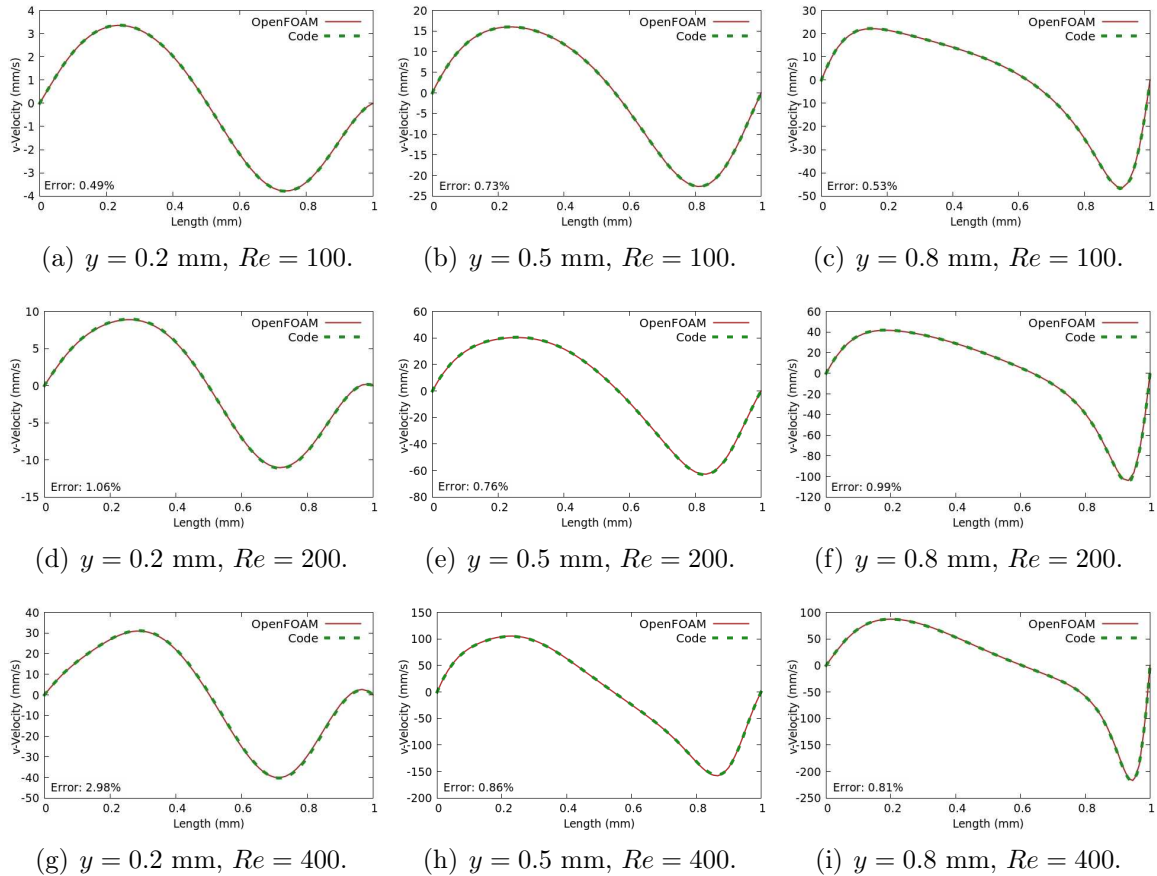


Figure 5.10: Comparison of the v -velocity profile at different heights and Re .

The vorticity field in the z -direction was obtained by the code and by OpenFOAM in terms of Re as is illustrated in Figures 5.11 and 5.12. The ParaView visualization software was responsible for generating the vorticity field from the velocity field calculated by OpenFOAM via its curl. Based on these figures, it is noted that by increasing the velocity inlet, it intensifies the vorticity, especially in areas close to the walls due to the viscous stress caused by the no-slip condition. Likewise, the fluid elements near the feed region are also rotated due to the velocity gradient caused by the movement of the lid where the velocity is higher (Figure 5.12(g)-(i)). Finally, qualitatively, both software provided similar results.

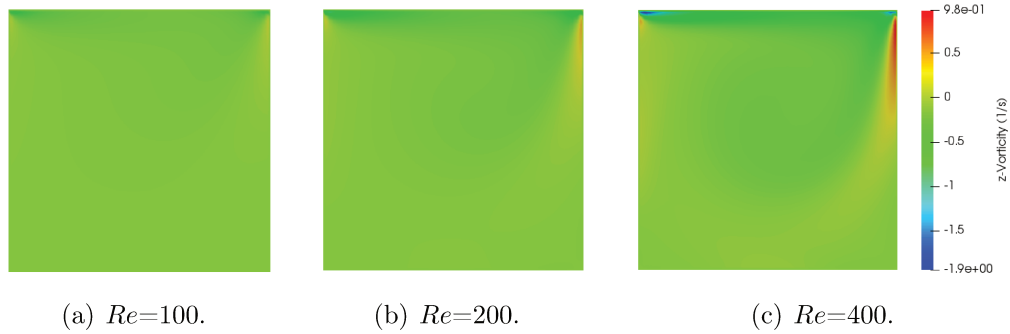


Figure 5.11: z -Vorticity component at different Reynolds numbers resulted by code.

The z -vorticity component was also measured quantitatively by plotting graphics in terms of Re and height of the cavity as shown in Figure 5.12. The highest mean relative error was 4.54% for z -vorticity when $Re = 400$ at $y = 0.2$ mm which allows to conclude that the vorticity parameter is also in agreement among both softwares.

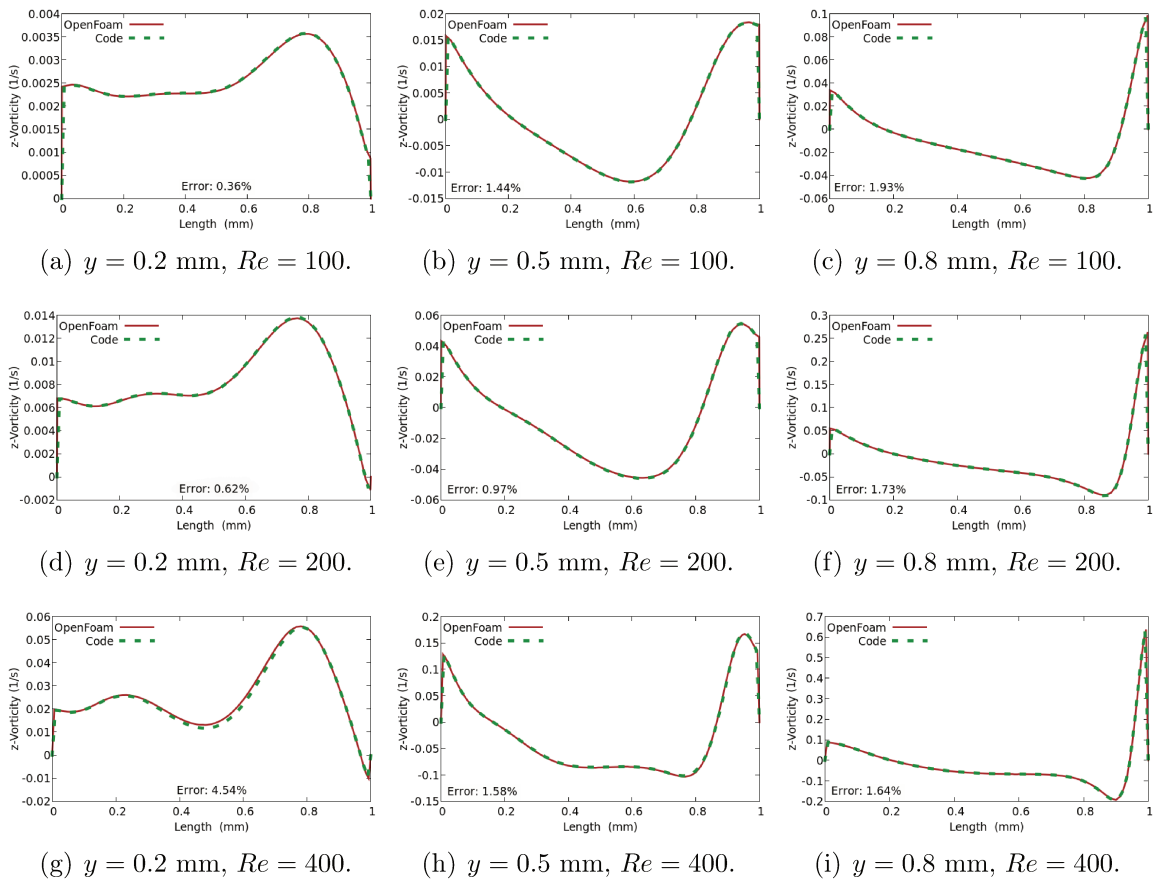


Figure 5.12: Comparison of the z -vorticity profile at different heights and Re .

The stream function field was evaluated only as in function of Re since both

OpenFOAM solver and ParaView had no functions available for the cavity case. In this way, Figure 5.13 shows how the stream function varies when Re increases, allowing to notice the recirculation zone that was previously mentioned. Moreover, the center of this vortex seeks the center of the cavity as Re increases, resulting in a greater and more uniform presence of fluid throughout the entire space. Lastly, a higher velocity also favors the formation of secondary and weaker vortices in the lower corners of the cavity.

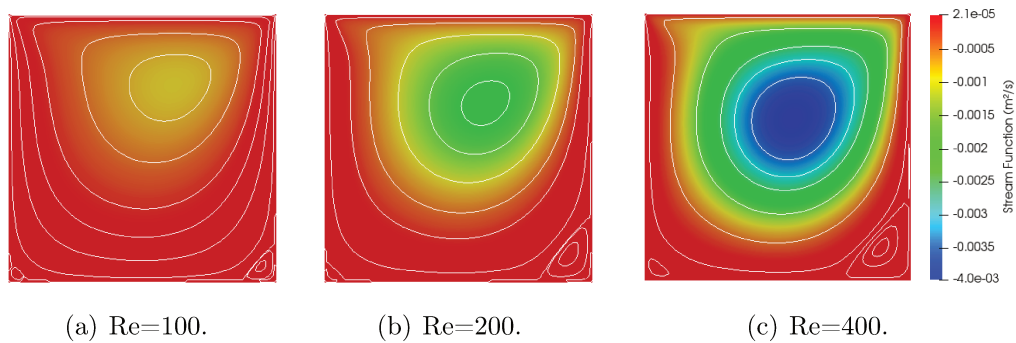


Figure 5.13: Stream function at different Reynolds numbers resulted by the code.

Thus, based on all these comparisons with OpenFOAM, in which the highest relative error was 5.50%, the discretization and subsequent implementation of the equations in the code showed an excellent agreement, and, therefore they are able to generate all fluid dynamics parameters worked herein on other devices. It is important to remember that the flow should have no turbulent contribution and no variation of temperature; and also, it needs to be incompressible with Newtonian fluid. Additionally, the flow regime is stationary with a no-slip condition on the walls.

5.2 Bumpy Microchannel

Three set of grids (1,800, 4,000 and 7,200 cells) were analyzed for the axial velocity profile along y -axis at $x = 0.8$ mm which represents the first throat caused by both top and bottom bumps. Table 5.1 lists the percentage of the averaged discretization error between these grids where GCI_{coarse} indicates the comparison between the grids with 4,000 and 1,800 cells, while GCI_{fine} compares 7,200 cells with 4,000 cells. In addition, the maximum uncertainty is determined considering the maximum value of GCI_{fine} and its respective u -velocity at its location. All these simulations were performed with $Re = 20$

| Mesh | Device's width d [μm] | Curvature α | GCI_{coarse} [%] | GCI_{fine} [%] | Maximum uncertainty [$\text{m}\cdot\text{s}^{-1}$] |
|------|---|-----------------------|-----------------------|---------------------|--|
| M1 | 200 | No bump | 0.81 | 0.79 | 0.1216 ± 0.0021 |
| M2 | | 1 | 9.06 | 3.92 | 0.0290 ± 0.0041 |
| M3 | | 2 | 6.05 | 2.95 | 0.4631 ± 0.0359 |
| M4 | | 4 | 3.93 | 1.50 | 0.0786 ± 0.0025 |
| M5 | | No bump | 0.44 | 0.42 | 0.1061 ± 0.0016 |
| M6 | 250 | 1 | 4.87 | 3.93 | 0.1775 ± 0.0342 |
| M7 | | 2 | 2.16 | 1.23 | 0.0587 ± 0.0033 |
| M8 | | 4 | 11.83 | 3.21 | 0.0137 ± 0.0028 |

Table 5.1: Discretization error (GCI), in percentage, for three grids in different sets of geometry configuration for $Re = 20$ and $s = 100\mu\text{m}$.

and $s=100\mu\text{m}$. Therefore, based on this table, for meshes M1 and M5, all analyzes were performed according to the mesh of 1,800 cells; while for the others, the grid with 4,000 cells was chosen.

The following sections assess how Reynolds number (Re) and the location of the feed (s) vary for a given device's width (d) and a given curvature of bump (α). Then, α é modified and Re and s are again measured for this new geometry configuration. Finally, the other width d is set and all parameters Re , s and α are evaluated again. All figures in terms of velocity, pressure, vorticity and stream-function fields are attached in Appendices C.3, C.4, C.5, and C.6, respectively.

5.2.1 Device's width: $d = 250\mu\text{m}$

In this section, the width of the microchannel is set constant and equal to $250\mu\text{m}$ while the curvatures of the bumps are analyzed in terms of Reynolds number and position of the feed.

5.2.1.1 Curvature of bumps: No bumps

The first geometry studied has no bumps along the microdevice while the operating conditions (Reynolds number) and the location (s) of the feed are varied. At the beginning, for the Re analyses, the location s is set as $100\mu\text{m}$.

(a) Reynolds number

Firstly, the magnitude of velocity is evaluated for a case with no insertions of bumps as shown in Figure 5.14 where $d = 250 \mu\text{m}$, $e s = 100 \mu\text{m}$. Based on this figure, it is possible to notice the main direction of flow of the fluid from the inlet to the outlet. In addition, the absence of bumps favors the flow to become fully-developed and thus laminar, allowing a profile similar to that presented in section 5.1.1 when the rectangular duct was evaluated. Therefore, the flow in the center line of the microchannel is intensified due to the weak action by the viscous forces originating from the walls. Moreover, the increase in Re also raises the flow rate of the fluid, making it more convective than diffusive.

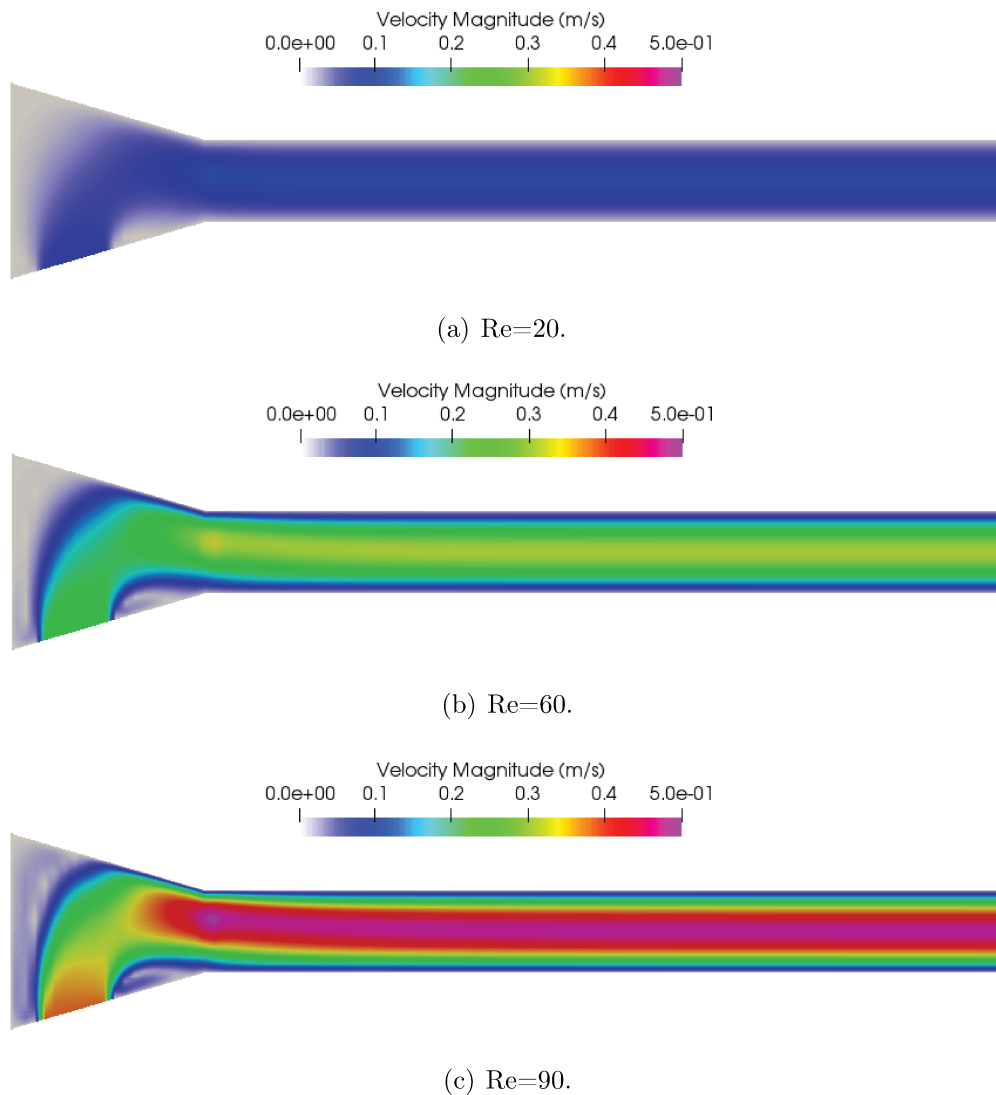


Figure 5.14: Magnitude of velocity regarding Reynolds number where $d=250 \mu\text{m}$, $s = 100 \mu\text{m}$ and there is no bumps.

Supported by this, the streamlines ratify what was said previously, in addition to showing weaker streams of fluid as shown in Figure 5.15. For $Re = 20$, tiny zone of circulation can be noted only at the corners of the nozzle and immediately downstream the feed. Likewise, along the microchannel, there is no recirculation zone for all Re chosen. For $Re = 60$, the recirculation seen at $Re = 20$ improves its area although it still has a value near zero. Finally, for the highest value of Re analyzed in this case, the vortices improve not only their area, but also their intensity as illustrated in Figure 5.15(c) at both sides of the feed where streamlines change their colors from white to blue.

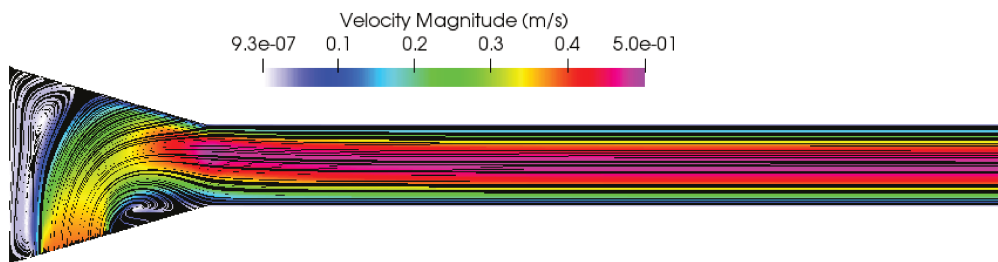
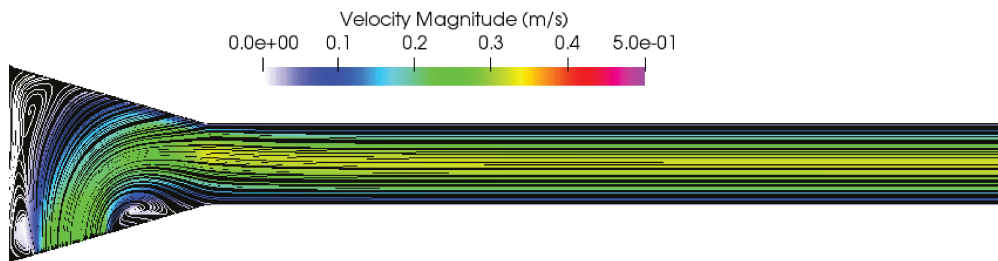
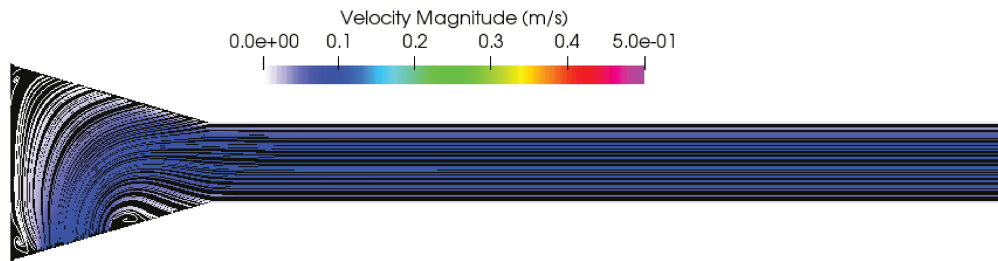


Figure 5.15: Streamlines along the microdevice where $d=250 \mu m$, $s = 100 \mu m$ and there is no bump.

The vorticity field could also be studied based on Figure 5.16 by increasing Re . The main areas where variation of vorticity is noted are near both walls and feed due to the velocity gradient. In this way, the upstream recirculation zone presents a lower velocity when compared to the main streamlines originated by the feed, and so this gradient favors the rotation of the fluid elements. Another important factor is that the maximum vorticity is obtained in the region where the cross-sectional area of the channel stops decreasing and becomes constant in the upper wall. This happens because the main streamlines reach the upper wall and undergo an abrupt change of direction making the fluid elements rotate and flow close to the wall. Additionally, the reduction of the

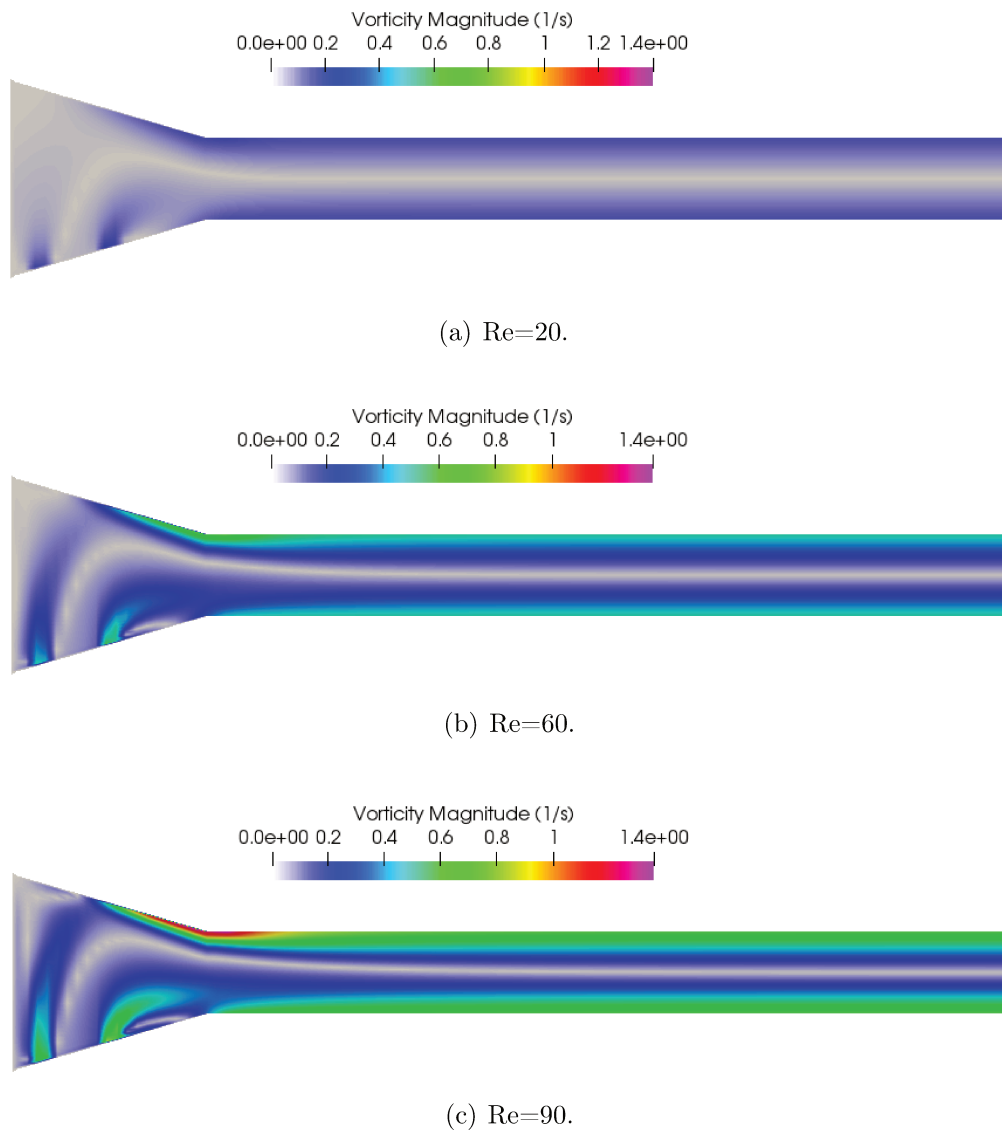


Figure 5.16: Vorticity field at different Reynolds numbers where $d=250 \mu m$, $s = 100 \mu m$ and there is no bumps.

cross-sectional area as it flows, makes it propel to increase its velocity and then, when it reaches the straight microchannel, the fluid tends to continue flowing in the direction of converging, thus creating a small region of positive pressure gradient in the upper corner of the microchannel, and hence making the fluid rotate. Therefore, by increasing Re , the velocity will get higher and, consequently, the rotational motion of the fluid elements will get greater.

The following Figure 5.17 illustrates the names for each position in which the graphs were plotted. Thus, Bump0 is located at $x = 0.6$ mm, while, Bump1: $x = 1.0$ mm, Bump2: $x = 1.42$ mm, Bump3: $x = 1.84$ mm, Bump4: $x = 2.26$ mm, Bump5: $x = 2.68$ mm. Although this device does not have bumps, these names were selected to maintain a standard with the other devices to be studied soon. These slices were selected in the neighboring planes for each bump, that is, in the cavities between the bumps.



Figure 5.17: Representation of the positions selected for the analyses in the following graphics.

In this way, some fluid-dynamic parameters can be evaluated in these positions. Figure 5.18 compares the velocity field in the x -direction with respect to the x -locations for the three Reynolds number values. As expected, the velocity field is maximized in the center of the microchannel due to the low shear stress contribution. In addition, only the velocity profile at Bump0 was asymmetrical, and this is because the fluid flow is mainly located in the upper wall due to the lateral feed. Further, as Re increases, the velocity profile enhance and becomes more asymmetrical and sharper due to the larger velocity gradient. Also, when $Re = 90$, it is noted that the velocity field at Bump1 starts becoming slightly asymmetrical as Bump0 affected by the feed.

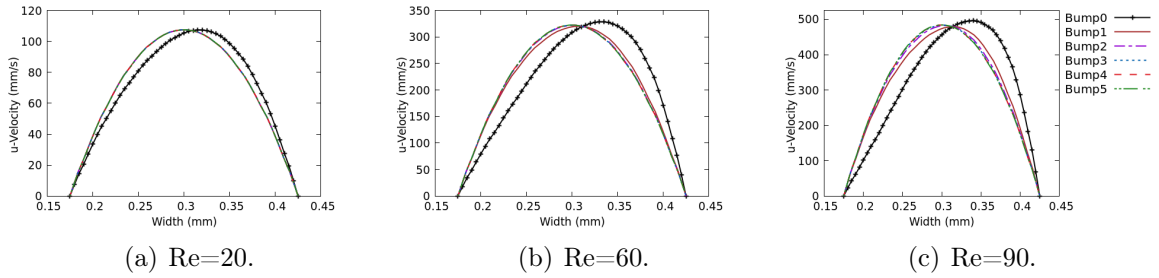


Figure 5.18: u-Velocity regarding Reynolds number and "location of bumps" where $d=250 \mu m$ and there is no bumps.

The kinematic pressure profile is shown in Figure 5.19 according to Re and the location of the slices. Note that the pressure does not depend on the y -axis along the straight microchannel, being only asymmetric at Bump0 due to the feed with subsequent channel narrowing. Lastly, the pressure is reduced until reaching the outlet where the pressure is set to zero.

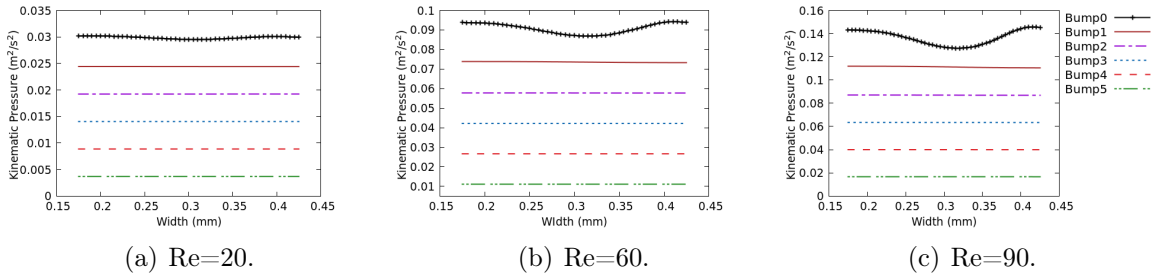


Figure 5.19: Kinematic pressure regarding Reynolds number "location of bumps" where $d=250 \mu m$ and there is no bumps.

The magnitude of the rotation of the fluid elements is shown in Figure 5.20. The vorticity is proportionally related to Re so that the effects of viscous forces are intensified, and therefore its value is greater for when $Re = 90$. On the other hand, along the straight duct, the vorticity field does not change in the x -positions set for all Re cases once the flow becomes fully-developed. Additionally, the vorticity is higher near the upper wall at the entrance of the device due to the flow is predominantly concentrated there, and there is a large velocity gradient.

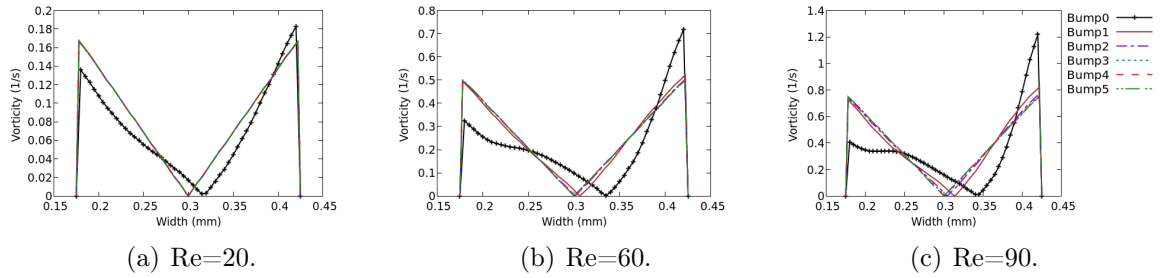


Figure 5.20: Magnitude of vorticity regarding Reynolds number and the "location of bumps" where $d=250 \mu\text{m}$ and there is no bumps.

It is also possible to plot a graph that shows how the average magnitude of the vorticity varies along the x -axis as shown in Figure 5.21(a). Note that the rotational motion adjacent to the main flow is improved at $x = 0.1 \text{ mm}$ and $x = 0.3 \text{ mm}$ because of the viscous forces again. Moreover, this vorticity is maximized when the flow leaves the converging nozzle and enters the straight duct ($x > 0.6 \text{ mm}$) due to the narrowing of the channel that results in a larger velocity gradient along the y -axis. Figure 5.21(b) shows a slight positive pressure gradient at $x = 0.6 \text{ mm}$ in the center-line when $Re = 90$ that favors the rotation of the fluids like it was explained in section 2.2 (Vorticity field).

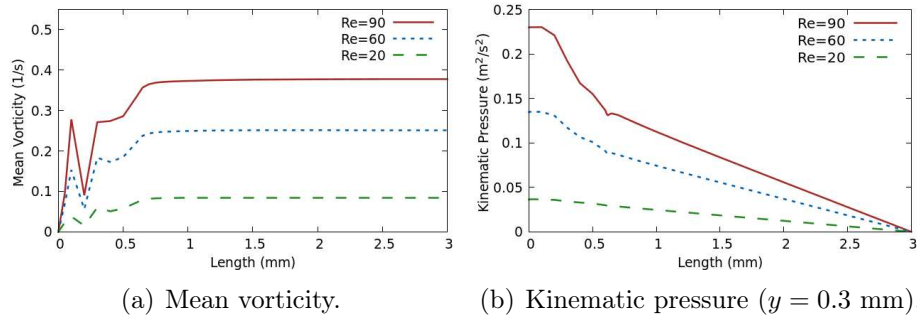


Figure 5.21: Mean vorticity and kinematic pressure performances along the device regarding Re for $s = 100 \mu\text{m}$, and $d = 250 \mu\text{m}$.

In the next sections, some geometry configurations will be presented and evaluated in order to intensify the fluid vorticity and analyze this pressure drop along the channel.

(b) Location of feed (s)

In this section, the distance between the feed and the left wall is analyzed at

three different positions: $0 \mu m$, $100 \mu m$, and $300 \mu m$. All following results are based on $Re = 90$ that is the best Reynolds number for increasing the vorticity (in the range studied) as discussed before. Figure 5.22 illustrates the velocity field for these three feed positions.

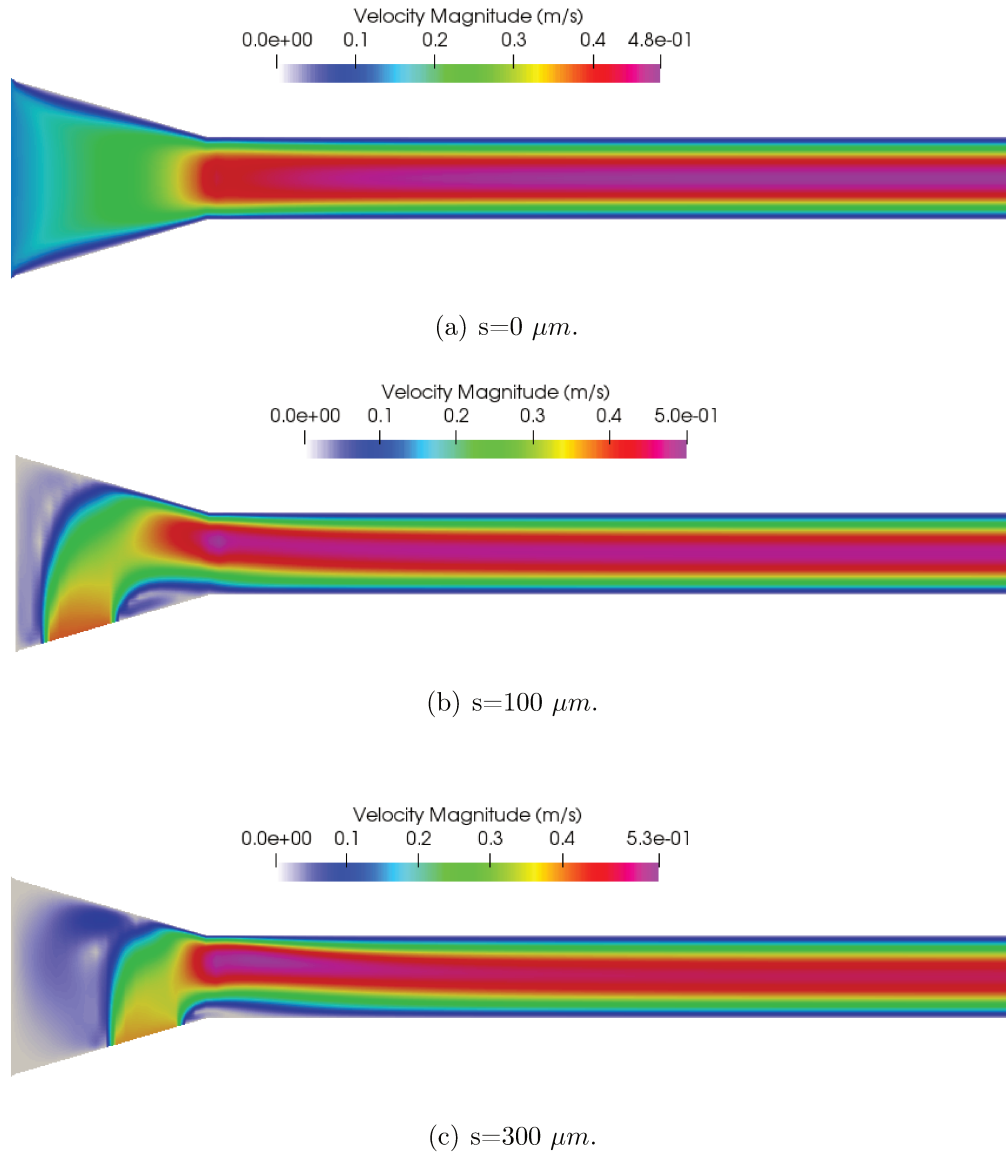


Figure 5.22: Magnitude of velocity regarding the location of the feed where $d=250 \mu m$, $Re = 90$ and there is no bumps (These figures do not have the same data range).

Based on this figure, the magnitude of the velocity field along the straight duct is barely affected in terms of entrance position; on the other hand, for $s = 300 \mu m$, there is a recirculation zone in the non-uniform region of the device that contributes to the formation of vortices. Further, it is possible to notice a slight increase of the velocity

at the beginning of this channel by checking the data range when the entrance is farthest from the wall ($s = 300 \mu\text{m}$). Thus, taking as a reference the maximum velocity obtained for the case with a feed on the left wall ($s = 0 \mu\text{m}$), there is an increase in the maximum velocity of 3.4% for the case with $s = 100 \mu\text{m}$, and 10.3% for when $s = 300 \mu\text{m}$.

Similarly, the vorticity field does not show great changes along the x -axis in the straight duct section when the three cases are compared as illustrated in Figure 5.23. Furthermore, the vorticity is maximized in the connection zone between the converging nozzle and the straight duct caused by the extension of the boundary layer with an increase

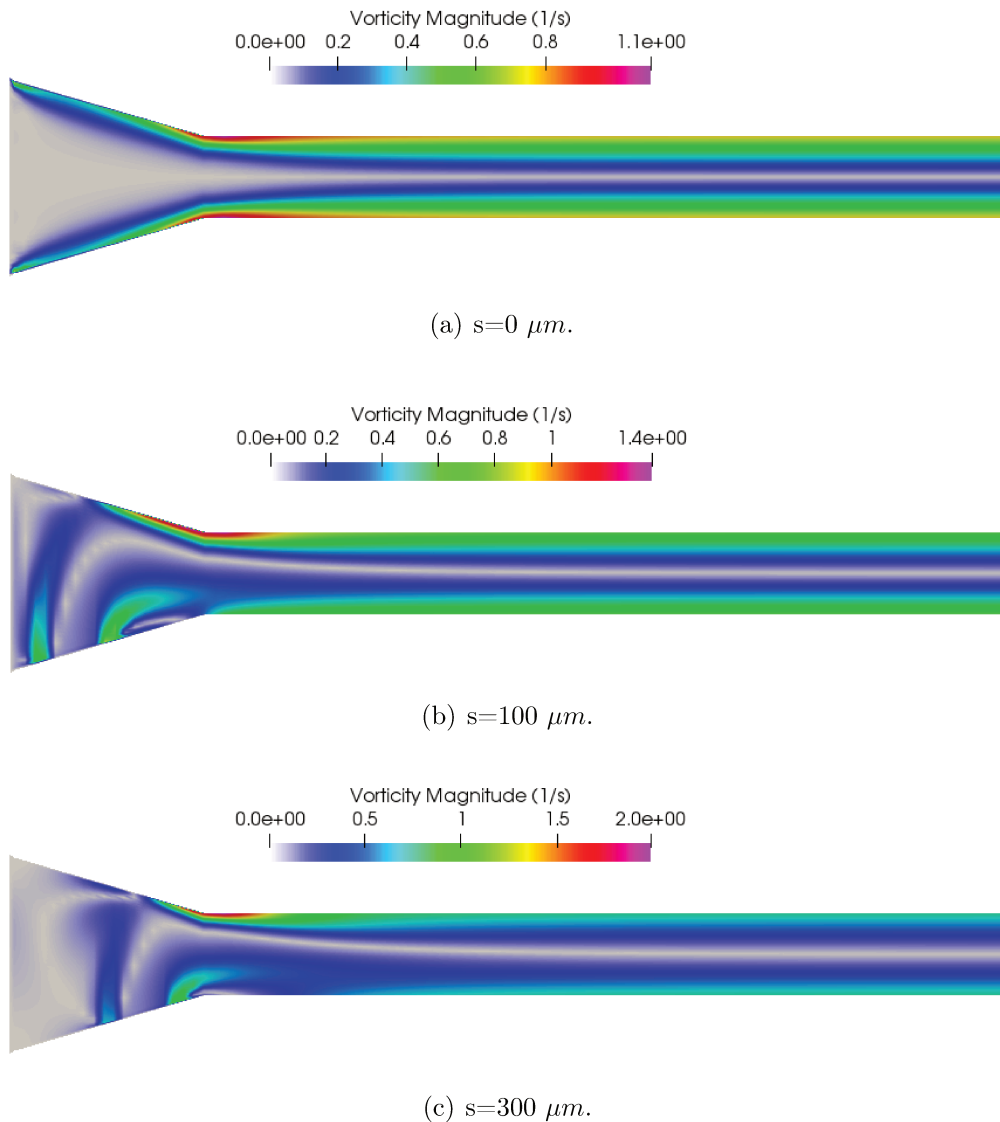


Figure 5.23: Vorticity field at different locations of the feed where $d=250 \mu\text{m}$, and $Re = 90$ (These figures do not have the same data range).

in the pressure, which results in a change in the flow direction. Consequently, by taking as a reference the maximum vorticity obtained for $s = 0 \mu\text{m}$, there is an improvement in this parameters of 23.0% when $s = 100 \mu\text{m}$, and 79.7% for when $s = 300 \mu\text{m}$.

Lastly, mean vorticity and pressure fields were plotted in terms of x -axis as shown in Figure 5.24. Note that these parameters only diverge in the first half of the device, and then they flow into the straight duct and present the same results because the flow has become developed. Also, although the microdevice with an entrance at $s = 300 \mu\text{m}$ reaches higher values of vorticity, its pressure drop is more accentuated; which would make its design and operation more costly.

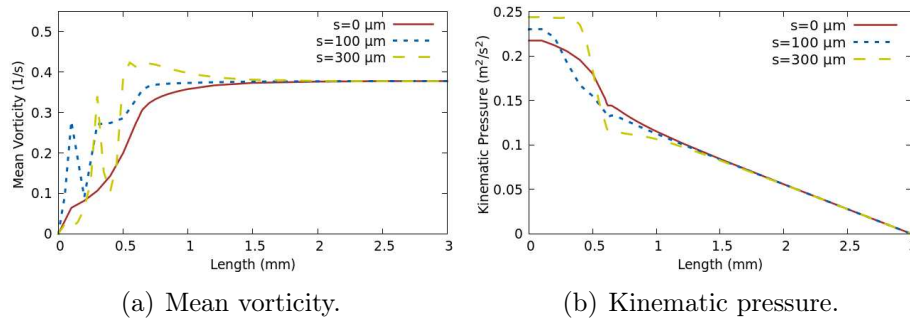


Figure 5.24: Mean vorticity and kinematic pressure performances along the device regarding s for $Re = 90$, and $d = 250 \mu\text{m}$.

5.2.1.2 Curvature of bumps: $\alpha = 1$

Based on the results obtained previously, a strategy that could take advantage of the straight microchannel was analyzed. Then, different types of curvatures of bumps were evaluated according to the equations 4.4 and 4.5 that projected convex bumps inside the channel that consequently narrowed the fluid flow. In this way, a smoother bump was firstly proposed, where α in these equations is equal to 1.

(a) Reynolds number

The operating condition related to Re was firstly studied in this new microdevice, and Figure 5.25 presents the velocity fields as a function of $Re = 20, 60$ and 90 when $s = 100 \mu\text{m}$. The insertion of bumps helped considerably to increase the flow rate of the fluid as illustrated in this figure. Additionally, comparing the maximum velocity values

located on the center line of the device ($y = 0.3 \text{ mm}$), it was found that the velocity raised 125.0% in relation to the microdevice with no bumps when $Re = 90$.

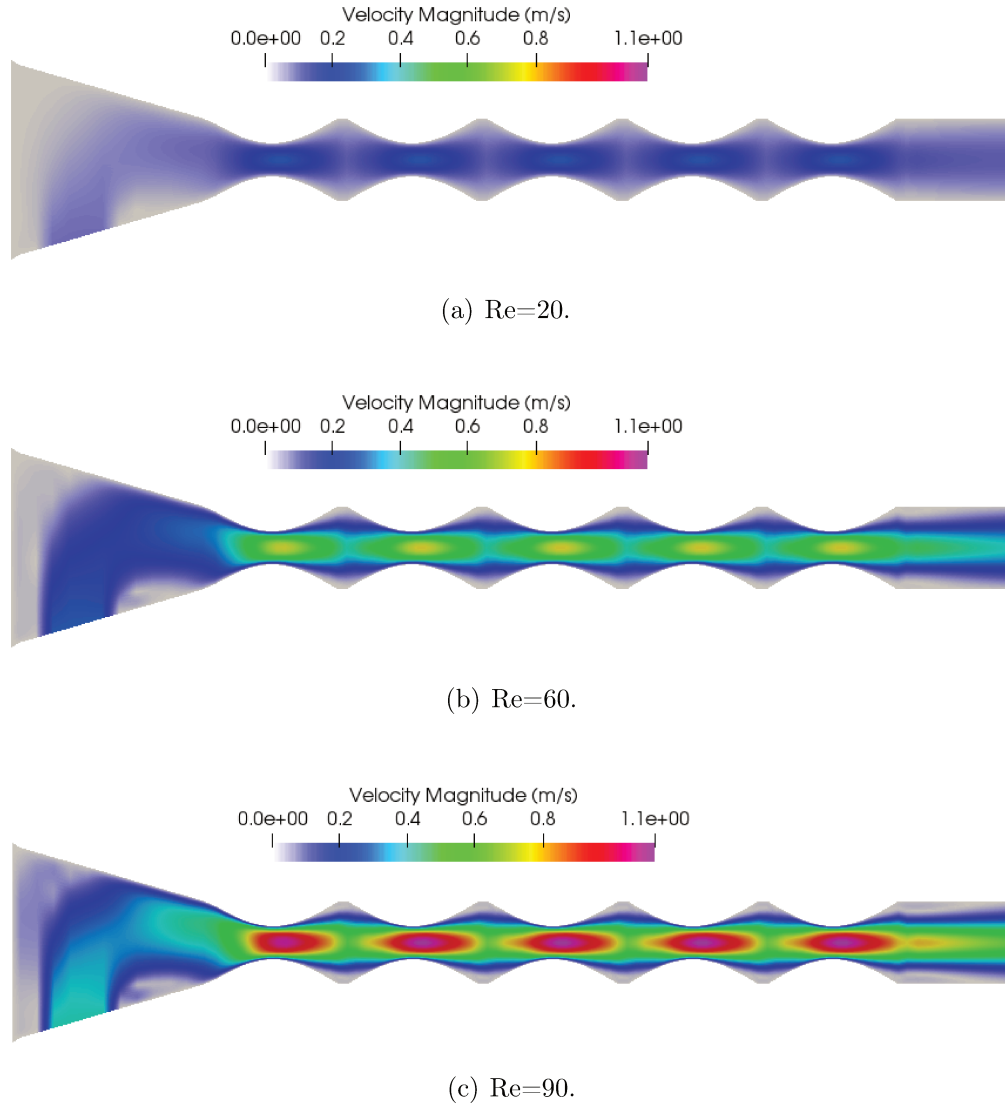


Figure 5.25: Magnitude of velocity regarding Reynolds number where $d=250 \mu\text{m}$, $s = 100 \mu\text{m}$ and $\alpha = 1$.

The streamlines provided by ParaView in Figure 5.26 were based on the velocity field obtained by the code, and they illustrate how the fluid behaves in the cavities between the bumps. Therefore, in addition to the recirculation zones formed in the region of the entrance in the converging nozzle (discussed previously), there are now new vortices being created mainly when $Re = 90$ where they are intensified and expanded. To make this explanation clearer, the vorticity field is illustrated in Figure 5.27 and its average

profile along the x -axis is plotted in Figure 5.29 along with the kinematic pressure and u -velocity performances.

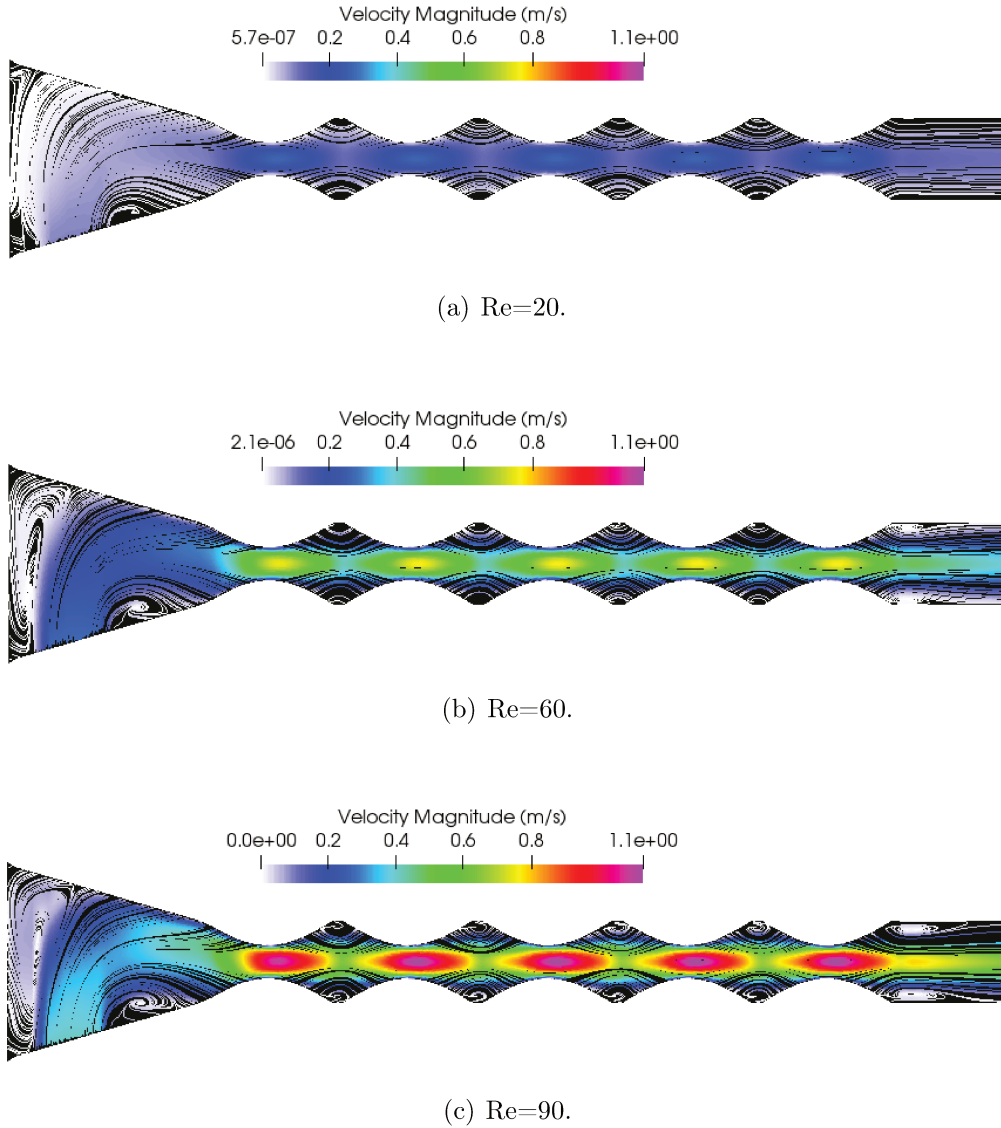


Figure 5.26: Streamlines along the microdevice where $d=250 \mu m$, $s = 100 \mu m$ and $\alpha = 1$.

The entry section of the microdevice in the converging nozzle has a great contribution to the increase in the velocity (and also in the vorticity) once the cross-sectional area is reduced. However, when there is inclusion of convex bumps, the fluid finds a narrower area to flow through, and thus it results in a greater increase in the velocity. Likewise, immediately after the constriction, the vorticity field increases considerably in the regions downstream close to the walls (Figure 5.27) due to the variation in the pressure

gradient that induces the fluid to change its direction.

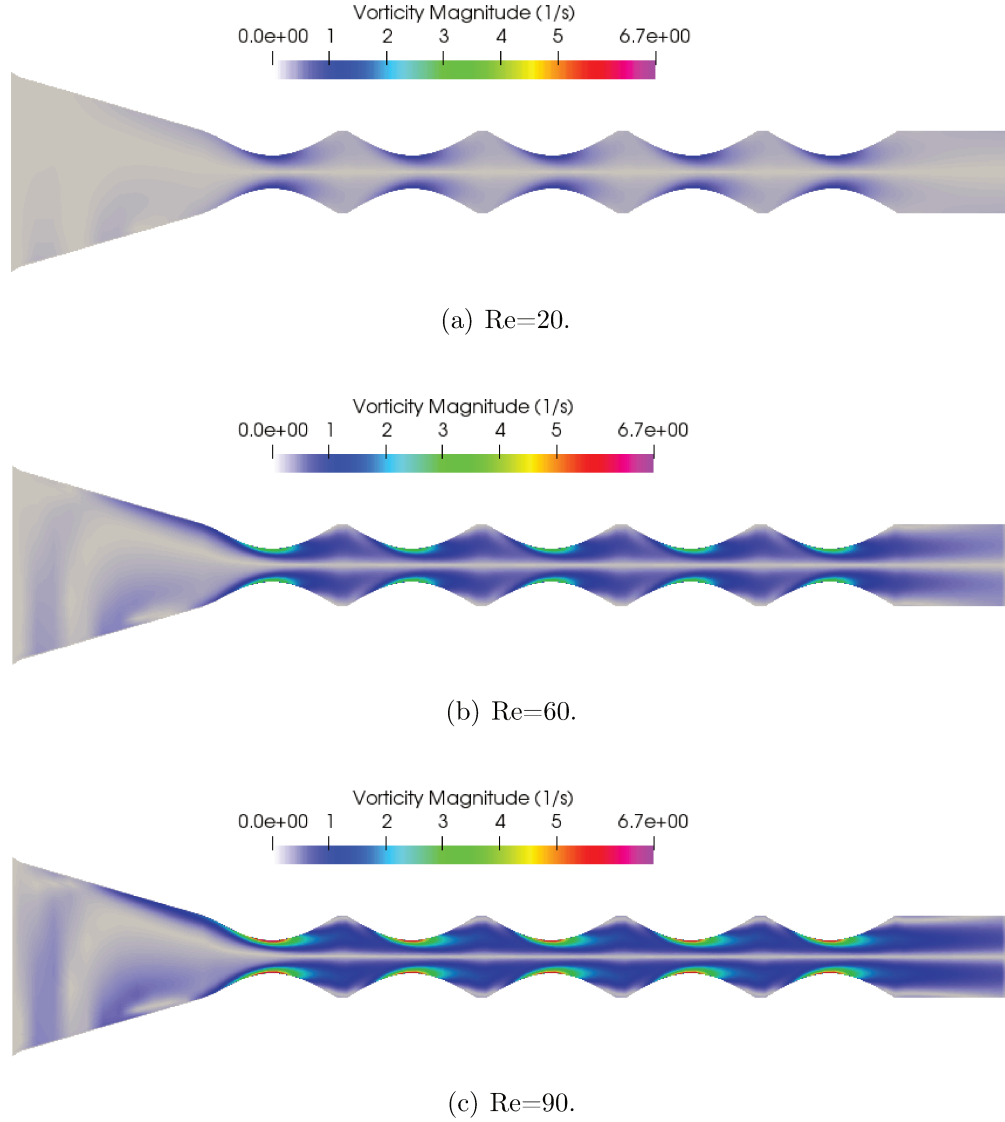


Figure 5.27: Vorticity field at different Reynolds numbers where $d=250 \mu m$, $s = 100 \mu m$ and $\alpha = 1$.

Figure 5.28 shows how the mean vorticity, the kinematic pressure and u -velocity fields vary along the x -axis. Note that in the bumpy section, when the velocity intensifies, the vorticity directly increases, and it is due to the enhancement of the velocity gradient along the y -axis; meanwhile, at the same time, the pressure decreases until the peak at $x = 0.83$ mm, for example, in Figure 5.29. Besides that, at every peak of pressure drop, the vorticity and the u -velocity reach their maximum value once they are related at each other. In addition, when compared to the device with no bumps, the mean vorticity

for when $\alpha = 1$ is approximately four times greater.

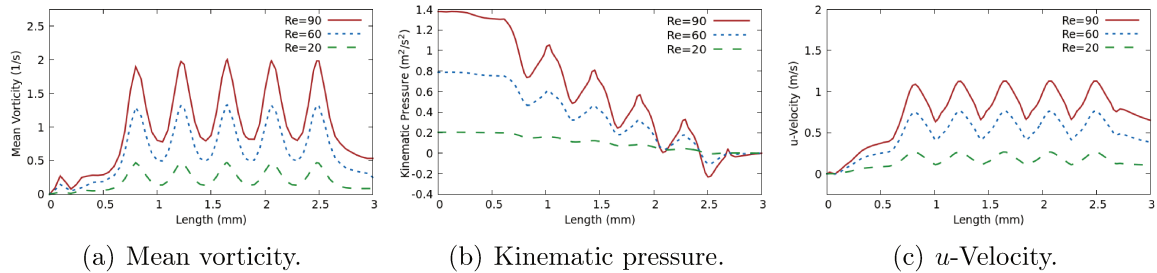


Figure 5.28: Performance of mean vorticity, kinematic pressure and u -velocity along the device regarding Re for $s = 100 \mu\text{m}$, and $d = 250 \mu\text{m}$.

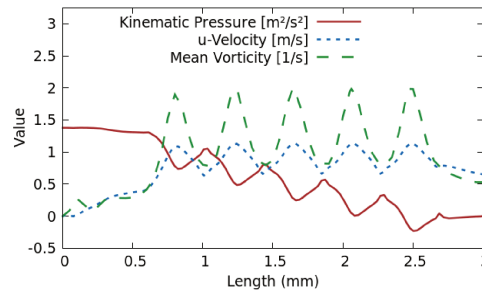


Figure 5.29: Comparison between vorticity, pressure and u -velocity along the x -axis for $Re = 90$ and $s = 100 \mu\text{m}$ with $d = 250 \mu\text{m}$.

Furthermore, it was analyzed how the sequence of bumps influences the formation of vortices along the microchannel. Again, six positions on the x -axis were selected: 0.58 mm (Bump0), 1.00 mm (Bump1), 1.42 mm (Bump2), 1.84 mm (Bump3), 2.26 mm (Bump4), and 2.68 mm (Bump5), and they are identified in Figure 5.30.

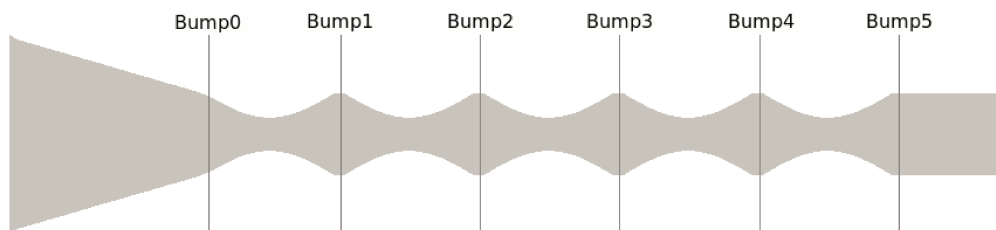


Figure 5.30: Representation of the positions selected for the analyses in the following graphics for when $\alpha = 1$.

The followings graphics show the u -velocity and the magnitude of vorticity fields' behavior at those six locations in x -axis. These positions represent the initial

location before the first bump (5.8 mm), the mean location between two bumps (10.0 mm, 14.2 mm, 18.4 mm, and 22.6 mm), and the position after the last bump.

Based on Figure 5.31, the velocity component in the x -direction is affected by the entry position at $s = 100 \mu\text{m}$ just before the first bump (Bump0) in which the asymmetry in the velocity profile is noticed. Even when the feed velocity is increased and the value of Re rises to 90, a negligible change occurs in the u -velocity profile in the Bump1 position; and therefore, it is concluded that the addition of bumps has a better contribution in the performance of the fluid-dynamic parameters than the feeding position.

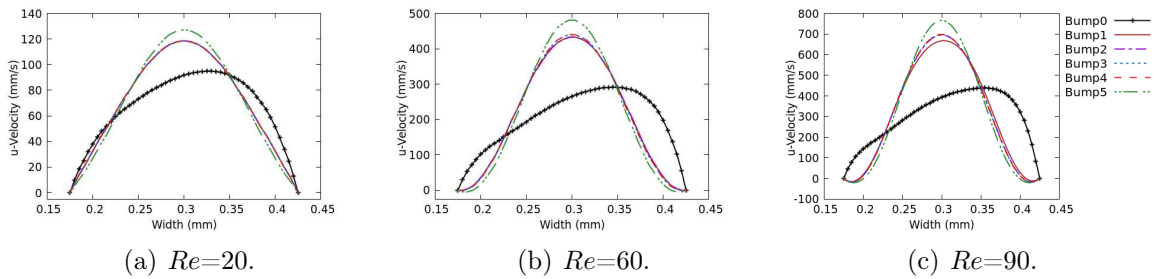


Figure 5.31: u -Velocity regarding Reynolds number and location of bumps where $d=250 \mu\text{m}$ and $\alpha = 1$.

Similar to what has been described for u -velocity, the vorticity field behaves as being affected only by the geometry of the bumps from the position Bump0. Note that in this case, the absolute values of the vorticity tend to be the same as shown in the graphs. It is important to note that the vorticity curves are opposite in sign once the vortex in the upper cavity rotates in a direction, and the other in the lower cavity rotates in the opposite direction.

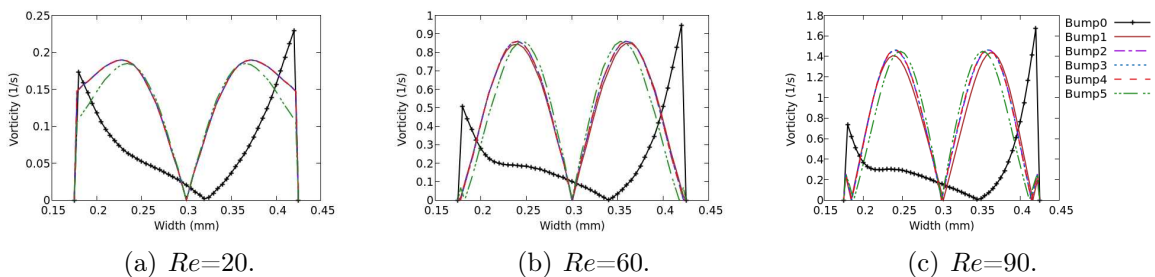
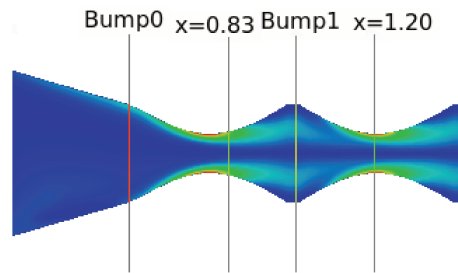


Figure 5.32: Magnitude of vorticity regarding Reynolds number and location of bumps where $d=250 \mu\text{m}$ and $\alpha = 1$.

An analysis of the pressure and vorticity profiles within a cavity can be performed based on Figure 5.33. Three locations were set: $x = 0.83$ mm (right after the first throat), $x = 1.00$ mm (in the middle of the cavity - Bump1), and $x = 1.20$ mm (in the second throat). Note that from 0.83 mm to 1.0 mm in Figure 5.33(b), the pressure increases in the flow where the fluid is decelerated due to the enlargement in the cross-sectional area. However, when the fluid starts speeding up again, the pressure profile reduces drastically with its higher values located near the walls, favoring the fluid to change its movement. Moreover, in the throats, the vorticity is intensified on the walls due to viscous stresses and the high velocity; while, in the middle of the cavity, the vortices are generated by the high variation of the pressure profile caused by the deceleration of the fluid, and consequently, they are induced to rotate close the main streamlines at the center line.



(a) Representative slices along the first cavity for the following plots.

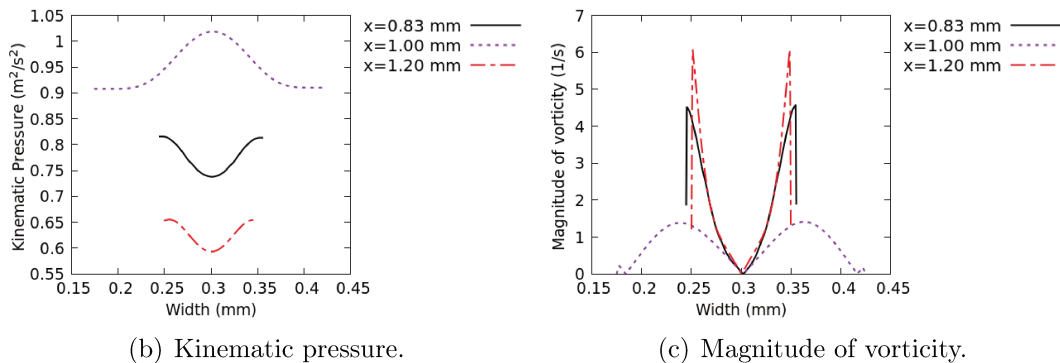
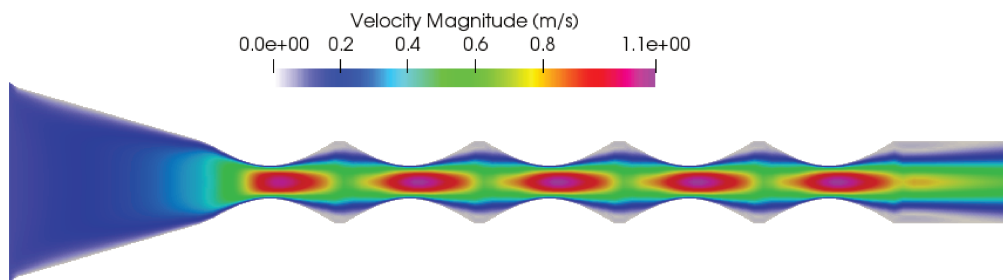


Figure 5.33: Comparison between pressure and vorticity at three positions (0.83, 1.00 and 1.20 mm) inside the first cavity when $Re = 90$ and $\alpha = 1$.

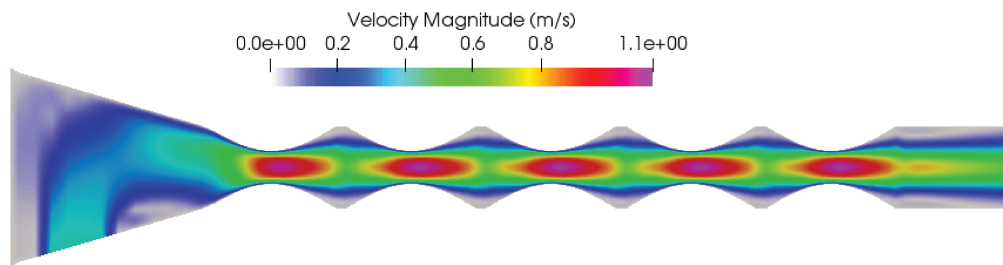
(b) Location of feed (s)

In this section, the distance between the feed and the left wall is analyzed at three different positions: $0 \mu m$, $100 \mu m$, and $300 \mu m$. Unlike the first case, it is now assessed how the feed position acts on a microchannel with bumps.

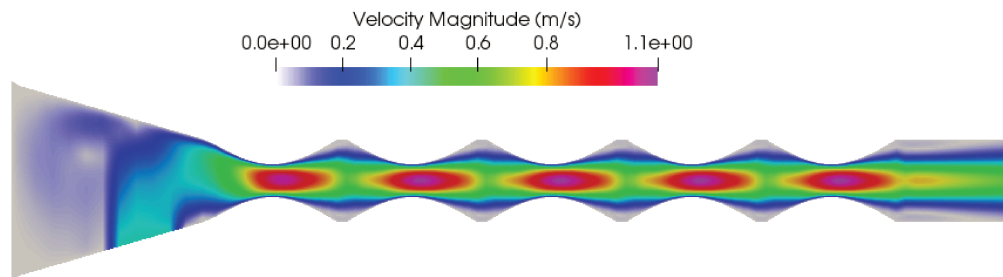
The magnitude of the velocity field at different locations of feed is shown in Figure 5.34 for when $Re = 90$, $d = 250 \mu m$, and $\alpha = 1$. All three cases show similar



(a) $s=0 \mu m$.



(b) $s=100 \mu m$.

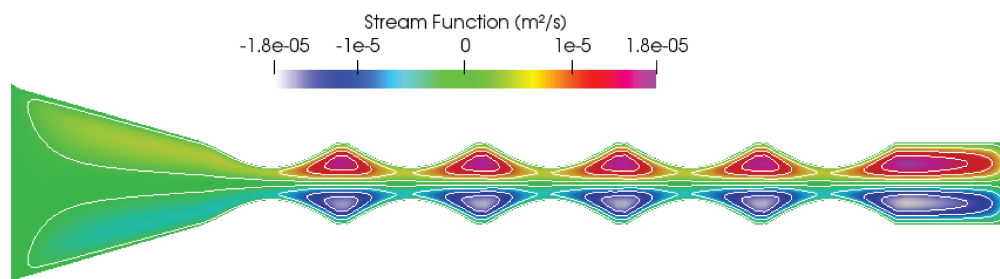


(c) $s=300 \mu m$.

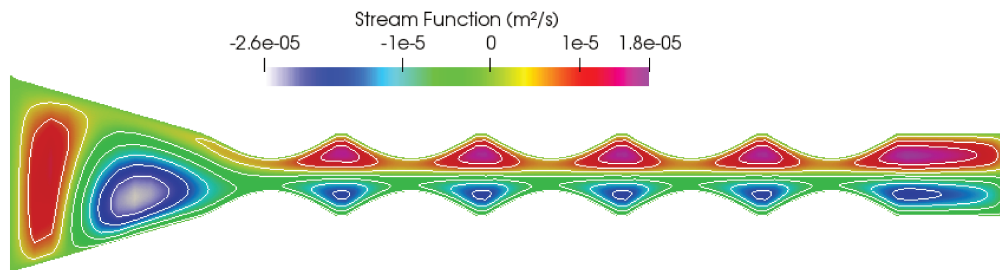
Figure 5.34: Magnitude of velocity regarding the location of the feed where $d=250 \mu m$, $\alpha = 1$ and $Re = 90$.

performance along the bumpy channel (including the data range), where in all throats there is the same maximum velocity. Again, only the entry region of the microdevice is affected by changing the position of the feed.

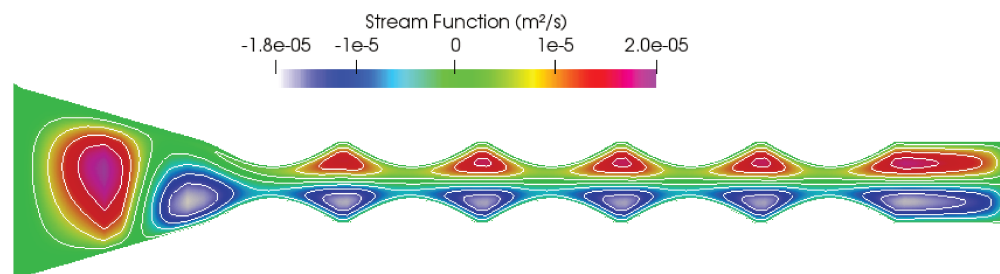
The recirculation zones of fluid elements can be viewed based on data from the stream function. Figure 5.35 illustrates the stream function field for the three positions. It is noticed that for $s = 0 \mu\text{m}$, the recirculation takes place only in the cavities between



(a) $s = 0 \mu\text{m}$.



(b) $s = 100 \mu\text{m}$.



(c) $s = 300 \mu\text{m}$.

Figure 5.35: Stream function with its contours along the microdevice where $d = 250 \mu\text{m}$, $\alpha = 1$ and $Re = 90$ (These figures do not have the same data range).

the bumps, while for the other two cases of lateral feeds, there is a formation of two large recirculation zones still at the entrance.

Regardless of the entry position, the maximum vorticity is still obtained in the region right after the constriction close to the wall due to the positive pressure gradient and, as shown in Figure 5.36, the maximum values obtained in the microdevices are very close. And again, the differences between these geometries are noticed only in the region of the entrance. Also, comparing the maximum vorticity obtained at $\alpha = 1$ with the case with no bumps, the vorticity was increased in 393.1%.

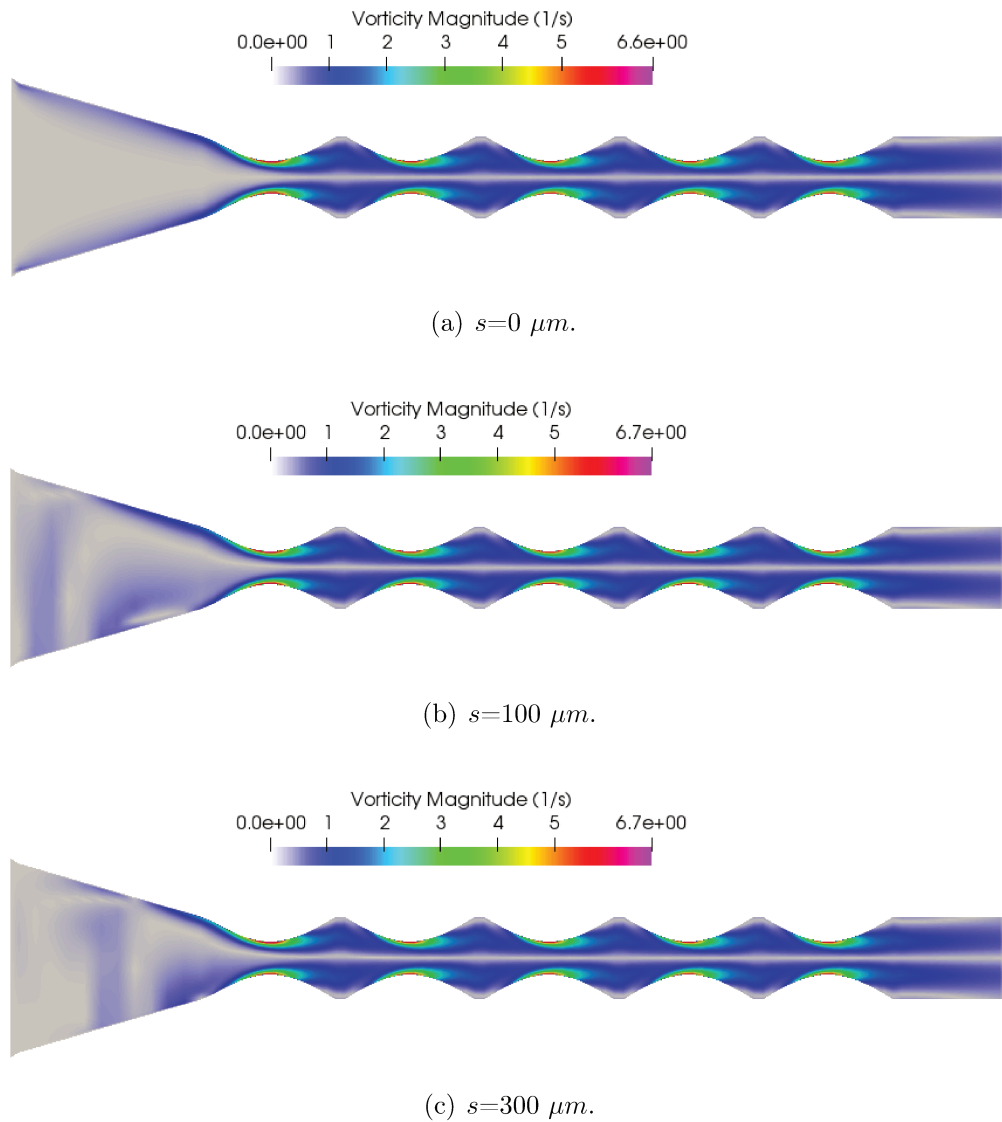


Figure 5.36: Vorticity field at different Reynolds numbers where $d=250 \mu m$, $a = 1$ and $Re = 90$.

Analyzing the vorticity field in the positions Bump0 and Bump1, two factors can be seen to cause the increase in vorticity. For example, in Figure 5.37, the fluid elements are subject to greater rotation surrounding the wall due to the velocity gradient resulting from the effect of viscous forces. In contrast, when the fluid elements are close to the center line, the rotational motion is barely affected by it.

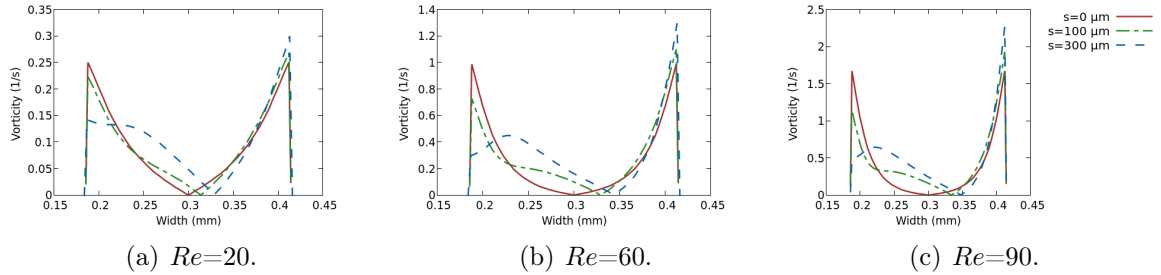


Figure 5.37: Magnitude of vorticity regarding Reynolds number and location of feed before the first throat at $x = 0.58 \text{ mm}$.

Nonetheless, the analysis of the vorticity field at Bump1 position (Figure 5.38) provides other conclusions. Firstly, it is noticed that right after the first constriction, the entire contribution of the feeding position becomes negligible regardless of Re , with only the curvature of bump's contribution prevailing over it, thus resulting in similar vorticity performances after the first bump. Moreover, the maximization of the vorticity is approximately halfway between the wall and the center line. of the channel, and this can be explained due to narrowing the channel by the bumps. This effect makes the fluid flow with greater speed, and therefore it generates a higher velocity gradient because part of the fluid tends to be stagnated inside the cavities. Therefore, this high speed drives the fluid in the cavity to circulate. Another factor that contributes to this is the formation of

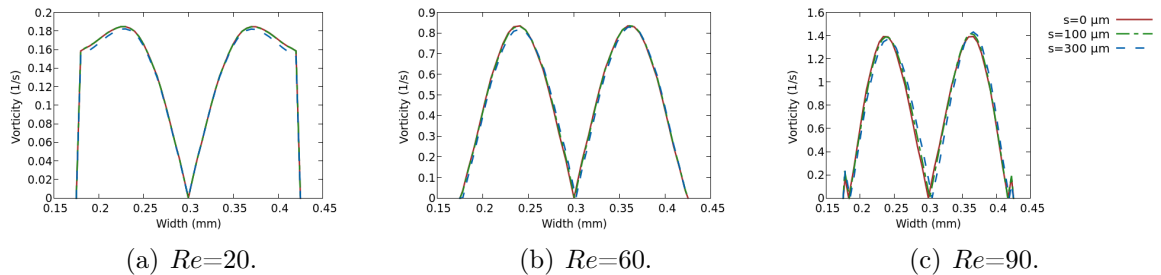


Figure 5.38: Magnitude of vorticity regarding Reynolds number and location of feed at Bump1 where $d=250 \mu\text{m}$ and $\alpha = 1$.

zones with a higher pressure right after the constriction next to the wall, and this tends to make the fluid elements to change their direction, spreading by diffusion into the cavity.

Finally, the mean vorticity field and the kinematic pressure field at $y = 0.3$ mm were plotted in Figure 5.39. The performance of these parameters are similar to each other beyond the occurrence of bumps, which means that under the applied conditions, the position of feeding influences the fluid-dynamic parameters only when $x < 0.6$ mm.

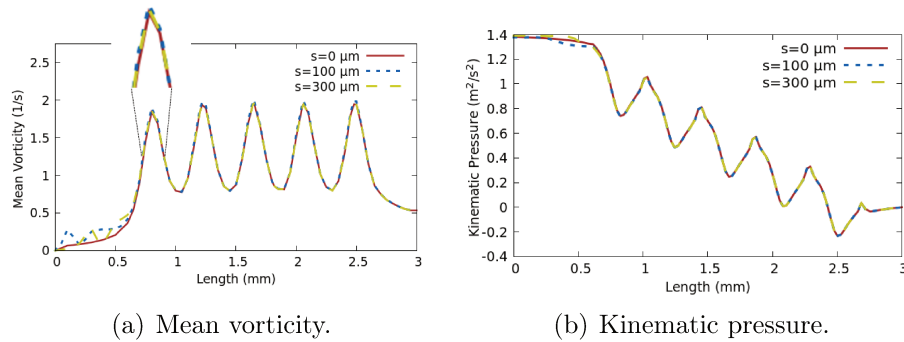


Figure 5.39: Mean vorticity and kinematic pressure performances along the device regarding s for $Re = 90$, and $d = 250 \mu\text{m}$ when $\alpha = 1$.

5.2.1.3 Curvature of bumps: $\alpha = 2$

A new bump curvature has been proposed now. In this case, the exponent from the equations 4.4 and 4.5 will be changed from 1 to 2, increasing the order of the equation, and consequently making the convex bump less smooth.

(a) Reynolds number

Figure 5.40 illustrates the velocity field with the streamlines in terms of the Reynolds number. For $Re = 90$, there is a clear formation of recirculation zones both in the initial region close to the feed and in the bumpy channel in the cavities. Whereas, when $Re = 60$, the fluid recirculates slightly in the cavities; and for $Re = 20$, the fluid only flows slowly in an entirely laminar and diffusive regime with no recirculation.

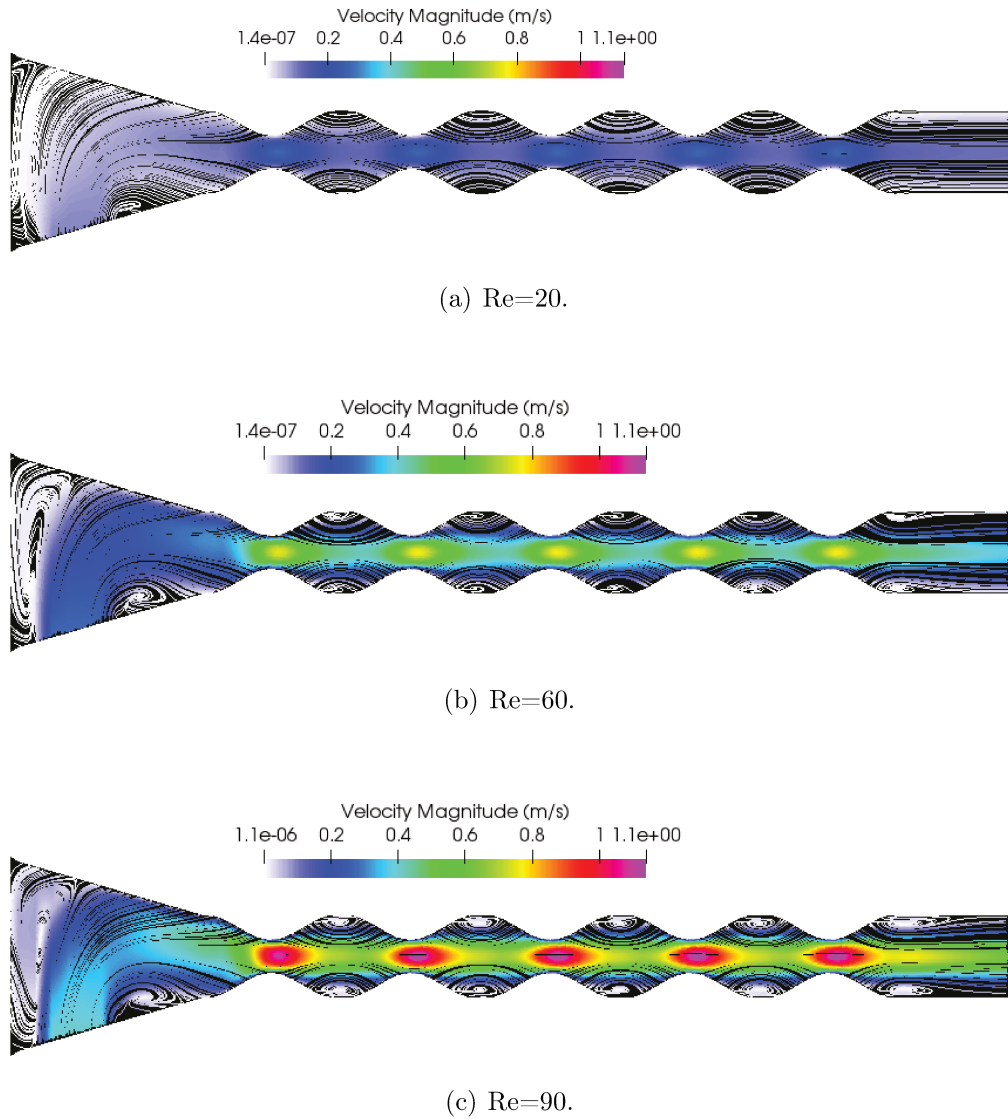


Figure 5.40: Streamlines along the microdevice where $d=250 \mu m$, $s = 100 \mu m$ and $\alpha = 2$.

The vorticity field for this new bump configuration regarding Re is shown in Figure 5.41. Again it is noticed that, the region where the vorticity is higher, it is predominantly after each bump due to the *separation* process where the boundary layer is extended by the deceleration of fluid and the variation of the pressure. Furthermore, the maximum vorticity obtained in this case exceeds the case with no insertion of bumps by 383.0%, however it is slightly lower (2.0%) when compared to $\alpha = 1$.

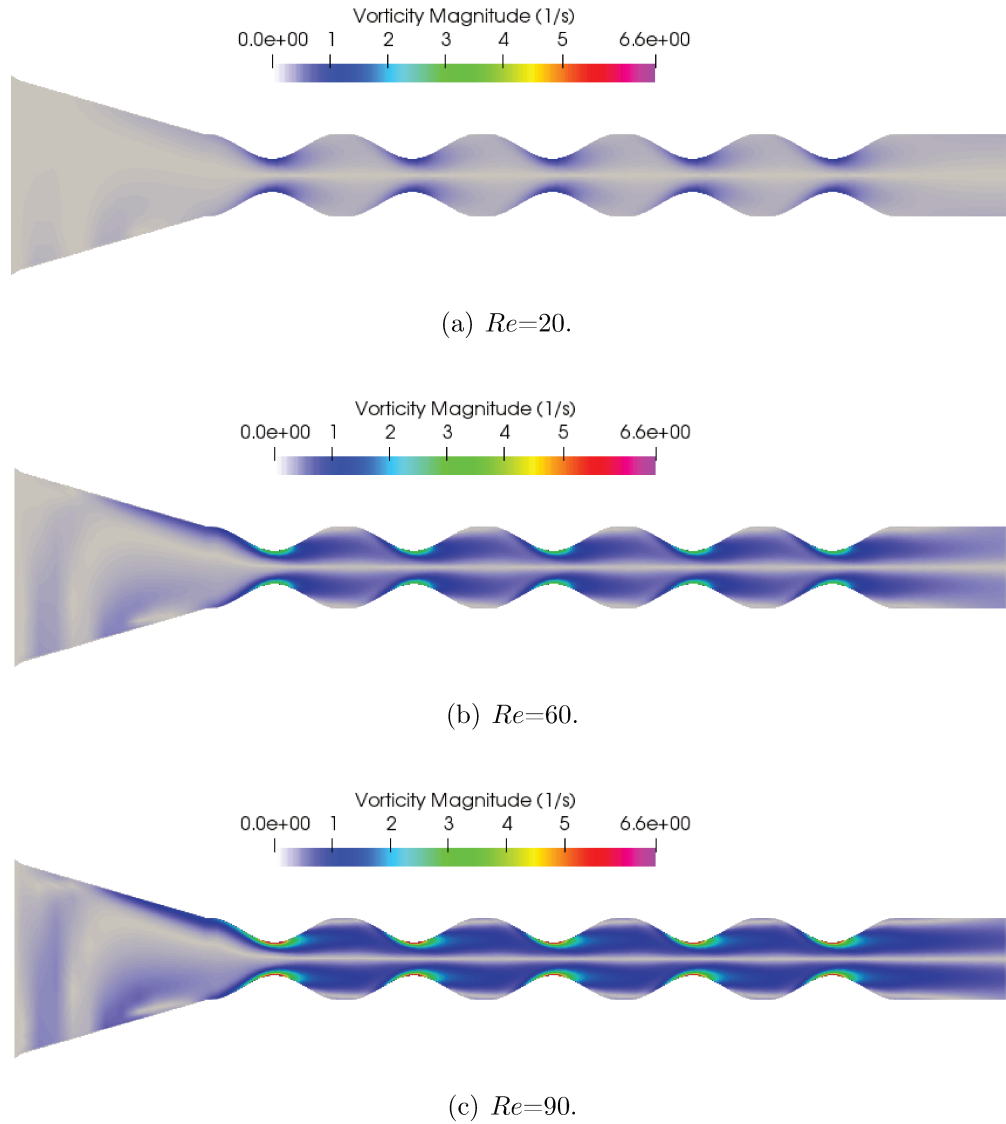


Figure 5.41: Vorticity field at different Reynolds numbers where $d=250 \mu m$, $s = 100 \mu m$ and $\alpha = 2$.

Qualitatively, the vorticity, the pressure and the velocity fields present similar performances when compared to the case with curvature of bump $\alpha = 1$ (Figure 5.28) as illustrated in Figure 5.42. However, the pressure variation for $\alpha = 2$ in the center line along x -axis was softer ($1.26 \text{ m}^2 \cdot \text{s}^{-2} < 1.38 \text{ m}^2 \cdot \text{s}^{-2}$), and in contrast, the maximum mean vorticity obtained was 8% lower.

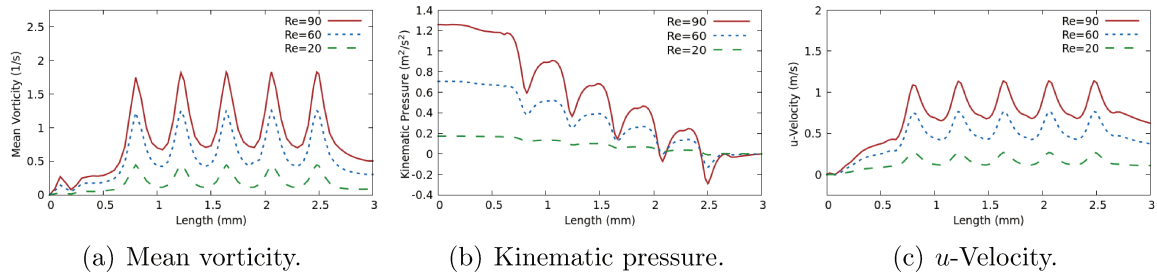


Figure 5.42: Performance of some fluid dynamics parameters along the device regarding Re for $s = 100 \mu\text{m}$, $\alpha = 2$ and $d = 250 \mu\text{m}$.

Besides that, the vorticity can be analyzed by plotting a few graphs according to the position at x -axis in the bumpy channel. Again, these positions were selected between the bumps and it is evaluated how this parameter progressed until the microdevice's exit. These locations are the same as those chosen for case with $\alpha = 1$: 0.58 mm (Bump0), 1.00 mm (Bump1), 1.42 mm (Bump2), 1.84 mm (Bump3), 2.26 mm (Bump4), and 2.68 mm (Bump5), as illustrated in Figure 5.43.

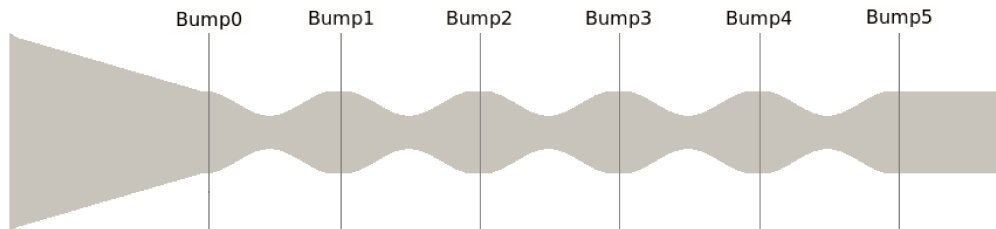


Figure 5.43: Representation of the positions selected for the analyses in the following graphics for when $\alpha = 2$.

The followings graphics show the magnitude of vorticity field at $Re = 20$, $=60$ and $=90$. Based on the Figure 5.44, the vorticity calculated in the Bump0 position before the fluid flows through the bumps is maximized in the region close to the top wall because the fluid initially reaches the upper wall, and hence it has to change its direction abruptly. Thus, the vorticity is predominantly dependent on the viscous forces in the region of entry of the microdevice. On the other hand, when flowing through the first couple of bumps, the rotation of the fluid is predominantly caused by the narrowing of the channel making the fluid elements deal with a positive pressure gradient, varying their moment of inertia, and then inducing them to rotate and flow from to the area with the

highest pressure to the lowest. Lastly, all other bumps have the same contribution with a negligible increase in the vorticity field caused by the feed position. However, it is possible to notice a small peak of vorticity nearby the regions close to the walls in the cavities when $Re = 90$ (Figure 5.44(c)). This rotation is induced in the opposite direction due to the larger adjacent circulation. In other words, by increasing the velocity, the main stream of fluid induces the formation of vortices inside the cavities, which consequently favors the creation of secondary vortices that flow in the opposite direction.

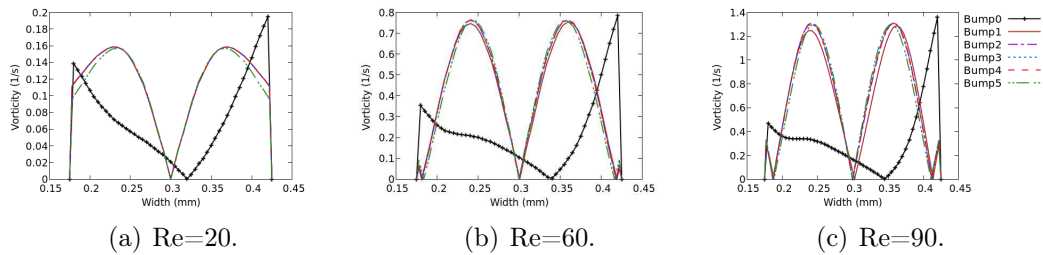
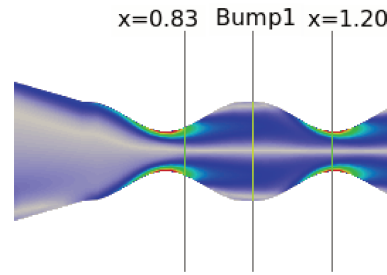
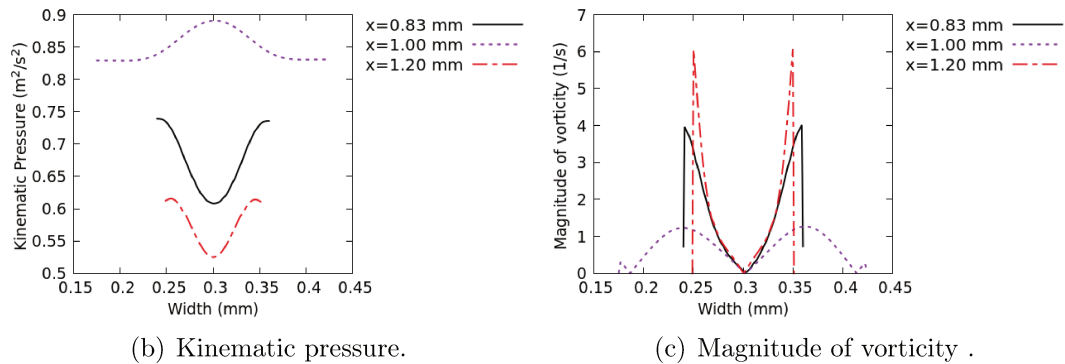


Figure 5.44: Magnitude of vorticity regarding Reynolds number and location of bumps where $d=250 \mu m$ and $\alpha = 2$.

Analyzing again the pressure and vorticity performances within the first cavity, qualitatively, the profiles for both $\alpha = 1$ (Figure 5.33) and $\alpha = 2$ (Figure 5.45) are similar. Therefore, the same phenomena are applied here as well; however, quantitatively, the highest variation of pressure between the first and second bumps is larger for $\alpha = 1$ (424.0 Pa) when compared to $\alpha = 2$ (364.4 Pa). Meanwhile, the vorticity profile has not undergone considerable changes.



(a) Representative slices along the first cavity for the following plots.



(b) Kinematic pressure.

(c) Magnitude of vorticity .

Figure 5.45: Comparison between pressure and vorticity at three positions (0.83, 1.00 and 1.20 mm) inside the first cavity when $Re = 90$, and $\alpha = 2$.

(b) Location of feed (s)

In this section, the distance between the feed and the left wall is analyzed again at three positions: $0 \mu m$, $100 \mu m$, and $300 \mu m$. Thereby, the feed position evaluated for the curvature of bump α equal to 2 shows similar results when compared to the case with $\alpha = 1$ as illustrated in Figure 5.46. The velocity field again has only variations in the converging nozzle section, while the maximum velocity obtained in constrictions has a difference smaller than 1% in all these cases of feeding.

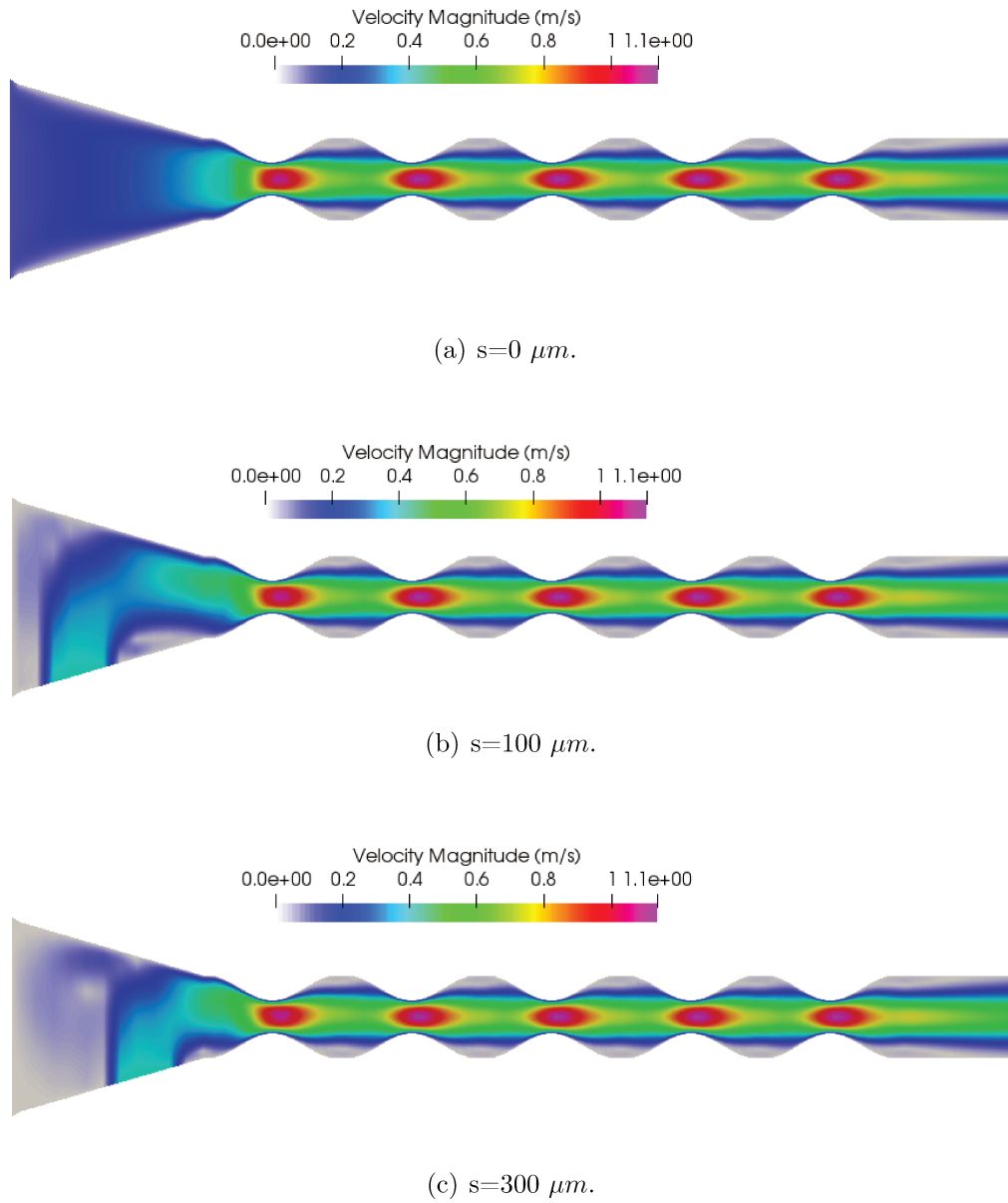


Figure 5.46: Magnitude of velocity regarding the location of the feed where $d=250 \mu m$, $\alpha = 2$ and $Re = 90$.

Figure 5.47 illustrates the stream function based on the three inlet positions with $Re = 90$. There are no significant differences obtained when compared to the $\alpha = 1$ curvature case, however it is important to emphasize that in this case the cavities are more rounded and extended than when $\alpha = 1$, which favors better fluid circulation inside of it with larger vortices.

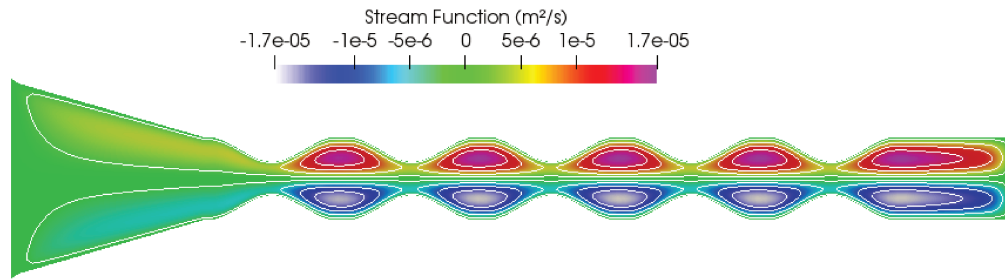
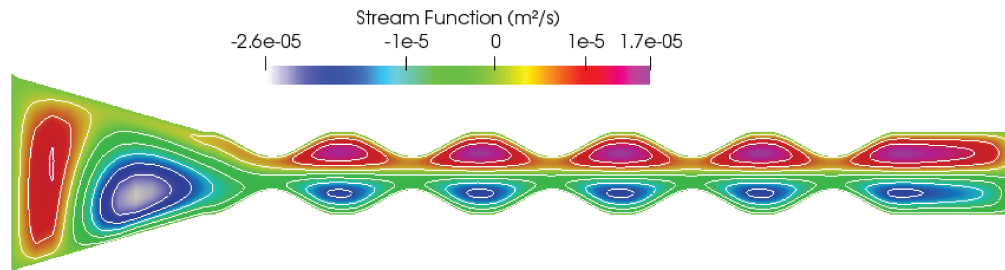
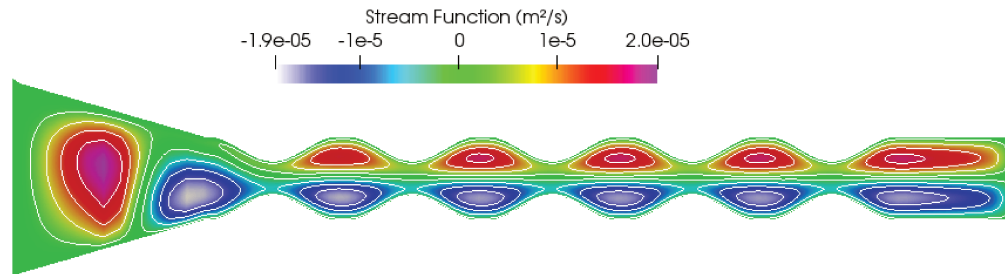
(a) $s=0 \mu m$.(b) $s=100 \mu m$.(c) $s=300 \mu m$.

Figure 5.47: Stream function with its contours along the microdevice where $d=250 \mu m$, $\alpha = 2$ and $Re = 90$.(These figures do not have the same data range)

The vorticity field also did not undergo major qualitative and quantitative changes when compared to the previous geometry as shown in Figure 5.48. Taking as a reference the maximum vorticity value obtained after the first bump when $s = 100 \mu m$, an increase of 1.6% was obtained in relation to the entry at $s = 0 \mu m$, and an increase of 0.5% for $s = 300 \mu m$. Whereas, the smoother curvature ($\alpha = 1$) with entry $s = 100 \mu m$ has a vorticity 2.0% higher than the curvature $\alpha = 2$.

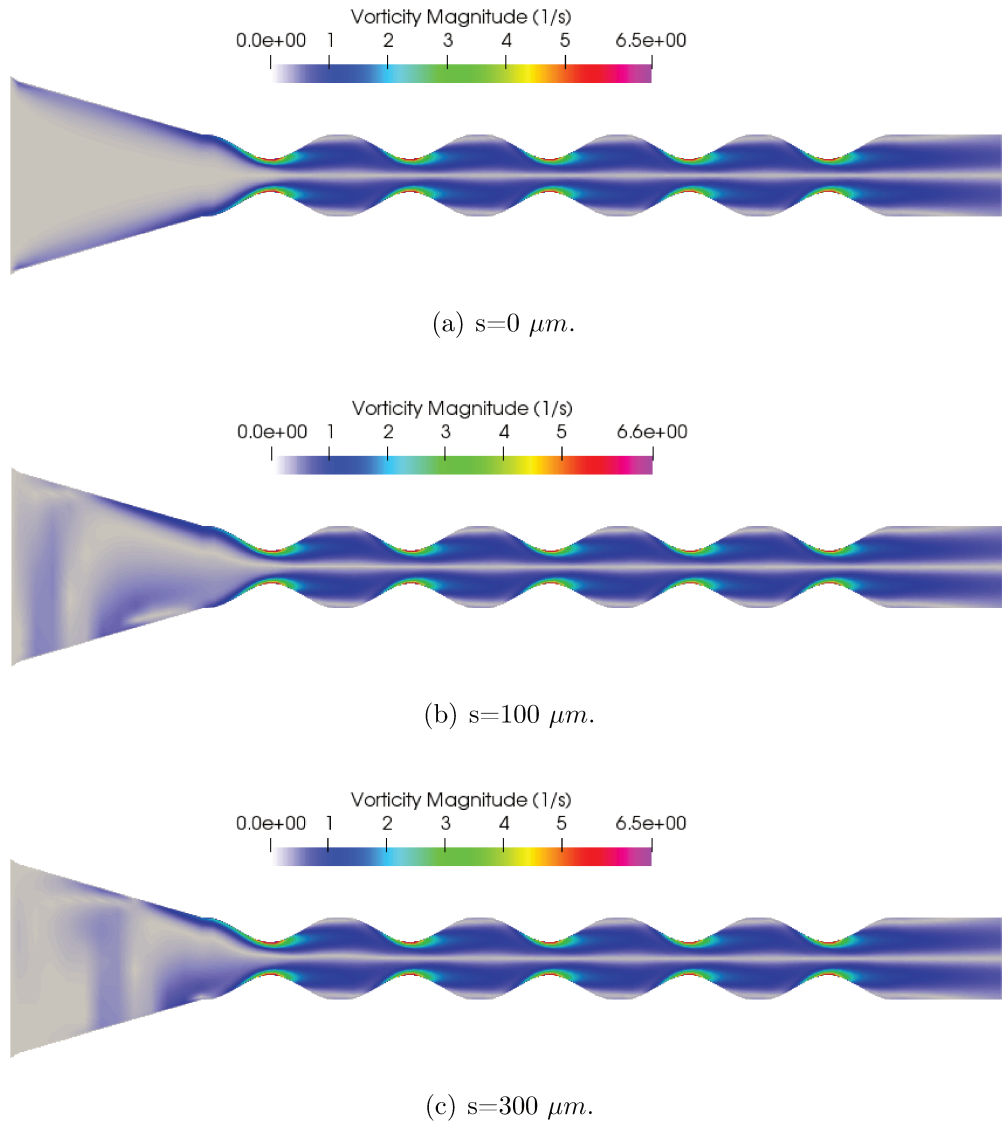


Figure 5.48: Vorticity field at different Reynolds numbers where $d=250 \mu m$, $a = 2$ and $Re = 90$.

Lastly, the vorticity profile can be analyzed in the positions before and after the first constriction (Bump0 and Bump1, respectively) from Figure 5.49. Similar to the previous cases, the vorticity is intensified in the region close to the upper wall due to the viscous torque of the elements, while in the Bump1 position, the vorticity can be assumed as independent of the value of s for Reynolds numbers from 20 to 90.

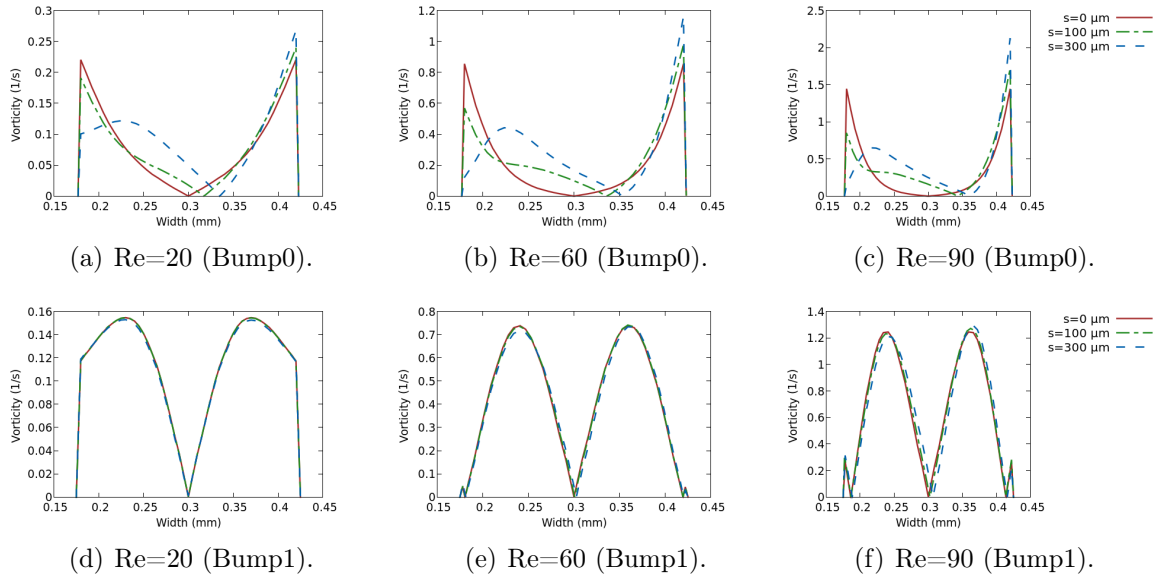


Figure 5.49: Magnitude of vorticity regarding Reynolds number and location of feed at Bump0 ($x = 0.58$ mm) and at Bump1 ($x = 1.0$ mm).

The last curvature of bump is related to a sharper geometry because the equations 4.5 and 4.4 have an exponent of the fourth order. The analyzes of the fluid-dynamic parameters for this case are again similar with a slight reduction in their values, however, all these figures of the respective fields of velocity, pressure, vorticity, and stream function are included in the Appendix section of this work.

5.2.1.4 Curvature of Bumps: Overall

The mean vorticity profile in the four different geometries in the duct section could be plotted in Figure 5.50. Note that as the order of equations 4.4 and 4.5 increases, the bumps get sharper and consequently, the vorticity gets lower. In addition, according to Figure 5.50(b), the pressure profile for the cases of $\alpha = 2$ and $\alpha = 4$ are almost similar although $\alpha = 2$ generates greater vorticity.

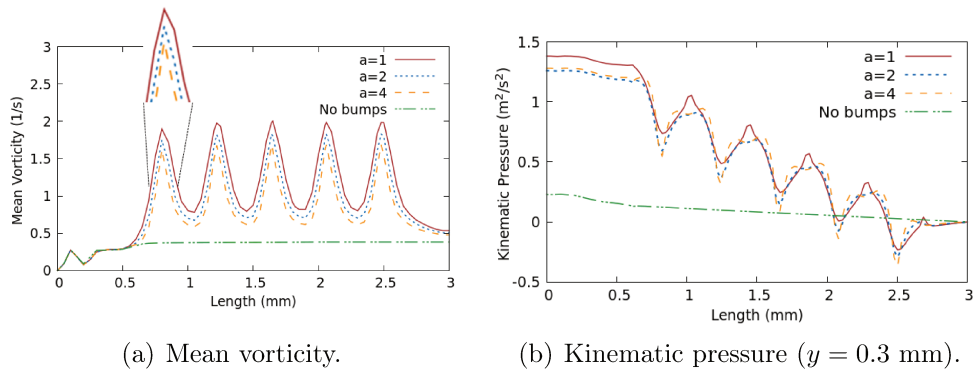


Figure 5.50: Performances of the vorticity magnitude and the kinematic pressure at $Re = 90$ regarding the curvature of bump α when $s = 100 \mu\text{m}$ and $d = 250 \mu\text{m}$.

After analyzing the fluid dynamics parameters for each curvature of bumps, they are now presented and compared in some graphs right after the first bump at $x = 1$ mm maintaining $d = 250 \mu\text{m}$, and $s = 100 \mu\text{m}$.

Firstly, the velocity component in the x -direction for each curvature of bump was plotted in Figure 5.51 as a function of Reynolds number. Despite having the same cross-sectional area at $x = 1.0$ mm, the absence of bumps does not favor the increase in the u -velocity as was noticed at the other three cases. In addition, u -velocity does not change when $\alpha = 2$ and $\alpha = 4$ for a range of Re from 20 to 90, while for $\alpha = 1$, there is a reduction of 5.44% in the maximum velocity value.

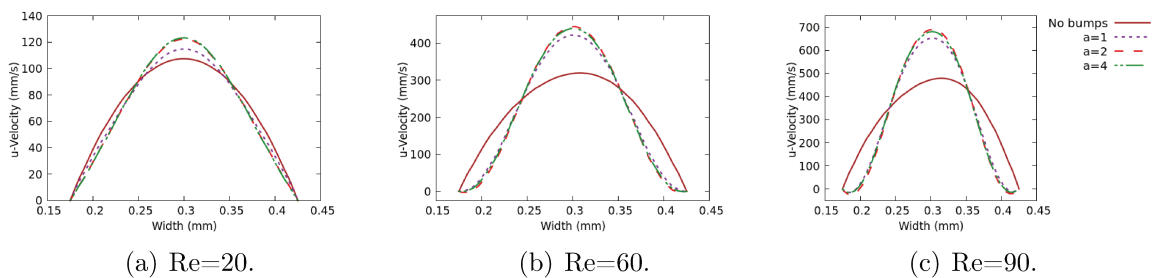


Figure 5.51: u -Velocity regarding Reynolds number and curvature of bumps where $d=250 \mu\text{m}$ and $s = 100 \mu\text{m}$.

The vorticity field can also be analyzed under the same conditions and the results are more divergent. Based on Figure 5.52, it is noticed that the vorticity profile for $\alpha = 1$ is predominant across the y -axis when $x = 1.0$ mm and $Re = 20$, and $Re = 60$. The same is almost valid for $Re = 90$, however, in the small region closer to the wall

where the vorticity in $\alpha = 1$ is as high as in $\alpha = 2$. The maximum vorticity obtained for $Re = 90$ and $\alpha = 1$ is higher in: 12.8% regarding $\alpha = 2$; 29.7% for $\alpha = 4$ and 91.2% for the case with no bumps ($a = 0$). This behavior of the vorticity can be explained due to the extensive narrowing of the channel that $\alpha = 1$ is submitted to, which allows greater action of the viscous forces in the throat region in a larger area of x , achieving a better vorticity.

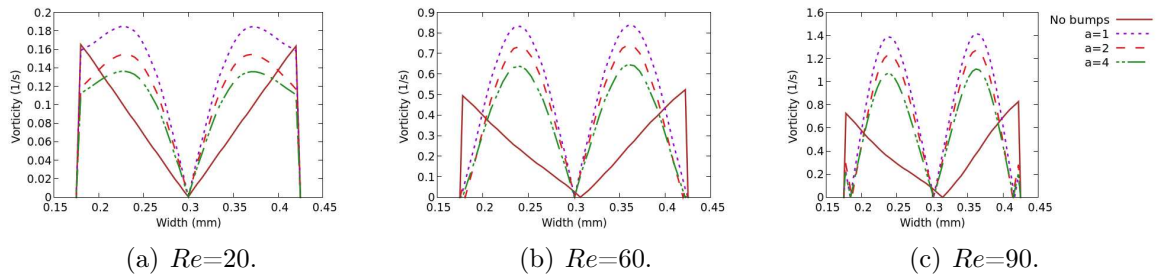


Figure 5.52: Magnitude of vorticity regarding Reynolds number and curvature of the bumps where $d=250 \mu\text{m}$ and $s = 100 \mu\text{m}$.

Finally, the pressure profile can also be studied. In theory, in predominantly laminar flows, it is suggested that the pressure variation in the y -direction is negligible when compared with the x -direction. However, analyzing Figure 5.53, it can be seen that the smoothest curvature of bump generates a notorious variation in pressure along the y -axis since from $Re = 60$. Although the inclusion of bumps in the flow helps in the rotation of fluid elements and in the creation of vortices, they also contribute to greater pressure gradients in these narrowing regions as shown previously. Thus, the pressure drop along the device must also be assessed. Its calculation was performed starting from the average pressure value calculated at the inlet minus its value at the outlet (which is set to zero).

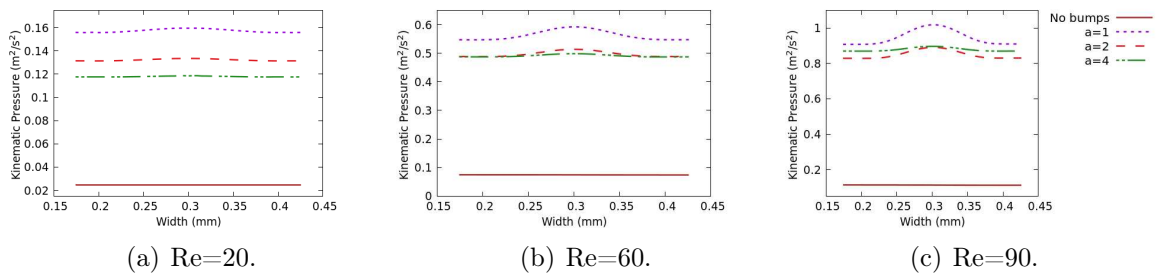


Figure 5.53: Kinematic pressure regarding Reynolds number and curvature of the bumps where $d=250 \mu\text{m}$ and $s = 100 \mu\text{m}$.

The pressure drop performance in Figure 5.54 is based on Re and a with $d=250 \mu m$ and $s=100 \mu m$. Taking the pressure drop of the case with no bumps as a reference, and setting $Re = 90$, the pressure drop is increased: by 636.0% when $\alpha = 1$; by 569.5% when $\alpha = 2$; and 581.1% for $\alpha = 4$. Moreover, Table 5.2 complements the other pressure drop values for the different feeding positions when $Re = 90$. Thus, although the velocity and vorticity fields are almost similar, the pressure drop at $s = 0 \mu m$ is higher at all curvatures of bumps.

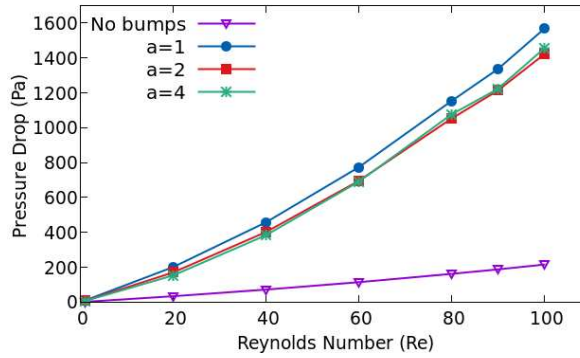


Figure 5.54: Pressure drop at different Reynolds numbers (Re) and curvature parameter a when $d=250 \mu m$ and $s=100 \mu m$.

Table 5.2: Pressure drop (Pa) at different locations of feed and curvature of bumps when $Re = 90$ and $d = 250 \mu m$.

| Curvature a | Location of the inlet s (μm) | | |
|---------------|---------------------------------------|---------|---------|
| | 0 | 100 | 300 |
| No bumps | 222.38 | 181.08 | 187.56 |
| 1 | 1378.55 | 1332.70 | 1336.13 |
| 2 | 1257.87 | 1212.36 | 1213.62 |
| 4 | 1279.15 | 1233.27 | 1222.79 |

5.2.2 Device's width: $d = 200 \mu m$

In this section, the width of the microchannel is changed to $200 \mu m$ while the curvatures of the bumps are analyzed again in terms of Reynolds number and position of the feed.

5.2.2.1 Curvature of bumps: No bumps

Firstly, the microdevice was evaluated without the presence of bumps. The range of the Reynolds number in this case was from 1 to 40 because the code did not converge in values greater than 50. Therefore, all simulations were performed for $Re = 1$, $Re = 20$ and $Re = 40$. At the beginning, for the Re analyses, the location s is set as $100 \mu m$.

(a) Reynolds Number

The streamlines in terms of the number of Reynolds are illustrated in Figure 5.55. Comparing with the case of $d = 250 \mu m$ (Figure 5.15), the zones of recirculation of fluid in the entrance region are minimized due to the low value of Re ; on the other hand, the narrowing in the channel makes the fluid flow with a higher velocity.

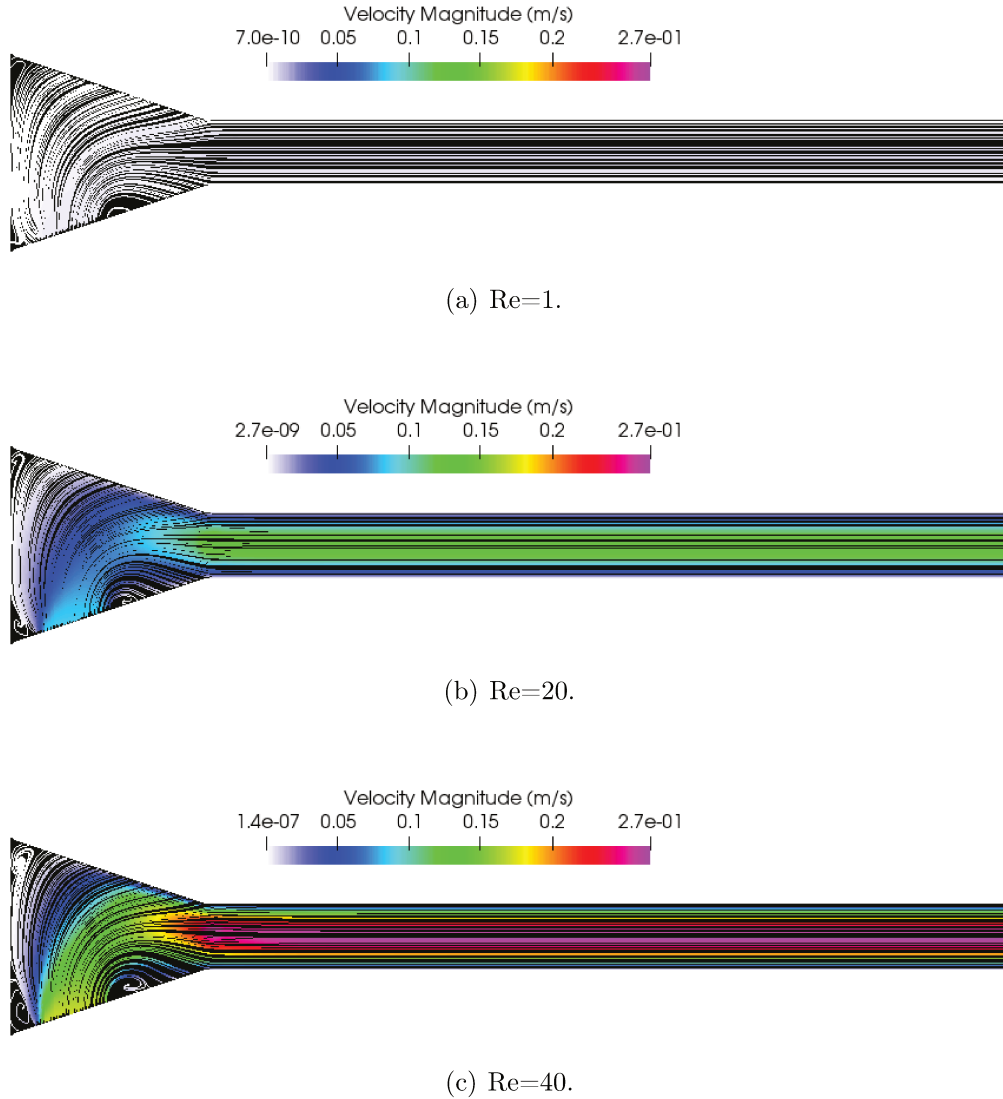


Figure 5.55: Streamlines along the microdevice where $d=200 \mu m$, $s = 100 \mu m$ and there is no bumps.

The vorticity field obtained in this condition with no bumps is exclusively affected by the viscous forces caused by the no-slip condition from the walls. Therefore, the regions with the highest vorticity are located adjacent to the walls. Figure 5.56 compares the profile of the vorticity exactly at the entrance of the straight channel at $x = 0.6 \text{ mm}$ for the Re equal to 20 and 40 in the two devices' widths d studied in this research. Based on this figure, the highest vorticity is obtained in the device with the smallest width where the fluid elements are flowing faster, and hence the shear stress gets more intense.

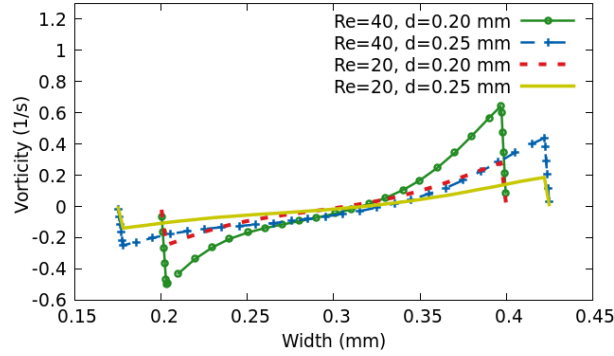


Figure 5.56: Vorticity performance at different Reynolds numbers (Re) and device's width d when there is no bumps and $s=100 \mu m$.

(b) Location of feed (s)

In this section, the distance between the feed and the left wall is analyzed at three positions: $0 \mu m$, $100 \mu m$, and $300 \mu m$. Besides, two positions along the x -axis were selected to assess the vorticity profile: 0.6 mm (Bump0) and 1.0 mm (Bump1). Figures 5.57 and 5.58 show respectively how the position of the inlet s affects the magnitude of the vorticity field, and the vorticity profile at each Re in two positions at x -axis. When $Re = 1$, the vorticity is independent of the feed position as shown in Figures 5.58(a) and 5.58(d). This fact is explained by the low velocity in the feed that makes the flow regime predominantly laminar and diffusive, which results in the symmetry of the vorticity profile. However, as the velocity is increased, the contribution of convective forces also enhances and an asymmetry caused by the different feeds can be seen as in Figures 5.58 (b) and 5.58 (c). Finally, as usual, at $x = 1.0 \text{ mm}$, the feed position has no influence on the rotation of the fluid elements, and therefore, only the viscous torque influences them in terms of vorticity.

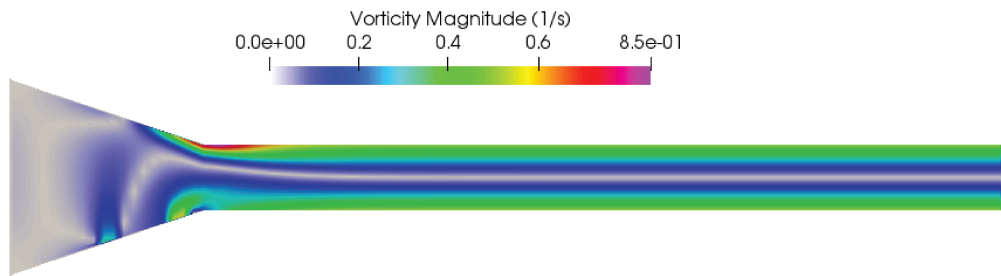
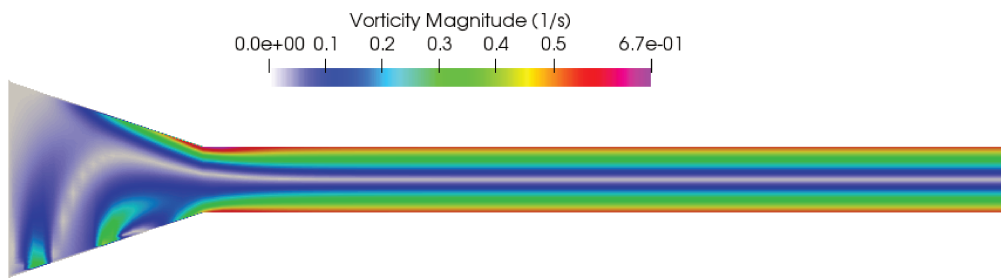
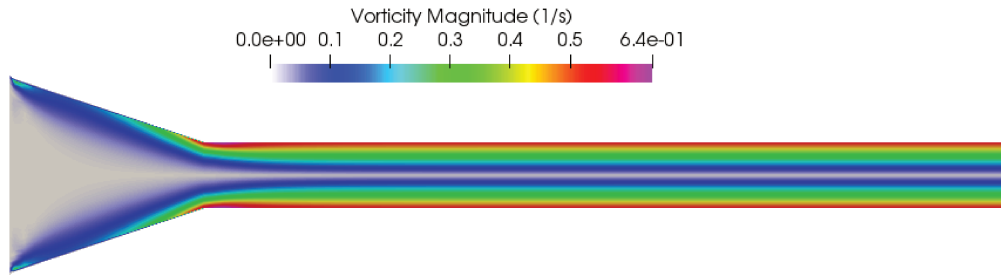


Figure 5.57: Vorticity field at different feed locations where $d=200 \mu m$, $Re = 40$ and there is no bumps (These figures do not have the same data range).

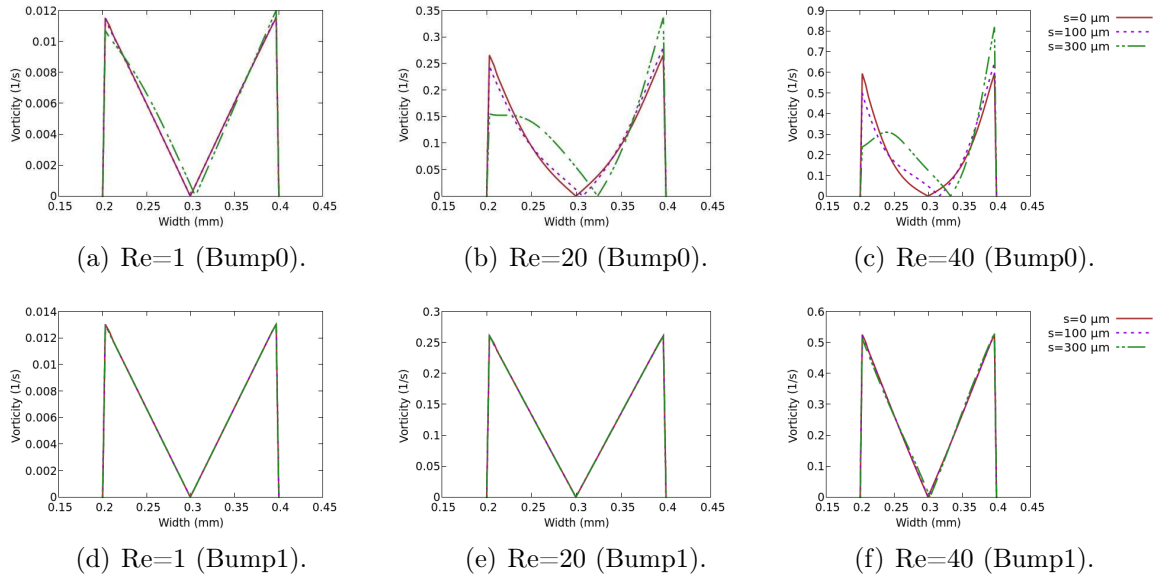


Figure 5.58: Magnitude of vorticity regarding Reynolds number and location of feed at $x = 0.6$ mm (Bump0) and $x = 1.0$ mm (Bump1) with $d=200$ μm and no bumps.

5.2.2.2 Curvature of bumps: $\alpha = 1$

The addition of convex bumps along the duct is evaluated in terms of Re and feed position s in the next sections in which the width d is reduced and equal to 200 μm . The first curvature of bump performed herein is the smoothest one ($\alpha = 1$).

(a) Reynolds Number

The presence of bumps considerably affects the flow of fluid through the microchannel. In fact, a few recirculation zones are formed in the cavities between these bumps when $Re = 40$ (Figure 5.59(c)), however, in the lower values of Re , these vortices are not noted. In addition, the maximum velocity is located in the center-line between the upper and lower bumps, and, when $Re = 20$, the velocity is increased by 101.5% in comparison to the value obtained for $d = 250$ μm . Furthermore, the maximum velocity when $Re = 90$ at $d = 250$ μm is only 8.8% higher than in the case of $Re = 40$ with $d = 200$ μm , resulting in a large contribution from the width of channel to the velocity value.

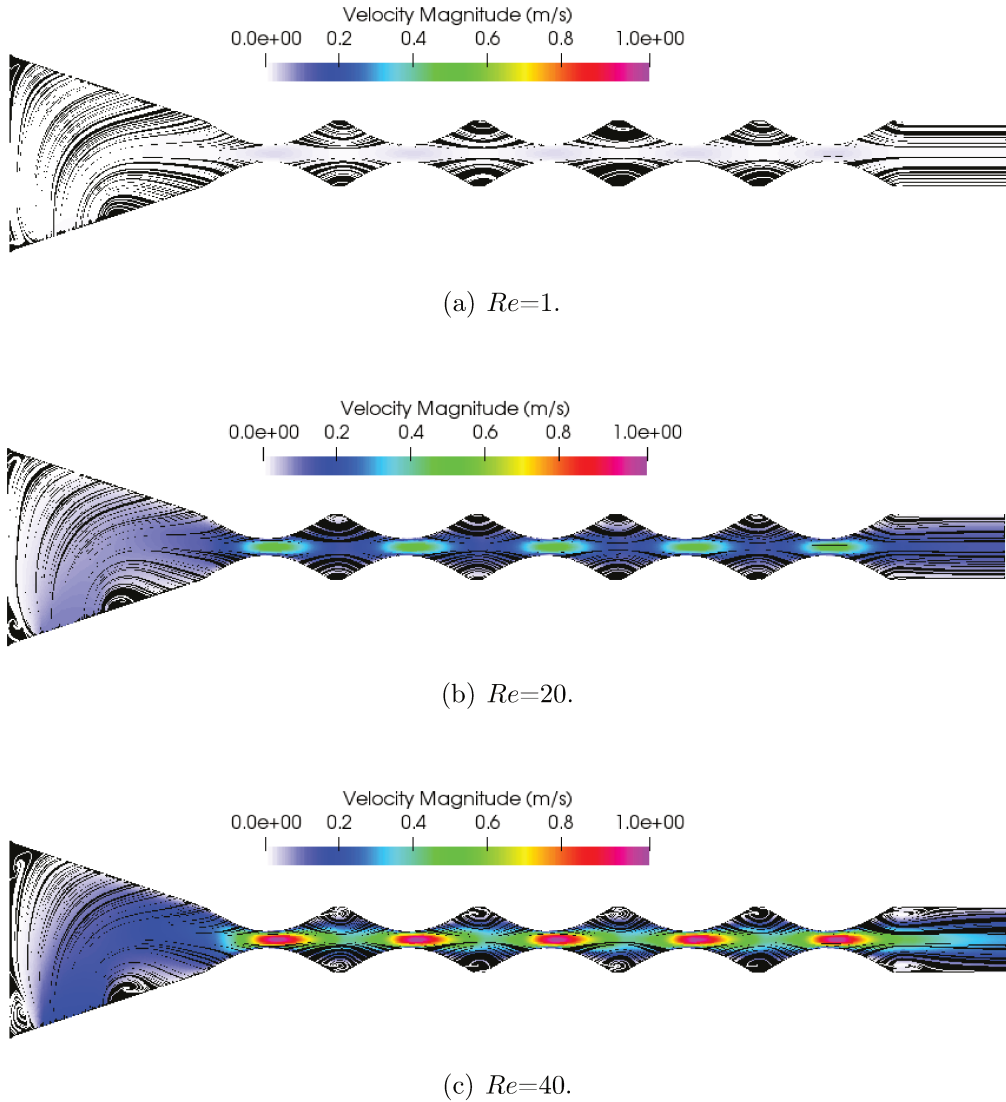


Figure 5.59: Streamlines along the microdevice where $d=200 \mu\text{m}$, $s = 100 \mu\text{m}$ and $\alpha = 1$.

Figure 5.60 illustrates the magnitude of the vorticity field when $Re = 1$, $Re = 20$, and $Re = 40$. The maximum vorticity value obtained in this case for $Re = 40$ right after a constriction is 1,334.2% higher than the case with no bumps at the same Re , and 43.7% superior when compared to the microdevice of $d = 250 \mu\text{m}$ and $\alpha = 1$ operating with $Re = 90$. Thus, even performing with lower Reynolds numbers, the narrowing of the channel resulted in better values of vorticity when compared with the best case for $d = 250 \mu\text{m}$.

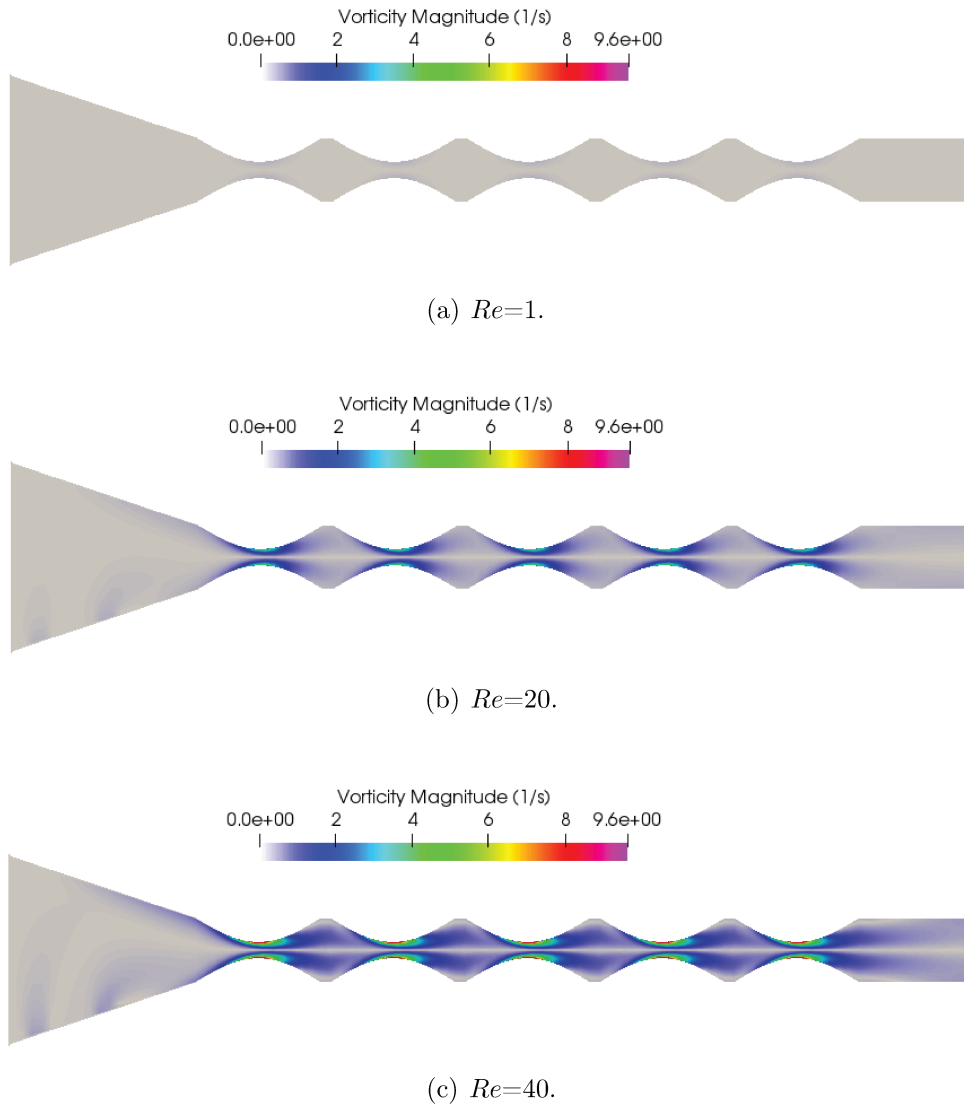


Figure 5.60: Vorticity field at different Reynolds numbers where $d=200 \mu m$, $s = 100 \mu m$ and $\alpha = 1$.

Furthermore, the vorticity and the u -velocity fields can be plotted in terms of Re at the position between the first and second couple of bumps ($x = 1 \text{ mm}$, Bump1). Figure 5.61(a) shows how the velocity field in the x -direction is dependent on Re . In the largest Reynolds number, it is noticed that the velocity close to the wall presents a opposite direction to the flow, and this is due to a weak recirculation inside the cavity. Besides, the vorticity field in Figure 5.61(b) corroborates what was analyzed in Figure 5.61(a) regarding the presence of a recirculation zone near the wall. Another factor is that the highest peak of vorticity at position $x = 1.0 \text{ mm}$ along the y -axis is 25.0% smaller when compared to the case of $Re = 90$ and $d = 250 \mu m$ in the same curvature. Thus,

although it generated a maximum vorticity value right after the constriction, its gradient is quite high, and this tends to cause instability both in computational simulation and in the device's performance.

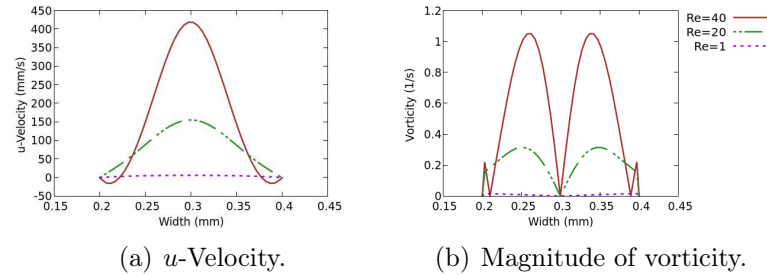


Figure 5.61: Fluid dynamics parameters regarding Reynolds numbers at $x = 1$ mm where $d=200 \mu\text{m}$, $s = 100 \mu\text{m}$ and $\alpha = 1$.

Figure 5.62 shows the performances of the mean vorticity, and kinematic pressure fields in the center-line in terms of Re . Qualitatively, these parameters behave similarly to the cases discussed in the previous sections; however, their gradients are considerably larger than the other cases. The variation of pressure in the case of a narrower channel is drastically superior compared to the $d = 250 \mu\text{m}$ (Figure 5.28). For instance, comparing $Re = 20$, the increase is 447.6% along the whole channel, while for $Re = 40$, the increase is 445.5%. Additionally, even when the microdevice with $d = 250 \mu\text{m}$ is operating at $Re = 90$, the pressure gradient for the case of $d = 200 \mu\text{m}$ and $Re = 40$ is still 84.4% superior. Besides that, the mean vorticity profile for cases of $d = 200 \mu\text{m}$ is also greater: when both devices operate at $Re = 20$, the maximum mean vorticity obtained is 312.1% higher, while, comparing $Re = 40$ ($d = 200 \mu\text{m}$) with $Re = 90$ ($d = 250 \mu\text{m}$), the maximum value is still 87.4% higher.

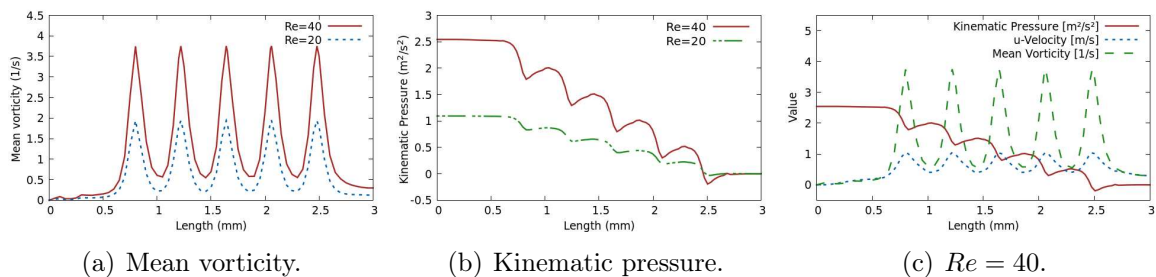
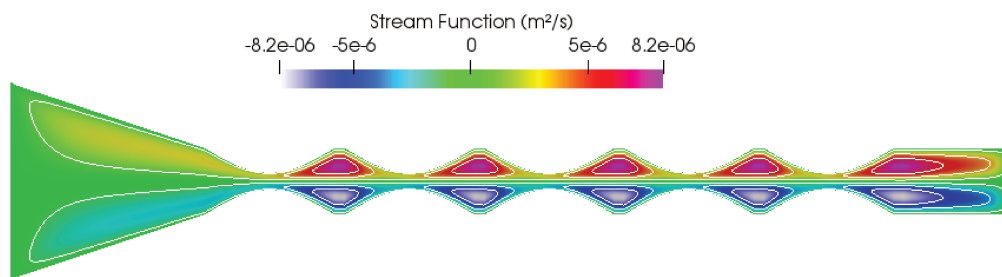


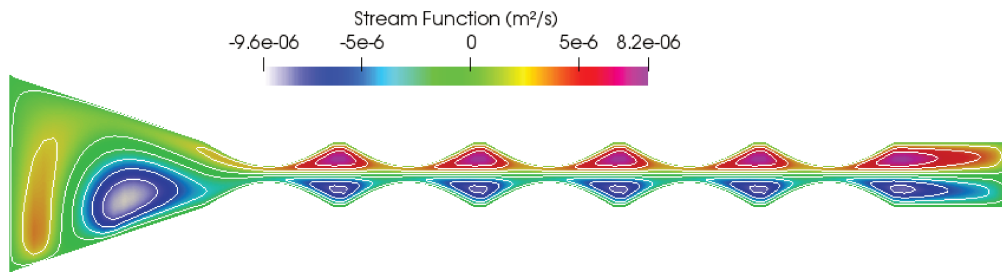
Figure 5.62: Performance of some fluid dynamics parameters along the device regarding Re for $s = 100 \mu\text{m}$, $\alpha = 1$ and $d = 200 \mu\text{m}$.

(b) Location of feed (s)

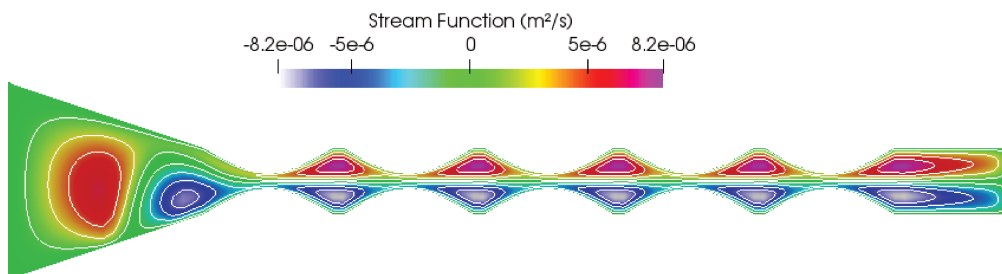
Again, it is assessed how the inlet location affects vorticity and pressure drop across the microdevice. The Reynolds number is set to 40 due to obtaining the best results. Figure 5.63 illustrates the stream function field for the feed positions: $s = 0 \mu\text{m}$, $s = 100 \mu\text{m}$ and $s = 300 \mu\text{m}$. Based on that, it is noticed that there are recirculation zones at the entrance when the lateral feed is equal to $s = 100 \mu\text{m}$ and $s = 300 \mu\text{m}$. In



(a) $s = 0 \mu\text{m}$.



(b) $s = 100 \mu\text{m}$.



(c) $s = 300 \mu\text{m}$.

Figure 5.63: Stream function with its contours along the microdevice where $d = 200 \mu\text{m}$, $a = 1$ and $Re = 40$.

addition, all these geometry configurations generate vortices within the cavities between the bumps.

In this comparison, the vorticity field is again differentiated only at the entrance region at the converging nozzle, and thus, when the fluid flows through the first constriction, the vorticity is increased considerably (Figure 5.62(a) at $x = 0.83$ mm) resulting in contribution only by other parameters: the device's width d and the curvature of the bump α . Qualitatively, the graphs (a)-(d) from Figure 5.64 are quite similar to those presented for the case with no insertion of bumps in the channel (Figure 5.58), however after the first pair of bumps at position Bump1, the vorticity profile is different, because, in this case, the rotation of the fluid elements is not exclusively caused by the shear stress of the walls. These elements increase angular momentum as they are submitted to a positive pressure gradient, and as they rotate, they are spread by diffusion towards the cavity. Lastly, there are small peaks of vorticity close to the wall inside the cavity (Figure 5.64(f)), which again indicates the formation of secondary vortices.

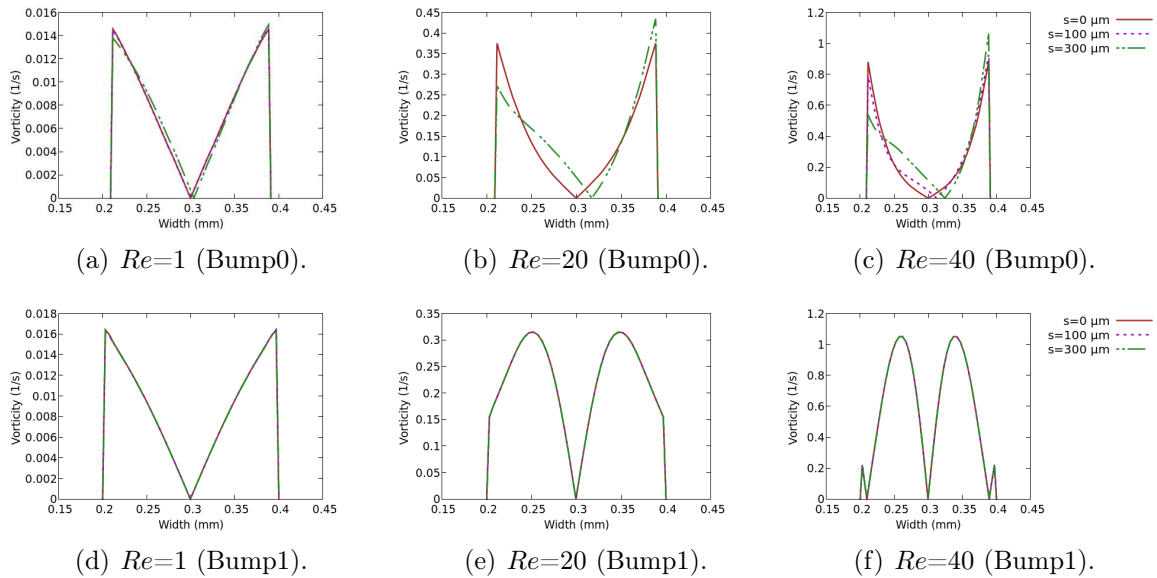


Figure 5.64: Magnitude of vorticity regarding Reynolds number and location of feed s at $x = 0.58$ mm (Bump0) and $x = 1.0$ mm (Bump1) where $d=200 \mu\text{m}$ and $\alpha = 1$.

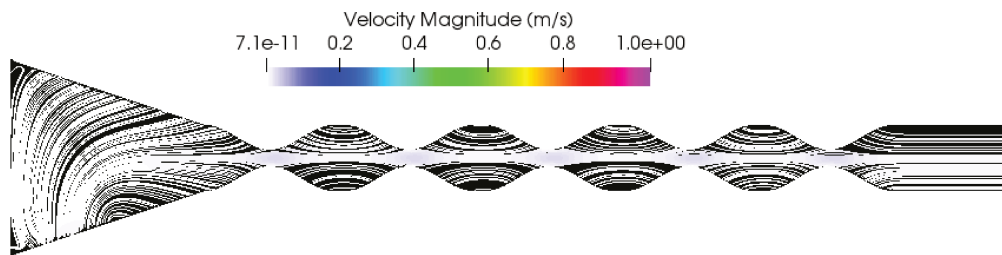
5.2.2.3 Curvature of bumps: $\alpha = 2$

The curvature of the bumps along the microchannel has been changed from $\alpha = 1$ to $\alpha = 2$ based on the equations 4.4 and 4.5 for each bump. Thus, as the exponent

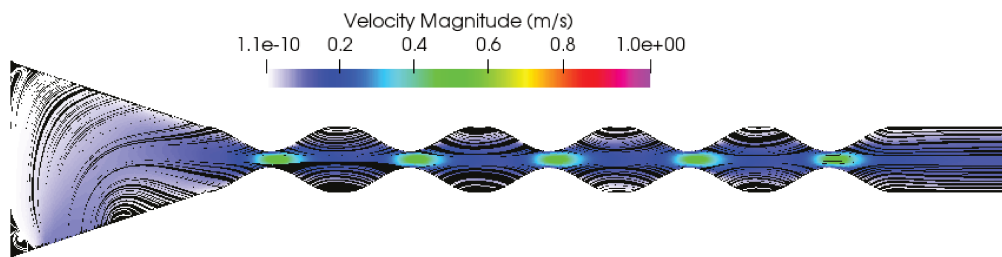
of the equation has been increased, the bump becomes sharper.

(a) Reynolds number

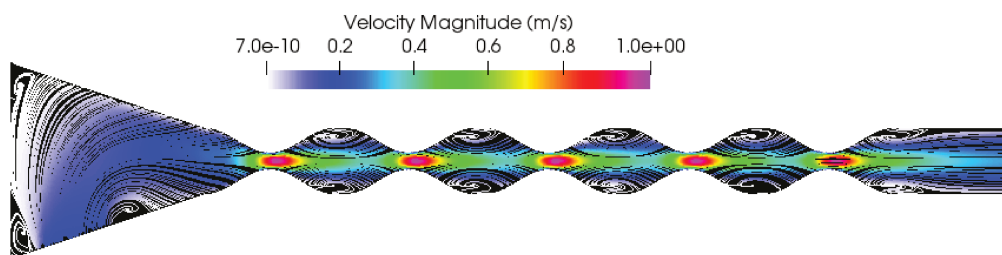
The velocity field can be evaluated in terms of the streamlines and Reynolds number as shown in Figure 5.65. As the entrance region is not directly subjected to the effects of the narrowing of the channel by d and α , the low Re value (from 1 to 40) does not allow a strong formation of circulation zones in this region, unlike it is observed in the cases of $d = 250 \mu\text{m}$ for a Re range from 20 to 90. Further, based on this figure, clear vortices are formed only when $Re = 40$ in the evaluated conditions.



(a) $Re=1$.



(b) $Re=20$.



(c) $Re=40$.

Figure 5.65: Streamlines along the microdevice where $d=200 \mu\text{m}$, $s = 100 \mu\text{m}$ and $\alpha = 2$.

Figure 5.66 shows the vorticity field in terms of Re , in which the phenomena that influence its intensification after the bumps were explained previously. In this way, it is possible to assess quantitatively the maximum value reached by this microdevice, and compare it with the other cases. Comparing different widths, for $Re = 20$, the maximum vorticity for $d = 200 \mu\text{m}$ is 319.4% higher than for $d = 250 \mu\text{m}$; while, when $Re = 40$, the increase is 318.3%. Finally, comparing $Re = 40$ ($d = 200 \mu\text{m}$) with $Re = 90$ ($d = 250 \mu\text{m}$), the maximum vorticity obtained in the narrowest throat is 54.6% superior.

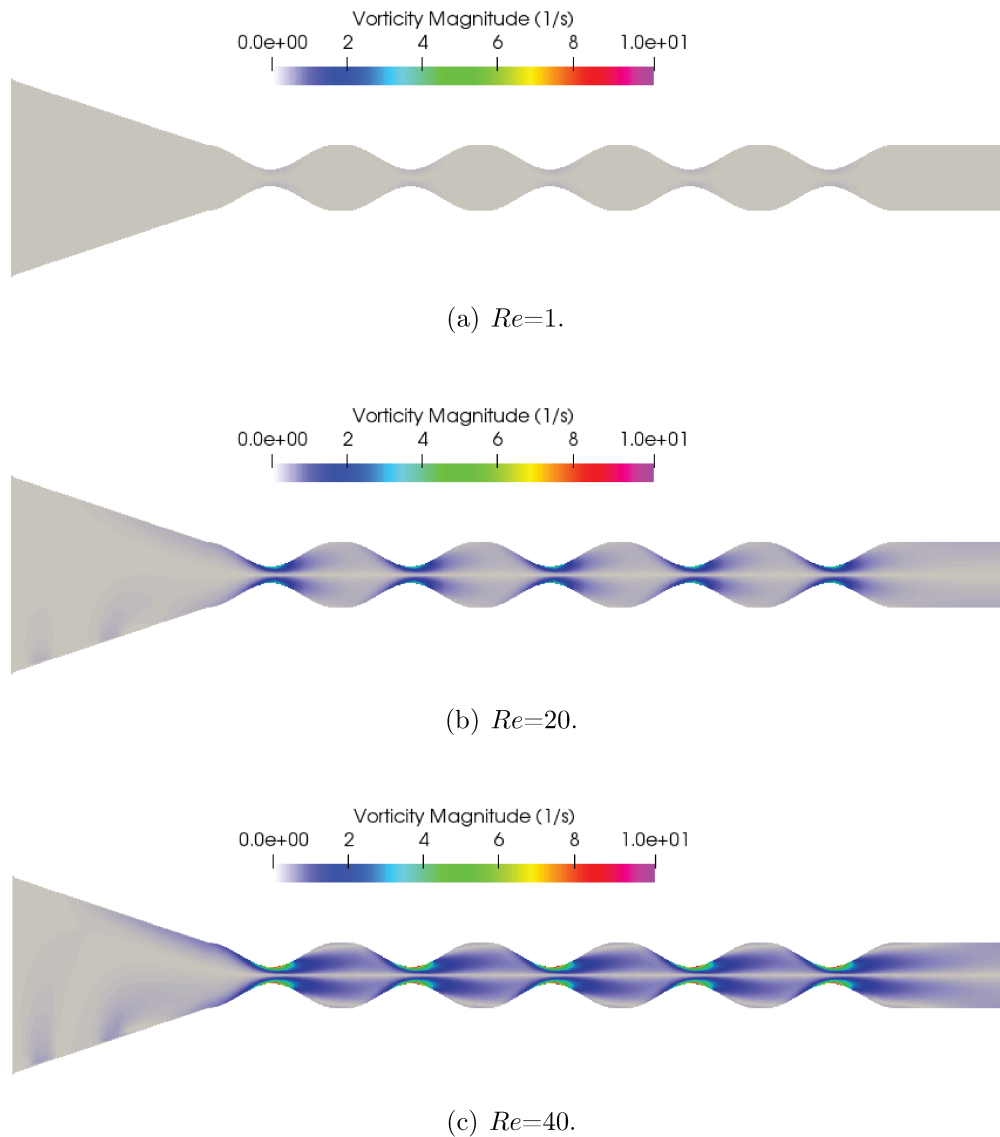


Figure 5.66: Vorticity field at different Reynolds numbers where $d=200 \mu\text{m}$, $s = 100 \mu\text{m}$ and $a = 2$.

The graphs in Figure 5.67 show the performance of the mean vorticity along the microdevice, and the kinematic pressure in the center-line ($y = 0.3 \text{ mm}$). In the throat positions, these parameters undergo high variations, and as Re increases, these gradients become larger. Moreover, comparing this case with the previous one where $\alpha = 1$, both variations are higher for $\alpha = 1$ where the peak of the mean vorticity is 10.6% superior while the pressure variation is 16.4% larger.

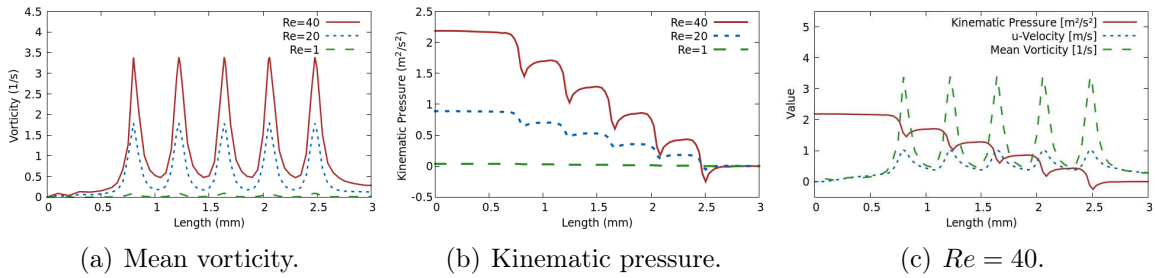


Figure 5.67: Performance of some fluid dynamics parameters along the device regarding Re for $s = 100 \mu\text{m}$, $\alpha = 2$ and $d = 200 \mu\text{m}$.

(b) Location of feed (s)

Finally, the position of the feed is evaluated in three positions ($0 \mu\text{m}$, $100 \mu\text{m}$, and $300 \mu\text{m}$) for a flow operating at $Re = 40$. Figure 5.68 illustrates the stream function field for these positions. In addition to the observations already presented for the case of curvature of bump equal to 1, it is noticed that $\alpha = 2$ creates a sharper bump, and subsequently, the cavity becomes more rounded and extensive, producing larger circulation zones. Moreover, this figure can also be compared with Figure 5.47 in the convergent nozzle region in which it is noted that the recirculation zones are not so intense for $d = 200 \mu\text{m}$ when compared with $d = 250 \mu\text{m}$ due to different Re .

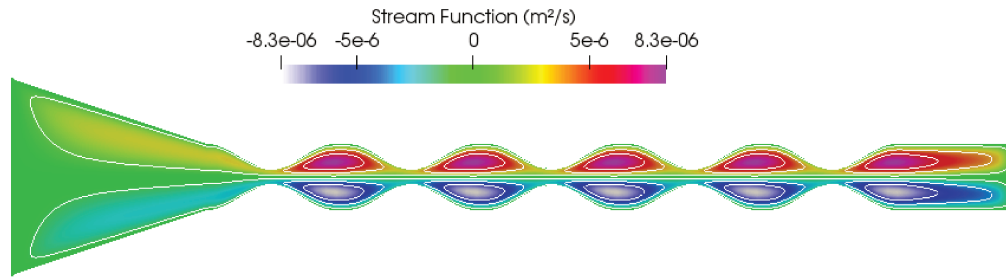
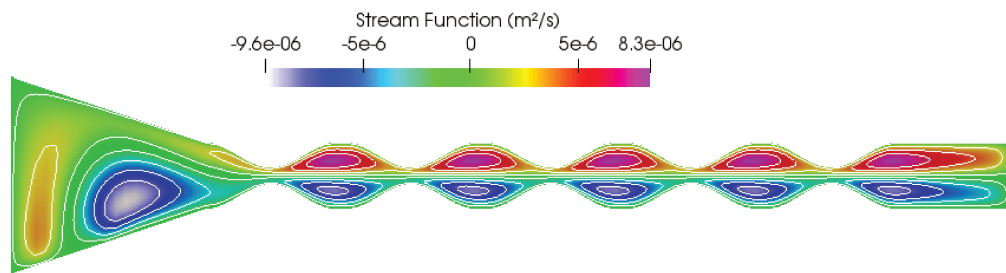
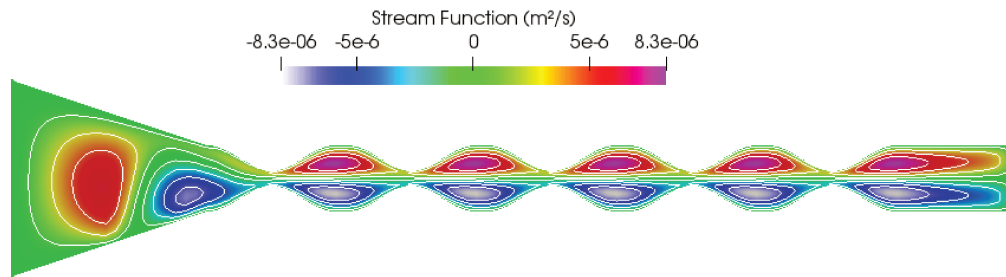
(a) $s=0 \mu m$.(b) $s=100 \mu m$.(c) $s=300 \mu m$.

Figure 5.68: Stream function with its contours along the microdevice where $d=200 \mu m$, $\alpha = 2$ and $Re = 40$.

The vorticity was evaluated in two positions at the x -axis: the cavities before (Bump0) and after (Bump1) the first pair of bumps. Again, before the fluid passing through the first bump, the vorticity is influenced exclusively by the action of the no-slip condition from the wall that generates a velocity gradient and makes the fluid elements rotate. On the other hand, after going through the bump, the deceleration of the particles inside the channel favors the increase of the pressure in the cavity, resulting in a change of direction of the flow therein. Lastly, for $Re = 1$, both positions have an entirely diffusive

flow with "vorticity generated only by the walls".

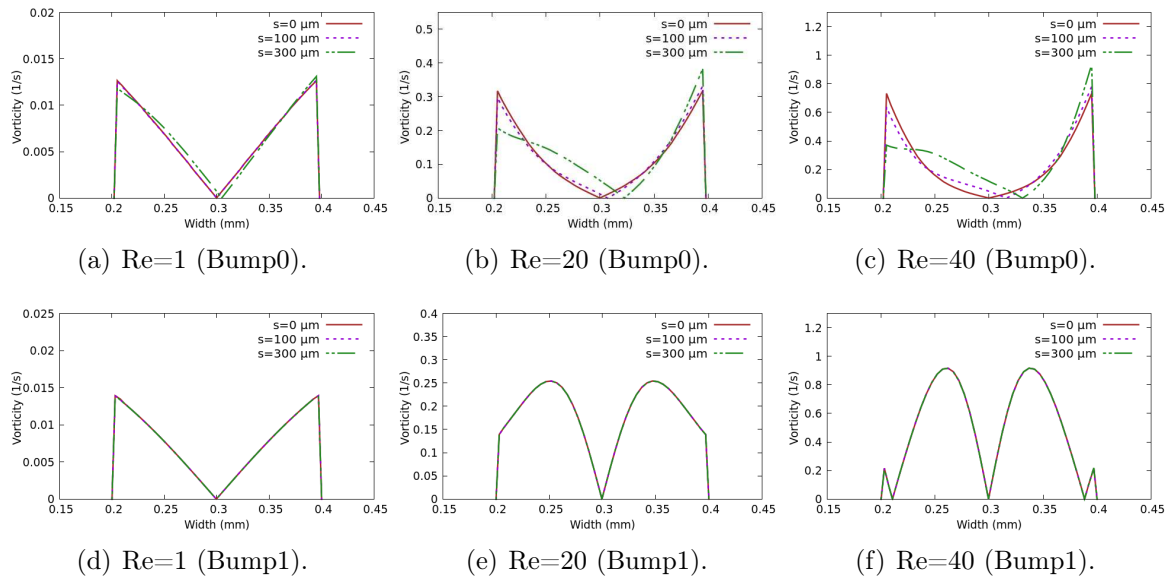


Figure 5.69: Magnitude of vorticity regarding Reynolds number and location of feed at $x = 0.6 \text{ mm}$ and at $x = 1.0 \text{ mm}$ with $d=200 \mu\text{m}$ and $a = 2$.

Before proceeding to the general analysis of the results, the case with $\alpha = 4$ was also studied, but its results are qualitatively similar, and also quantitatively they are lower than the others, so it is not included here in this section; however, the fluid dynamics parameters referring to this case can be checked in the appendices.

5.2.2.4 Curvature of Bumps: Overall

After analyzing the vorticity field for each curvature of bumps separately, they are now presented and compared in same graphics for when $x = 1 \text{ mm}$ (Bump1) maintaining $d = 200 \mu\text{m}$, and $s = 100 \mu\text{m}$ according to Figure 5.70. It is clearly noticed that even the fluid flowing into the bumpiness channel, for $Re = 1$, the vorticity does not depend on the type of curvature of bump, being dependent only on the diffusion and the shear stress caused by the walls. However, for $Re = 20$, the vorticity profile already has a different structure because the rotational motion is enhanced mainly by the narrowing of the channel caused by the convex bumps, and resulting in an increasing of the velocity of the fluid elements close to the center line. In addition, when Re is increased to 40, secondary recirculation regions are created within the cavities between the bumps, favoring the intertwined between the fluid streams. To conclude, at the three Re , the curvature

$\alpha = 4$ presents the worst vorticity performance among the other curvatures: the case with $\alpha = 2$ has a maximum vorticity 13.8% higher while for $\alpha = 1$, it is 30.4% superior than the case where $\alpha = 4$.

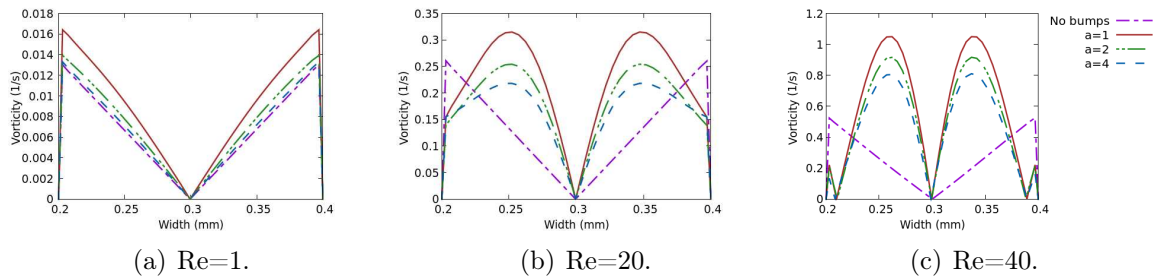


Figure 5.70: Magnitude of vorticity regarding Reynolds number and curvature of the bumps where $d=200 \mu m$ and $s = 100 \mu m$.

An essential factor for equipment design is to measure the pressure drop in the fluid flow, as, for example, a pump is proposed to compensate for this value and make the fluid flow. Thus, high-pressure drop values require pumps with higher power and hence make the process more costly. Figure 5.71 shows the pressure drop performance by varying Re and a with $d=200 \mu m$ and $s=100 \mu m$. Thus, taking the pressure drop value for the microdevice with $\alpha = 4$ operating at $Re = 40$ as a reference, this parameter is increased by 9.4% when compared to $\alpha = 2$; while for $\alpha = 1$, the pressure drop is 27.4% larger. On the other hand, the microdevice with no bumps has a pressure drop of approximately 14x less than that for $\alpha = 4$.

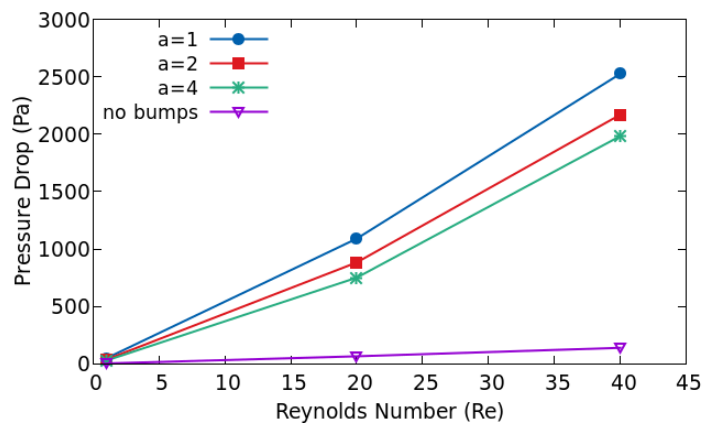


Figure 5.71: Pressure drop at different Reynolds numbers (Re) and curvature α when $d=200 \mu m$ and $s=100 \mu m$.

Furthermore, after analyzing the fluid dynamics parameters for each width d of the microchannel separately, a slice is taken at $x = 0.58$ mm (before the first bump) and at $x = 1.0$ mm (after the first bump) in order to compare these widths by maintaining $s = 100$ μm , for $Re = 20$ and $Re = 40$, and for all curvatures of bumps studied herein. Figure 5.72 illustrates the vorticity profiles at $x = 0.58$ mm for $Re = 20$ and $Re = 40$ and all bump curvatures in terms of the device's widths d . In this slice, the fluid has not been

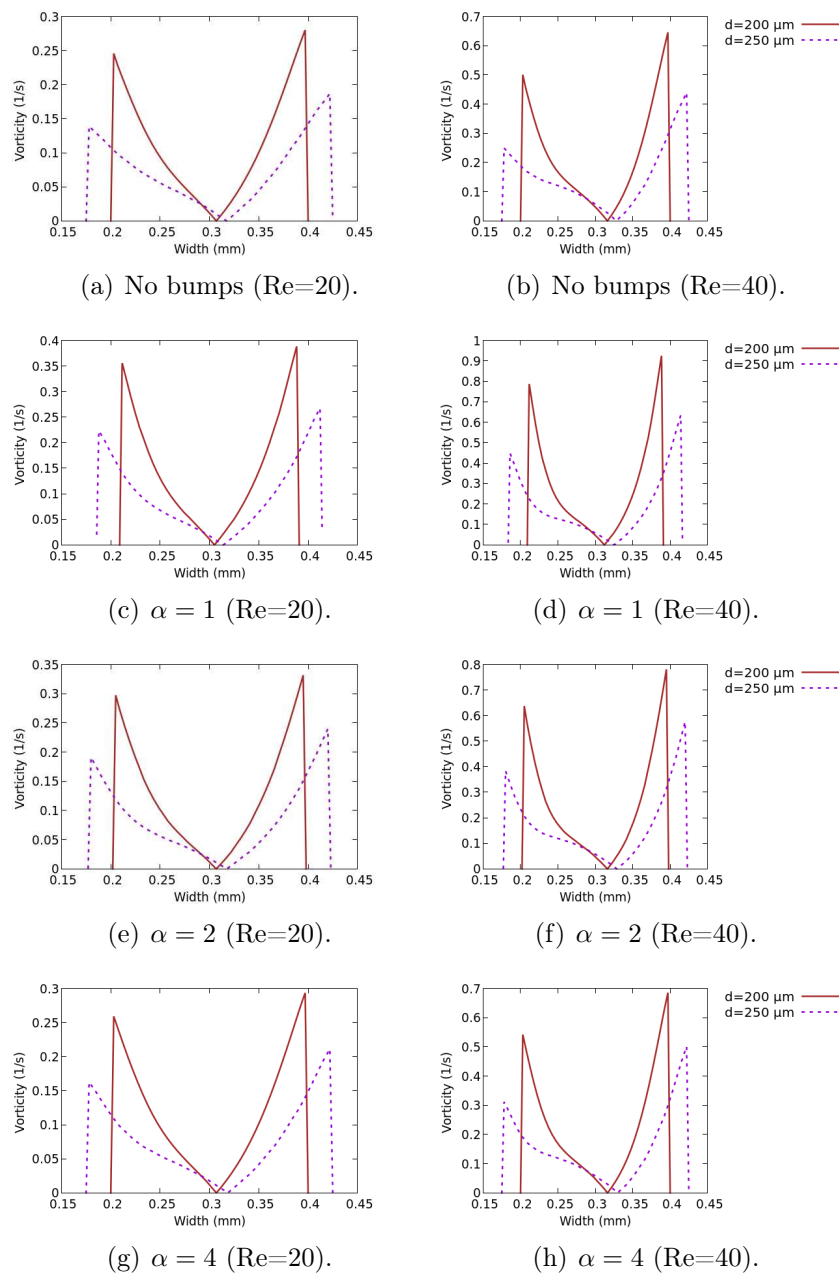


Figure 5.72: Magnitude of vorticity regarding Reynolds number and curvature of bumps comparing both values of d when $x = 0.58$ mm.

affected to the action of bumps yet, so the greatest contribution to the vorticity comes from the fluid flowing close to the wall caused by the feed. However, for $d = 200 \mu\text{m}$, the cross-sectional area is more reduced, which favors the increase in the u -velocity with a higher angular momentum when compared to $d = 250 \mu\text{m}$.

And finally, it is compared both widths d by taking a slice at $x = 1 \text{ mm}$ (Bump1) and maintaining $s = 100 \mu\text{m}$, for $Re = 20$ and $Re = 40$, and for all curvatures

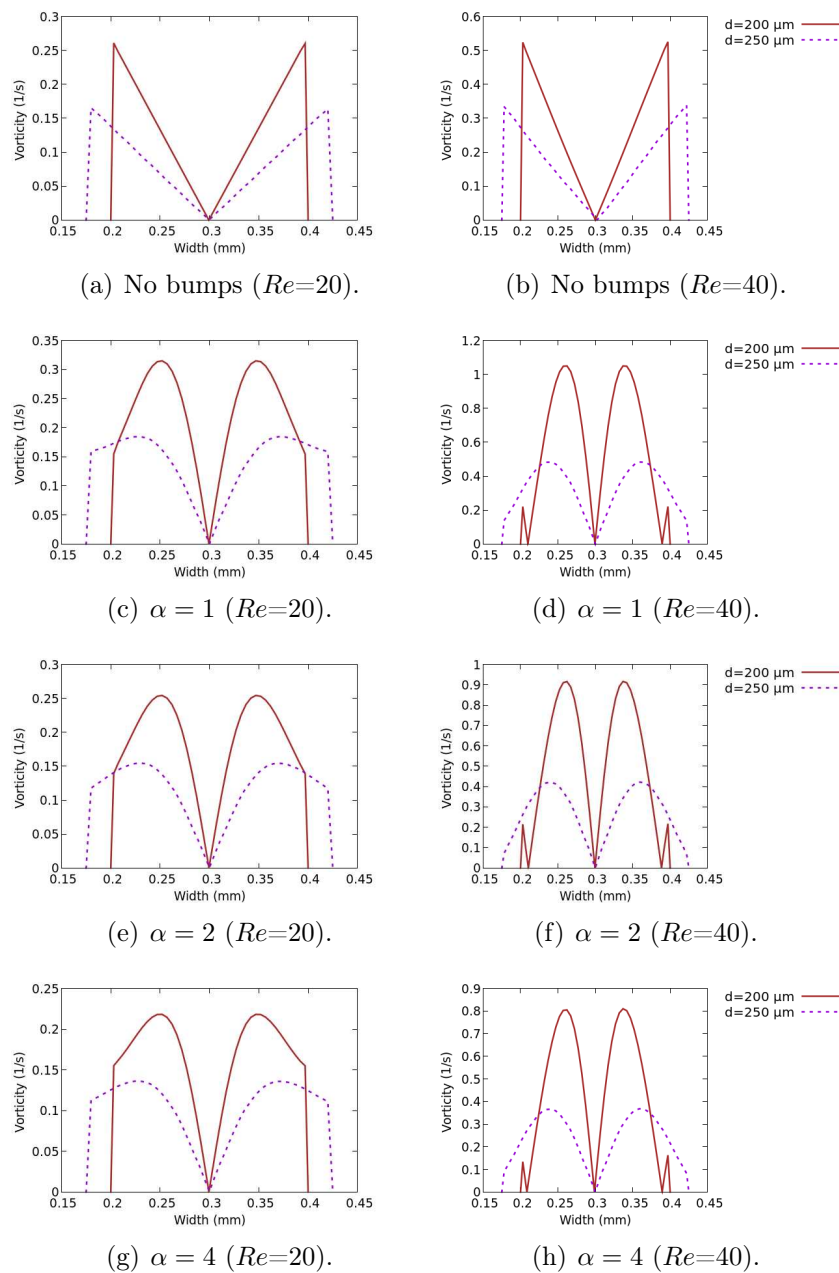


Figure 5.73: Magnitude of vorticity regarding Reynolds number and curvature of bumps comparing both values of d when $x = 1.0 \text{ mm}$.

of bumps studied herein. The vorticity profiles inside the cavities are shown in Figure 5.73. Thus, in all scenarios, the vorticity performance is vastly superior for the case with narrowing of the channel. In addition, the secondary peaks near the wall when $Re = 40$ are similar for $\alpha = 1$ and $\alpha = 2$, while for $\alpha = 4$ both the main and secondary vorticity peaks are lower.

In general, Table 5.3 lists the pressure drop, in Pascal, in all microdevices evaluated in this research in terms of Re . First, reducing the channel's width from $250 \mu\text{m}$ to $200 \mu\text{m}$ increases considerably the pressure drop by approximately five times more in cases with bumps. Moreover, almost all simulations performed for microdevices with entry into the lower wall of the nozzle show a slightly lower pressure drop when compared to those entering in the left wall ($s = 0 \mu\text{m}$). Likewise, for values of Re over 80, it is

Table 5.3: Pressure drop (Pa) for all simulations performed during this work.

| Device's width (μm) | Reynolds number | Location feed (μm) | Curvature of the bumps | | | | |
|----------------------------------|-----------------|---------------------------------|------------------------|---------|----------|----------|----------|
| | | | No bumps | 1 | 2 | 4 | |
| 200 | 1 | 0 | 3.093 | 48.887 | 37.158 | 28.645 | |
| | | 100 | 3.127 | 48.897 | 37.181 | 28.672 | |
| | | 300 | 3.080 | 48.654 | 37.104 | 28.623 | |
| | 20 | 20 | 0 | 67.548 | 1092.202 | 884.965 | 752.437 |
| | | | 100 | 65.824 | 1090.058 | 882.895 | 750.430 |
| | | | 300 | 65.175 | 1087.814 | 882.120 | 749.649 |
| | | 40 | 0 | 147.704 | 2535.458 | 2178.111 | 1992.059 |
| | | | 100 | 139.490 | 2525.420 | 2168.754 | 1982.755 |
| | | | 300 | 139.455 | 2524.037 | 2167.556 | 1981.676 |
| 250 | 20 | 0 | 35.876 | 202.980 | 171.639 | 153.564 | |
| | | 100 | 34.218 | 201.254 | 169.929 | 151.858 | |
| | | 300 | 33.725 | 200.841 | 170.192 | 153.107 | |
| | 40 | 0 | 80.068 | 462.534 | 404.534 | 382.241 | |
| | | 100 | 72.000 | 454.737 | 396.829 | 374.677 | |
| | | 300 | 71.610 | 457.329 | 401.565 | 383.443 | |
| | 60 | 60 | 0 | 130.750 | 782.166 | 699.042 | 685.294 |
| | | | 100 | 112.324 | 764.534 | 681.624 | 668.256 |
| | | | 300 | 114.260 | 773.133 | 694.716 | 690.328 |
| | | 80 | 0 | 189.892 | 1163.264 | 1055.226 | 1061.925 |
| | | | 100 | 157.152 | 1124.063 | 1017.778 | 1021.135 |
| | | | 300 | 161.892 | 1153.039 | 1052.166 | 1076.380 |
| | 90 | 90 | 0 | 222.383 | 1378.550 | 1257.873 | 1279.152 |
| | | | 100 | 181.080 | 1332.698 | 1212.360 | 1233.266 |
| | | | 300 | 187.562 | 1336.134 | 1213.622 | 1222.793 |

noticed that the pressure drop to $\alpha = 2$ follows a tendency becoming smaller among all cases with curvatures of bumps.

The final vorticity comparison includes the two best results for each width. For $d = 200 \mu\text{m}$, the case with $Re = 40$, $s = 100 \mu\text{m}$ and $\alpha = 2$ is chosen, while for $d = 250 \mu\text{m}$, the results of the simulation with $Re = 90$, $s = 100 \mu\text{m}$ and $\alpha = 2$ has been analyzed. Note: although $\alpha = 1$ has gotten larger vorticity quantities, the geometry with $\alpha = 2$ was chosen to study due to its lower pressure drop and better arrangement of the bumps. In this way, the channel with the smallest width reaches very high values of vorticity (as well as pressure drop as seen previously) over short distances as illustrated in Figure 5.74(a). However, these values are also reduced quickly as Figure 5.74(b) shows that the case with $d = 250 \mu\text{m}$ and $Re = 90$ has better vorticity in the cavity. Therefore, these strong oscillations in the parameters may affect badly the convergence of a simulation, and they can also cause instability in a process.

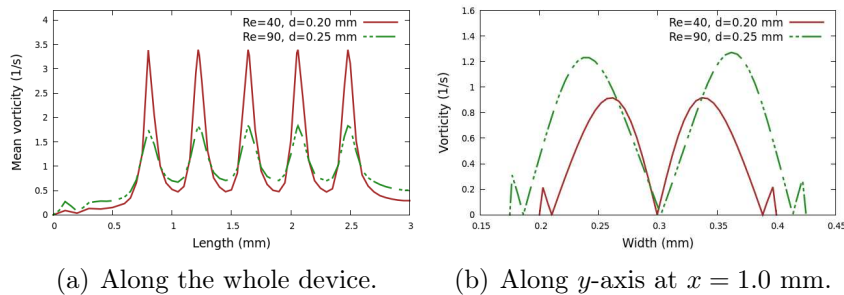


Figure 5.74: Vorticity profiles comparing the best results for each device's width d when $s = 100 \mu\text{m}$ and $\alpha = 2$.

Mondal et al. (2019) evaluated micromixers with an entrance similar to a T-shaped, but with a waviness duct. They showed that for $Re = 40$, the pressure drop range is approximately from 500 Pa to 1,600 Pa in the proposed geometries, while when $Re = 90$, these values varied from 1.5 kPa to 5.0 kPa with mixing index approximately equal to 60%. Meanwhile, some authors analyzed a few geometries with high pressure drop over 20 kPa in order to achieve over 85% of mixing (Borgohain et al., 2018), (Chen et al., 2020). Supported by this, the microdevice with width $d = 250 \mu\text{m}$, curvature of bump $\alpha = 2$, location of feed $s = 100 \mu\text{m}$ and Reynolds number $Re = 90$ is chosen as the most viable for intensifying the vorticity with a lower pressure drop (1212.36 Pa).

Chapter 6

Conclusion

“Focused, hard work is the real key to success. Keep your eyes on the goal, and just keep taking the next step towards completing it. If you aren’t sure which way to do something, do it both ways and see which works better.”

John Carmack

The purpose of this work consisted of: writing a numerical code on Fortran language by applying CFD concepts, and obtaining the fluid dynamics performance of a few parameters along microdevices. Additionally, it has been proposed to evaluate a geometry configuration that enhances the vorticity without a large increase in the pressure drop. Therefore, based on the previous chapters, some statements can be presented.

The code was divided into three files. The first file is more extensive and it is responsible for: discretizing the computational domain, implementing the solver, and exporting the calculated data to a *.vtk* file created by the code. Furthermore, there is a subroutine referring to the boundary conditions (location of walls, feeds, and fluid outlet) that the user should evaluate/change when necessary. The second file refers to the geometry to be studied and it is named GEOM. The data to be added can be generated in any spreadsheet document. Finally, the FLOW file is intended for the properties of the mesh, and the fluid, the feed velocity, the sub-relaxation factors, and the number of iterations. These two files can be easily handled by the user. In fact, the intention is to

make it easier for beginners to run a simulation, so removing the boundary condition's subroutine from the main file and inserting it into one of the additional files is already included in the next update of this code.

The values of the sub-relaxation factors were not discussed in this research, and indeed, these values depend on the conditions applied to each case study, and in some situations, they need to be guessed until the simulation converges. In fact, there is a pattern for them: when α_u , α_v , α_p are about 1, they make the iterative process more conservative, storing a very small quantity of the data obtained by the solver, and therefore requiring more iterations with a low possibility of instability in the simulation. On the other hand, in order to make the convergence quicker with fewer iterations, small values of these factors are chosen. Another conclusion is that, for a small Reynolds number, the set of values applicable to sub-relaxation factors is larger, which facilitates the convergence. However, as Re increases, this range of values is reduced, and the chance of oscillations along the execution of the code is higher, and consequently, this setup becomes more guessed.

The grid-dependent tests based on the determination of the GCI_{fine} were evaluated among the conditions accessible to which the code and computer's processor run. The maximum number of cells achieved for the mesh was 7,200 cells due to the memory usage limit, and the proposed methodology for calculating GCI_{fine} requires a grid refinement factor greater than 1.3, so the other meshes had to have approximately 3,600 cells and 1,600 cells. Even so, the maximum error is 3.93% for the bumpy microchannel, which is appropriate for the proposed mesh size. Another point is, the absolute value of the u -velocity is considerably small in these analyses, and this effect may also result in a large percentage of these discretization errors.

As a verification method for the code, the results obtained were compared with version 7 of OpenFOAM for two traditional CFD case studies: the rectangular duct and the lid-driven cavity. The largest relative error calculated is 5.5% when $Re = 400$ in the region close to the feed of the cavity. Considering that there are limitations regarding the maximum number of cells in the mesh, this value is satisfactory once it is close to a region of high velocity/pressure gradients.

The study of fluid dynamics in the bumpy microdevice resulted in velocity, pressure, vorticity, and stream-function fields in terms of Reynolds numbers, different locations of feed, curvatures of bumps, and widths of the bumpiness channel. The increase in Re favors the improvement of the convective contribution in the flow, forming recirculation zones and intensifying the rotational motion of the fluid elements as noticed for the cases with convex bumps for $Re = 40$ ($d = 200 \mu\text{m}$) and $Re = 90$ ($d = 250 \mu\text{m}$).

The position of the fluid inlet was studied in three locations: $s = 0 \mu\text{m}$, $s = 100 \mu\text{m}$ and $s = 300 \mu\text{m}$. In all simulations, this parameter just affects the vorticity in the region of the converging nozzle, so when the fluid passes through the first bump, the contribution in the vorticity becomes predominantly caused by the *separation* effect where fluid elements decelerate, and consequently, some zones of high pressure show up downstream the bump, inducing the flow to change its direction. The lateral feed on the lower wall makes the fluid reach the upper wall abruptly and change its direction, inducing the fluid elements to rotate. Likewise, the flow close to the upper wall also favors the increase of angular momentum once there is an effect of the viscous forces from the wall. In addition, comparing the three different positions of feed, both the maximum vorticity and the average vorticity profile are quite similar along the microdevice; however, the pressure drop for the entry at $s = 0 \mu\text{m}$ is slightly higher, while for the case with $s = 300 \mu\text{m}$, the large recirculation zone upstream of the entrance may reduce the performance/yield of a supposed mixing or reaction system.

The curvature of the bumps was assessed using equations 4.4 and 4.5 in terms of α that dictate whether the convex bump is flatter or sharper. The values chosen for α were: 1, 2, and 4; and one more case with no bumps. Firstly, the inclusion of bumps considerably increases the magnitude of the vorticity compared to cases with no bumps. The vorticity in a bumpiness microchannel is the result of an extensive narrowing of the channel which causes an increase in the fluid velocity, resulting in high velocity gradient, with strong shear stress. On the other hand, the action of viscous torque caused by the no-slip condition from the walls is the only source of vorticity for cases with no bumps along a straight duct. Further, it is noticed that as the bump becomes smoother, the rotation of the particles gets higher due to a longer residence time throughout the throat. Indeed, devices with $\alpha = 1$ have more extensive regions with this narrowing, and therefore, the

pressure gradient gets larger inducing the change in the direction of flow. Nonetheless, its pressure gradient is higher when compared to the other cases, and therefore it is concluded that the curvature $\alpha = 2$ is more viable once it still has vorticity close enough to the case with a flatter bump, and it also has a more rounded/continuous geometry (bump+cavity).

Finally, the width of the duct where the bumps are inserted is analyzed for two values: $200 \mu\text{m}$ and $250 \mu\text{m}$. Again, the reduction of the channel where the fluid flows favors the increasing of velocity of the fluid elements and causes subsequently a larger pressure gradient after the throat, resulting in an intensification of the vorticity. However, for $Re \geq 50$, the high-pressure gradient values when $d = 200 \mu\text{m}$ did not lead the iterative process from this code to converge even after refining the post-bump regions; and therefore, the maximum value of Re worked on that width was only 40. Thus, although high vorticity values are obtained at low Re , the pressure drop is also large, which would make the system more expensive with the addition of high-pressure pumps, making the process infeasible. Therefore, based on these results, this research suggests the device's width $d = 250 \mu\text{m}$ with curvature of bumps $\alpha = 2$ and feed position at $s = 100 \mu\text{m}$ operating at $Re = 90$ as the best geometry configuration for the enhancement of vorticity. Nonetheless, further studies should still be carried out in order to provoke formation of vortices with a lower Reynolds number and a lower pressure drop. Moreover, a response surface methodology would help not only to optimize the vorticity but also to analyze the best combination of geometry parameters in terms of vorticity.

Lastly, the code has become a tool to assist in the study of fluid dynamics in cases in milli and micro scale. It can be used for future research with other new geometries to evaluate streamlines, velocity, pressure, and vorticity fields; as well as it can also be used inside a classroom for students to understand/assess why some fluid-dynamic parameters behave after a fluid flows through a throat, or how the flow characteristics are affected when the Reynolds number is changed.

However, as future works, some improvements can still be applied to both code and research. In addition to including the boundary condition subroutine in a secondary file to help the user, the mass transport equation can be easily implemented since the velocity field is already discretized and solved within the solver. Consequently, studies

can be carry out in also a three-dimension perspective by evaluating the maximization of the mixing index between two compounds based on proposing geometries of micromixers. Moreover, it would be interesting to propose an optimization equation or method (such as a response surface) in terms of vorticity, Reynolds number, and pressure drop in order to support the conclusion about which geometry is the most viable. Lastly, a step of validation of the final results, either by simulations in Ansys or by experiments, would contribute to the ratification of the data obtained.

Bibliography

- D. Ahmed, X. Mao, B. K. J. J. Shi, and T. J. Huang. A Millisecond Micromixer Via Single-Bubble-Based Acoustic Streaming . *Lab on a chip*, 18(9):2738–2741, 2009.
- A. Alam and K. Kim. Analysis of mixing in a curved microchannel with rectangular grooves. *Chemical Engineering Journal*, 181-182:708–716, 2012. doi: 10.1016/j.cej.2011.12.076.
- J. Blazek. Chapter 3 - Principles of Solution of the Governing Equations. *Computational Fluid Dynamics: Principles and Applications*, 3:29–72, 2015.
- D. Bluestein. Utilizing Computational Fluid Dynamics in Cardiovascular Engineering and Medicine - What You Need to Know. *Artificial Organs*, 41:117–121, 2017.
- P. Borgohain, J. Arumughan, A. Dalal, and G. Natarajan. Design and performance of a three-dimensional micromixer with curved ribs. *Chemical Engineering Research and Design*, 136:761–775, 2018. doi: 10.1016/j.cherd.2018.06.027.
- B. Bruijns, A. V. Asten, R. Tiggelaar, and H. Gardeniers. Microfluidic Devices for Forensic DNA Analysis: A Review. *Biosensors*, 6:41–76, 2016.
- L. Capretto, W. Cheng, M. Hill, and X. Zhang. Micromixing within Microfluidic Devices. *Topics in Current Chemistry*, 304:27–68, 2011.
- Y. C. Chao and W. C. Ho. Behavior Of Five Solution Algorithms On Turbulent Calculations . *Communications In Applied Numerical Methods*, 5:253–261, 1989.
- I. L. Chaves, L. C. Duarte, W. K. T. Coltro, and D. A. Santos. Droplet length and generation rate investigation inside microfluidic devices by means of cfd simulations
-

-
- and experiments. *Chemical Engineering Research and Design*, 161:260–270, 2020. doi: 10.1016/j.cherd.2020.07.015.
- X. Chen and J. Shen. Numerical analysis of mixing behaviors of two types of E-shape micromixers. *International Journal of Heat and Mass Transfer*, 106:593–600, 2017.
- X. Chen, T. Li, H. Zeng, Z. Hu, and B. Fu. Numerical and experimental investigation on micromixers with serpentine microchannels. *International Journal of Heat and Mass Transfer*, 98:131–140, 2016. doi: 10.1016/j.ijheatmasstransfer.2016.03.041.
- Y. Chen, X. Chen, and S. Liu. Numerical and experimental investigations of novel passive micromixers with fractal-like tree structures. *Chemical Physics Letters*, 747, 2020. doi: 10.1016/j.cplett.2020.137330.
- S. Colin. *Microfluidics*. John Wiley & Sons - Inc, Hoboken, 2010.
- C. A. Cortes-Quiroz, A. Azarbadegan, and M. Zangeneh. Evaluation of Flow Characteristics that give Higher Mixing Performance in The 3-D T-Mixer versus The Typical T-Mixer. *Sensors and Actuators B: Chemical*, 202:1209–1219, 2014.
- P. A. Davidson. *Turbulence: An Introduction for Scientists and Engineers*. Oxford University Press, New York, 2004.
- S. Dreher, N. Kockmann, and P. Woias. Characterization of Laminar Transient Flow Regimes and Mixing in T-shaped Micromixers. *Heat Transfer Engineering*, 30:91–100, 2009. doi: 10.1080/01457630802293480.
- F. Farshchi and M. Hasanzadeh. Microfluidic biosensing of circulating tumor cells (ctcs): Recent progress and challenges in efficient diagnosis of cancer. *Biomedicine & Pharmacotherapy*, 134, 2021. doi: 10.1016/j.biopha.2020.111153.
- R. W. Fox, P. J. Pritchard, and A. T. McDonald. *Introduction to Fluid Mechanics*. Wiley, Chichester, 2011.
- C. Galletti, M. Roudgar, E. Brunazzi, and R. Mauri. Effect of inlet conditions on the engulfment pattern in a T-shaped micro-mixer. *Chemical Engineering Journal*, 185-186: 300–313, 2012. doi: 10.1016/j.cej.2012.01.046.
-

- G. Hamilton. Geraldine hamilton: Body parts on a chip, December 2013. URL <https://www.youtube.com/watch?v=CpkXmtJOH84>.
- F. H. Harlow and J. E. Welch. Numerical Calculation of Time-dependent Viscous Incompressible Flow of Fluid with Free Surface. *Physics of Fluids*, 8:2182–2189, 1965.
- C. Hirsch. *Numerical Computational Of Internal & External Flows*. John Wiley & Sons, Ltd, Burlington, 2007.
- C. Hoch. LumiraDx Receives SARS-CoV-2 Antigen Test Authorization in Japan and Brazil; Italy Recommends Expansion of Microfluidic Antigen Testing, 2021. URL <https://www.lumiradx.com/za-en/news-events/lumiradx-receives-sars-cov-2-ag-test-authorization-in-japan-and-brazil>.
- S. H. Hong, D. S. Jang, S. Yun, J. H. Baek, and Y. Kim. Performance improvement of heat pumps using novel microchannel heat exchangers with plain-louver fins during periodic frosting and defrosting cycles in electric vehicles. *Energy Conversion and Management*, 223, 2020. doi: 10.1016/j.enconman.2020.113306.
- D. K. Jaiswal, K. Kumar, and R. R. Yadav. Analytical Solution To The One-Dimensional Advection-Diffusion Equation With Temporally Dependent Coefficients . *Journal of Water Resource and Protection*, 3:76–84, 2011.
- S. A. Khan, A. Aabid, and M. A. A. Baig. CFD Analysis of CD Nozzle and Effect of Nozzle Pressure Ratio on Pressure and Velocity for Suddenly Expanded Flows. *Transstellar Journal Publications*, 3:1147–1158, 2018.
- V. Khaydarov, E. S. Borovinskaya, and W. Reschetilowski. Numerical and Experimental Investigations of a Micromixer with Chicane Mixing Geometry. *Applied Science*, 8: 2458–2474, 2018.
- P. K. Kundu and I. M. Cohen. *Fluid Mechanics*. Elsevier Academic Press, Chicago, 2004.
- C. Liu, Y. Li, and B. Liu. Micromixers and their applications in kinetic analysis of biochemical reactions. *Talanta*, 205, 2019. doi: 10.1016/j.talanta.2019.120136.
-

-
- P. R. Mashaei, S. Asiaei, and S. M. Hosseinalipour. Mixing efficiency enhancement by a modified curved micromixer: A numerical study. *International Journal of Mechanical Sciences*, 154, 2020. doi: 10.1016/j.cep.2020.108006.
- S. Mazumder. Simple algorithm on staggered mesh - part 3 of 5, January 2018. URL <https://www.youtube.com/watch?v=Lre5wg0TSuU>.
- S. Mazumder. Simple algorithm on co-located mesh—part 3 of 5, November 2019. URL https://www.youtube.com/watch?v=yWUc2D_WTMY&t=382s.
- T. F. Miller and F. W. Schmidt. Use of a pressure-weighted interpolation method for the solution of the incompressible navier-stokes equations on a nonstaggered grid system. *Numerical Heat Transfer*, 14:213–233, 1988. doi: 10.1080/10407788808913641.
- A. Mojtabi and M. O. Deville. One-Dimensional Linear Advection–Diffusion Equation: Analytical And Finite Element Solutions . *Computers and Fluids*, 107:189–195, 2015.
- B. Mondal, S. K. Mehta, P. K. Patowari, and S. Pati. Numerical Study Of Mixing In Wavy Micromixers: Comparison Between Raccoon And Serpentine Mixer. *Chemical Engineering & Processing: Process Intensification*, 136:44–61, 2019.
- D. R. Mott, P. B. Howell-Jr, K. S. Obenschain, and E. S. Oran. The Numerical Toolbox: An Approach for Modeling and Optimizing Microfluidic Components. *Mechanics Research Communications*, 36:104–109, 2009.
- B. Nasser, N. Soleimani, N. Rabiee, A. Kalbasi, M. Karimi, and M. R. Hamblin. Point-of-care microfluidic devices for pathogen detection. *Biosensors and Bioelectronics*, 117: 112–128, 2018. doi: 10.1016/j.bios.2018.05.050.
- N.-T. Nguyen. *Micromixers: Fundamentals, Design and Fabrication*. William Andrew Inc. , Singapore, 2008.
- N.-T. Nguyen and Z. Wu. Micromixers—A Review. *Journal of Micromechanics and Microengineering*, 15:R1–R16, 2005. doi: 10.1088/0960-1317/15/2/R01.
- D. Nouri, A. Zabihi-Hesari, and M. Passandideh-Fard. Rapid Mixing In Micromixers Using Magnetic Field. *Sensors and Actuators A: Physical*, 255:79–86, 2017.
-

-
- J. O'Connor, P. Day, P. Mandal, and A. Revell. A Computational Fluid Dynamics in The Microcirculation and Microfluidics: What Role can The Lattice Boltzmann Method play? *Integrative biology*, 8:589–602, 2016.
- G. Orsi, M. Roudgar, E. Brunazzi, C. Galletti, and R. Mauri. Water-Ethanol Mixing in T-Shaped Microdevices. *Chemical Engineering Science*, 95:174–183, 2013.
- J. Ortega-Casanova and C. H. Lai. CFD study about the effect of using multiple inlets on the efficiency of a micromixer. Assessment of the optimal inlet configuration working as a microreactor. *Chemical Engineering and Processing - Process Intensification*, 125:163–172, 2018. doi: 10.1016/j.cep.2018.01.017.
- J. Pan, J. Shao, H. Qu, and X. Gong. Ethanol precipitation of codonopsis radix concentrate with a membrane dispersion micromixer. *Journal of Cleaner Production*, 251, 2020. doi: 10.1016/j.jclepro.2019.119633.
- S. V. Patankar. *Numerical Heat Transfer and Fluid Flow*. McGraw-Hill Book Company, New York, 1980.
- S. V. Patankar and D. B. Spalding. A Calculation Procedure for Heat, Mass and Momentum Transfer in Three-dimensional Parabolic Flows. *International Journal of Heat and Mass Transfer*, 15:1787, 1972.
- J. M. Pearce. A review of open source ventilators for COVID-19 and future pandemics. *F1000Research*, 9, 2020. doi: 10.12688/f1000research.22942.2.
- C. Potrich, L. Lunelli, M. Cocuzza, S. L. Marasso, C. F. Pirri, and C. Pederzoli. Simple pdms microdevice for biomedical applications. *Talanta*, 193:44–50, 2019. doi: 10.1016/j.talanta.2018.09.080.
- E. K. Ramasetti, V. Visuri, P. Sulasalmi, and T. Fabritius. A CFD and Experimental Investigation of Slag Eye in Gas Stirred Ladle. *Journal of Fluid Flow, Heat and Mass Transfer*, 5:78–86, 2018.
- L. Raynal, F. Augier, F. Bazer-Bachi, Y. Haroun, and C. P. D. Fonte. CFD applied to Process Development in The Oil and Gas Industry - a Review. *Oil & Gas Science and Technology*, 71:42–66, 2015.
-

- C. M. Rhie and W. L. Chow. Numerical study of the turbulent flow past an airfoil with trailing edge separation. *AIAA Journal*, 21:1525–1532, 1983. doi: 10.2514/3.8284.
- H. S. Santana. *Síntese De Biodiesel Em Microcanais*. diploma thesis, Faculdade de Engenharia Química, 2016.
- H. S. Santana, J. L. Silva-Júnior, and O. P. Taranto. Numerical Simulations Of Biodiesel Synthesis In Microchannels With Circular Obstructions. *Chemical Engineering and Processing: Process Intensification*, 98:137–146, 2015.
- H. S. Santana, D. S. Tortola, E. M. Reis, J. L. S. Jr., and O. P. Taranto. Transesterification Reaction Of Sunflower Oil And Ethanol For Biodiesel Synthesis In Microchannel Reactor: Experimental And Simulation Studies. *Chemical Engineering Journal*, 302:752–762, 2016. doi: 10.1016/j.cej.2016.05.122.
- N. Sen, K. K. Singh, S. Mukhopadhyay, and K. T. Shenoy. Continuous synthesis of tributyl phosphate in microreactor. *Progress in Nuclear Energy*, 126, 2020. doi: 10.1016/j.pnucene.2020.103402.
- I. Shaha, S. W. Kima, K. Kima, Y. H. Dohb, and K. H. Choi. Experimental And Numerical Analysis Of Y-shaped Split And Recombination Micro-mixer With Different Mixing Units . *Chemical Engineering Journal*, 358:691–706, 2019.
- S. Singh, R. Mohan, V. Gosu, and U. K. A. Kumar. Process Intensification of Propionic Acid Extraction and its Recovery by Distillation in Microchannel. *Chemical Engineering and Processing - Process Intensification*, 157, 2020. doi: 10.1016/j.cep.2020.108150.
- R. D. Sochol, E. Sweet, C. C. Glick, S. Wu, and C. Yang. 3D Printed Microfluidics and Microelectronics. *Microelectronic Engineering*, 189:52–68, 2018.
- P. R. Spalart and V. Venkatakrisnan. On the Role and Challenges of CFD in the Aerospace Industry. *The Aeronautical Journal*, 120:209–232, 2016.
- D. B. Spalding. A Novel Finite-Difference Formulation for Differential Expressions Involving Both First and Second Derivatives. *International Journal for Numerical Methods in Engineering*, 4:551, 1972.
-

- A. I. Stankiewicz and J. A. Moulijn. Process Intensification: Transforming Chemical Engineering. *Chemical Engineering Progress*, 96(1):22–33, 2000.
- W. Tian and E. Finehout. *Microfluidics for Biological Applications: Microfluidic Applications in Biodefense*. Springer, Boston, 2008.
- P. Vatankhah and A. Shamloo. Parametric Study on Mixing Process in an in-Plane Spiral Micromixer Utilizing Chaotic Advection. *Analytica Chimica Acta*, 1022:96–105, 2018.
- H. K. Versteeg and W. Malalasekera. *An Introduction To Computational Fluid Dynamics: The Finite Volume Method*. Prentice Hall, Harlow, 2007.
- D. Wang, T. Zhang, Y. Yang, and S. Tang. Simulation and design microreactor configured with micromixers to intensify the isobutane/1-butene alkylation process. *Journal of the Taiwan Institute of Chemical Engineers*, 98:53–62, 2019.
- G. M. Whitesides. The Origins And The Future Of Microfluidics. *NATURE*, 442:368–373, 2006.
-

Appendix A

Rectangular Duct Case

A.1 FLOW File

```
1      80      40
2      8.935E-7      9.97E-7
3      358.5      0.
4      0.98      0.98      0.02
5      100000
```

Listing A.1: Parameters stored by the user.

A.2 GEOM File

```
1 'Duct '  
2 0.0000 0.0000 0.0000 0.2500  
3 0.0375 0.0000 0.0375 0.2500  
4 0.0750 0.0000 0.0750 0.2500  
5 0.1125 0.0000 0.1125 0.2500  
6 0.1500 0.0000 0.1500 0.2500  
7 0.1875 0.0000 0.1875 0.2500  
8 0.2250 0.0000 0.2250 0.2500  
9 0.2625 0.0000 0.2625 0.2500  
10 0.3000 0.0000 0.3000 0.2500  
11 0.3375 0.0000 0.3375 0.2500  
12 0.3750 0.0000 0.3750 0.2500  
13 0.4125 0.0000 0.4125 0.2500  
14 0.4500 0.0000 0.4500 0.2500  
15 0.4875 0.0000 0.4875 0.2500  
16 0.5250 0.0000 0.5250 0.2500  
17 0.5625 0.0000 0.5625 0.2500  
18 0.6000 0.0000 0.6000 0.2500  
19 0.6375 0.0000 0.6375 0.2500  
20 0.6750 0.0000 0.6750 0.2500  
21 0.7125 0.0000 0.7125 0.2500  
22 0.7500 0.0000 0.7500 0.2500  
23 0.7875 0.0000 0.7875 0.2500  
24 0.8250 0.0000 0.8250 0.2500  
25 0.8625 0.0000 0.8625 0.2500  
26 0.9000 0.0000 0.9000 0.2500  
27 0.9375 0.0000 0.9375 0.2500  
28 0.9750 0.0000 0.9750 0.2500  
29 1.0125 0.0000 1.0125 0.2500  
30 1.0500 0.0000 1.0500 0.2500  
31 1.0875 0.0000 1.0875 0.2500  
32 1.1250 0.0000 1.1250 0.2500  
33 1.1625 0.0000 1.1625 0.2500  
34 1.2000 0.0000 1.2000 0.2500  
35 1.2375 0.0000 1.2375 0.2500
```

| | | | | |
|----|--------|--------|--------|--------|
| 36 | 1.2750 | 0.0000 | 1.2750 | 0.2500 |
| 37 | 1.3125 | 0.0000 | 1.3125 | 0.2500 |
| 38 | 1.3500 | 0.0000 | 1.3500 | 0.2500 |
| 39 | 1.3875 | 0.0000 | 1.3875 | 0.2500 |
| 40 | 1.4250 | 0.0000 | 1.4250 | 0.2500 |
| 41 | 1.4625 | 0.0000 | 1.4625 | 0.2500 |
| 42 | 1.5000 | 0.0000 | 1.5000 | 0.2500 |
| 43 | 1.5375 | 0.0000 | 1.5375 | 0.2500 |
| 44 | 1.5750 | 0.0000 | 1.5750 | 0.2500 |
| 45 | 1.6125 | 0.0000 | 1.6125 | 0.2500 |
| 46 | 1.6500 | 0.0000 | 1.6500 | 0.2500 |
| 47 | 1.6875 | 0.0000 | 1.6875 | 0.2500 |
| 48 | 1.7250 | 0.0000 | 1.7250 | 0.2500 |
| 49 | 1.7625 | 0.0000 | 1.7625 | 0.2500 |
| 50 | 1.8000 | 0.0000 | 1.8000 | 0.2500 |
| 51 | 1.8375 | 0.0000 | 1.8375 | 0.2500 |
| 52 | 1.8750 | 0.0000 | 1.8750 | 0.2500 |
| 53 | 1.9125 | 0.0000 | 1.9125 | 0.2500 |
| 54 | 1.9500 | 0.0000 | 1.9500 | 0.2500 |
| 55 | 1.9875 | 0.0000 | 1.9875 | 0.2500 |
| 56 | 2.0250 | 0.0000 | 2.0250 | 0.2500 |
| 57 | 2.0625 | 0.0000 | 2.0625 | 0.2500 |
| 58 | 2.1000 | 0.0000 | 2.1000 | 0.2500 |
| 59 | 2.1375 | 0.0000 | 2.1375 | 0.2500 |
| 60 | 2.1750 | 0.0000 | 2.1750 | 0.2500 |
| 61 | 2.2125 | 0.0000 | 2.2125 | 0.2500 |
| 62 | 2.2500 | 0.0000 | 2.2500 | 0.2500 |
| 63 | 2.2875 | 0.0000 | 2.2875 | 0.2500 |
| 64 | 2.3250 | 0.0000 | 2.3250 | 0.2500 |
| 65 | 2.3625 | 0.0000 | 2.3625 | 0.2500 |
| 66 | 2.4000 | 0.0000 | 2.4000 | 0.2500 |
| 67 | 2.4375 | 0.0000 | 2.4375 | 0.2500 |
| 68 | 2.4750 | 0.0000 | 2.4750 | 0.2500 |
| 69 | 2.5125 | 0.0000 | 2.5125 | 0.2500 |
| 70 | 2.5500 | 0.0000 | 2.5500 | 0.2500 |
| 71 | 2.5875 | 0.0000 | 2.5875 | 0.2500 |
| 72 | 2.6250 | 0.0000 | 2.6250 | 0.2500 |
| 73 | 2.6625 | 0.0000 | 2.6625 | 0.2500 |

```
74 2.7000 0.0000 2.7000 0.2500
75 2.7375 0.0000 2.7375 0.2500
76 2.7750 0.0000 2.7750 0.2500
77 2.8125 0.0000 2.8125 0.2500
78 2.8500 0.0000 2.8500 0.2500
79 2.8875 0.0000 2.8875 0.2500
80 2.9250 0.0000 2.9250 0.2500
81 2.9625 0.0000 2.9625 0.2500
82 3.0000 0.0000 3.0000 0.2500
```

Listing A.2: Nodal points stored along the walls.

Appendix B

Lid-Driven Cavity Case

B.1 FLOW File

```
1 60      60
2 8.935e-7  9.97e-7
3 89.62    0.
4 0.65    0.65    0.35
5 3000
```

Listing B.1: Parameters stored by the user.

B.2 GEOM File

```
1 'Cavity'  
2 0.0000 0.000 0.0000 1.000  
3 0.0167 0.000 0.0167 1.000  
4 0.0333 0.000 0.0333 1.000  
5 0.0500 0.000 0.0500 1.000  
6 0.0667 0.000 0.0667 1.000  
7 0.0833 0.000 0.0833 1.000  
8 0.1000 0.000 0.1000 1.000  
9 0.1167 0.000 0.1167 1.000  
10 0.1333 0.000 0.1333 1.000  
11 0.1500 0.000 0.1500 1.000  
12 0.1667 0.000 0.1667 1.000  
13 0.1833 0.000 0.1833 1.000  
14 0.2000 0.000 0.2000 1.000  
15 0.2167 0.000 0.2167 1.000  
16 0.2333 0.000 0.2333 1.000  
17 0.2500 0.000 0.2500 1.000  
18 0.2667 0.000 0.2667 1.000  
19 0.2833 0.000 0.2833 1.000  
20 0.3000 0.000 0.3000 1.000  
21 0.3167 0.000 0.3167 1.000  
22 0.3333 0.000 0.3333 1.000  
23 0.3500 0.000 0.3500 1.000  
24 0.3667 0.000 0.3667 1.000  
25 0.3833 0.000 0.3833 1.000  
26 0.4000 0.000 0.4000 1.000  
27 0.4167 0.000 0.4167 1.000  
28 0.4333 0.000 0.4333 1.000  
29 0.4500 0.000 0.4500 1.000  
30 0.4667 0.000 0.4667 1.000  
31 0.4833 0.000 0.4833 1.000  
32 0.5000 0.000 0.5000 1.000  
33 0.5167 0.000 0.5167 1.000  
34 0.5333 0.000 0.5333 1.000  
35 0.5500 0.000 0.5500 1.000
```

```
36 0.5667 0.000 0.5667 1.000
37 0.5833 0.000 0.5833 1.000
38 0.6000 0.000 0.6000 1.000
39 0.6167 0.000 0.6167 1.000
40 0.6333 0.000 0.6333 1.000
41 0.6500 0.000 0.6500 1.000
42 0.6667 0.000 0.6667 1.000
43 0.6833 0.000 0.6833 1.000
44 0.7000 0.000 0.7000 1.000
45 0.7167 0.000 0.7167 1.000
46 0.7333 0.000 0.7333 1.000
47 0.7500 0.000 0.7500 1.000
48 0.7667 0.000 0.7667 1.000
49 0.7833 0.000 0.7833 1.000
50 0.8000 0.000 0.8000 1.000
51 0.8167 0.000 0.8167 1.000
52 0.8333 0.000 0.8333 1.000
53 0.8500 0.000 0.8500 1.000
54 0.8667 0.000 0.8667 1.000
55 0.8833 0.000 0.8833 1.000
56 0.9000 0.000 0.9000 1.000
57 0.9167 0.000 0.9167 1.000
58 0.9333 0.000 0.9333 1.000
59 0.9500 0.000 0.9500 1.000
60 0.9667 0.000 0.9667 1.000
61 0.9833 0.000 0.9833 1.000
62 1.0000 0.000 1.0000 1.000
```

Listing B.2: Nodal points stored along the walls.

Appendix C

Bumpy Microchannel Case

C.1 FLOW File

```
1 100      40
2 8.935e-7 9.97e-7
3 403.28   0.
4 0.5     0.15  0.01
5 360000
```

Listing C.1: Parameters stored by the user.

C.2 GEOM Files

C.2.1 Curvature of bumps: no bumps

```
1 'NoBumpy - a0'  
2 0.00000 0.00000 0.00000 0.60000  
3 0.05000 0.01458 0.05000 0.58542  
4 0.10000 0.02917 0.10000 0.57083  
5 0.15000 0.04375 0.15000 0.55625  
6 0.20000 0.05833 0.20000 0.54167  
7 0.25000 0.07292 0.25000 0.52708  
8 0.30000 0.08750 0.30000 0.51250  
9 0.35000 0.10208 0.35000 0.49792  
10 0.40000 0.11667 0.40000 0.48333  
11 0.45000 0.13125 0.45000 0.46875  
12 0.50000 0.14583 0.50000 0.45417  
13 0.55000 0.16042 0.55000 0.43958  
14 0.60000 0.17500 0.60000 0.42500  
15 0.65000 0.17500 0.65000 0.42500  
16 0.70000 0.17500 0.70000 0.42500  
17 0.75000 0.17500 0.75000 0.42500  
18 0.80000 0.17500 0.80000 0.42500  
19 0.85000 0.17500 0.85000 0.42500  
20 0.90000 0.17500 0.90000 0.42500  
21 0.95000 0.17500 0.95000 0.42500  
22 1.00000 0.17500 1.00000 0.42500  
23 1.05000 0.17500 1.05000 0.42500  
24 1.10000 0.17500 1.10000 0.42500  
25 1.15000 0.17500 1.15000 0.42500  
26 1.20000 0.17500 1.20000 0.42500  
27 1.25000 0.17500 1.25000 0.42500  
28 1.30000 0.17500 1.30000 0.42500  
29 1.35000 0.17500 1.35000 0.42500  
30 1.40000 0.17500 1.40000 0.42500  
31 1.45000 0.17500 1.45000 0.42500  
32 1.50000 0.17500 1.50000 0.42500  
33 1.55000 0.17500 1.55000 0.42500
```

```
34 1.60000 0.17500 1.60000 0.42500
35 1.65000 0.17500 1.65000 0.42500
36 1.70000 0.17500 1.70000 0.42500
37 1.75000 0.17500 1.75000 0.42500
38 1.80000 0.17500 1.80000 0.42500
39 1.85000 0.17500 1.85000 0.42500
40 1.90000 0.17500 1.90000 0.42500
41 1.95000 0.17500 1.95000 0.42500
42 2.00000 0.17500 2.00000 0.42500
43 2.05000 0.17500 2.05000 0.42500
44 2.10000 0.17500 2.10000 0.42500
45 2.15000 0.17500 2.15000 0.42500
46 2.20000 0.17500 2.20000 0.42500
47 2.25000 0.17500 2.25000 0.42500
48 2.30000 0.17500 2.30000 0.42500
49 2.35000 0.17500 2.35000 0.42500
50 2.40000 0.17500 2.40000 0.42500
51 2.45000 0.17500 2.45000 0.42500
52 2.50000 0.17500 2.50000 0.42500
53 2.55000 0.17500 2.55000 0.42500
54 2.60000 0.17500 2.60000 0.42500
55 2.65000 0.17500 2.65000 0.42500
56 2.70000 0.17500 2.70000 0.42500
57 2.75000 0.17500 2.75000 0.42500
58 2.80000 0.17500 2.80000 0.42500
59 2.85000 0.17500 2.85000 0.42500
60 2.90000 0.17500 2.90000 0.42500
61 2.95000 0.17500 2.95000 0.42500
62 3.00000 0.17500 3.00000 0.42500
```

Listing C.2: Nodal points stored along the walls.

C.2.2 Curvature of bumps: $\alpha = 1$

```
1 'Bumpy - a 1'  
2 0.00000 0.00000 0.00000 0.60000  
3 0.05000 0.01458 0.05000 0.58542  
4 0.10000 0.02917 0.10000 0.57083  
5 0.15000 0.04375 0.15000 0.55625  
6 0.20000 0.05833 0.20000 0.54167  
7 0.25000 0.07292 0.25000 0.52708  
8 0.30000 0.08750 0.30000 0.51250  
9 0.35000 0.10208 0.35000 0.49792  
10 0.40000 0.11667 0.40000 0.48333  
11 0.45000 0.13125 0.45000 0.46875  
12 0.50000 0.14583 0.50000 0.45417  
13 0.55000 0.16042 0.55000 0.43958  
14 0.60000 0.17500 0.60000 0.42500  
15 0.62625 0.19059 0.62625 0.40941  
16 0.65250 0.20550 0.65250 0.39450  
17 0.67875 0.21908 0.67875 0.38092  
18 0.70500 0.23073 0.70500 0.36927  
19 0.73125 0.23995 0.73125 0.36005  
20 0.75750 0.24633 0.75750 0.35367  
21 0.78375 0.24959 0.78375 0.35041  
22 0.81000 0.24959 0.81000 0.35041  
23 0.83625 0.24633 0.83625 0.35367  
24 0.86250 0.23995 0.86250 0.36005  
25 0.88875 0.23074 0.88875 0.36926  
26 0.91500 0.21909 0.91500 0.38091  
27 0.94125 0.20551 0.94125 0.39449  
28 0.96750 0.19060 0.96750 0.40940  
29 0.99375 0.17501 0.99375 0.42499  
30 1.02000 0.17500 1.02000 0.42500  
31 1.04625 0.19059 1.04625 0.40941  
32 1.07250 0.20550 1.07250 0.39450  
33 1.09875 0.21908 1.09875 0.38092  
34 1.12500 0.23073 1.12500 0.36927  
35 1.15125 0.23995 1.15125 0.36005  
36 1.17750 0.24633 1.17750 0.35367
```

| | | | | |
|----|---------|---------|---------|---------|
| 37 | 1.20375 | 0.24959 | 1.20375 | 0.35041 |
| 38 | 1.23000 | 0.24959 | 1.23000 | 0.35041 |
| 39 | 1.25625 | 0.24633 | 1.25625 | 0.35367 |
| 40 | 1.28250 | 0.23995 | 1.28250 | 0.36005 |
| 41 | 1.30875 | 0.23074 | 1.30875 | 0.36926 |
| 42 | 1.33500 | 0.21909 | 1.33500 | 0.38091 |
| 43 | 1.36125 | 0.20551 | 1.36125 | 0.39449 |
| 44 | 1.38750 | 0.19060 | 1.38750 | 0.40940 |
| 45 | 1.41375 | 0.17501 | 1.41375 | 0.42499 |
| 46 | 1.44000 | 0.17500 | 1.44000 | 0.42500 |
| 47 | 1.46625 | 0.19059 | 1.46625 | 0.40941 |
| 48 | 1.49250 | 0.20550 | 1.49250 | 0.39450 |
| 49 | 1.51875 | 0.21908 | 1.51875 | 0.38092 |
| 50 | 1.54500 | 0.23073 | 1.54500 | 0.36927 |
| 51 | 1.57125 | 0.23995 | 1.57125 | 0.36005 |
| 52 | 1.59750 | 0.24633 | 1.59750 | 0.35367 |
| 53 | 1.62375 | 0.24959 | 1.62375 | 0.35041 |
| 54 | 1.65000 | 0.24959 | 1.65000 | 0.35041 |
| 55 | 1.67625 | 0.24633 | 1.67625 | 0.35367 |
| 56 | 1.70250 | 0.23995 | 1.70250 | 0.36005 |
| 57 | 1.72875 | 0.23074 | 1.72875 | 0.36926 |
| 58 | 1.75500 | 0.21909 | 1.75500 | 0.38091 |
| 59 | 1.78125 | 0.20551 | 1.78125 | 0.39449 |
| 60 | 1.80750 | 0.19060 | 1.80750 | 0.40940 |
| 61 | 1.83375 | 0.17501 | 1.83375 | 0.42499 |
| 62 | 1.86000 | 0.17500 | 1.86000 | 0.42500 |
| 63 | 1.88625 | 0.19059 | 1.88625 | 0.40941 |
| 64 | 1.91250 | 0.20550 | 1.91250 | 0.39450 |
| 65 | 1.93875 | 0.21908 | 1.93875 | 0.38092 |
| 66 | 1.96500 | 0.23073 | 1.96500 | 0.36927 |
| 67 | 1.99125 | 0.23995 | 1.99125 | 0.36005 |
| 68 | 2.01750 | 0.24633 | 2.01750 | 0.35367 |
| 69 | 2.04375 | 0.24959 | 2.04375 | 0.35041 |
| 70 | 2.07000 | 0.24959 | 2.07000 | 0.35041 |
| 71 | 2.09625 | 0.24633 | 2.09625 | 0.35367 |
| 72 | 2.12250 | 0.23995 | 2.12250 | 0.36005 |
| 73 | 2.14875 | 0.23074 | 2.14875 | 0.36926 |
| 74 | 2.17500 | 0.21909 | 2.17500 | 0.38091 |

```
75 2.20125 0.20551 2.20125 0.39449
76 2.22750 0.19060 2.22750 0.40940
77 2.25375 0.17501 2.25375 0.42499
78 2.28000 0.17500 2.28000 0.42500
79 2.30625 0.19059 2.30625 0.40941
80 2.33250 0.20550 2.33250 0.39450
81 2.35875 0.21908 2.35875 0.38092
82 2.38500 0.23073 2.38500 0.36927
83 2.41125 0.23995 2.41125 0.36005
84 2.43750 0.24633 2.43750 0.35367
85 2.46375 0.24959 2.46375 0.35041
86 2.49000 0.24959 2.49000 0.35041
87 2.51625 0.24633 2.51625 0.35367
88 2.54250 0.23995 2.54250 0.36005
89 2.56875 0.23074 2.56875 0.36926
90 2.59500 0.21909 2.59500 0.38091
91 2.62125 0.20551 2.62125 0.39449
92 2.64750 0.19060 2.64750 0.40940
93 2.67375 0.17501 2.67375 0.42499
94 2.70000 0.17500 2.70000 0.42500
95 2.73750 0.17500 2.73750 0.42500
96 2.77500 0.17500 2.77500 0.42500
97 2.81250 0.17500 2.81250 0.42500
98 2.85000 0.17500 2.85000 0.42500
99 2.88750 0.17500 2.88750 0.42500
100 2.92500 0.17500 2.92500 0.42500
101 2.96250 0.17500 2.96250 0.42500
102 3.00000 0.17500 3.00000 0.42500
```

Listing C.3: Nodal points stored along the walls.

C.2.3 Curvature of bumps: $\alpha = 2$

```
1 'Bumpy - a2'  
2 0.00000 0.00000 0.00000 0.60000  
3 0.05000 0.01458 0.05000 0.58542  
4 0.10000 0.02917 0.10000 0.57083  
5 0.15000 0.04375 0.15000 0.55625  
6 0.20000 0.05833 0.20000 0.54167  
7 0.25000 0.07292 0.25000 0.52708  
8 0.30000 0.08750 0.30000 0.51250  
9 0.35000 0.10208 0.35000 0.49792  
10 0.40000 0.11667 0.40000 0.48333  
11 0.45000 0.13125 0.45000 0.46875  
12 0.50000 0.14583 0.50000 0.45417  
13 0.55000 0.16042 0.55000 0.43958  
14 0.60000 0.17500 0.60000 0.42500  
15 0.62625 0.17824 0.62625 0.42176  
16 0.65250 0.18741 0.65250 0.41259  
17 0.67875 0.20091 0.67875 0.39909  
18 0.70500 0.21642 0.70500 0.38358  
19 0.73125 0.23125 0.73125 0.36875  
20 0.75750 0.24284 0.75750 0.35716  
21 0.78375 0.24918 0.78375 0.35082  
22 0.81000 0.24918 0.81000 0.35082  
23 0.83625 0.24284 0.83625 0.35716  
24 0.86250 0.23125 0.86250 0.36875  
25 0.88875 0.21642 0.88875 0.38358  
26 0.91500 0.20092 0.91500 0.39908  
27 0.94125 0.18741 0.94125 0.41259  
28 0.96750 0.17824 0.96750 0.42176  
29 0.99375 0.17500 0.99375 0.42500  
30 1.02000 0.17500 1.02000 0.42500  
31 1.04625 0.17824 1.04625 0.42176  
32 1.07250 0.18741 1.07250 0.41259  
33 1.09875 0.20091 1.09875 0.39909  
34 1.12500 0.21642 1.12500 0.38358  
35 1.15125 0.23125 1.15125 0.36875  
36 1.17750 0.24284 1.17750 0.35716
```

| | | | | |
|----|---------|---------|---------|---------|
| 37 | 1.20375 | 0.24918 | 1.20375 | 0.35082 |
| 38 | 1.23000 | 0.24918 | 1.23000 | 0.35082 |
| 39 | 1.25625 | 0.24284 | 1.25625 | 0.35716 |
| 40 | 1.28250 | 0.23125 | 1.28250 | 0.36875 |
| 41 | 1.30875 | 0.21642 | 1.30875 | 0.38358 |
| 42 | 1.33500 | 0.20092 | 1.33500 | 0.39908 |
| 43 | 1.36125 | 0.18741 | 1.36125 | 0.41259 |
| 44 | 1.38750 | 0.17824 | 1.38750 | 0.42176 |
| 45 | 1.41375 | 0.17500 | 1.41375 | 0.42500 |
| 46 | 1.44000 | 0.17500 | 1.44000 | 0.42500 |
| 47 | 1.46625 | 0.17824 | 1.46625 | 0.42176 |
| 48 | 1.49250 | 0.18741 | 1.49250 | 0.41259 |
| 49 | 1.51875 | 0.20091 | 1.51875 | 0.39909 |
| 50 | 1.54500 | 0.21642 | 1.54500 | 0.38358 |
| 51 | 1.57125 | 0.23125 | 1.57125 | 0.36875 |
| 52 | 1.59750 | 0.24284 | 1.59750 | 0.35716 |
| 53 | 1.62375 | 0.24918 | 1.62375 | 0.35082 |
| 54 | 1.65000 | 0.24918 | 1.65000 | 0.35082 |
| 55 | 1.67625 | 0.24284 | 1.67625 | 0.35716 |
| 56 | 1.70250 | 0.23125 | 1.70250 | 0.36875 |
| 57 | 1.72875 | 0.21642 | 1.72875 | 0.38358 |
| 58 | 1.75500 | 0.20092 | 1.75500 | 0.39908 |
| 59 | 1.78125 | 0.18741 | 1.78125 | 0.41259 |
| 60 | 1.80750 | 0.17824 | 1.80750 | 0.42176 |
| 61 | 1.83375 | 0.17500 | 1.83375 | 0.42500 |
| 62 | 1.86000 | 0.17500 | 1.86000 | 0.42500 |
| 63 | 1.88625 | 0.17824 | 1.88625 | 0.42176 |
| 64 | 1.91250 | 0.18741 | 1.91250 | 0.41259 |
| 65 | 1.93875 | 0.20091 | 1.93875 | 0.39909 |
| 66 | 1.96500 | 0.21642 | 1.96500 | 0.38358 |
| 67 | 1.99125 | 0.23125 | 1.99125 | 0.36875 |
| 68 | 2.01750 | 0.24284 | 2.01750 | 0.35716 |
| 69 | 2.04375 | 0.24918 | 2.04375 | 0.35082 |
| 70 | 2.07000 | 0.24918 | 2.07000 | 0.35082 |
| 71 | 2.09625 | 0.24284 | 2.09625 | 0.35716 |
| 72 | 2.12250 | 0.23125 | 2.12250 | 0.36875 |
| 73 | 2.14875 | 0.21642 | 2.14875 | 0.38358 |
| 74 | 2.17500 | 0.20092 | 2.17500 | 0.39908 |

```
75 2.20125 0.18741 2.20125 0.41259
76 2.22750 0.17824 2.22750 0.42176
77 2.25375 0.17500 2.25375 0.42500
78 2.28000 0.17500 2.28000 0.42500
79 2.30625 0.17824 2.30625 0.42176
80 2.33250 0.18741 2.33250 0.41259
81 2.35875 0.20091 2.35875 0.39909
82 2.38500 0.21642 2.38500 0.38358
83 2.41125 0.23125 2.41125 0.36875
84 2.43750 0.24284 2.43750 0.35716
85 2.46375 0.24918 2.46375 0.35082
86 2.49000 0.24918 2.49000 0.35082
87 2.51625 0.24284 2.51625 0.35716
88 2.54250 0.23125 2.54250 0.36875
89 2.56875 0.21642 2.56875 0.38358
90 2.59500 0.20092 2.59500 0.39908
91 2.62125 0.18741 2.62125 0.41259
92 2.64750 0.17824 2.64750 0.42176
93 2.67375 0.17500 2.67375 0.42500
94 2.70000 0.17500 2.70000 0.42500
95 2.73750 0.17500 2.73750 0.42500
96 2.77500 0.17500 2.77500 0.42500
97 2.81250 0.17500 2.81250 0.42500
98 2.85000 0.17500 2.85000 0.42500
99 2.88750 0.17500 2.88750 0.42500
100 2.92500 0.17500 2.92500 0.42500
101 2.96250 0.17500 2.96250 0.42500
102 3.00000 0.17500 3.00000 0.42500
```

Listing C.4: Nodal points stored along the walls.

C.2.4 Curvature of bumps: $\alpha = 4$

```
1 'Bumpy - a4'  
2 0.00000 0.00000 0.00000 0.60000  
3 0.05000 0.01458 0.05000 0.58542  
4 0.10000 0.02917 0.10000 0.57083  
5 0.15000 0.04375 0.15000 0.55625  
6 0.20000 0.05833 0.20000 0.54167  
7 0.25000 0.07292 0.25000 0.52708  
8 0.30000 0.08750 0.30000 0.51250  
9 0.35000 0.10208 0.35000 0.49792  
10 0.40000 0.11667 0.40000 0.48333  
11 0.45000 0.13125 0.45000 0.46875  
12 0.50000 0.14583 0.50000 0.45417  
13 0.55000 0.16042 0.55000 0.43958  
14 0.60000 0.17500 0.60000 0.42500  
15 0.62625 0.17514 0.62625 0.42486  
16 0.65250 0.17705 0.65250 0.42295  
17 0.67875 0.18395 0.67875 0.41605  
18 0.70500 0.19787 0.70500 0.40213  
19 0.73125 0.21718 0.73125 0.38282  
20 0.75750 0.23636 0.75750 0.36364  
21 0.78375 0.24837 0.78375 0.35163  
22 0.81000 0.24837 0.81000 0.35163  
23 0.83625 0.23636 0.83625 0.36364  
24 0.86250 0.21719 0.86250 0.38281  
25 0.88875 0.19788 0.88875 0.40212  
26 0.91500 0.18396 0.91500 0.41604  
27 0.94125 0.17705 0.94125 0.42295  
28 0.96750 0.17514 0.96750 0.42486  
29 0.99375 0.17500 0.99375 0.42500  
30 1.02000 0.17500 1.02000 0.42500  
31 1.04625 0.17514 1.04625 0.42486  
32 1.07250 0.17705 1.07250 0.42295  
33 1.09875 0.18395 1.09875 0.41605  
34 1.12500 0.19787 1.12500 0.40213  
35 1.15125 0.21718 1.15125 0.38282  
36 1.17750 0.23636 1.17750 0.36364
```

| | | | | |
|----|---------|---------|---------|---------|
| 37 | 1.20375 | 0.24837 | 1.20375 | 0.35163 |
| 38 | 1.23000 | 0.24837 | 1.23000 | 0.35163 |
| 39 | 1.25625 | 0.23636 | 1.25625 | 0.36364 |
| 40 | 1.28250 | 0.21719 | 1.28250 | 0.38281 |
| 41 | 1.30875 | 0.19788 | 1.30875 | 0.40212 |
| 42 | 1.33500 | 0.18396 | 1.33500 | 0.41604 |
| 43 | 1.36125 | 0.17705 | 1.36125 | 0.42295 |
| 44 | 1.38750 | 0.17514 | 1.38750 | 0.42486 |
| 45 | 1.41375 | 0.17500 | 1.41375 | 0.42500 |
| 46 | 1.44000 | 0.17500 | 1.44000 | 0.42500 |
| 47 | 1.46625 | 0.17514 | 1.46625 | 0.42486 |
| 48 | 1.49250 | 0.17705 | 1.49250 | 0.42295 |
| 49 | 1.51875 | 0.18395 | 1.51875 | 0.41605 |
| 50 | 1.54500 | 0.19787 | 1.54500 | 0.40213 |
| 51 | 1.57125 | 0.21718 | 1.57125 | 0.38282 |
| 52 | 1.59750 | 0.23636 | 1.59750 | 0.36364 |
| 53 | 1.62375 | 0.24837 | 1.62375 | 0.35163 |
| 54 | 1.65000 | 0.24837 | 1.65000 | 0.35163 |
| 55 | 1.67625 | 0.23636 | 1.67625 | 0.36364 |
| 56 | 1.70250 | 0.21719 | 1.70250 | 0.38281 |
| 57 | 1.72875 | 0.19788 | 1.72875 | 0.40212 |
| 58 | 1.75500 | 0.18396 | 1.75500 | 0.41604 |
| 59 | 1.78125 | 0.17705 | 1.78125 | 0.42295 |
| 60 | 1.80750 | 0.17514 | 1.80750 | 0.42486 |
| 61 | 1.83375 | 0.17500 | 1.83375 | 0.42500 |
| 62 | 1.86000 | 0.17500 | 1.86000 | 0.42500 |
| 63 | 1.88625 | 0.17514 | 1.88625 | 0.42486 |
| 64 | 1.91250 | 0.17705 | 1.91250 | 0.42295 |
| 65 | 1.93875 | 0.18395 | 1.93875 | 0.41605 |
| 66 | 1.96500 | 0.19787 | 1.96500 | 0.40213 |
| 67 | 1.99125 | 0.21718 | 1.99125 | 0.38282 |
| 68 | 2.01750 | 0.23636 | 2.01750 | 0.36364 |
| 69 | 2.04375 | 0.24837 | 2.04375 | 0.35163 |
| 70 | 2.07000 | 0.24837 | 2.07000 | 0.35163 |
| 71 | 2.09625 | 0.23636 | 2.09625 | 0.36364 |
| 72 | 2.12250 | 0.21719 | 2.12250 | 0.38281 |
| 73 | 2.14875 | 0.19788 | 2.14875 | 0.40212 |
| 74 | 2.17500 | 0.18396 | 2.17500 | 0.41604 |

```
75 2.20125 0.17705 2.20125 0.42295
76 2.22750 0.17514 2.22750 0.42486
77 2.25375 0.17500 2.25375 0.42500
78 2.28000 0.17500 2.28000 0.42500
79 2.30625 0.17514 2.30625 0.42486
80 2.33250 0.17705 2.33250 0.42295
81 2.35875 0.18395 2.35875 0.41605
82 2.38500 0.19787 2.38500 0.40213
83 2.41125 0.21718 2.41125 0.38282
84 2.43750 0.23636 2.43750 0.36364
85 2.46375 0.24837 2.46375 0.35163
86 2.49000 0.24837 2.49000 0.35163
87 2.51625 0.23636 2.51625 0.36364
88 2.54250 0.21719 2.54250 0.38281
89 2.56875 0.19788 2.56875 0.40212
90 2.59500 0.18396 2.59500 0.41604
91 2.62125 0.17705 2.62125 0.42295
92 2.64750 0.17514 2.64750 0.42486
93 2.67375 0.17500 2.67375 0.42500
94 2.70000 0.17500 2.70000 0.42500
95 2.73750 0.17500 2.73750 0.42500
96 2.77500 0.17500 2.77500 0.42500
97 2.81250 0.17500 2.81250 0.42500
98 2.85000 0.17500 2.85000 0.42500
99 2.88750 0.17500 2.88750 0.42500
100 2.92500 0.17500 2.92500 0.42500
101 2.96250 0.17500 2.96250 0.42500
102 3.00000 0.17500 3.00000 0.42500
```

Listing C.5: Nodal points stored along the walls.

C.3 Velocity Fields

C.3.1 Device's width, $d = 250 \mu\text{m}$

C.3.1.1 No bumps, $s = 100 \mu\text{m}$

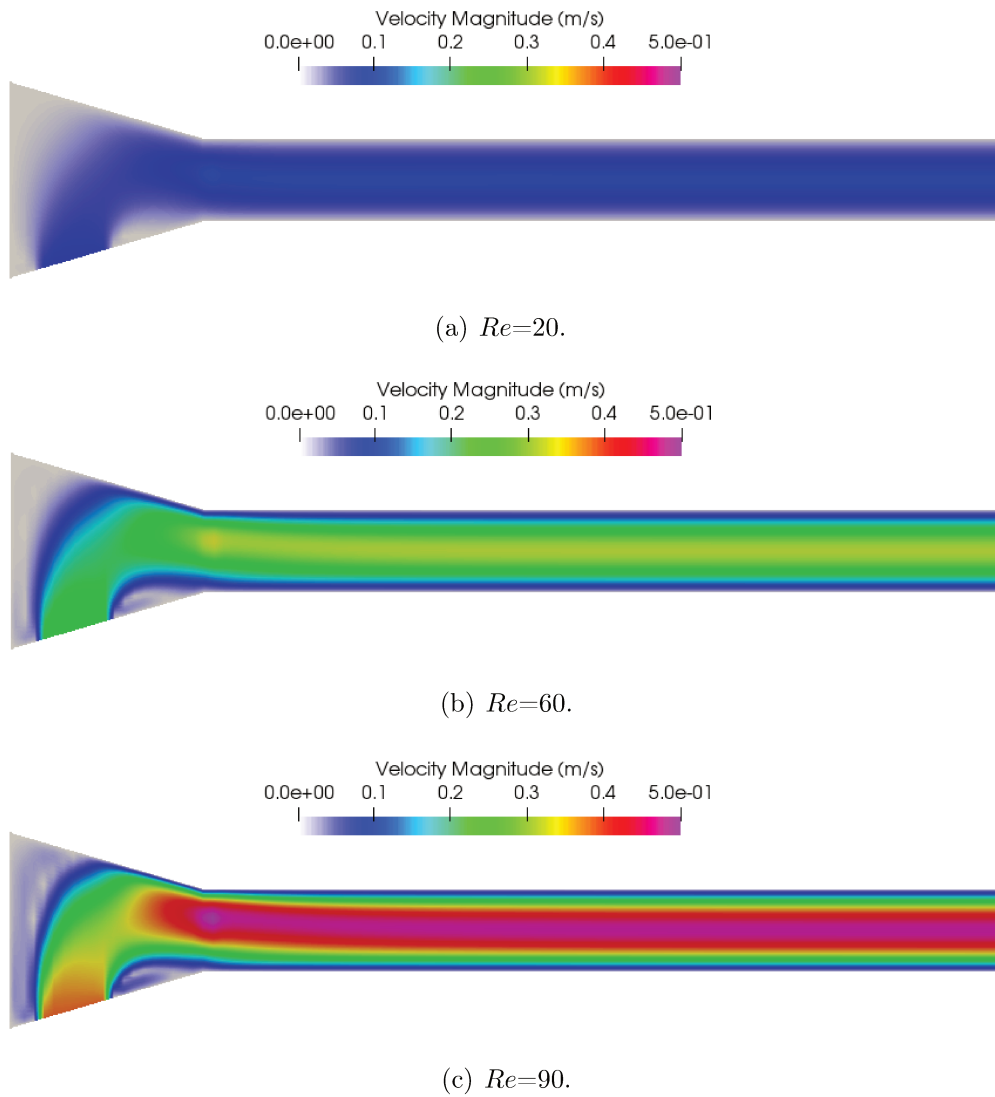
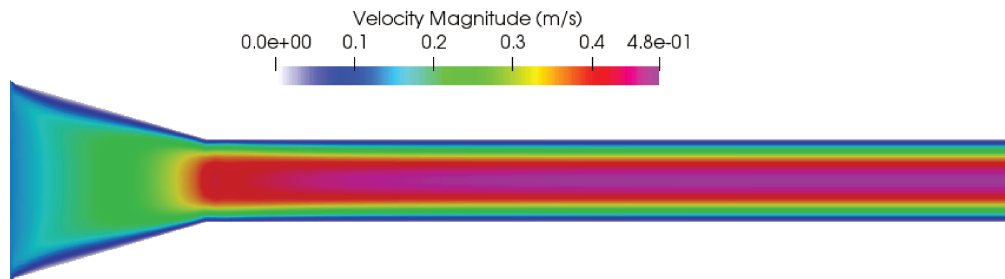
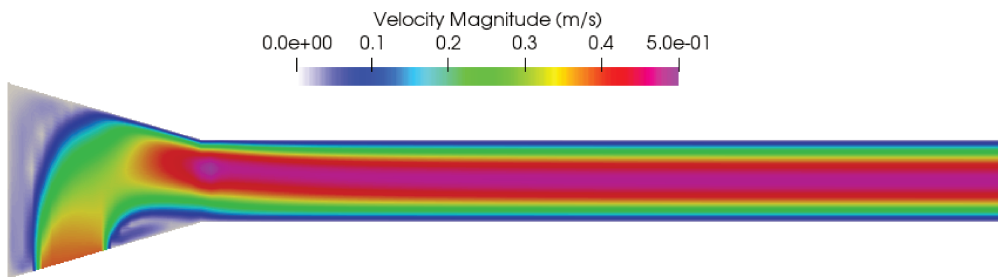


Figure C.1: Magnitude of velocity regarding Reynolds number where $d=250 \mu\text{m}$, $s = 100 \mu\text{m}$ and there is no bumps.

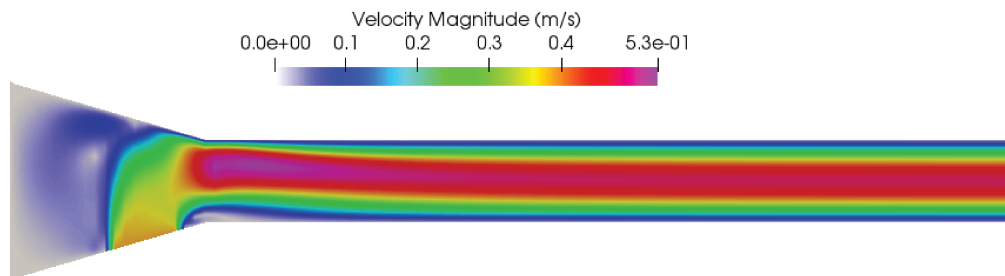
C.3.1.2 No bumps, $Re = 90$



(a) $s=0 \mu\text{m}$.



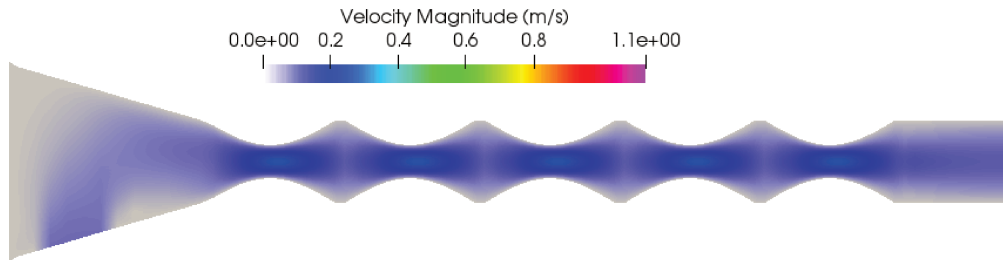
(b) $s=100 \mu\text{m}$.



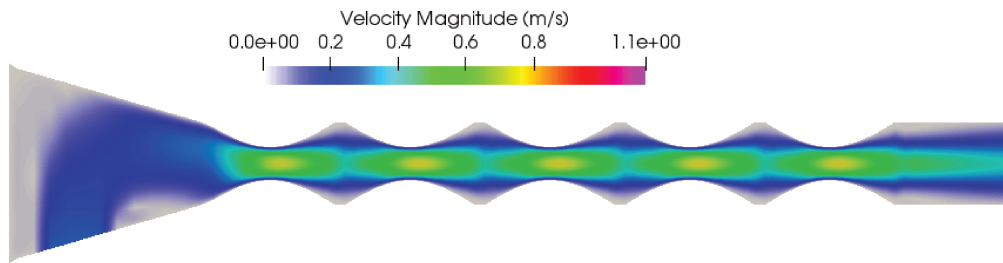
(c) $s=300 \mu\text{m}$.

Figure C.2: Magnitude of velocity regarding the location of the feed where $d=250 \mu\text{m}$, $Re = 90$, and there is no bumps (These figures do not have the same data range).

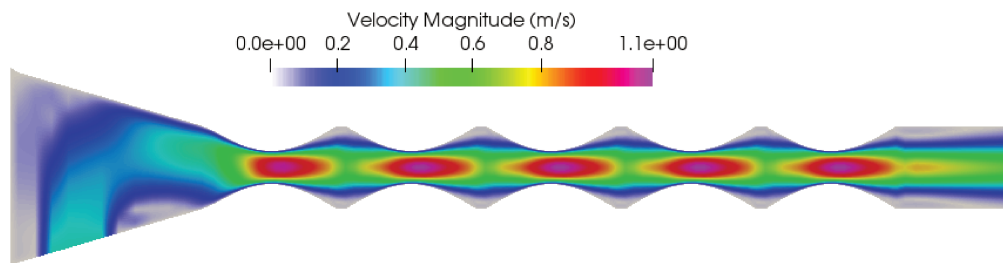
C.3.1.3 Curvature of bumps $\alpha = 1, s = 100 \mu\text{m}$



(a) $Re=20$.



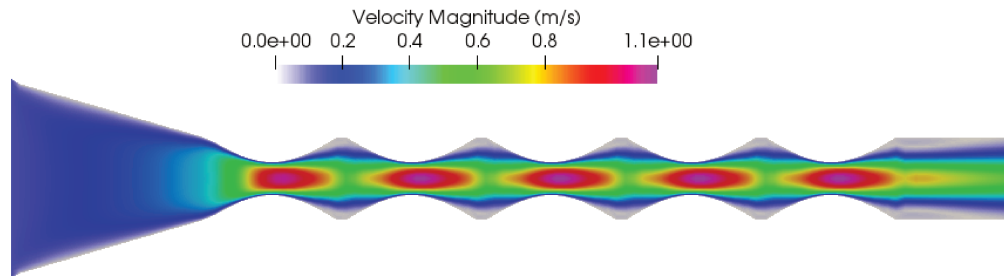
(b) $Re=60$.



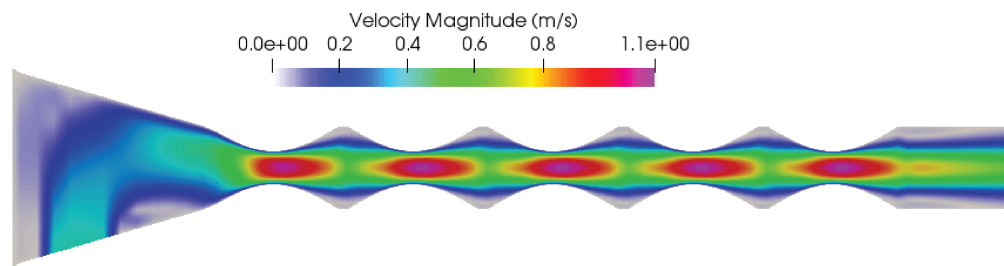
(c) $Re=90$.

Figure C.3: Magnitude of velocity regarding Reynolds number where $d=250 \mu\text{m}$, $s = 100 \mu\text{m}$ and $\alpha = 1$.

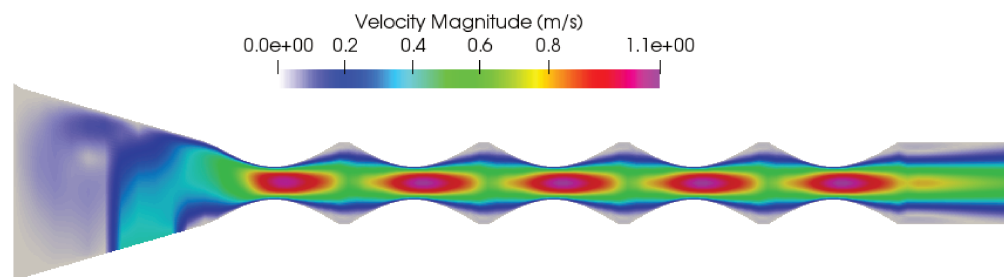
C.3.1.4 Curvature of bumps $\alpha = 1$, $Re = 90$



(a) $s=0 \mu m$.



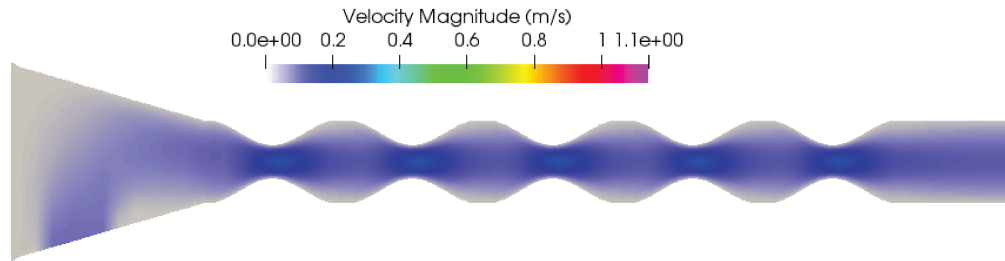
(b) $s=100 \mu m$.



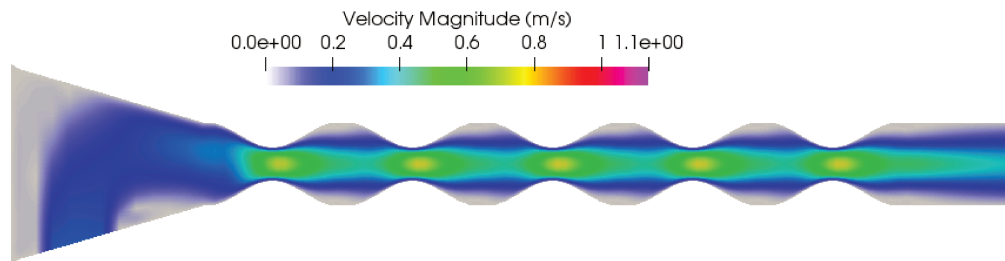
(c) $s=300 \mu m$.

Figure C.4: Magnitude of velocity regarding the location of the feed where $d=250 \mu m$, $\alpha = 1$ and $Re = 90$.

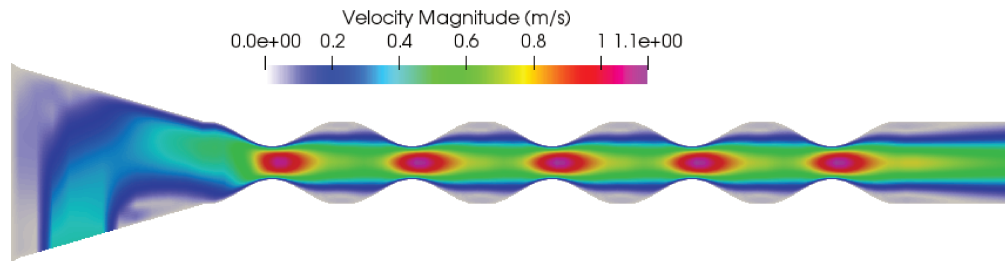
C.3.1.5 Curvature of bumps $\alpha = 2, s = 100 \mu\text{m}$



(a) $Re=20$.



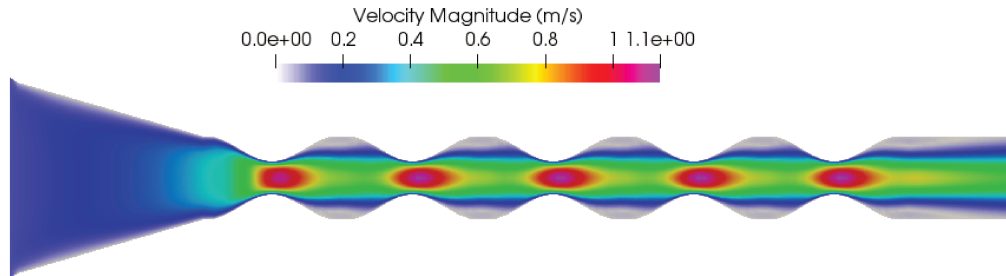
(b) $Re=60$.



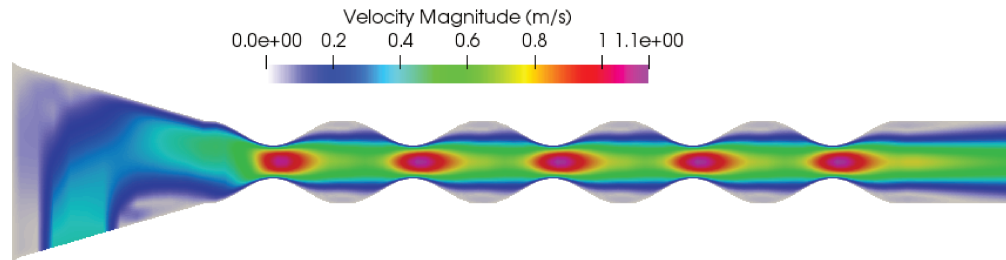
(c) $Re=90$.

Figure C.5: Magnitude of velocity regarding Reynolds number where $d=250 \mu\text{m}$, $s = 100 \mu\text{m}$ and $\alpha = 2$.

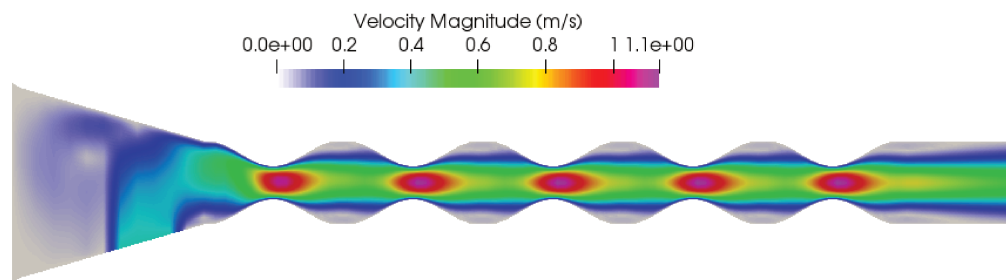
C.3.1.6 Curvature of bumps $\alpha = 2$, $Re = 90$



(a) $s=0 \mu\text{m}$.



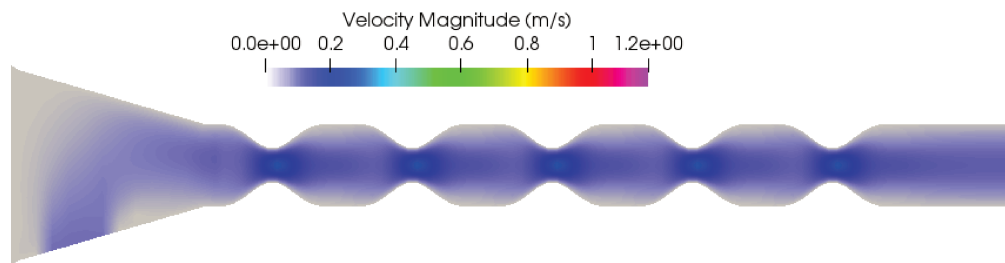
(b) $s=100 \mu\text{m}$.



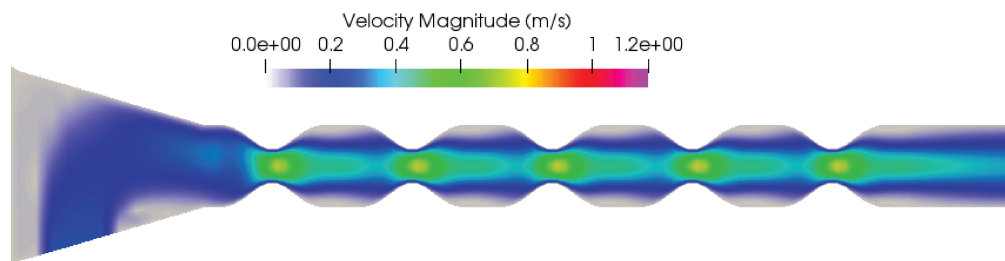
(c) $s=300 \mu\text{m}$.

Figure C.6: Magnitude of velocity regarding the location of the feed where $d=250 \mu\text{m}$, $\alpha = 2$ and $Re = 90$.

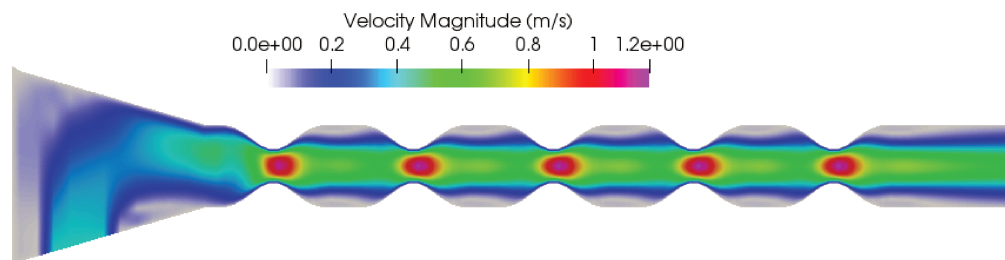
C.3.1.7 Curvature of bumps $\alpha = 4, s = 100 \mu\text{m}$



(a) $Re=20$.



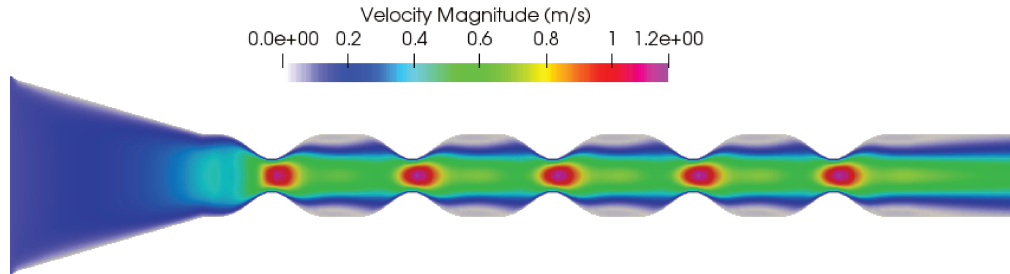
(b) $Re=60$.



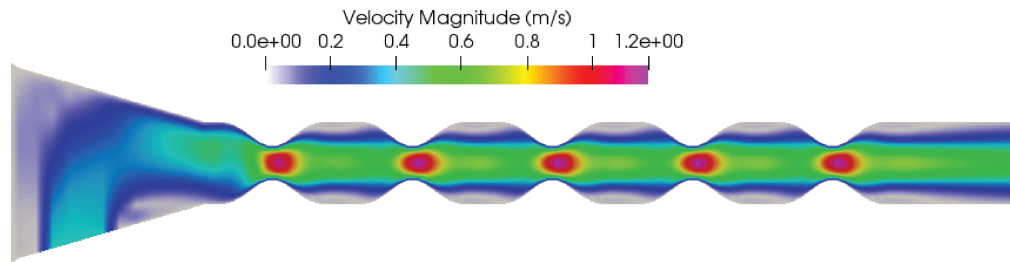
(c) $Re=90$.

Figure C.7: Magnitude of velocity regarding Reynolds number where $d=250 \mu\text{m}$, $s = 100 \mu\text{m}$ and $\alpha = 4$.

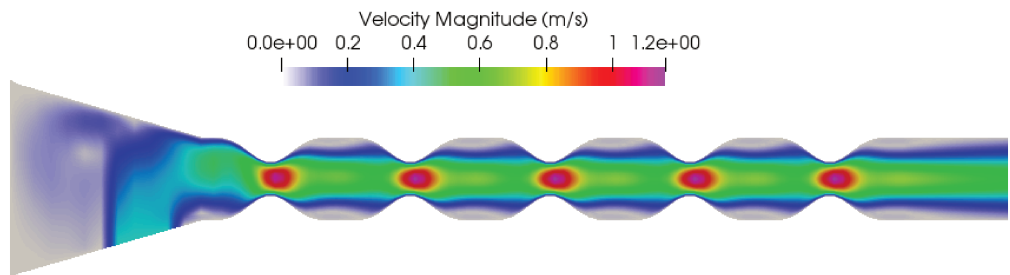
C.3.1.8 Curvature of bumps $\alpha=4$, $Re = 90$



(a) $s=0 \mu m$.



(b) $s=100 \mu m$.

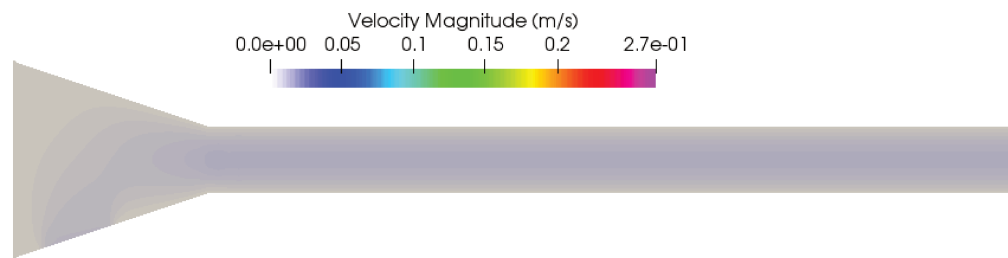


(c) $s=300 \mu m$.

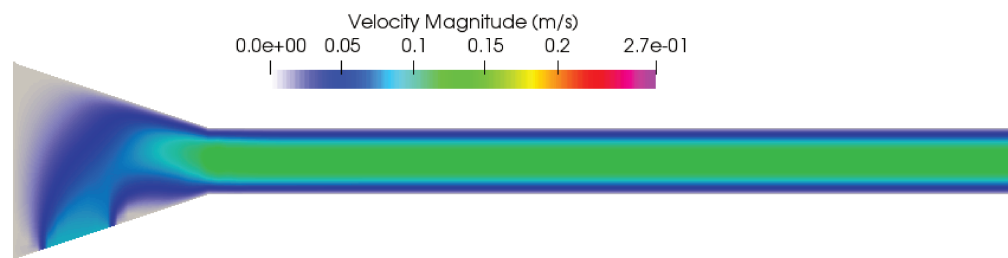
Figure C.8: Magnitude of velocity regarding the location of the feed where $d=250 \mu m$, $\alpha = 4$ and $Re = 90$.

C.3.2 Device's width, $d = 200 \mu\text{m}$

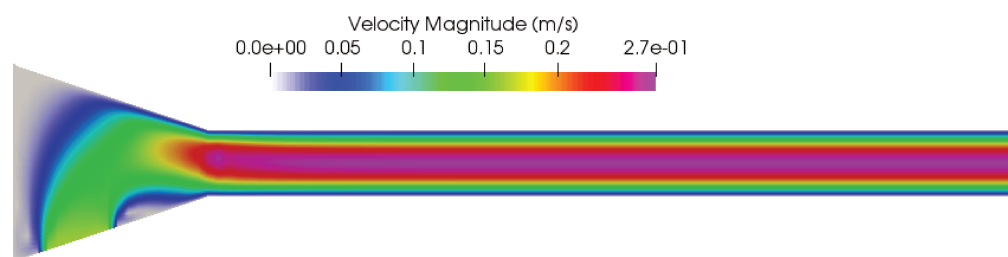
C.3.2.1 No bumps, $s = 100 \mu\text{m}$



(a) $Re=1$.



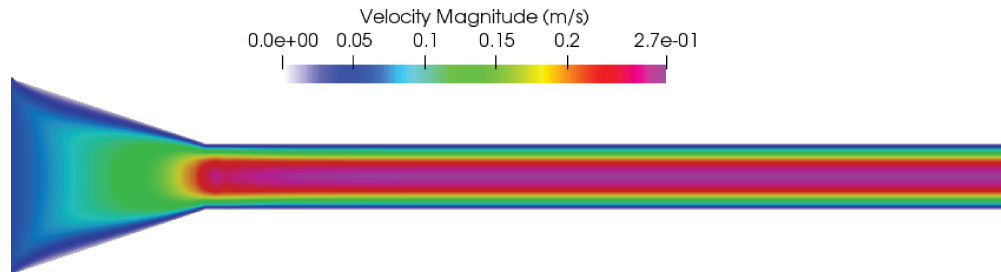
(b) $Re=20$.



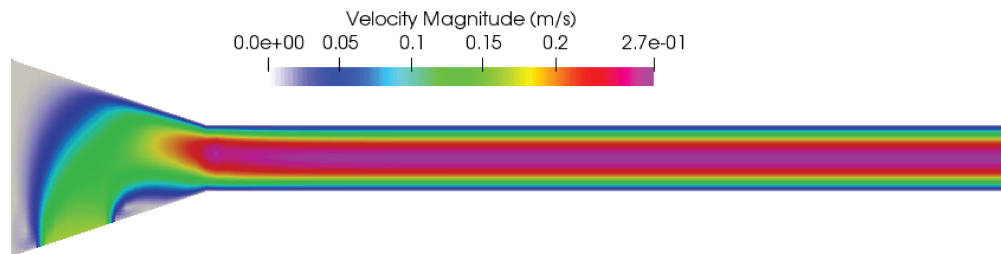
(c) $Re=40$.

Figure C.9: Magnitude of velocity regarding Reynolds number where $d=200 \mu\text{m}$ and $s = 100 \mu\text{m}$.

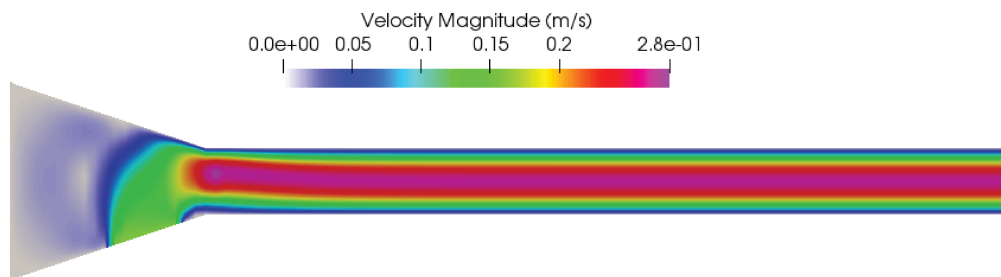
C.3.2.2 No bumps, $Re = 40$



(a) $s=0 \mu m$.



(b) $s=100 \mu m$.



(c) $s=300 \mu m$.

Figure C.10: Magnitude of velocity regarding the location of the feed where $d=200 \mu m$ and $Re = 40$.

C.3.2.3 Curvature of bumps $\alpha = 1, s = 100 \mu\text{m}$

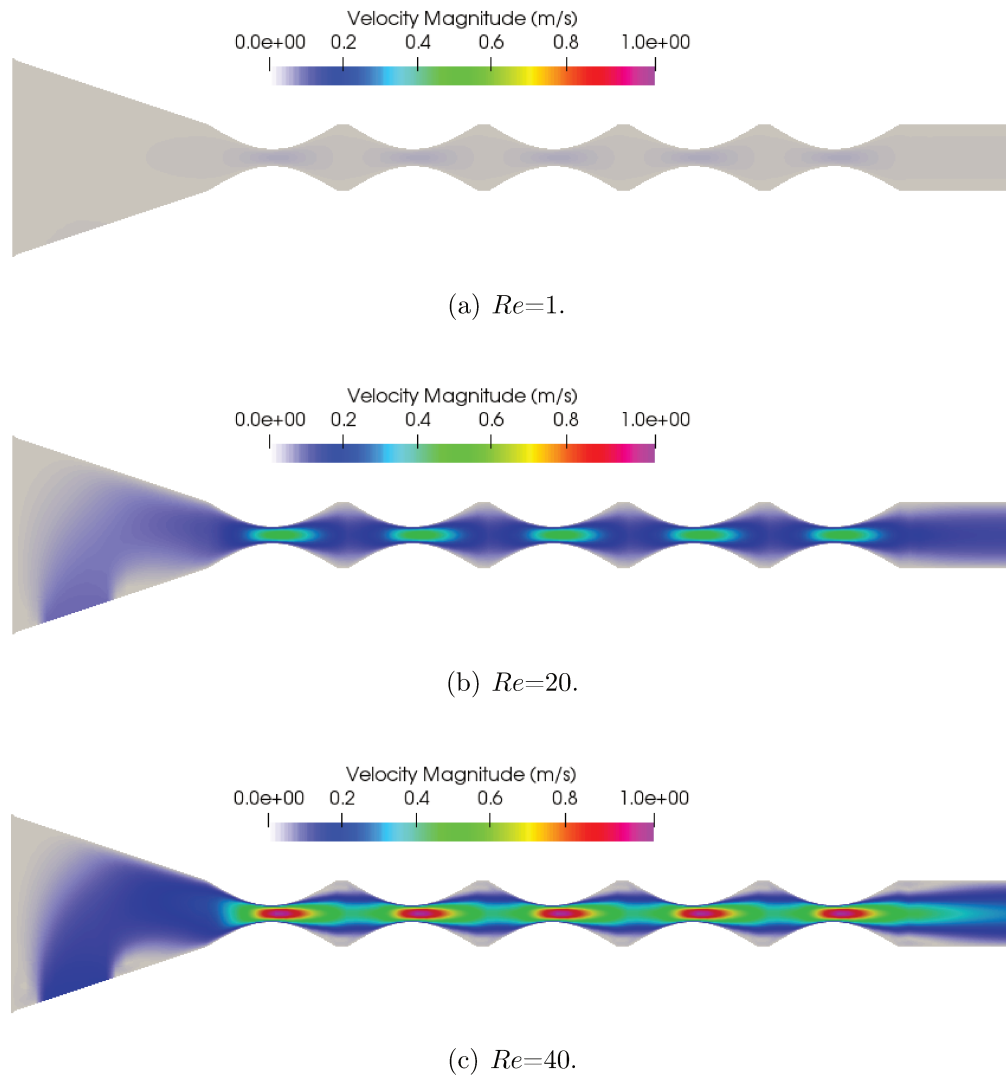
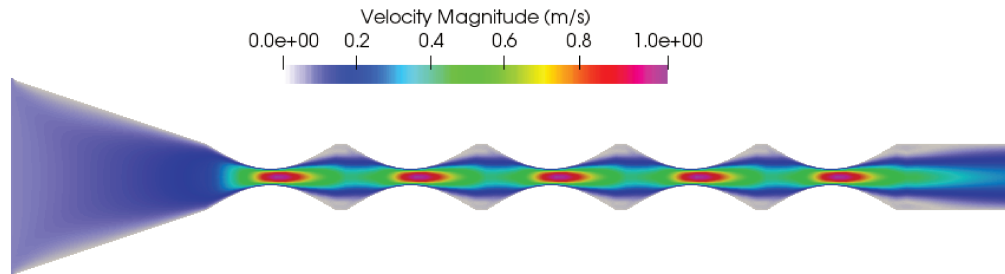
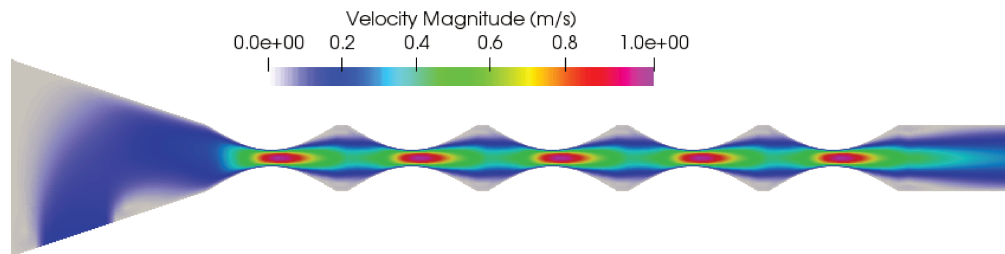


Figure C.11: Magnitude of velocity regarding Reynolds number where $d=200 \mu\text{m}$, $s = 100 \mu\text{m}$ and $\alpha = 1$.

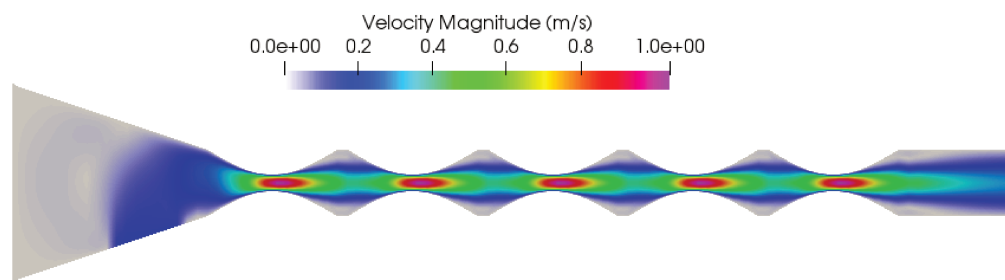
C.3.2.4 Curvature of bumps $\alpha = 1$, $Re = 40$



(a) $s=0 \mu\text{m}$.



(b) $s=100 \mu\text{m}$.



(c) $s=300 \mu\text{m}$.

Figure C.12: Magnitude of velocity regarding the location of the feed where $d=200 \mu\text{m}$, $\alpha = 1$ and $Re = 40$.

C.3.2.5 Curvature of bumps $\alpha = 2, s = 100 \mu\text{m}$

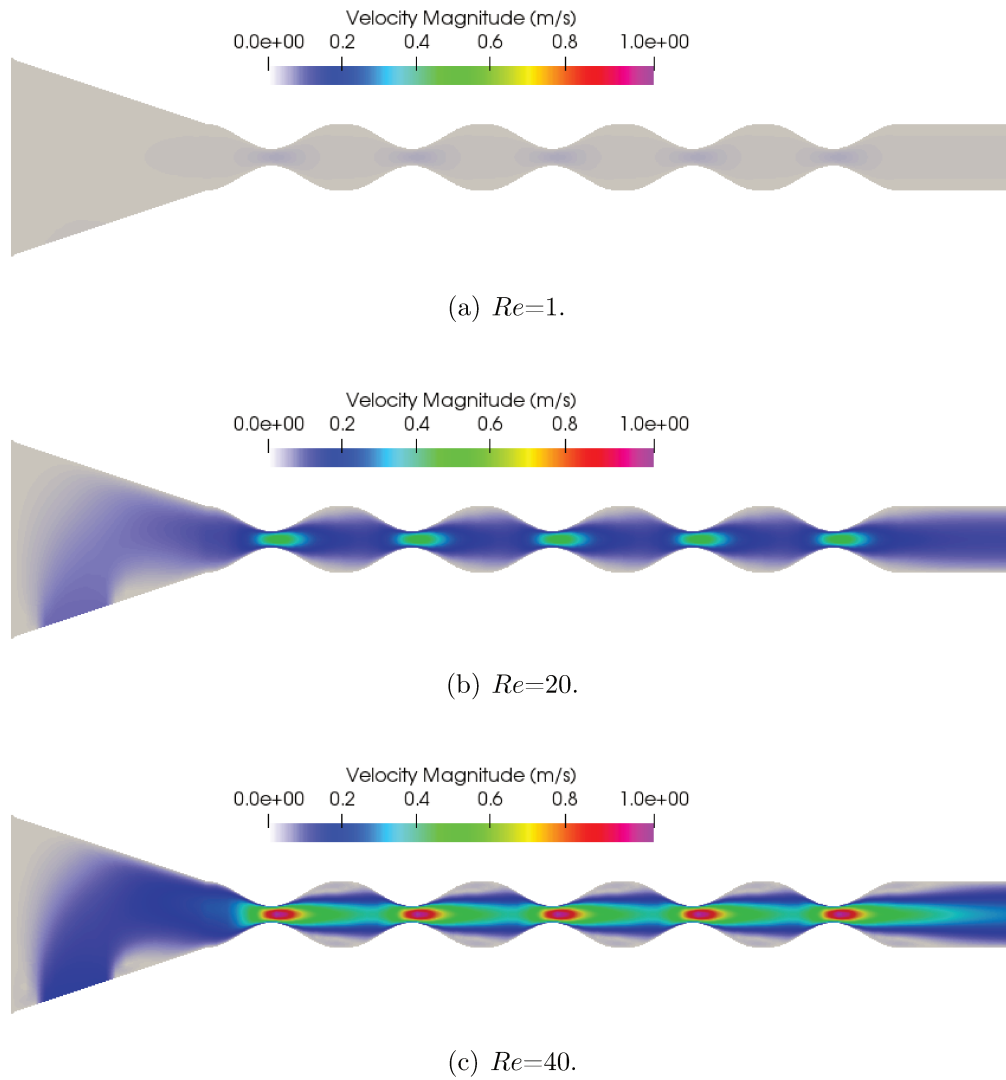
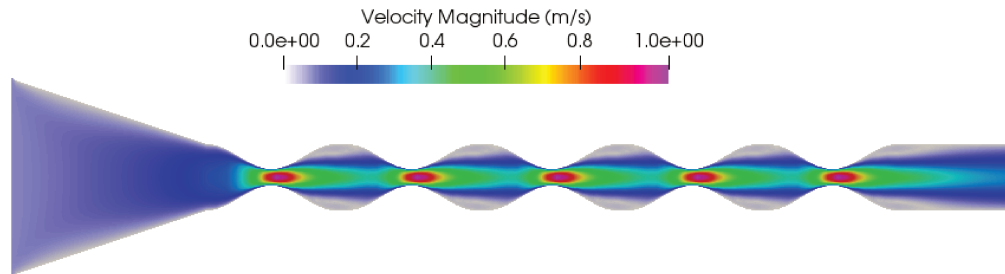
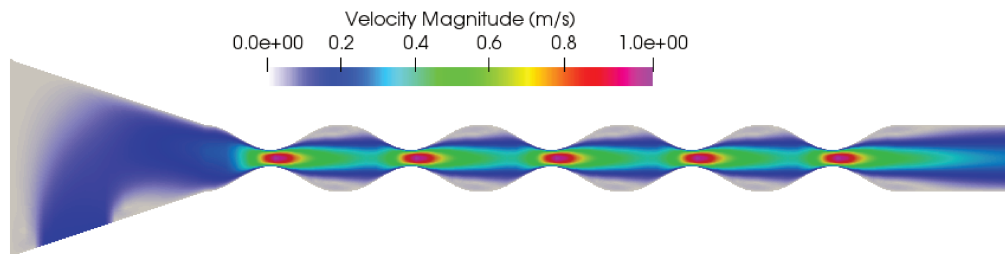


Figure C.13: Magnitude of velocity regarding Reynolds number where $d=200 \mu\text{m}$, $s = 100 \mu\text{m}$ and $\alpha = 2$.

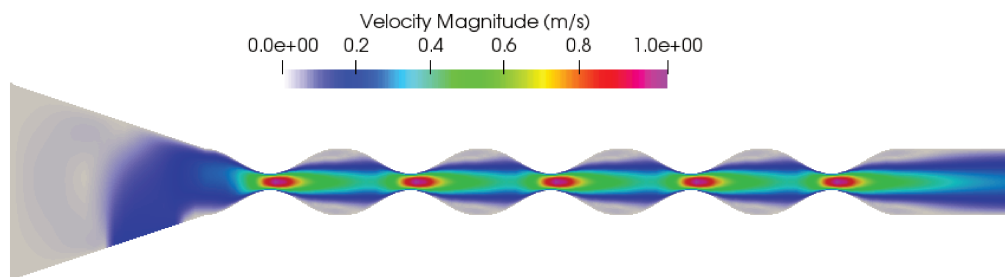
C.3.2.6 Curvature of bumps $\alpha = 2$, $Re = 40$



(a) $s=0 \mu m$.



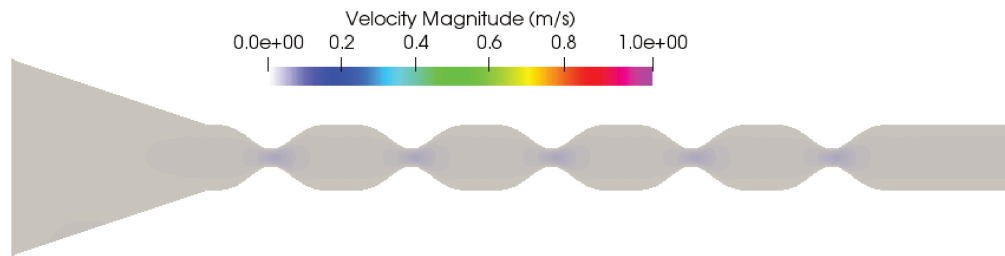
(b) $s=100 \mu m$.



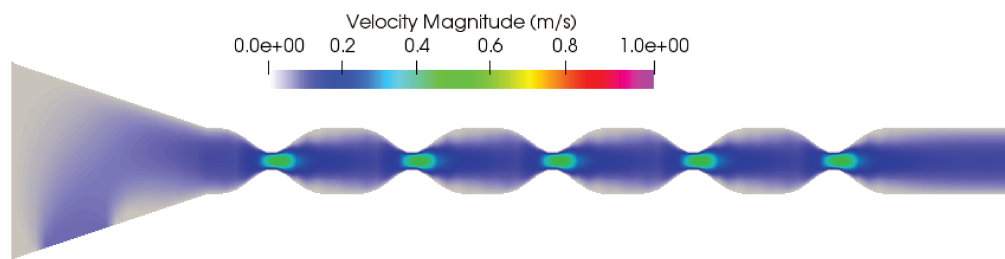
(c) $s=300 \mu m$.

Figure C.14: Magnitude of velocity regarding the location of the feed where $d=200 \mu m$, $\alpha = 2$ and $Re = 40$.

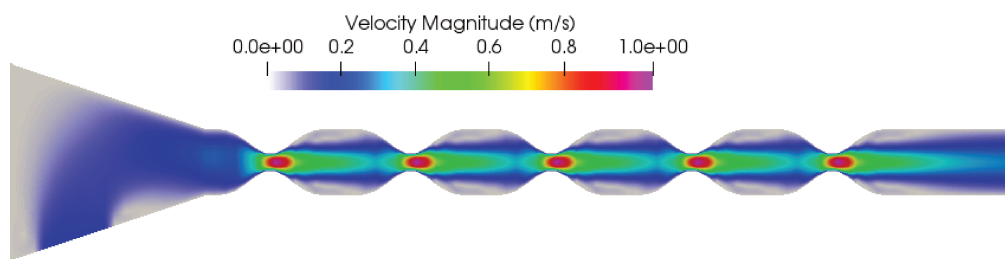
C.3.2.7 Curvature of bumps $\alpha = 4, s = 100 \mu\text{m}$



(a) $Re=1$.



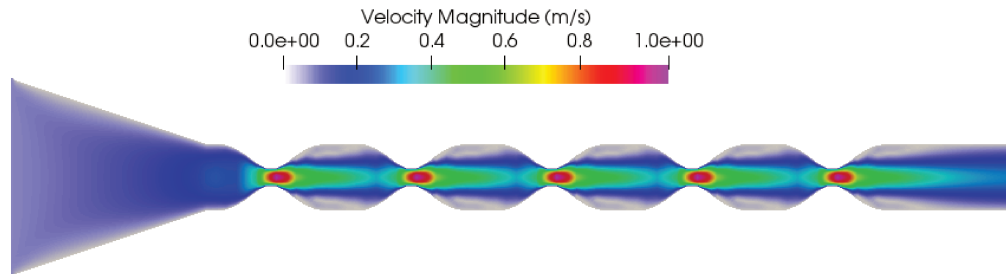
(b) $Re=20$.



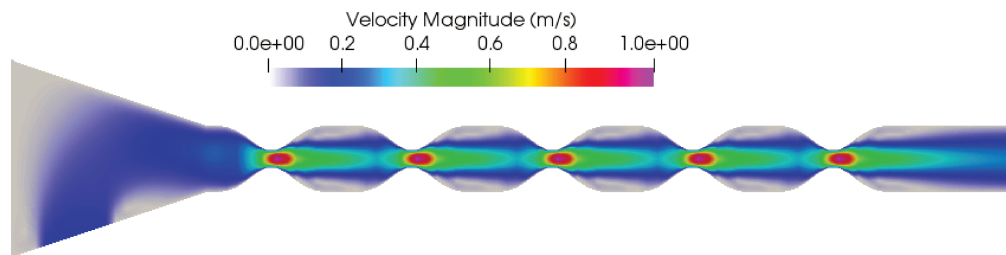
(c) $Re=40$.

Figure C.15: Magnitude of velocity regarding Reynolds number where $d=200 \mu\text{m}$, $s = 100 \mu\text{m}$ and $\alpha = 4$.

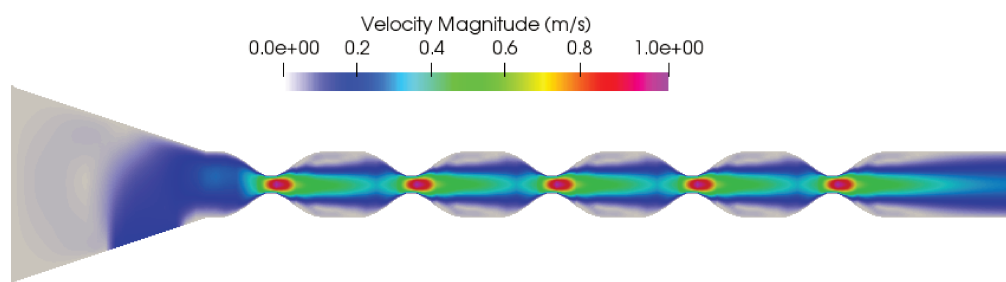
C.3.2.8 Curvature of bumps $\alpha=4$, $Re = 40$



(a) $s=0 \mu m$.



(b) $s=100 \mu m$.



(c) $s=300 \mu m$.

Figure C.16: Magnitude of velocity regarding the location of the feed where $d=200 \mu m$, $\alpha = 4$ and $Re = 40$.

C.4 Pressure Fields

C.4.1 Device's width, $d = 250 \mu\text{m}$

C.4.1.1 No bumps, $s = 100 \mu\text{m}$

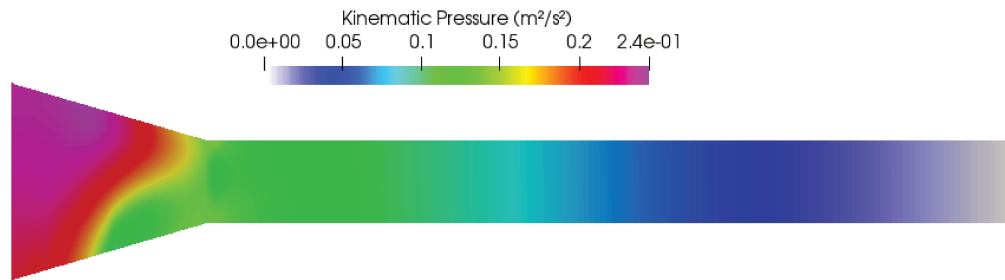
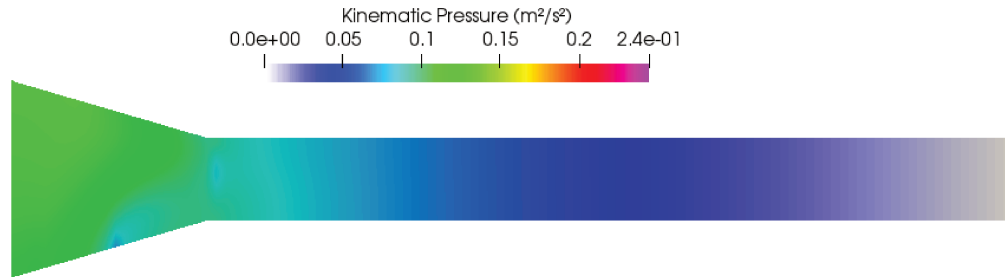
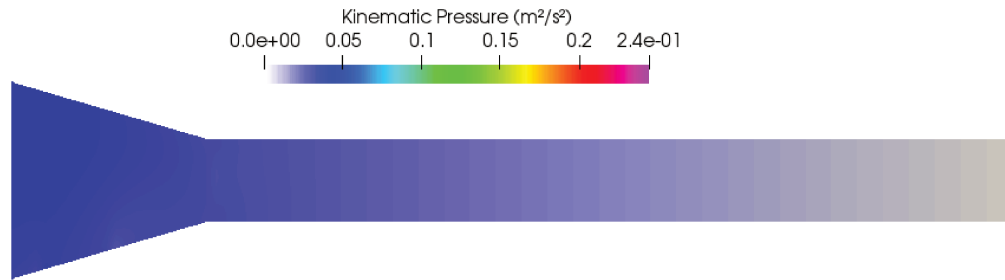
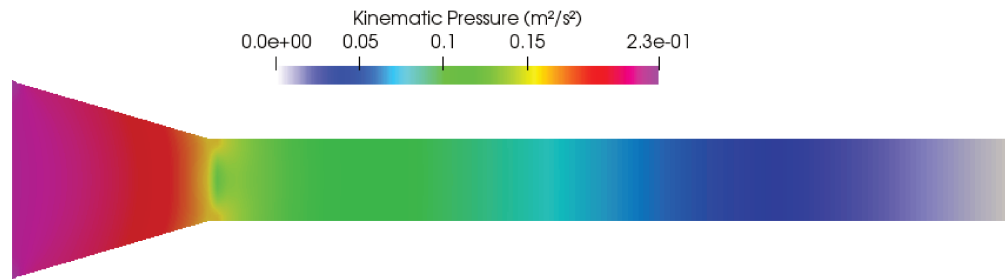
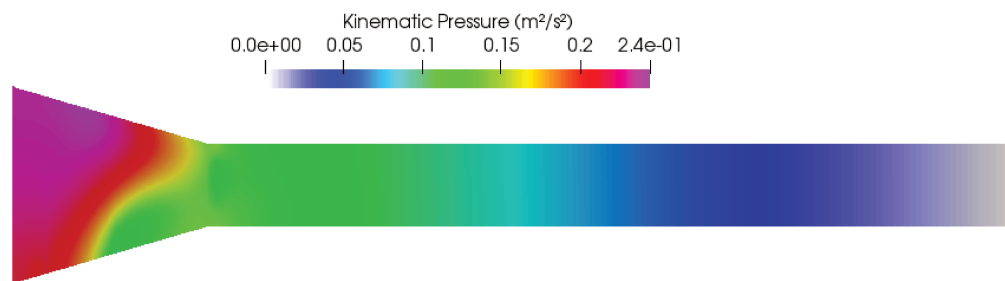


Figure C.17: Pressure field at different Reynolds numbers where $d=250 \mu\text{m}$, and $s = 100 \mu\text{m}$.

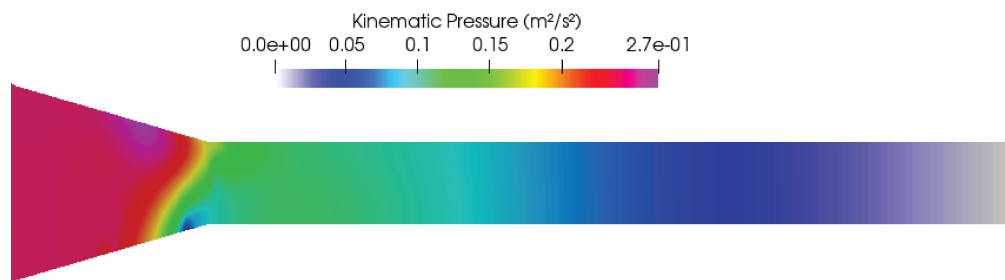
C.4.1.2 No bumps, $Re = 90$



(a) $s=0 \mu m$.



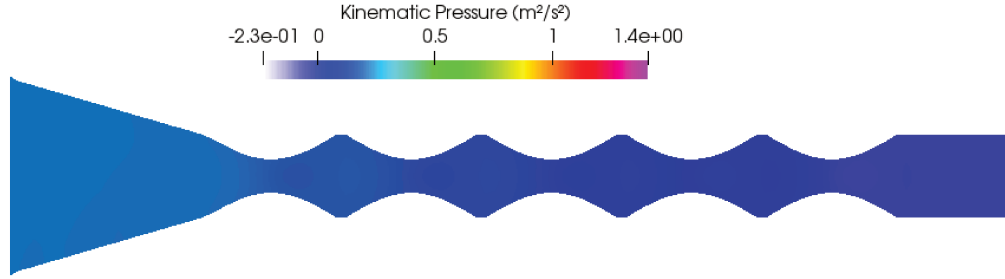
(b) $s=100 \mu m$.



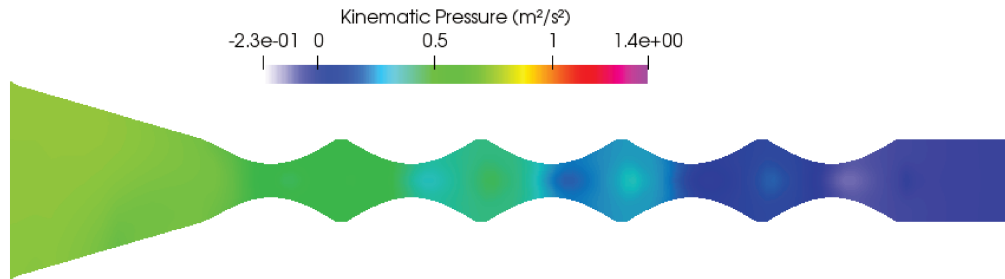
(c) $s=300 \mu m$.

Figure C.18: Pressure field at different inlet locations where $d=250 \mu m$, and $Re = 90$ (These figures do not have the same data range).

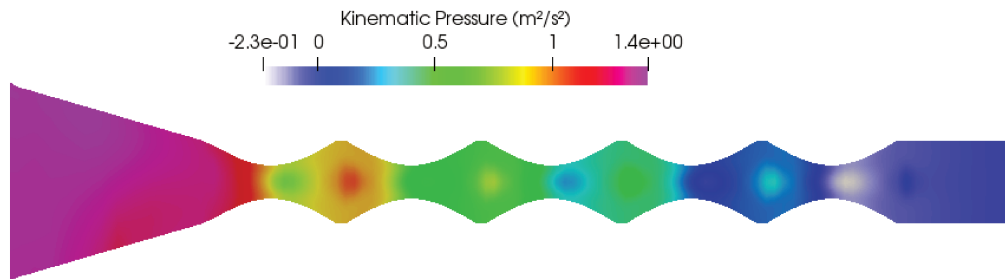
C.4.1.3 Curvature of bumps $\alpha = 1, s = 100 \mu\text{m}$



(a) $Re=20$.



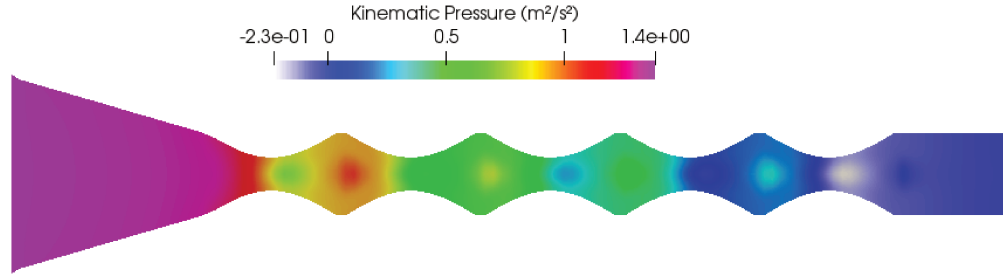
(b) $Re=60$.



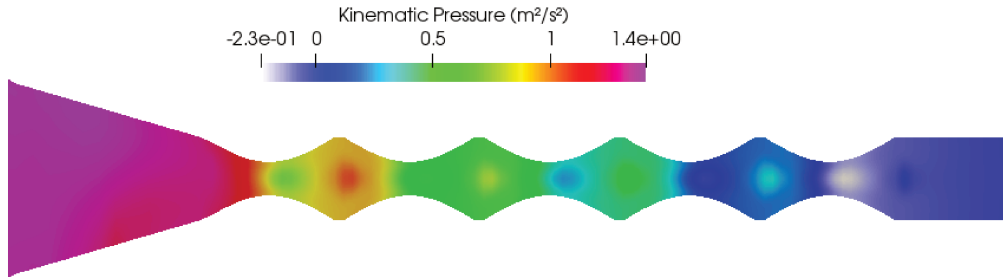
(c) $Re=90$.

Figure C.19: Pressure field at different Reynolds numbers where $d=250 \mu\text{m}$, $s = 100 \mu\text{m}$ and $\alpha = 1$.

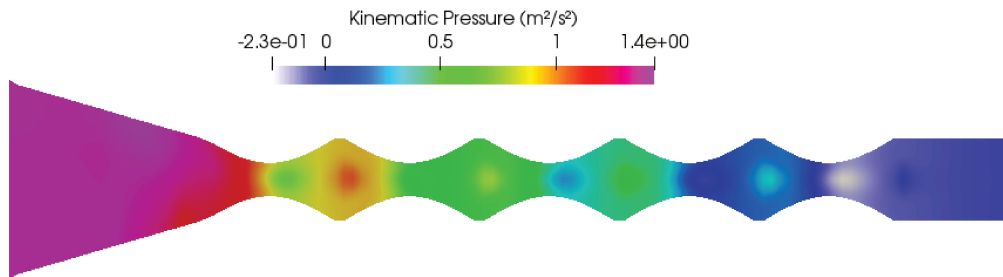
C.4.1.4 Curvature of bumps $\alpha = 1$, $Re = 90$



(a) $s=0 \mu m$.



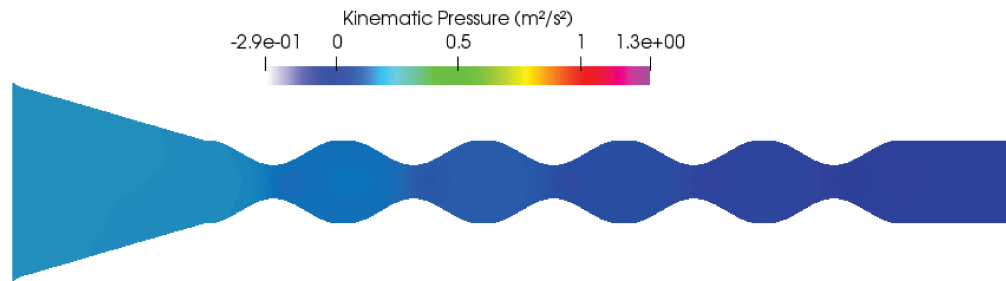
(b) $s=100 \mu m$.



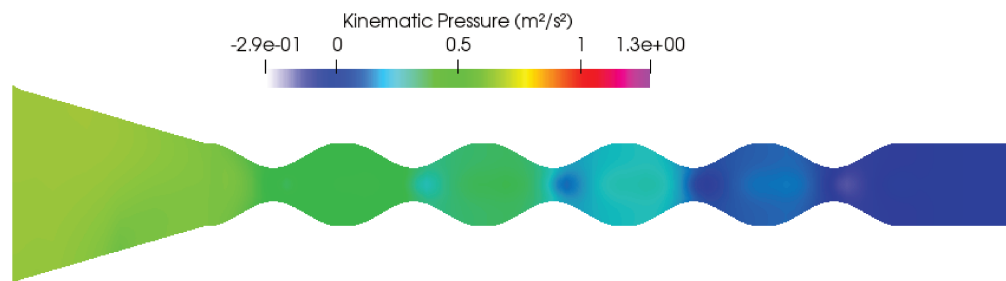
(c) $s=300 \mu m$.

Figure C.20: Pressure field at different inlet locations where $d=250 \mu m$, $\alpha = 1$ and $Re = 90$.

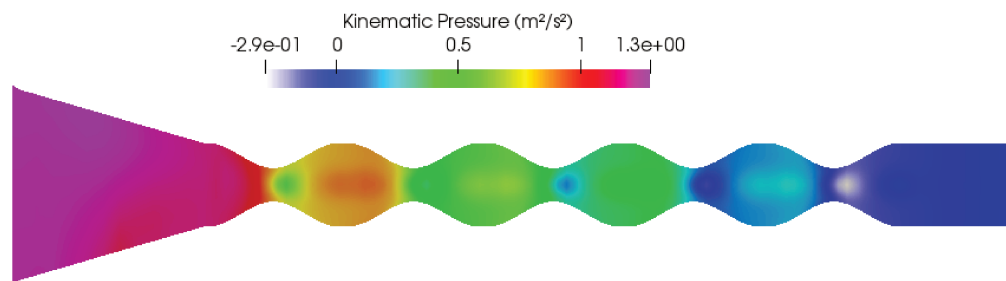
C.4.1.5 Curvature of bumps $\alpha = 2, s = 100 \mu\text{m}$



(a) $Re=20$.



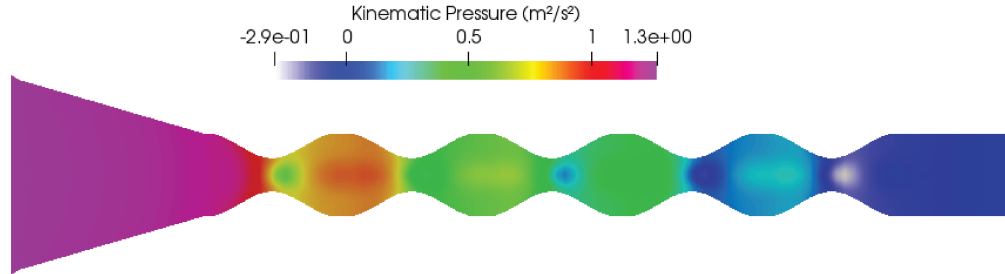
(b) $Re=60$.



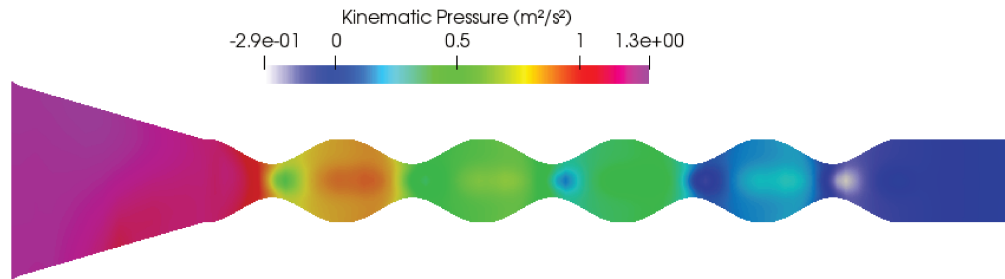
(c) $Re=90$.

Figure C.21: Pressure field at different Reynolds numbers where $d=250 \mu\text{m}$, $s = 100 \mu\text{m}$ and $\alpha = 2$.

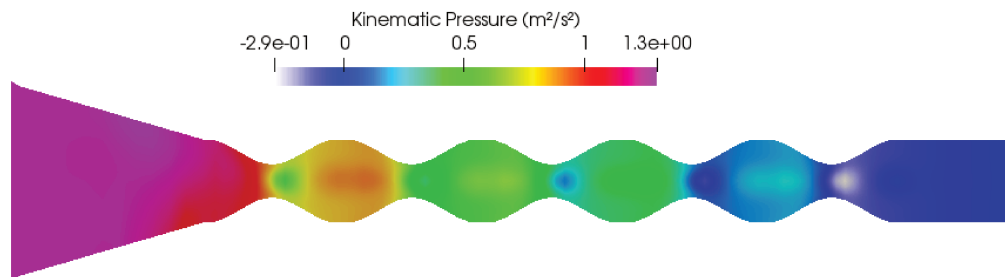
C.4.1.6 Curvature of bumps $\alpha = 2$, $Re = 90$



(a) $s=0 \mu m$.



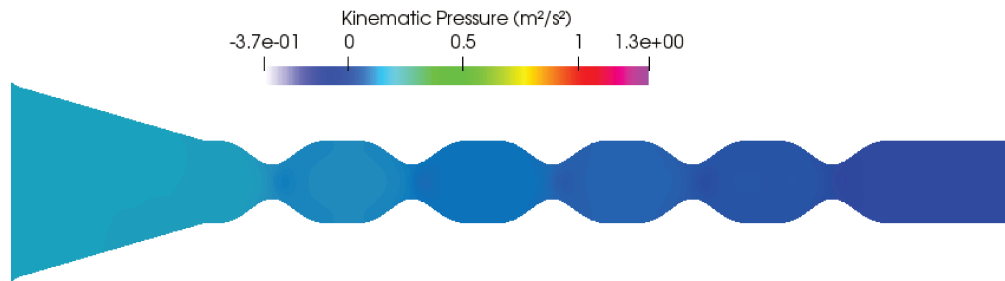
(b) $s=100 \mu m$.



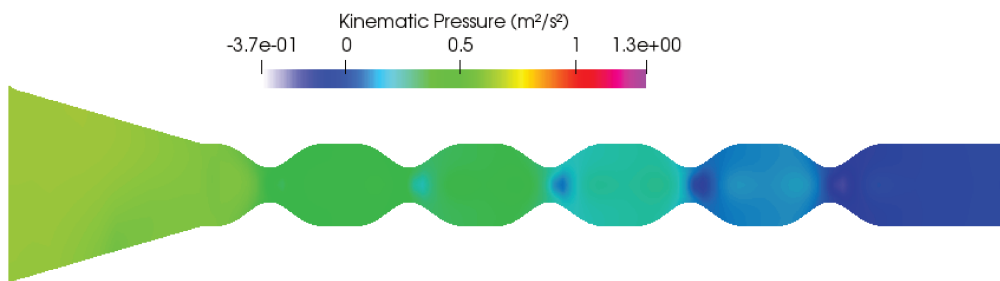
(c) $s=300 \mu m$.

Figure C.22: Pressure field at different locations of feed where $d=250 \mu m$, $\alpha = 2$ and $Re = 90$.

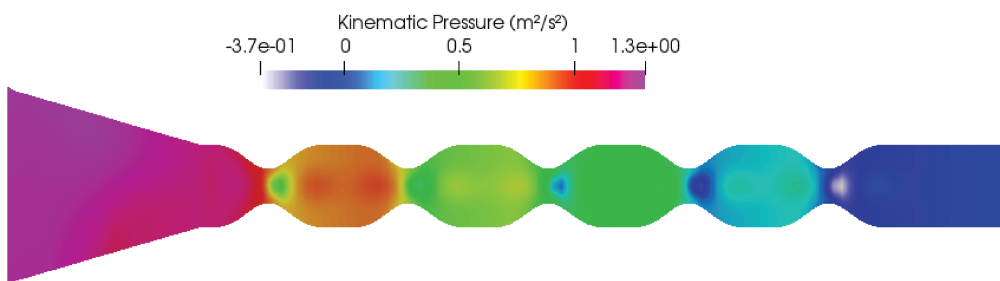
C.4.1.7 Curvature of bumps $\alpha = 4, s = 100 \mu\text{m}$



(a) $Re=20$.



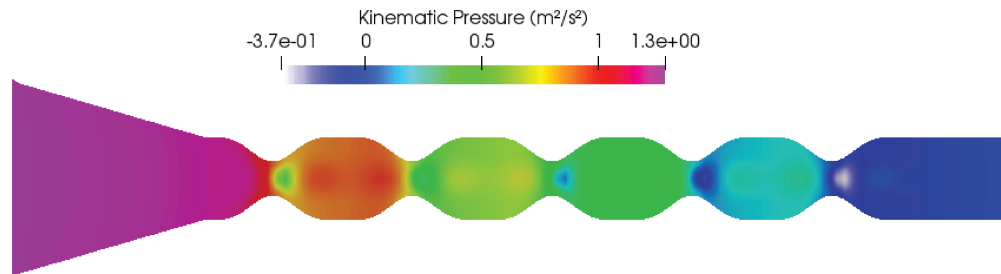
(b) $Re=60$.



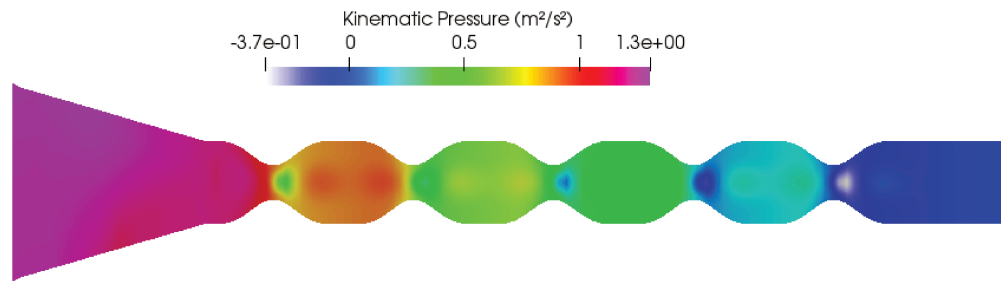
(c) $Re=90$.

Figure C.23: Pressure field at different Reynolds numbers where $d=250 \mu\text{m}$, $s = 100 \mu\text{m}$ and $\alpha = 4$.

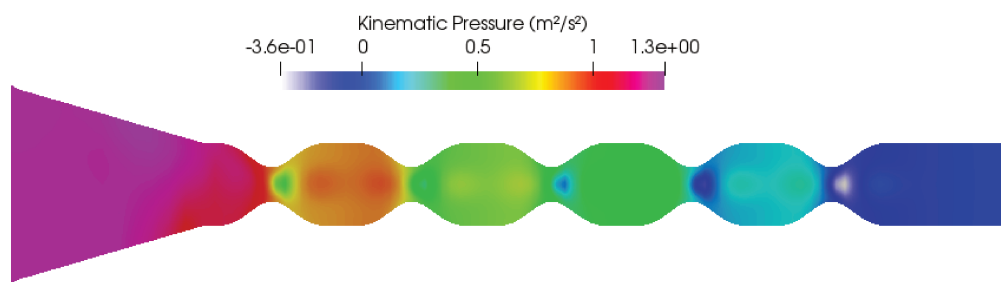
C.4.1.8 Curvature of bumps $\alpha=4$, $Re = 90$



(a) $s=0 \mu m$.



(b) $s=100 \mu m$.



(c) $s=300 \mu m$.

Figure C.24: Pressure field at different locations of feed where $d=250 \mu m$, $\alpha = 4$ and $Re = 90$.

C.4.2 Device's width, $d = 200 \mu\text{m}$

C.4.2.1 No bumps, $s = 100 \mu\text{m}$

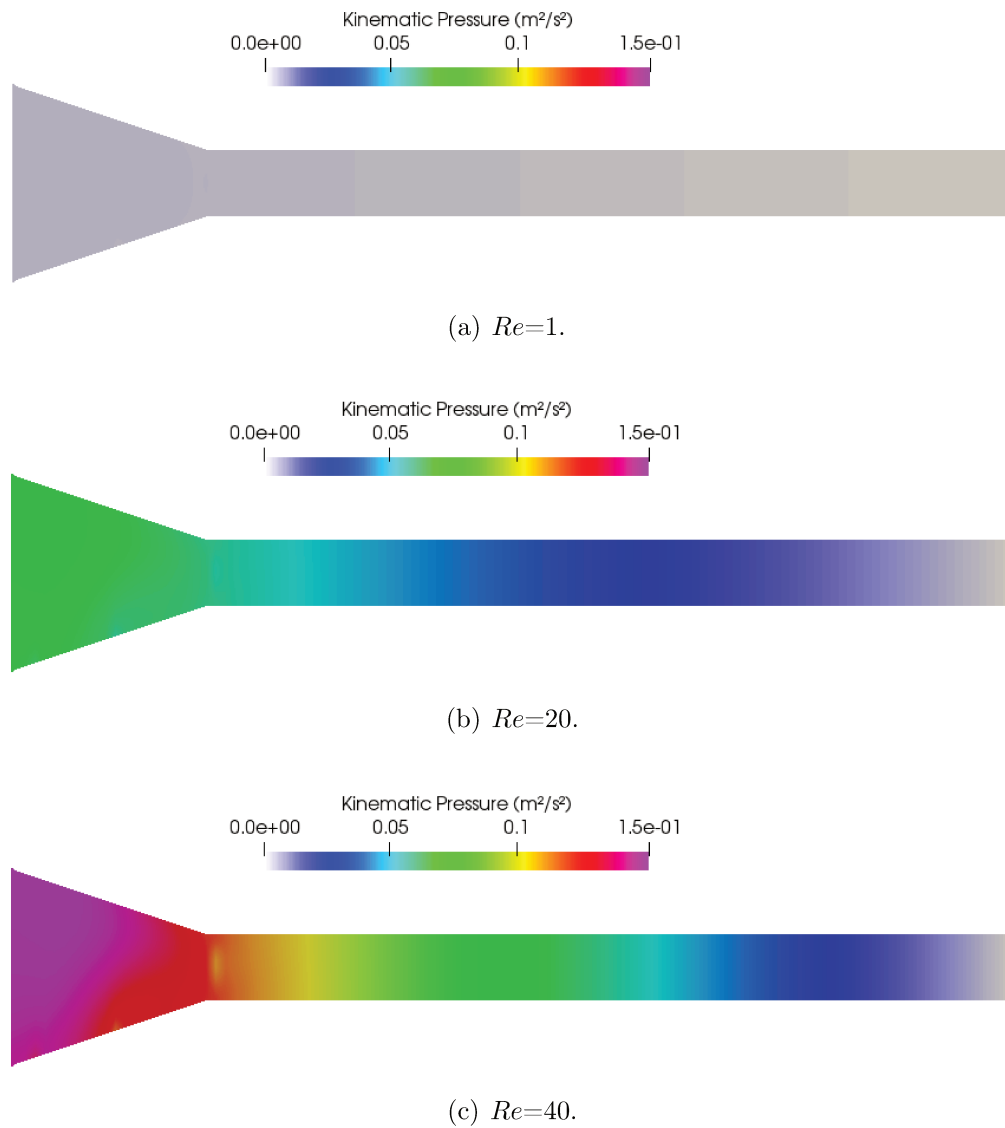
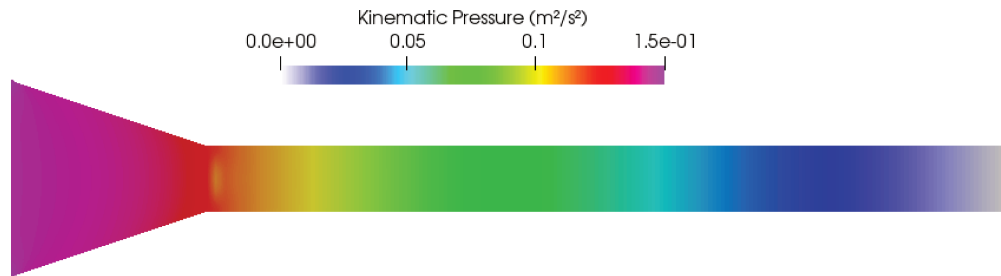
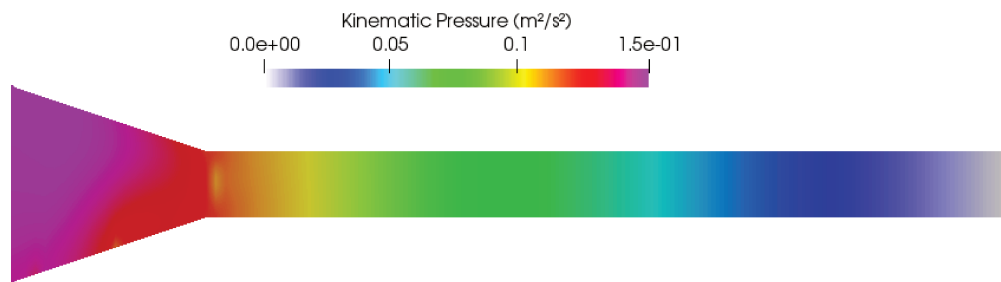


Figure C.25: Pressure field at different Reynolds numbers where $d=200 \mu\text{m}$, and $s = 100 \mu\text{m}$.

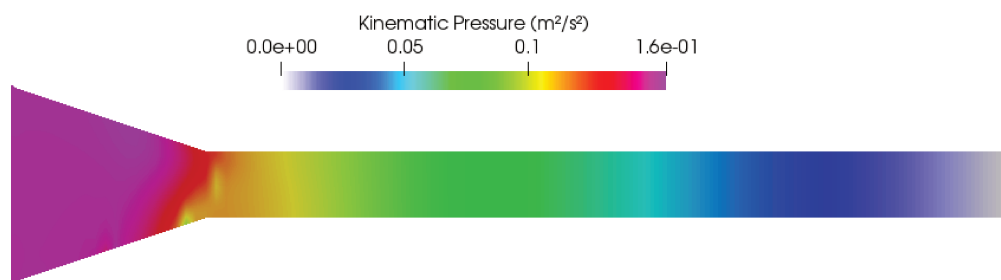
C.4.2.2 No bumps, $Re = 40$



(a) $s=0 \mu m$.



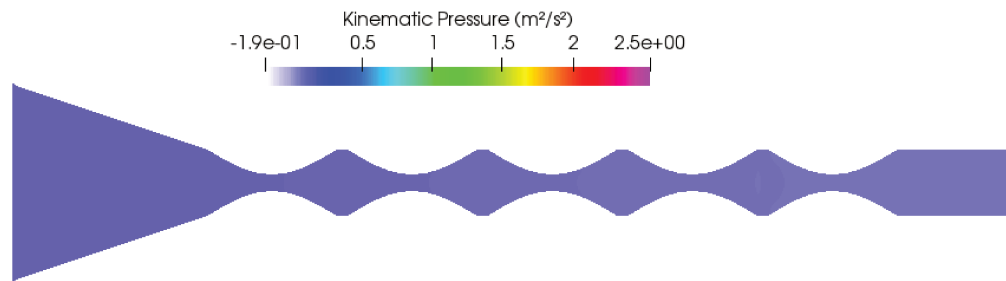
(b) $s=100 \mu m$.



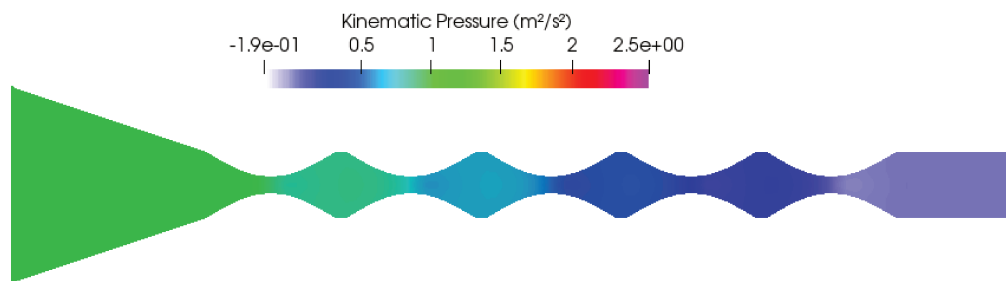
(c) $s=300 \mu m$.

Figure C.26: Pressure field at different locations of feed where $d=200 \mu m$, and $Re = 40$.

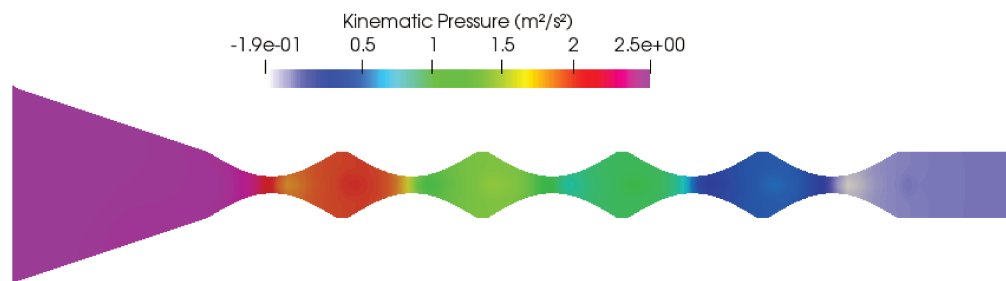
C.4.2.3 Curvature of bumps $\alpha = 1, s = 100 \mu\text{m}$



(a) $Re=1$.



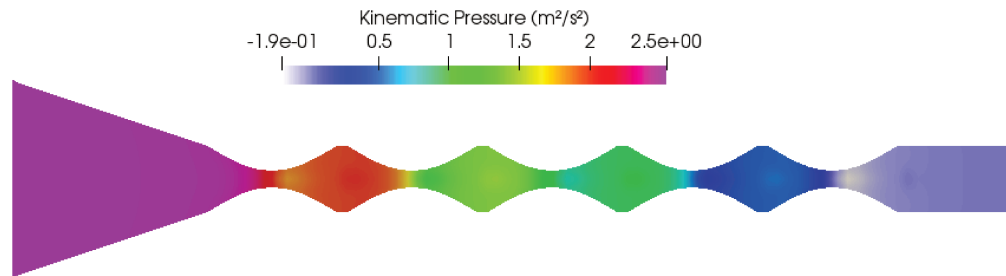
(b) $Re=20$.



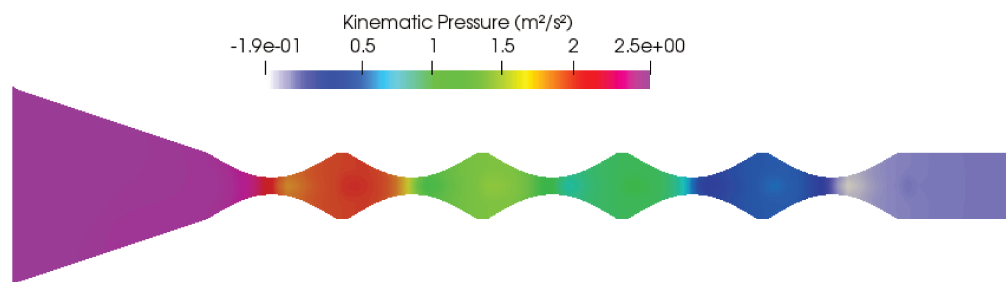
(c) $Re=40$.

Figure C.27: Pressure field at different Reynolds numbers where $d=200 \mu\text{m}$, $s = 100 \mu\text{m}$ and $\alpha = 1$.

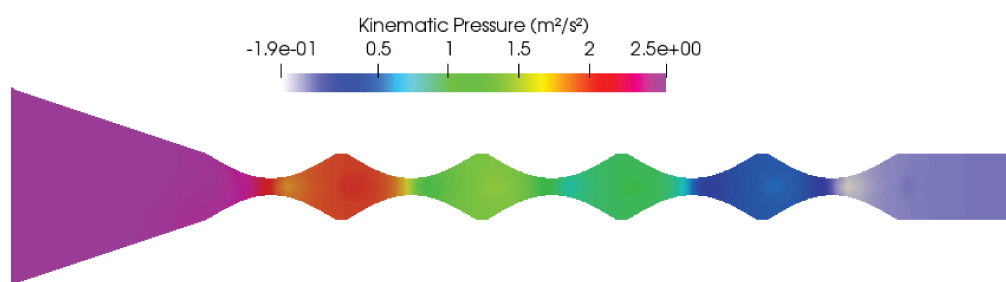
C.4.2.4 Curvature of bumps $\alpha = 1$, $Re = 40$



(a) $s=0 \mu m$.



(b) $s=100 \mu m$.



(c) $s=300 \mu m$.

Figure C.28: Pressure field at different locations of feed where $d=200 \mu m$, $\alpha = 1$ and $Re = 40$.

C.4.2.5 Curvature of bumps $\alpha = 2, s = 100 \mu\text{m}$

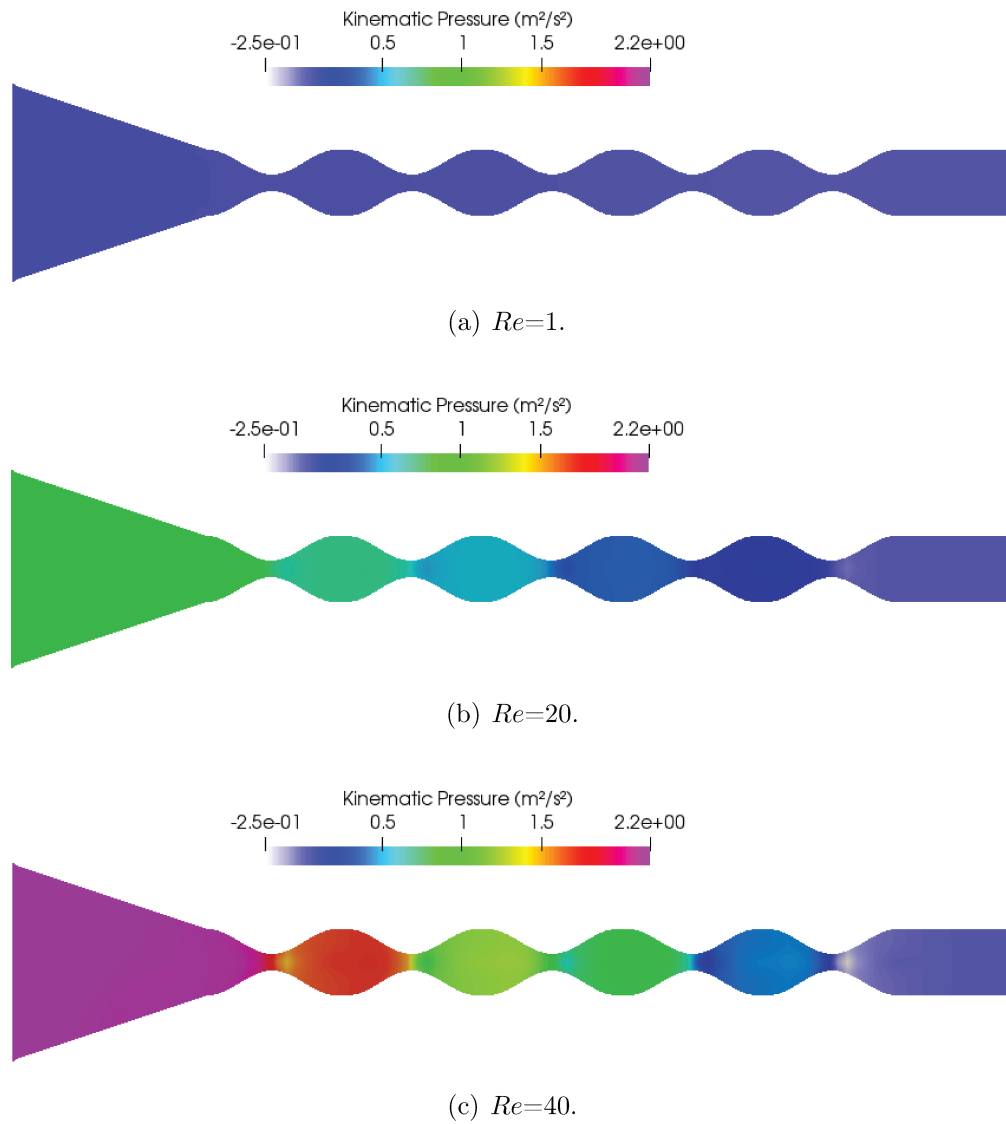
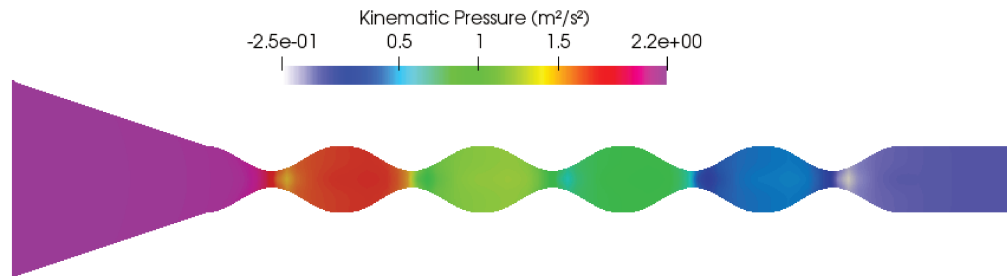
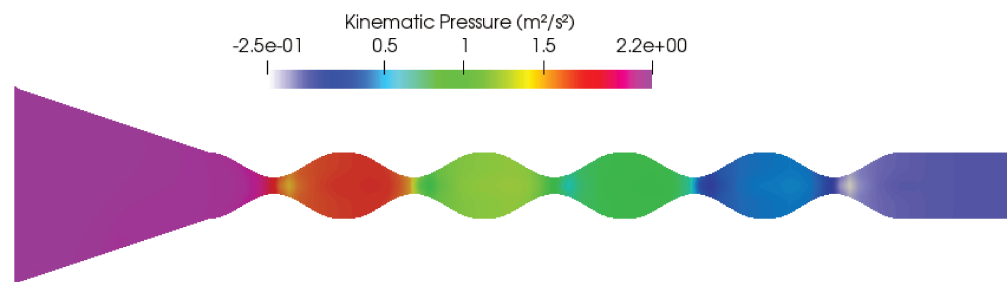


Figure C.29: Pressure field at different Reynolds numbers where $d=200 \mu\text{m}$, $s = 100 \mu\text{m}$ and $\alpha = 2$.

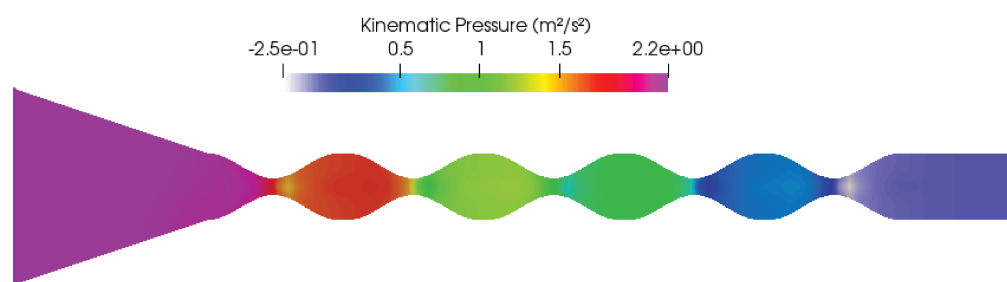
C.4.2.6 Curvature of bumps $\alpha = 2$, $Re = 40$



(a) $s=0 \mu m$.



(b) $s=100 \mu m$.



(c) $s=300 \mu m$.

Figure C.30: Pressure field at different locations of feed where $d=200 \mu m$, $\alpha = 2$ and $Re = 40$.

C.4.2.7 Curvature of bumps $\alpha = 4, s = 100 \mu\text{m}$

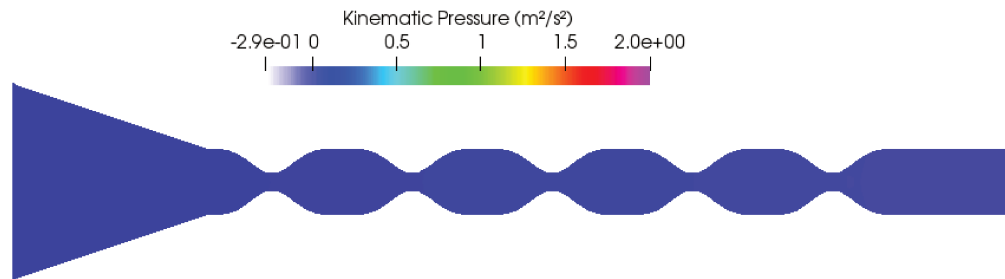
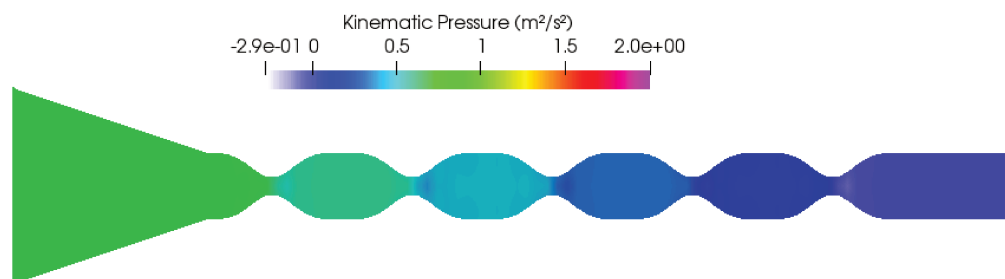
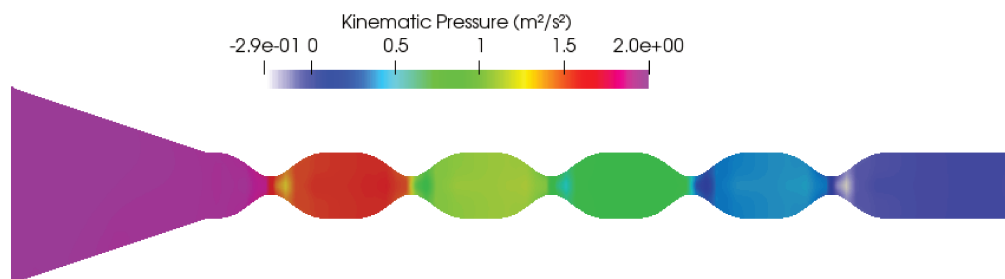
(a) $Re=1$.(b) $Re=20$.(c) $Re=40$.

Figure C.31: Pressure field at different Reynolds numbers where $d=200 \mu\text{m}$, $s = 100 \mu\text{m}$ and $\alpha = 4$.

C.4.2.8 Curvature of bumps $\alpha=4, Re = 40$

t

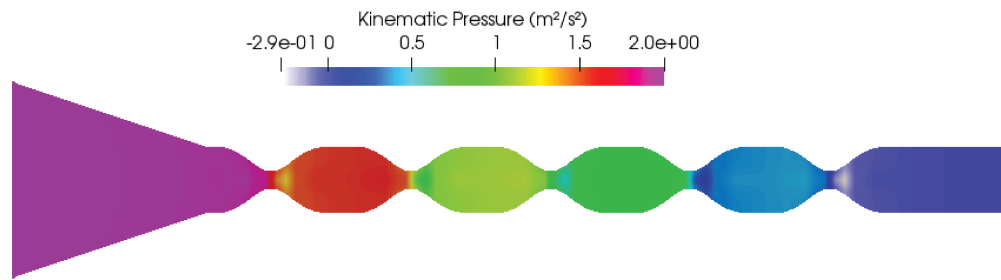
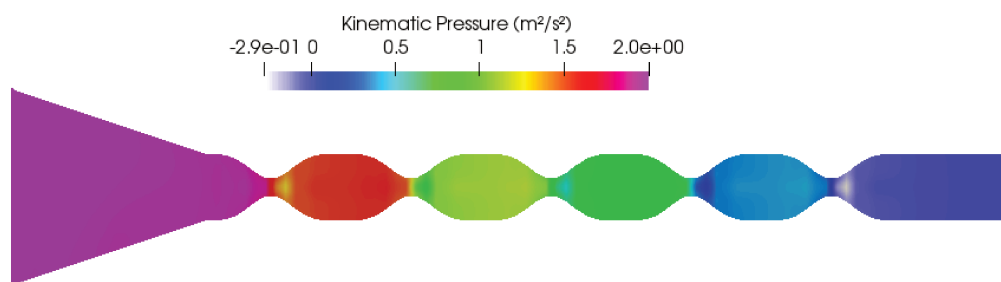
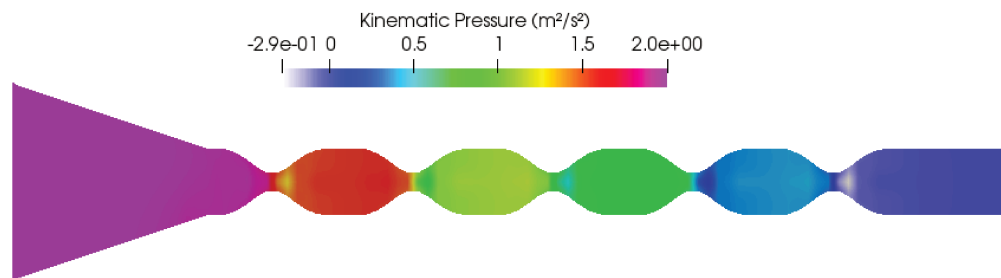
(a) $s=0 \mu\text{m}$.(b) $s=100 \mu\text{m}$.(c) $s=300 \mu\text{m}$.

Figure C.32: Pressure field at different locations of feed where $d=200 \mu\text{m}$, $\alpha = 4$ and $Re = 40$.

C.5 Vorticity Fields

C.5.1 Device's width, $d = 250 \mu\text{m}$

C.5.1.1 No bumps, $s = 100 \mu\text{m}$

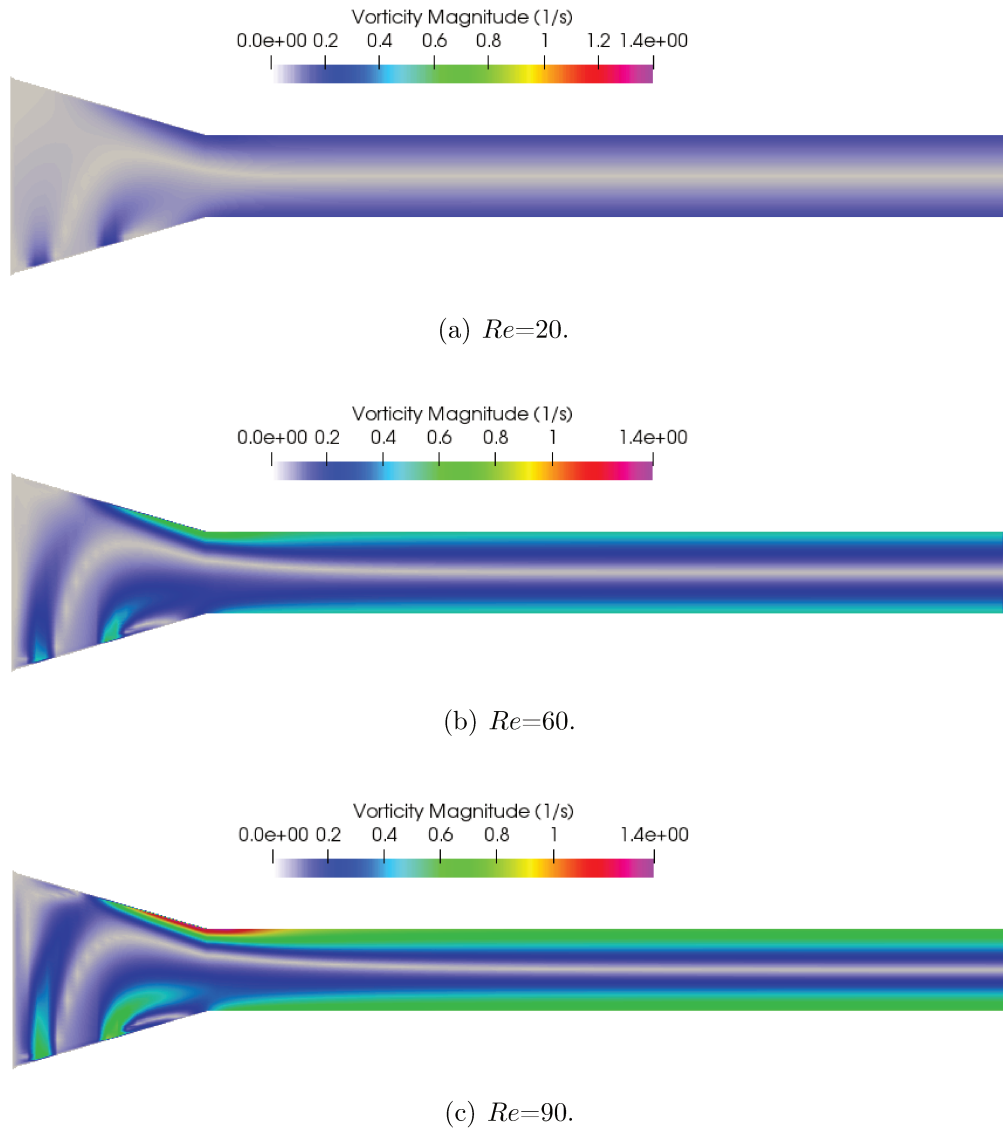
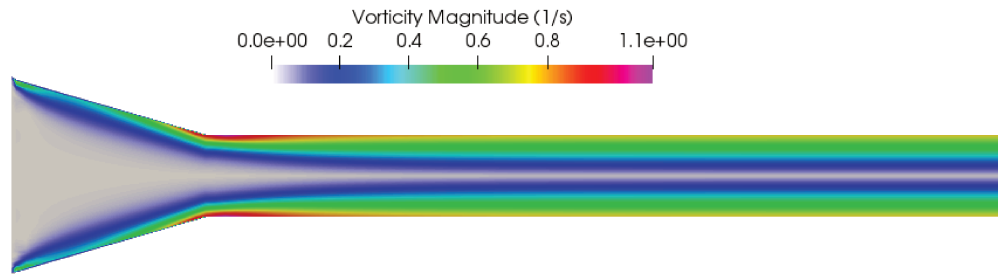
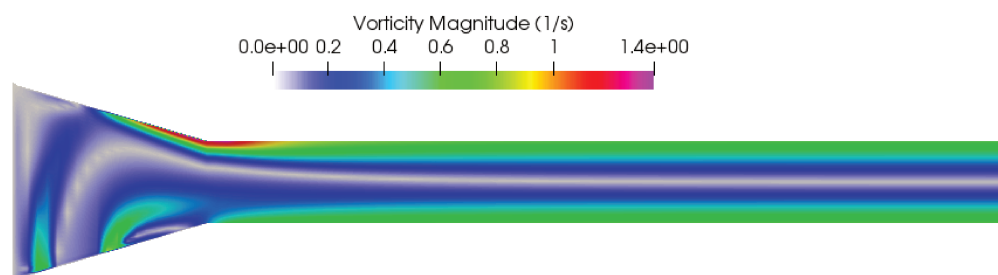


Figure C.33: Vorticity field at different Reynolds numbers where $d=250 \mu\text{m}$, and $s = 100 \mu\text{m}$.

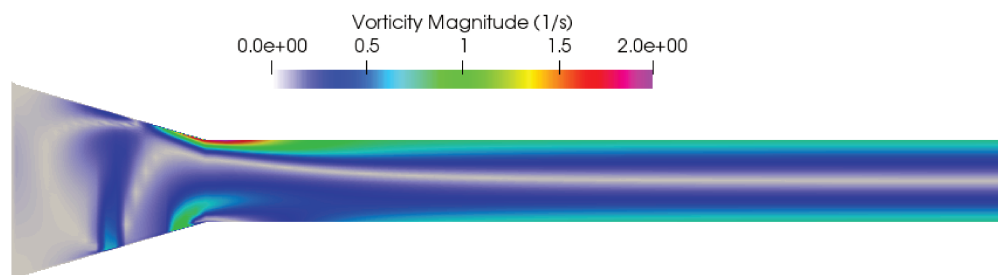
C.5.1.2 No bumps, $Re = 90$



(a) $s=0 \mu m$.



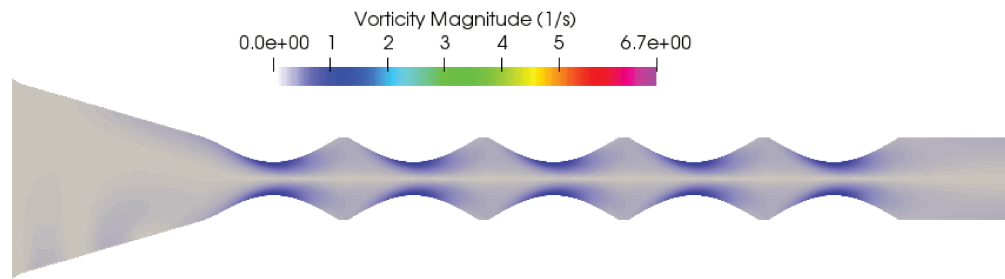
(b) $s=100 \mu m$.



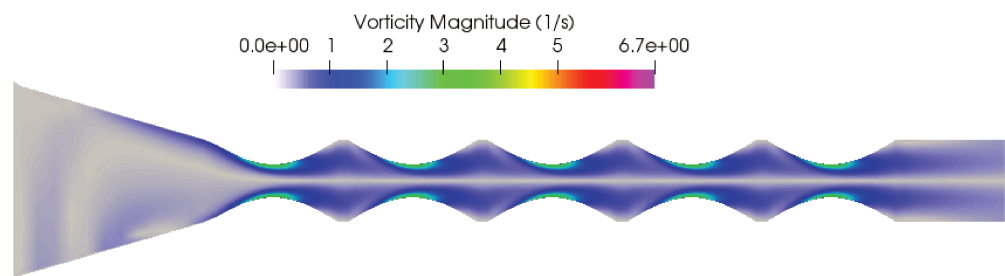
(c) $s=300 \mu m$.

Figure C.34: Vorticity field at different locations of feed where $d=250 \mu m$, and $Re = 90$ (These figures do not have the same data range).

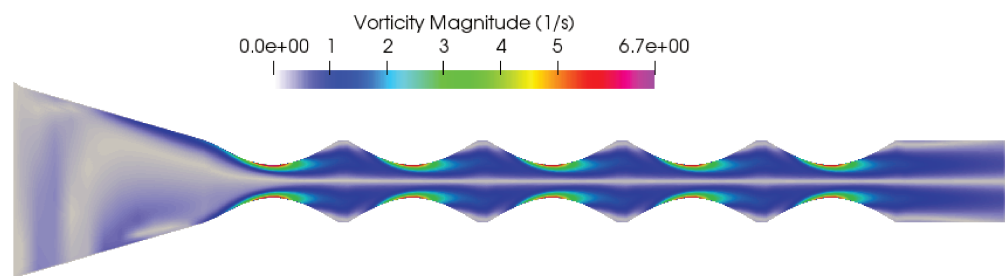
C.5.1.3 Curvature of bumps $\alpha = 1, s = 100 \mu\text{m}$



(a) $Re=20$.



(b) $Re=60$.



(c) $Re=90$.

Figure C.35: Vorticity field at different Reynolds numbers where $d=250 \mu\text{m}$, $s = 100 \mu\text{m}$ and $\alpha = 1$.

C.5.1.4 Curvature of bumps $\alpha = 1$, $Re = 90$

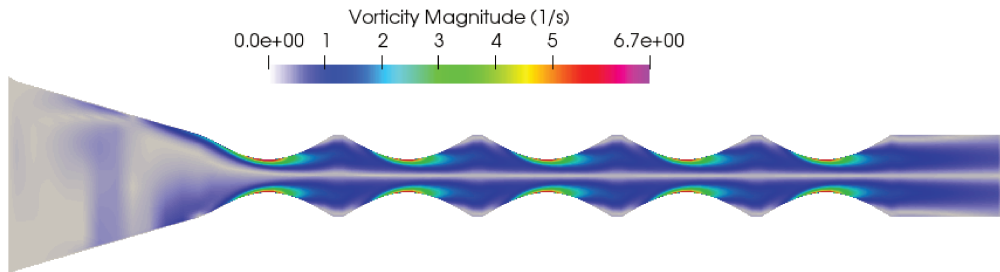
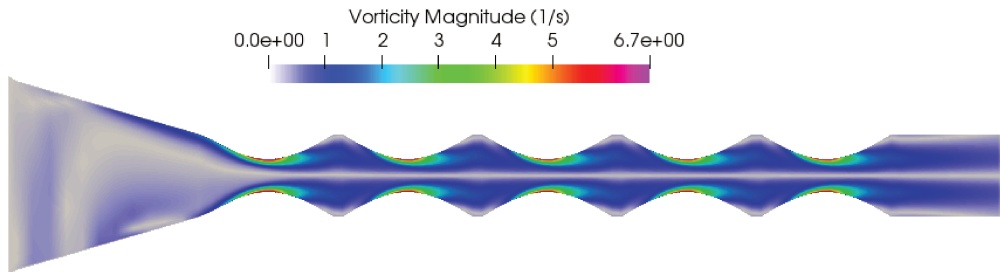
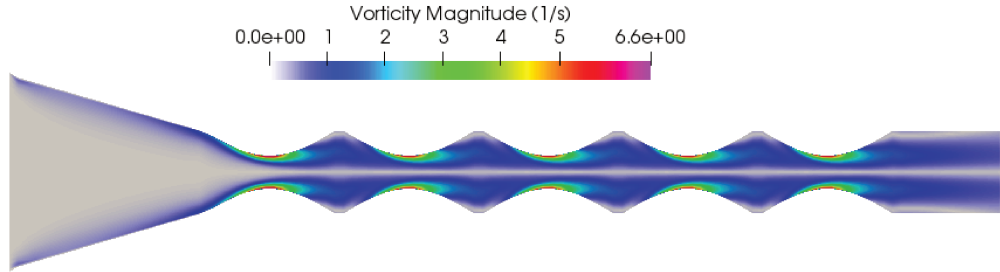
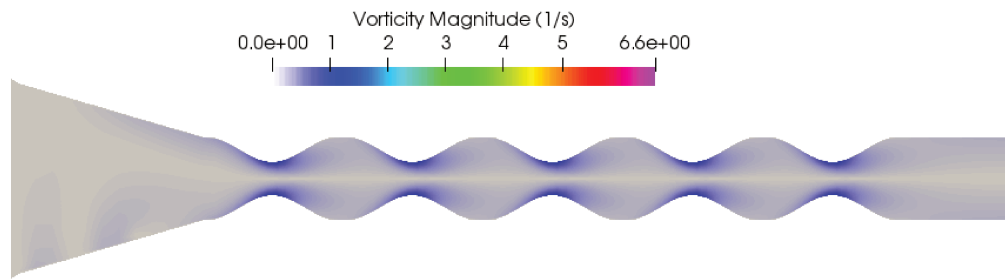
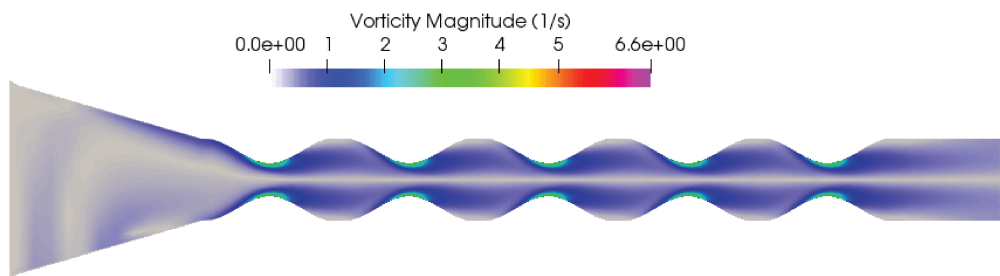


Figure C.36: Vorticity field at different locations of feed where $d=250 \mu m$, $\alpha = 1$ and $Re = 90$.

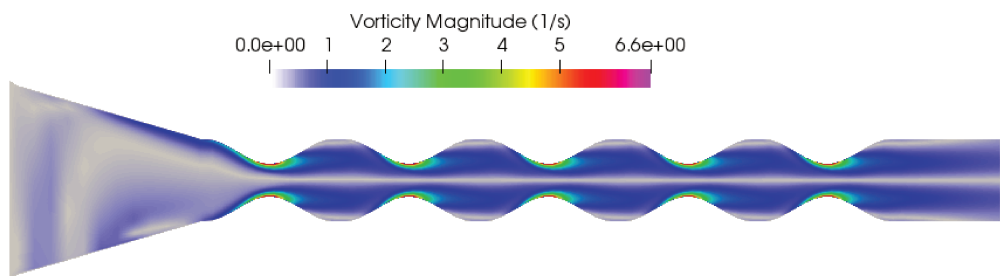
C.5.1.5 Curvature of bumps $\alpha = 2, s = 100 \mu\text{m}$



(a) $Re=20$.



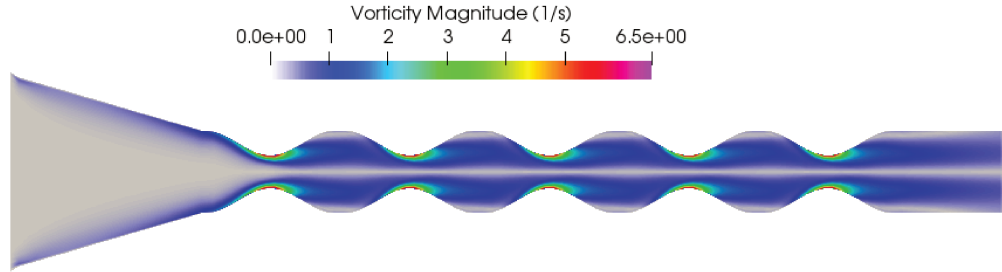
(b) $Re=60$.



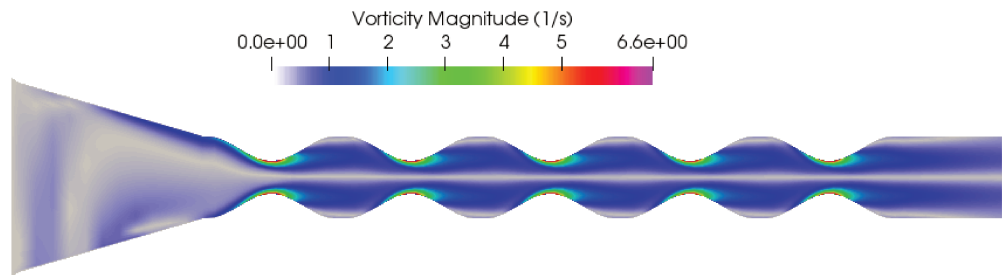
(c) $Re=90$.

Figure C.37: Vorticity field at different Reynolds numbers where $d=250 \mu\text{m}$, $s = 100 \mu\text{m}$ and $\alpha = 2$.

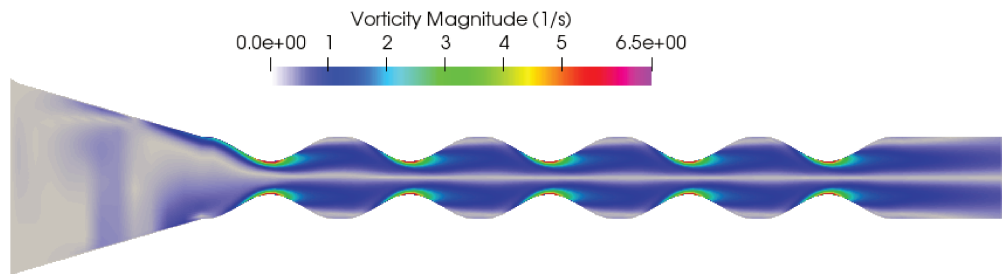
C.5.1.6 Curvature of bumps $\alpha = 2$, $Re = 90$



(a) $s=0 \mu m$.



(b) $s=100 \mu m$.



(c) $s=300 \mu m$.

Figure C.38: Vorticity field at different locations of feed where $d=250 \mu m$, $\alpha = 2$ and $Re = 90$.

C.5.1.7 Curvature of bumps $\alpha = 4$, $s = 100 \mu\text{m}$

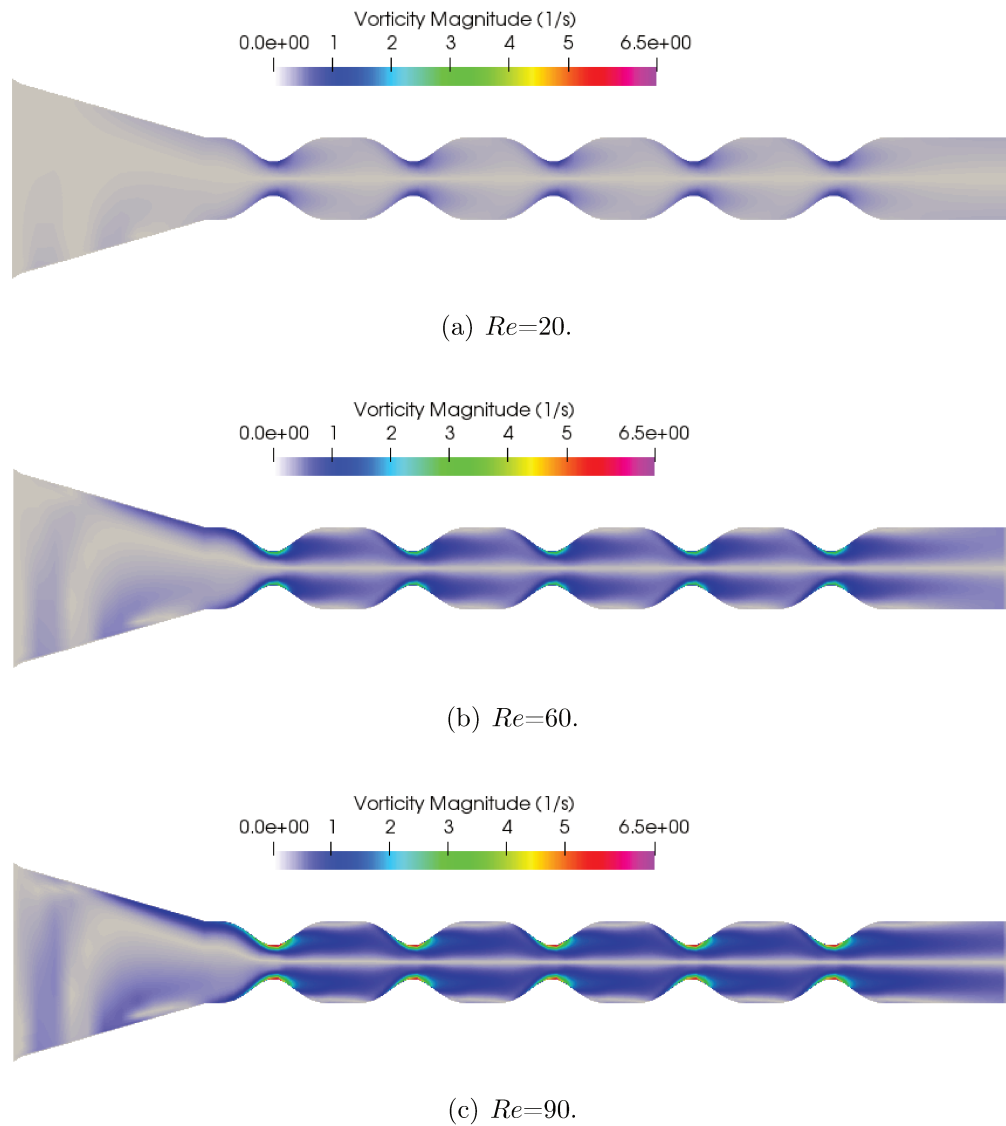
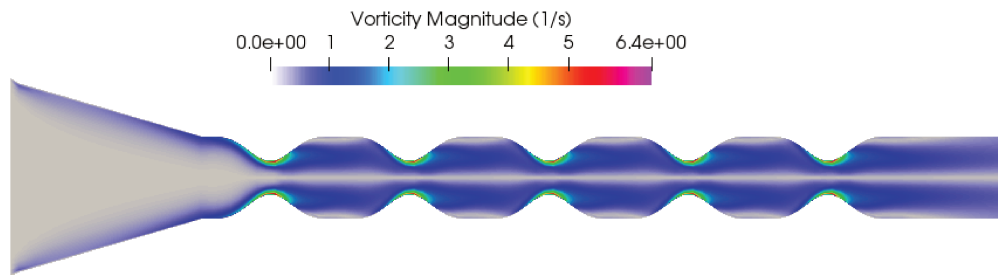
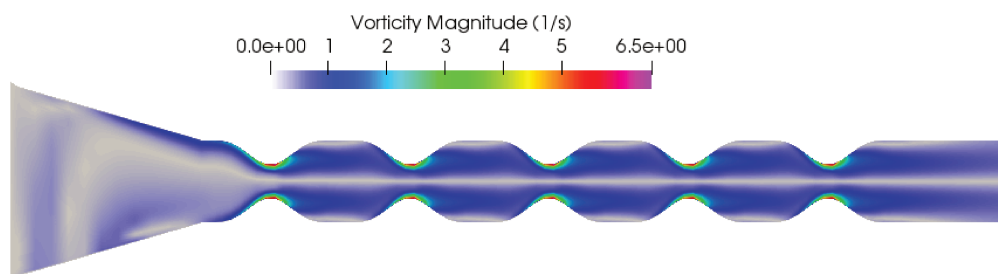


Figure C.39: Vorticity field at different Reynolds numbers where $d=250 \mu\text{m}$, $s = 100 \mu\text{m}$ and $\alpha = 4$.

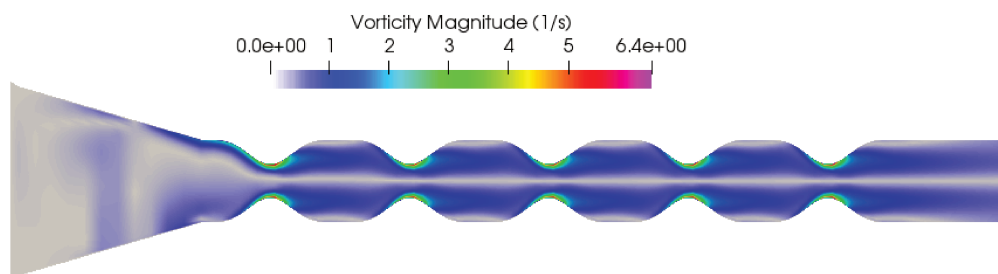
C.5.1.8 Curvature of bumps $\alpha=4$, $Re = 90$



(a) $s=0 \mu m$.



(b) $s=100 \mu m$.



(c) $s=300 \mu m$.

Figure C.40: Vorticity field at different positions of feed where $d=250 \mu m$, $\alpha = 4$ and $Re = 90$.

C.5.2 Device's width, $d = 200 \mu\text{m}$

C.5.2.1 No bumps, $s = 100 \mu\text{m}$

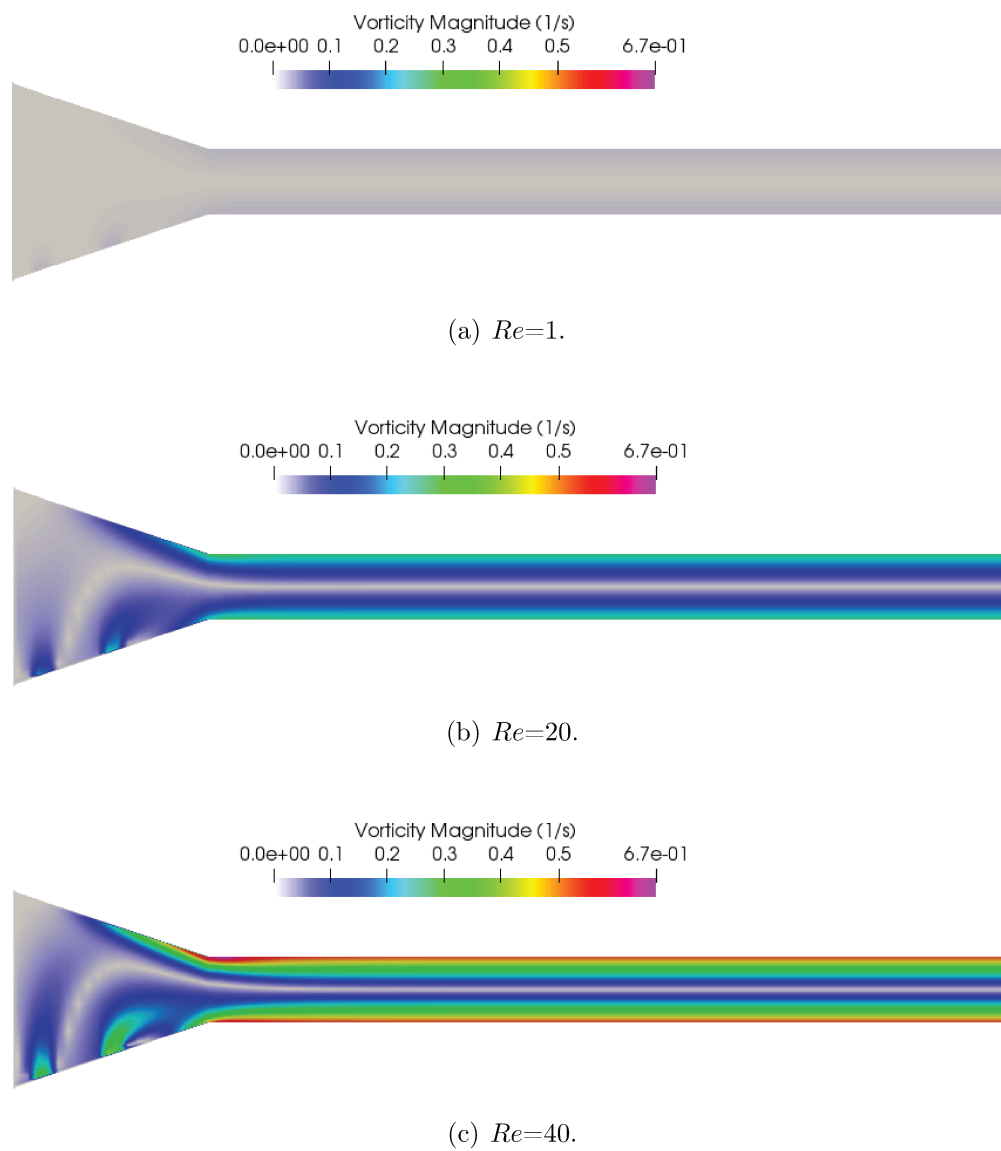
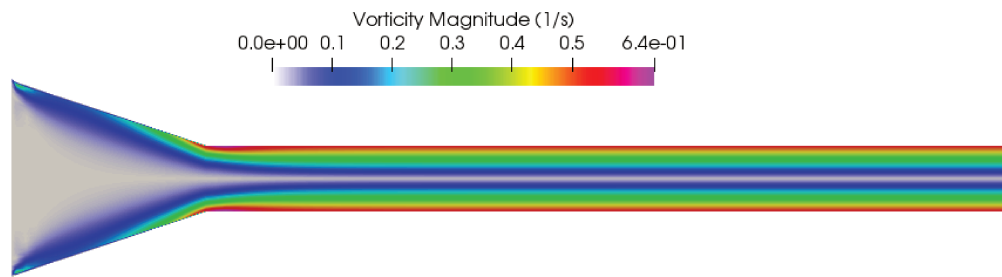
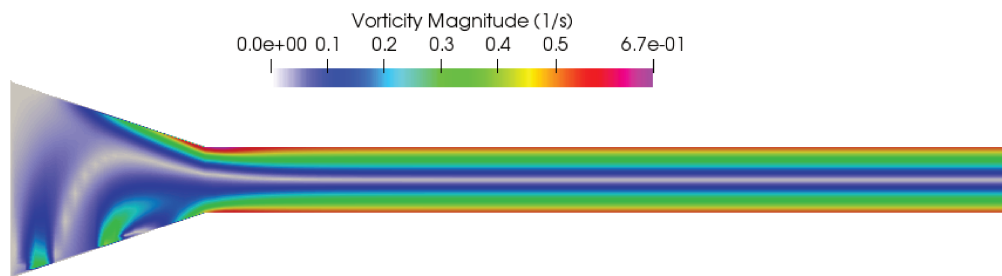


Figure C.41: Vorticity field at different Reynolds numbers where $d=200 \mu\text{m}$, and $s = 100 \mu\text{m}$.

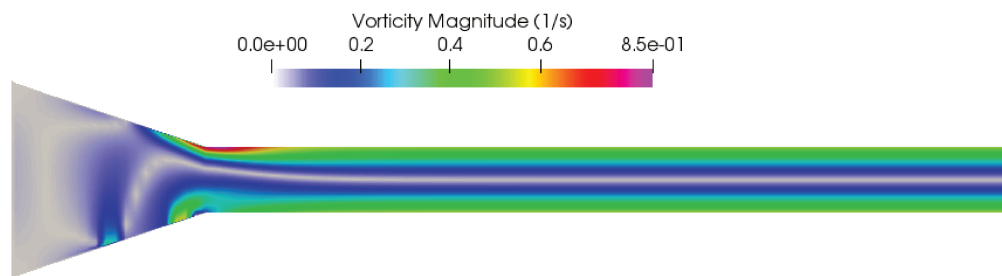
C.5.2.2 No bumps, $Re = 40$



(a) $s=0 \mu m$.



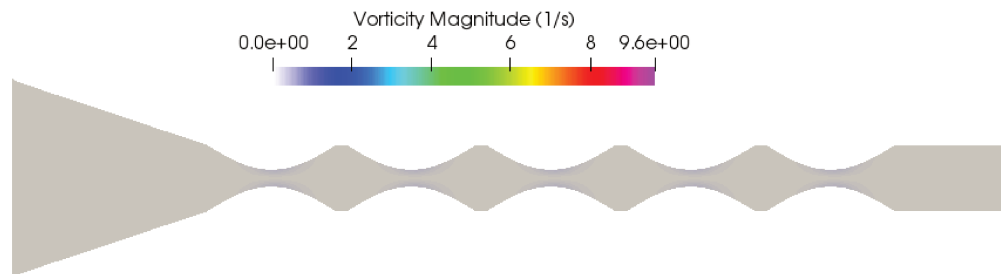
(b) $s=100 \mu m$.



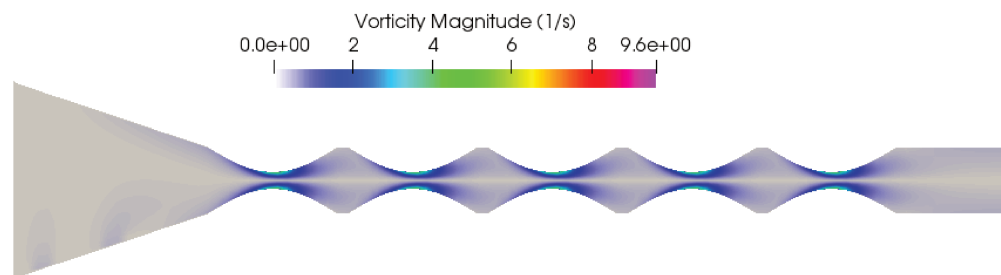
(c) $s=300 \mu m$.

Figure C.42: Vorticity field at different locations of feed where $d=200 \mu m$, and $Re = 40$ (These figures do not have the same data range).

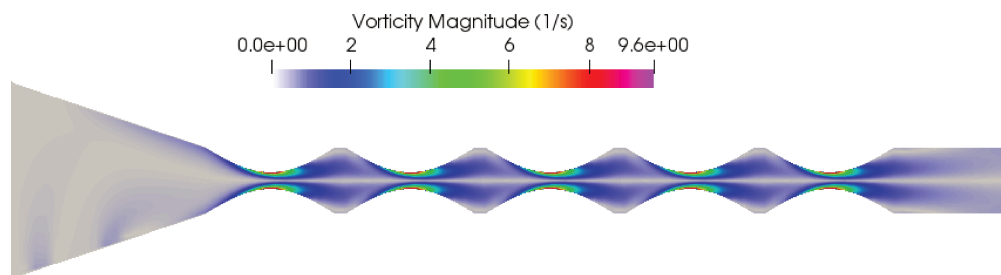
C.5.2.3 Curvature of bumps $\alpha = 1, s = 100 \mu\text{m}$



(a) $Re=1$.



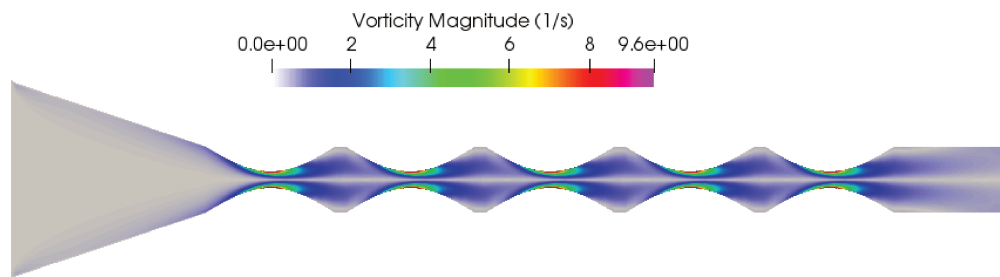
(b) $Re=20$.



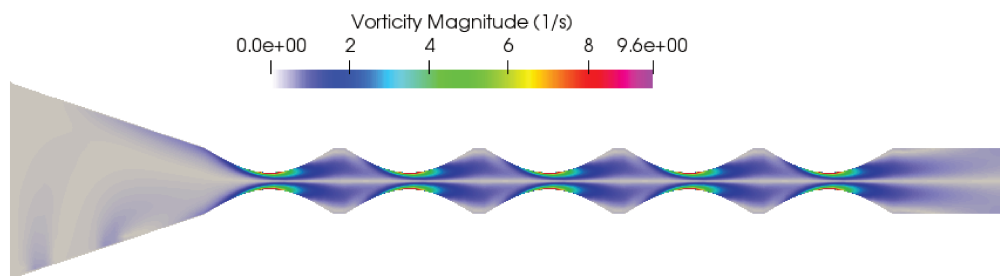
(c) $Re=40$.

Figure C.43: Vorticity field at different Reynolds numbers where $d=200 \mu\text{m}$, $s = 100 \mu\text{m}$ and $\alpha = 1$.

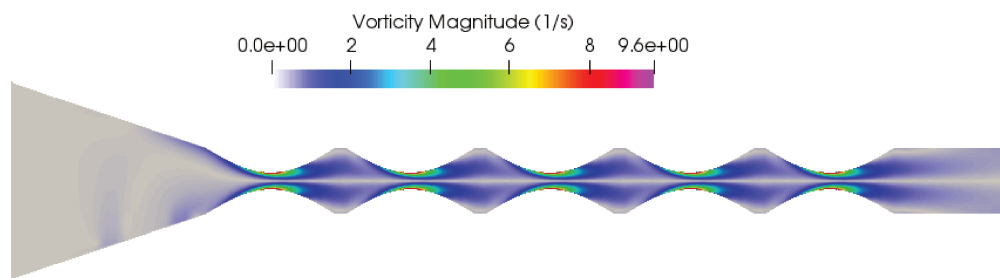
C.5.2.4 Curvature of bumps $\alpha = 1$, $Re = 40$



(a) $s=0 \mu m$.



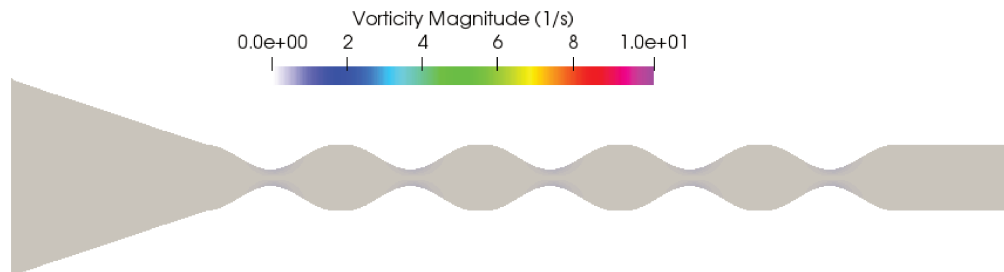
(b) $s=100 \mu m$.



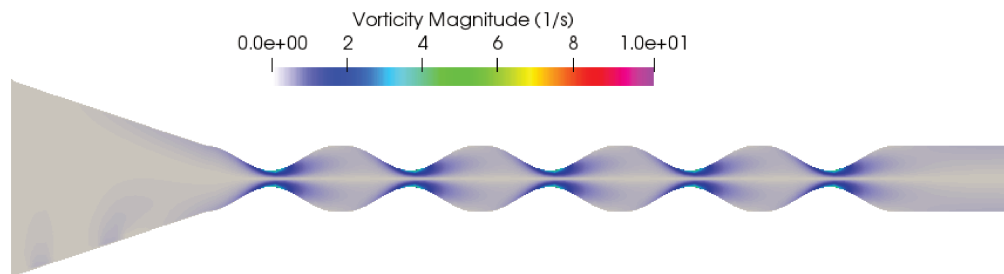
(c) $s=300 \mu m$.

Figure C.44: Vorticity field at different locations of feed where $d=200 \mu m$, $\alpha = 1$ and $Re = 40$.

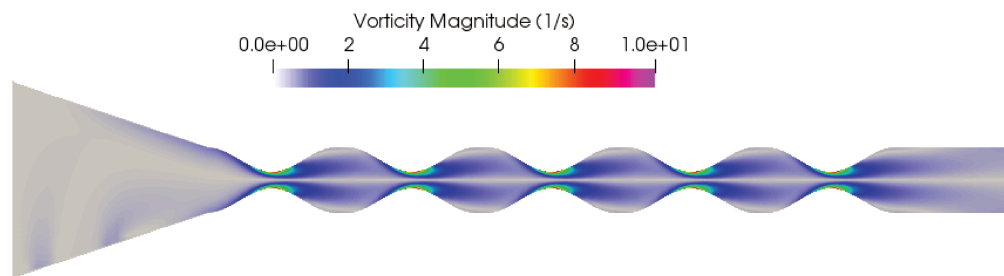
C.5.2.5 Curvature of bumps $\alpha = 2, s = 100 \mu\text{m}$



(a) $Re=1$.



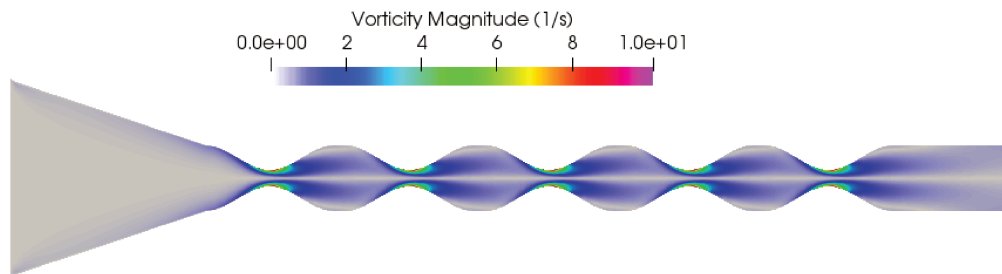
(b) $Re=20$.



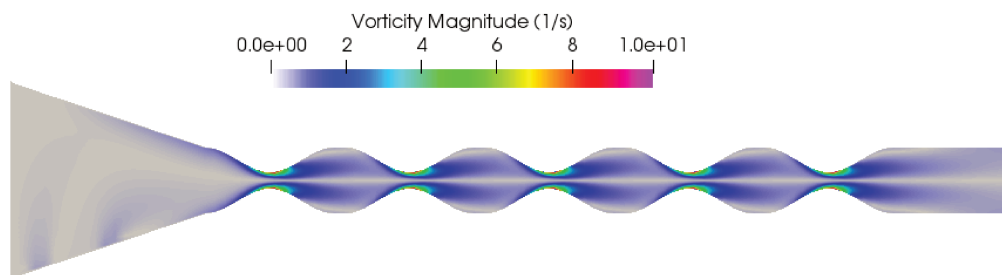
(c) $Re=40$.

Figure C.45: Vorticity field at different Reynolds numbers where $d=200 \mu\text{m}$, $s = 100 \mu\text{m}$ and $\alpha = 2$.

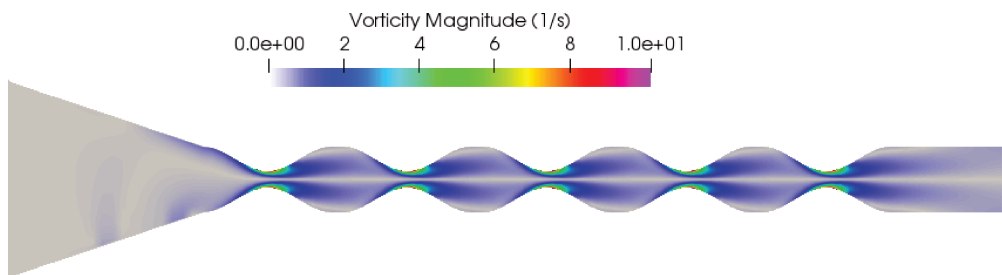
C.5.2.6 Curvature of bumps $\alpha = 2$, $Re = 40$



(a) $s=0 \mu m$.



(b) $s=100 \mu m$.



(c) $s=300 \mu m$.

Figure C.46: Vorticity field at different locations of feed where $d=200 \mu m$, $\alpha = 2$ and $Re = 40$.

C.5.2.7 Curvature of bumps $\alpha = 4, s = 100 \mu\text{m}$

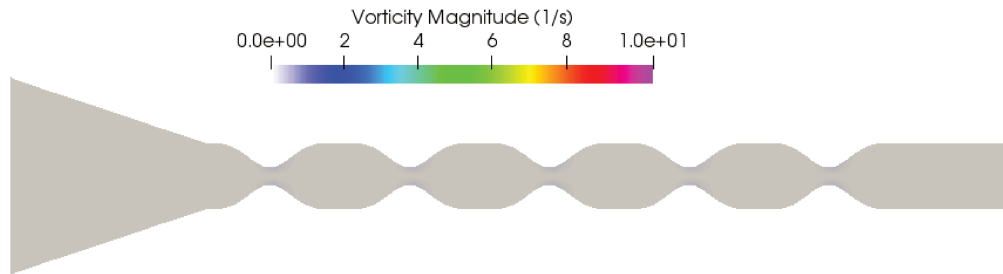
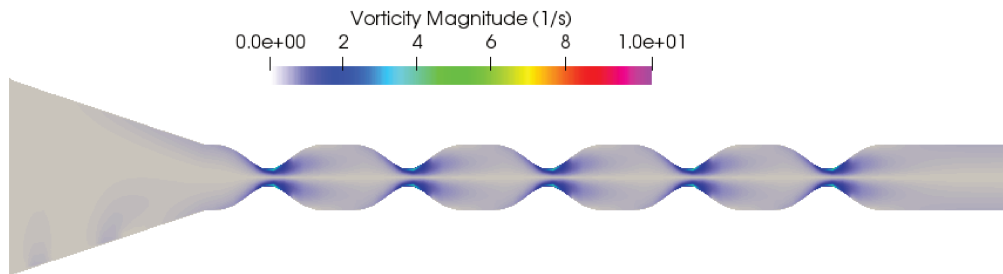
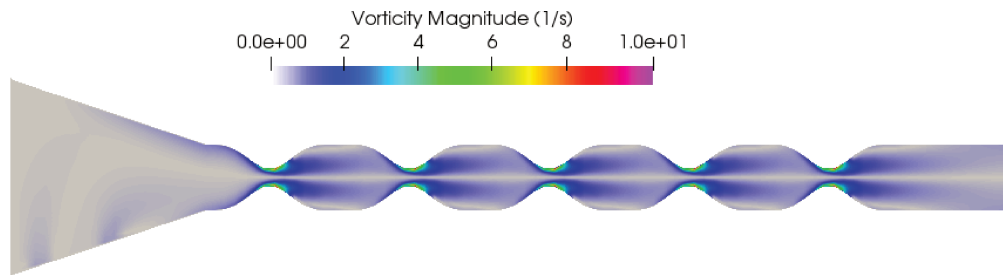
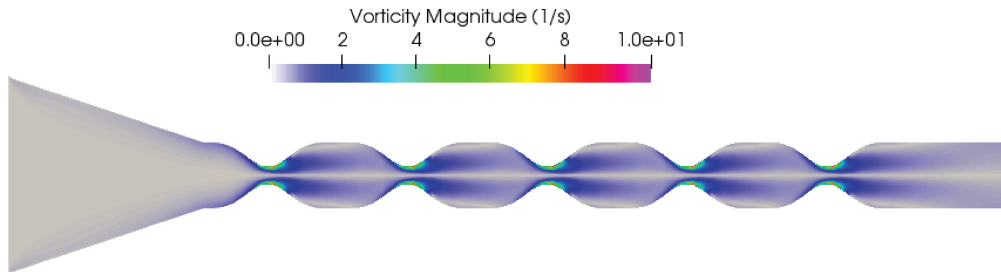
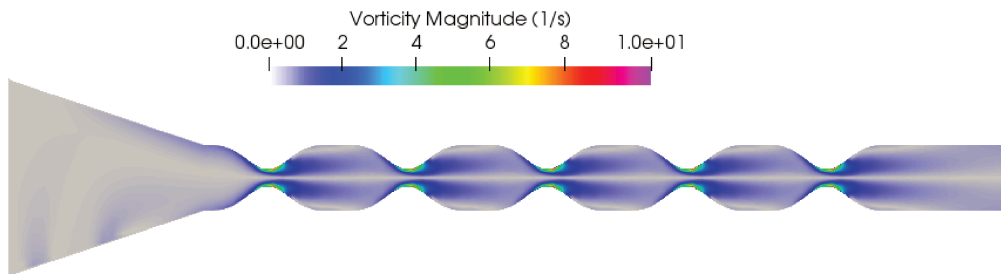
(a) $Re=1$.(b) $Re=20$.(c) $Re=40$.

Figure C.47: Vorticity field at different Reynolds numbers where $d=200 \mu\text{m}$, $s = 100 \mu\text{m}$ and $\alpha = 4$.

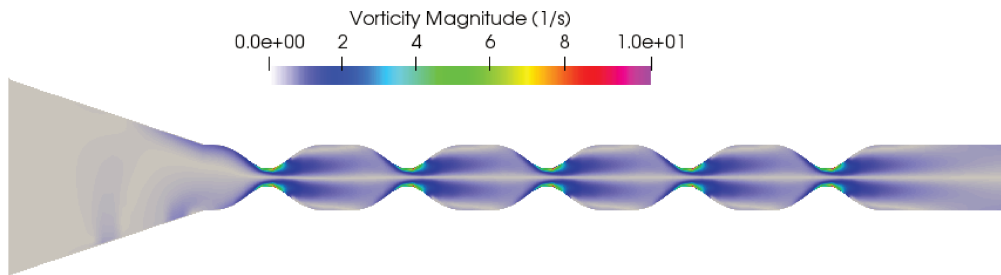
C.5.2.8 Curvature of bumps $\alpha=4$, $Re = 40$



(a) $s=0 \mu m$.



(b) $s=100 \mu m$.



(c) $s=300 \mu m$.

Figure C.48: Vorticity field at different locations of feed where $d=200 \mu m$, $\alpha = 4$ and $Re = 40$.

C.6 Stream-Function Fields

C.6.1 Device's width, $d = 250 \mu\text{m}$

C.6.1.1 No bumps, $s = 100 \mu\text{m}$

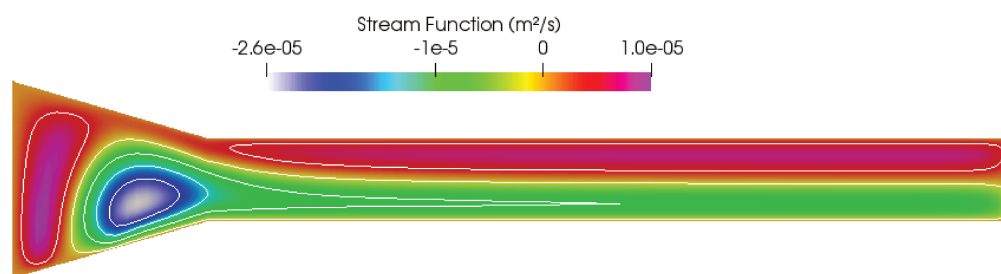
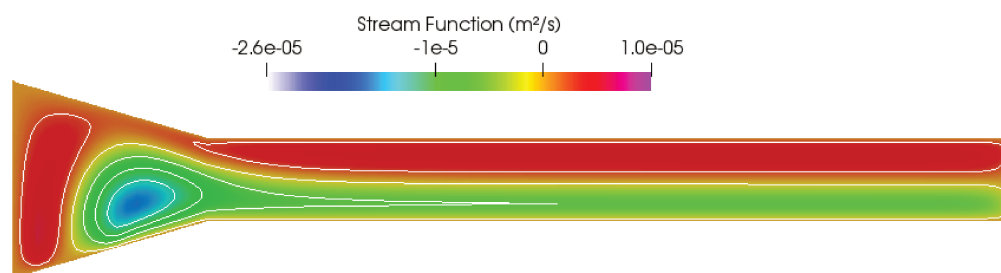
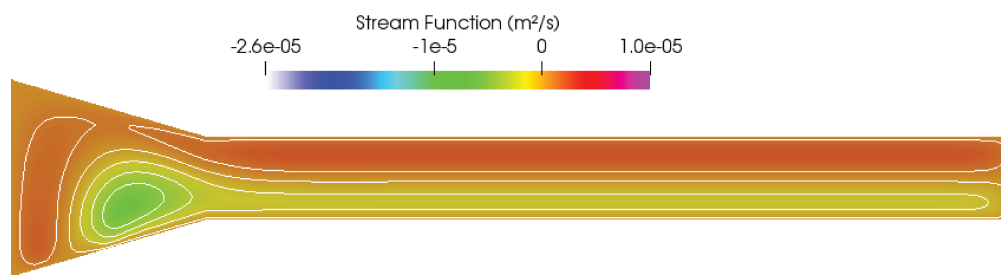
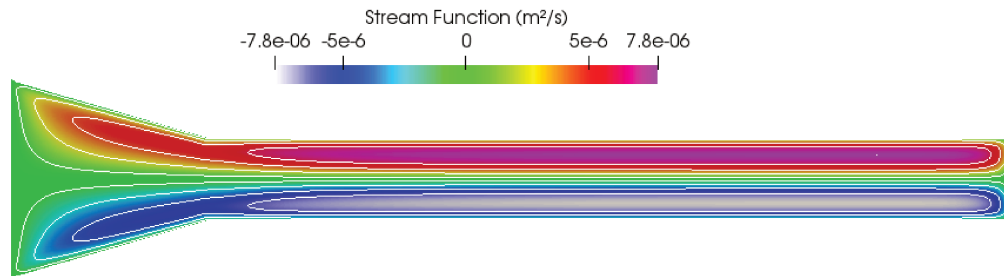
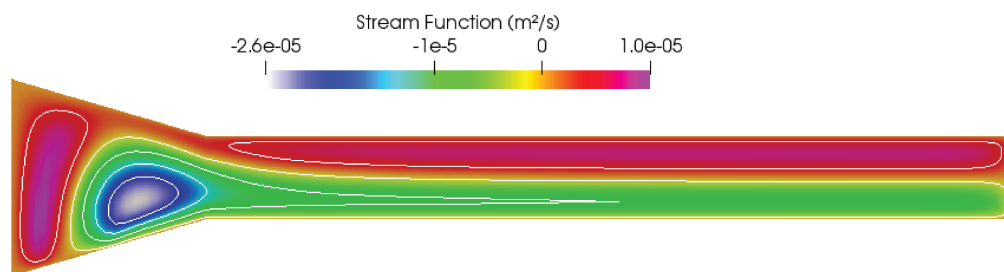


Figure C.49: Stream function with its contours along the microdevice regarding Reynolds number where $d=250 \mu\text{m}$, and $s = 100 \mu\text{m}$.

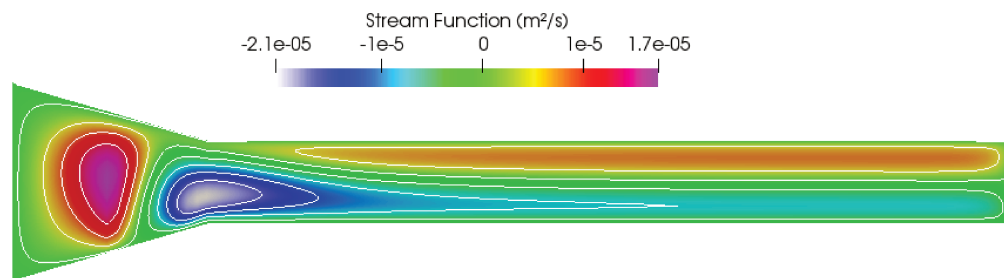
C.6.1.2 No bumps, $Re = 90$



(a) $s=0 \mu m$.



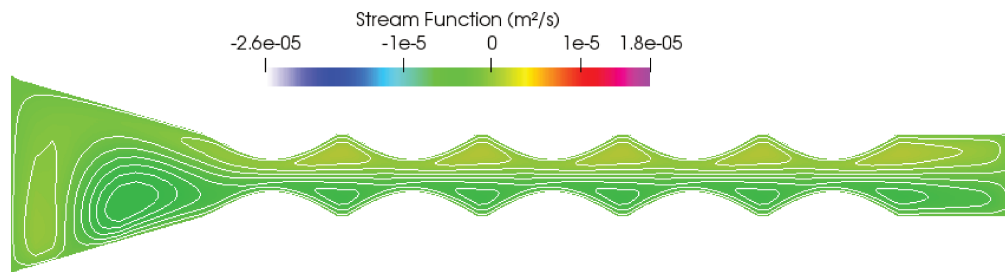
(b) $s=100 \mu m$.



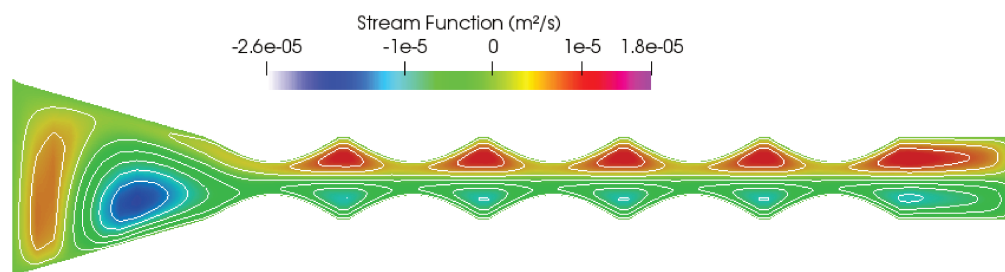
(c) $s=300 \mu m$.

Figure C.50: Stream function with its contours along the microdevice in terms of the feed position where $d=250 \mu m$, and $Re = 90$ (These figures do not have the same data range).

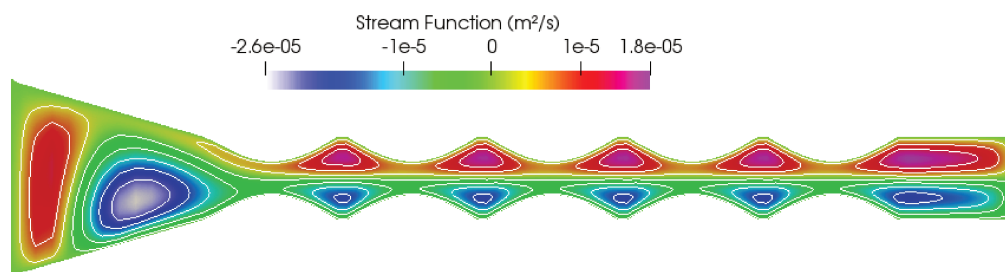
C.6.1.3 Curvature of bumps $\alpha = 1, s = 100 \mu\text{m}$



(a) $Re=20$.



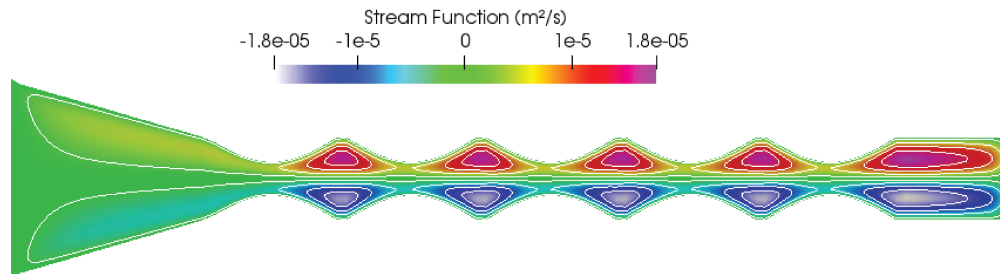
(b) $Re=60$.



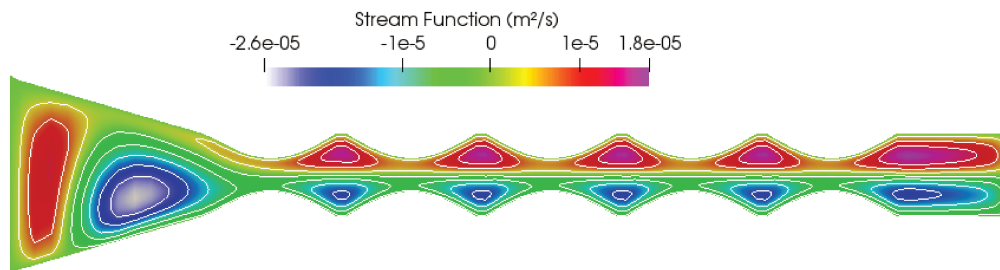
(c) $Re=90$.

Figure C.51: Stream function with its contours along the microdevice regarding Reynolds number where $d=250 \mu\text{m}$, $s = 100 \mu\text{m}$ and $\alpha = 1$.

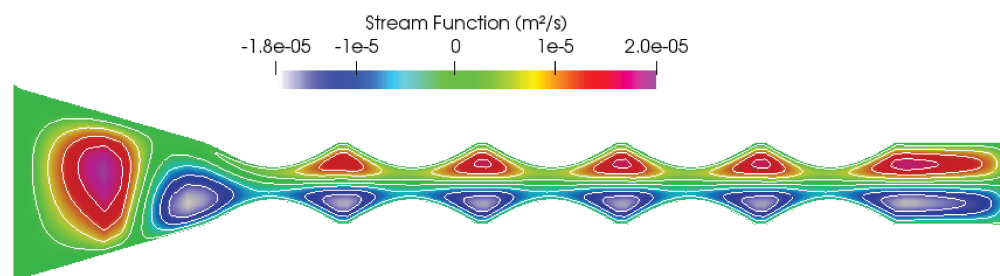
C.6.1.4 Curvature of bumps $\alpha = 1$, $Re = 90$



(a) $s=0 \mu m$.



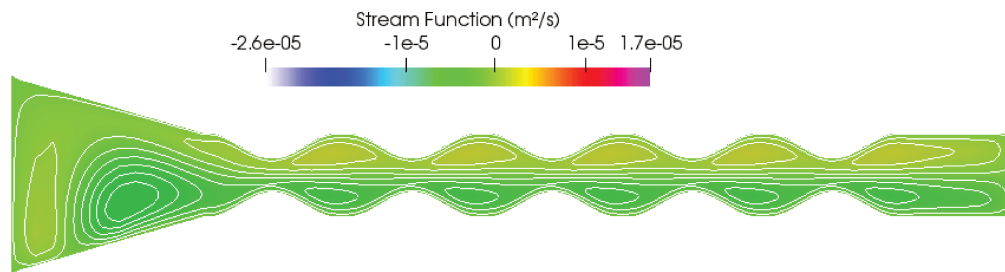
(b) $s=100 \mu m$.



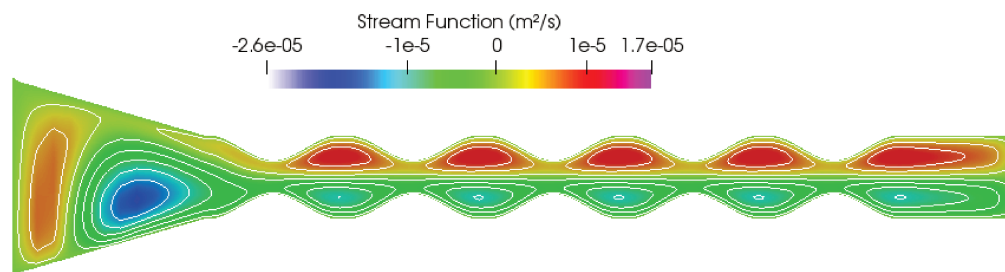
(c) $s=300 \mu m$.

Figure C.52: Stream function with its contours along the microdevice in terms of the feed position where $d=250 \mu m$, $\alpha = 1$ and $Re = 90$ (These figures do not have the same data range).

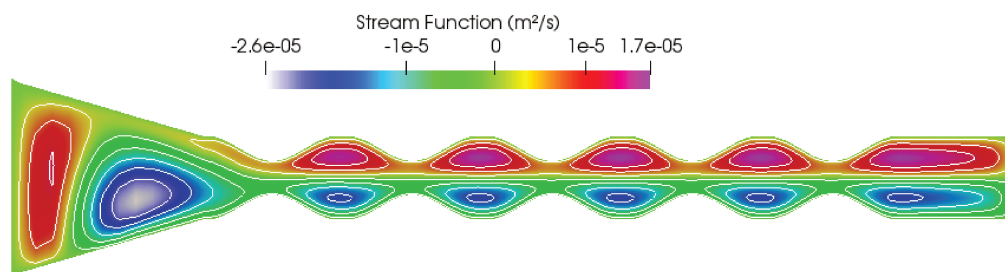
C.6.1.5 Curvature of bumps $\alpha = 2, s = 100 \mu\text{m}$



(a) $Re=20$.



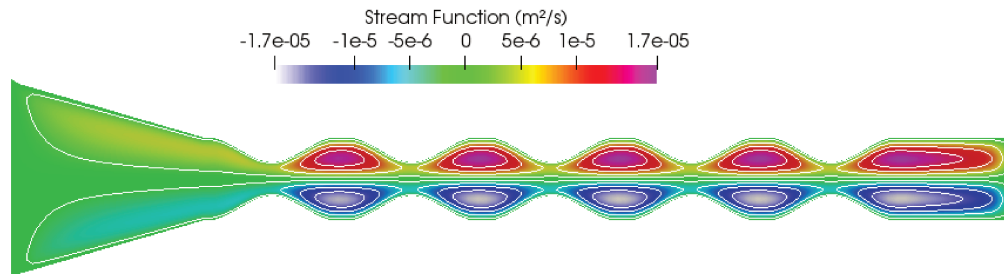
(b) $Re=60$.



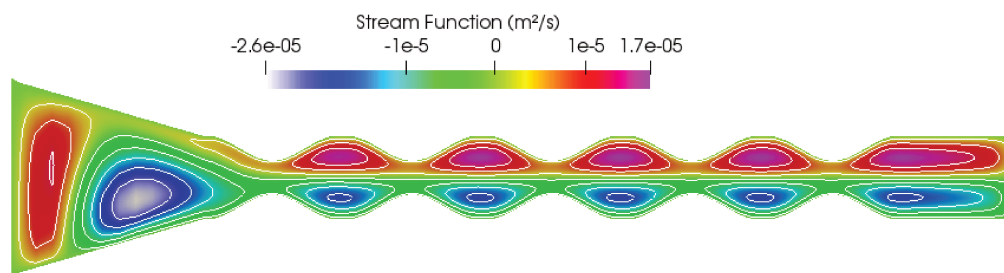
(c) $Re=90$.

Figure C.53: Stream function with its contours along the microdevice regarding Reynolds number where $d=250 \mu\text{m}$, $s = 100 \mu\text{m}$ and $\alpha = 2$.

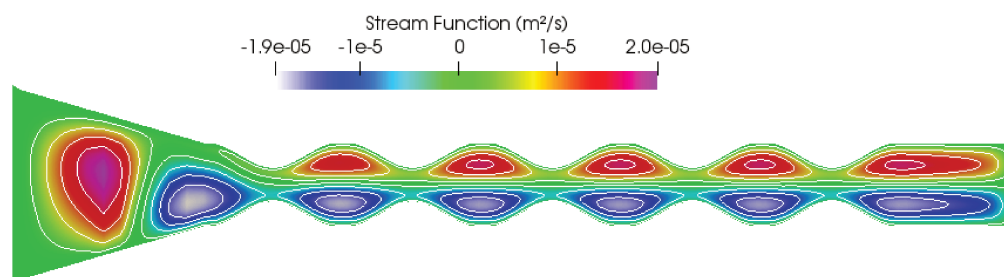
C.6.1.6 Curvature of bumps $\alpha = 2$, $Re = 90$



(a) $s=0 \mu m$.



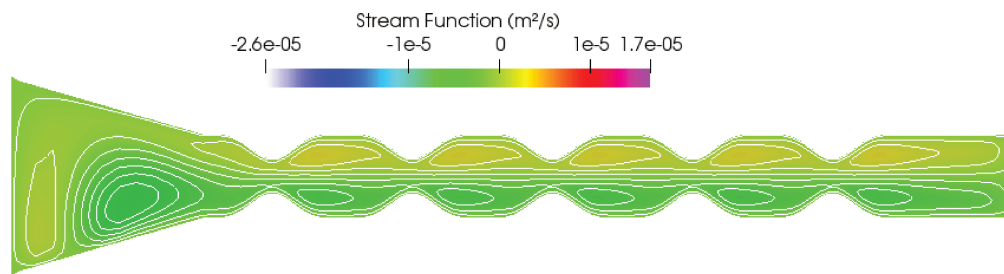
(b) $s=100 \mu m$.



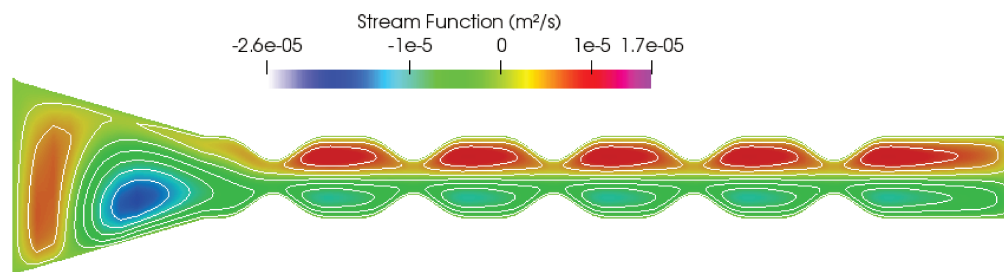
(c) $s=300 \mu m$.

Figure C.54: Stream function with its contours along the microdevice in terms of the feed position where $d=250 \mu m$, $\alpha = 2$ and $Re = 90$ (These figures do not have the same data range).

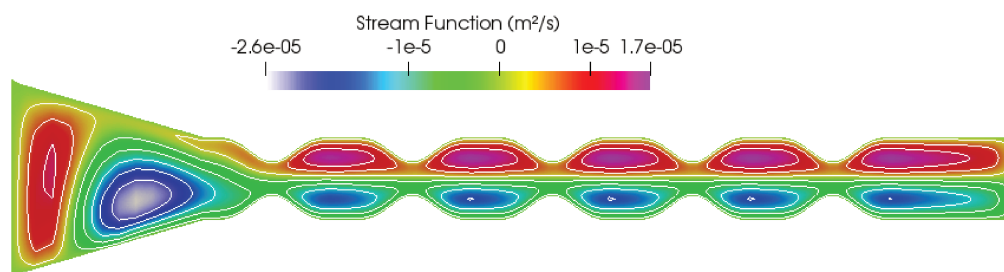
C.6.1.7 Curvature of bumps $\alpha = 4, s = 100 \mu\text{m}$



(a) $Re=20$.



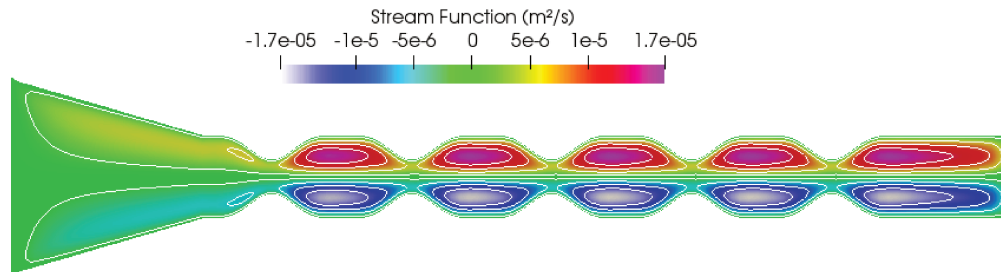
(b) $Re=60$.



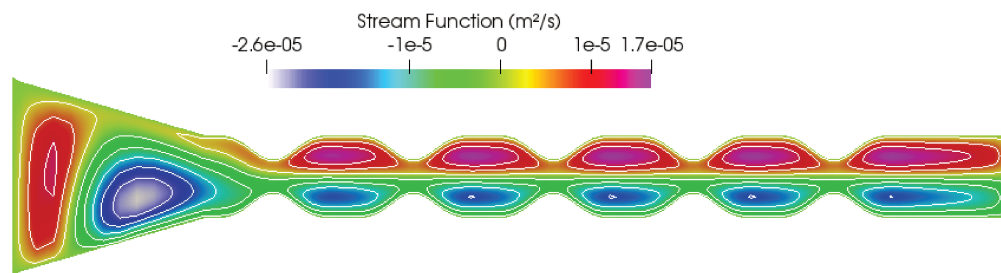
(c) $Re=90$.

Figure C.55: Stream function with its contours along the microdevice regarding Reynolds number where $d=250 \mu\text{m}$, $s = 100 \mu\text{m}$ and $\alpha = 4$.

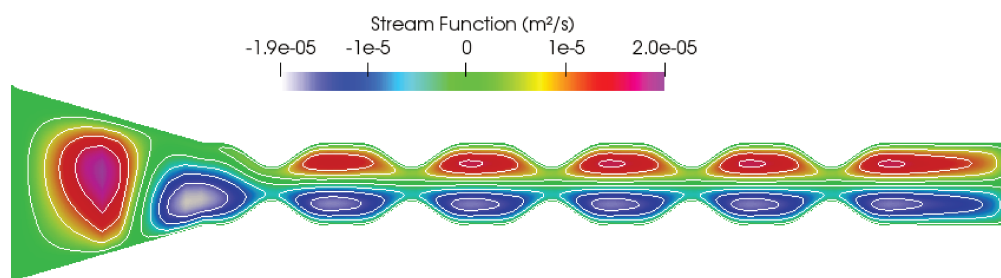
C.6.1.8 Curvature of bumps $\alpha=4$, $Re = 90$



(a) $s=0 \mu m$.



(b) $s=100 \mu m$.



(c) $s=300 \mu m$.

Figure C.56: Stream function with its contours along the microdevice in terms of the feed position where $d=250 \mu m$, $\alpha = 4$ and $Re = 90$ (These figures do not have the same data range).

C.6.2 Device's width, $d = 200 \mu\text{m}$

C.6.2.1 No bumps, $s = 100 \mu\text{m}$

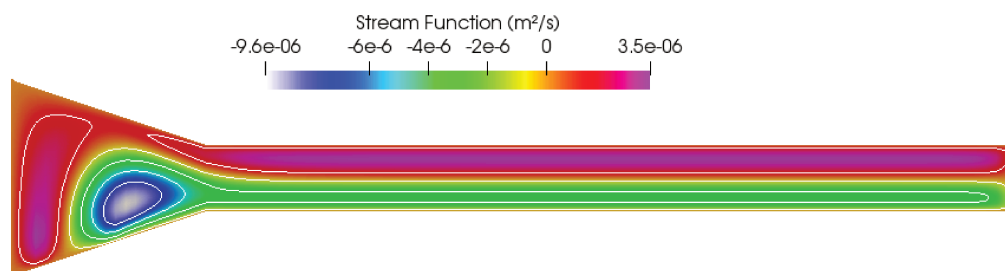
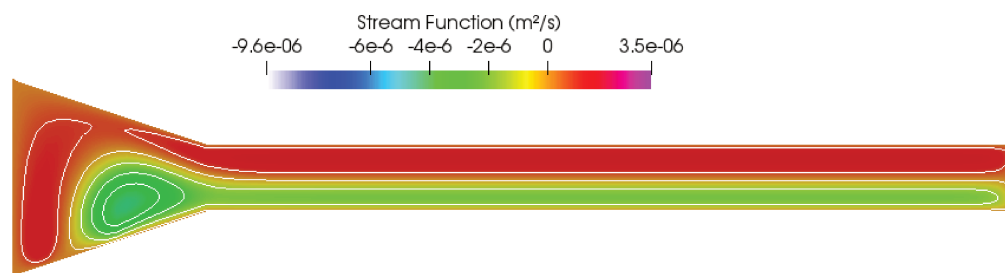
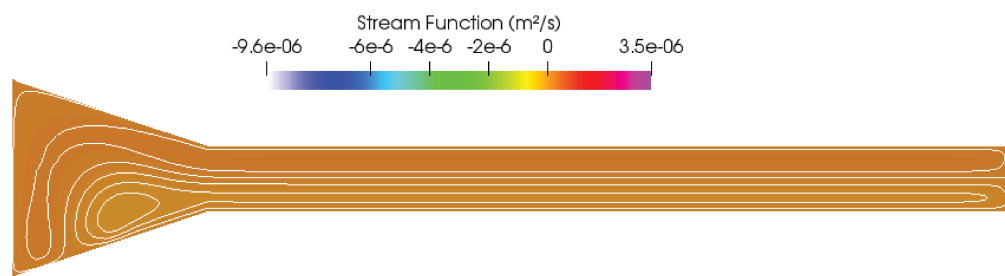
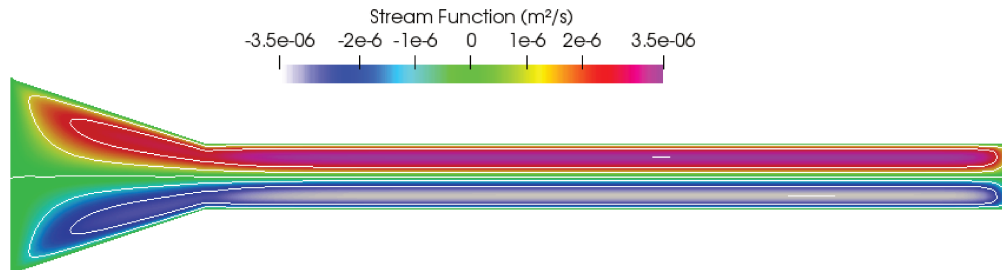
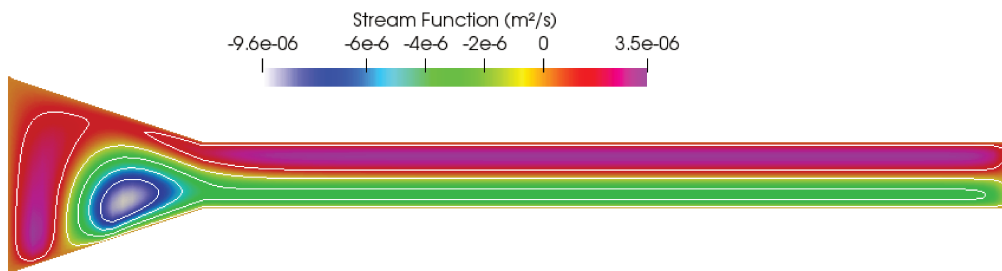


Figure C.57: Stream function with its contours along the microdevice regarding Reynolds number where $d=200 \mu\text{m}$, and $s = 100 \mu\text{m}$.

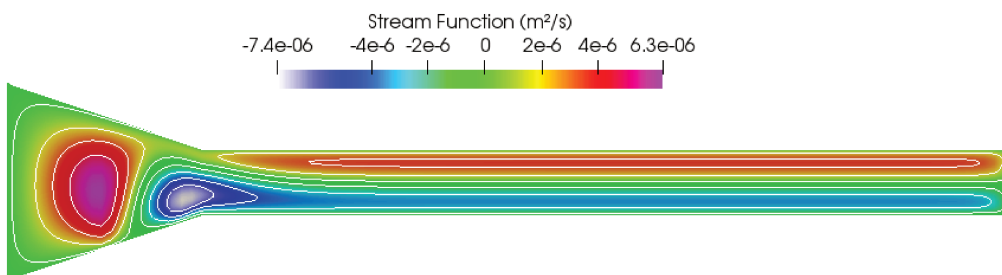
C.6.2.2 No bumps, $Re = 40$



(a) $s=0 \mu m$.



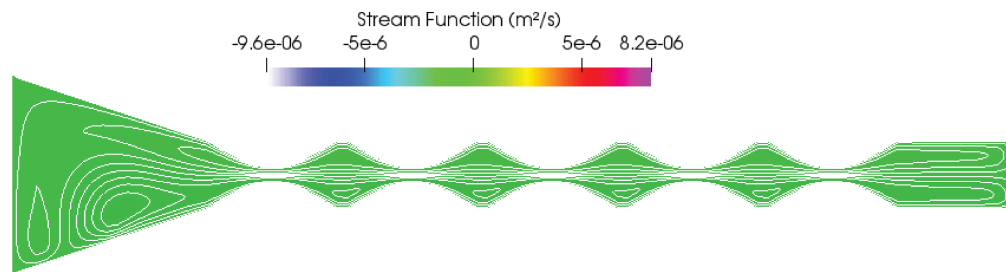
(b) $s=100 \mu m$.



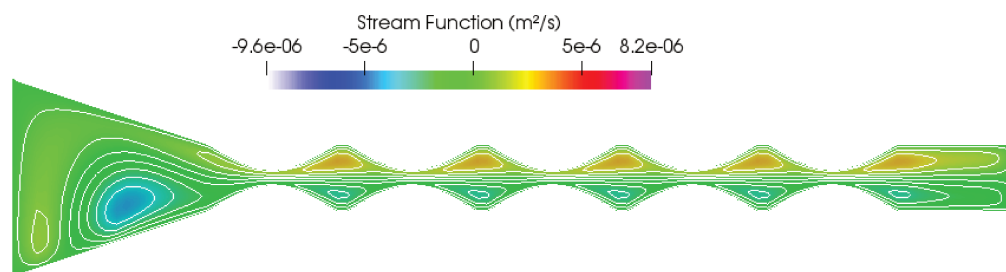
(c) $s=300 \mu m$.

Figure C.58: Stream function with its contours along the microdevice in terms of the feed position where $d=200 \mu m$, and $Re = 40$ (These figures do not have the same data range).

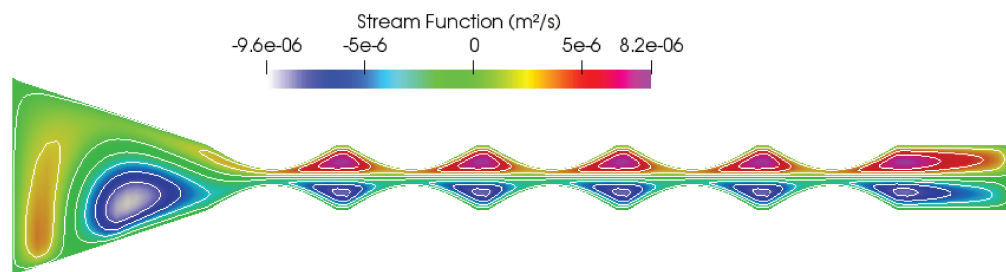
C.6.2.3 Curvature of bumps $\alpha = 1, s = 100 \mu\text{m}$



(a) $Re=1$.



(b) $Re=20$.



(c) $Re=40$.

Figure C.59: Stream function with its contours along the microdevice regarding Reynolds number where $d=200 \mu\text{m}$, $s = 100 \mu\text{m}$ and $\alpha = 1$.

C.6.2.4 Curvature of bumps $\alpha = 1$, $Re = 40$

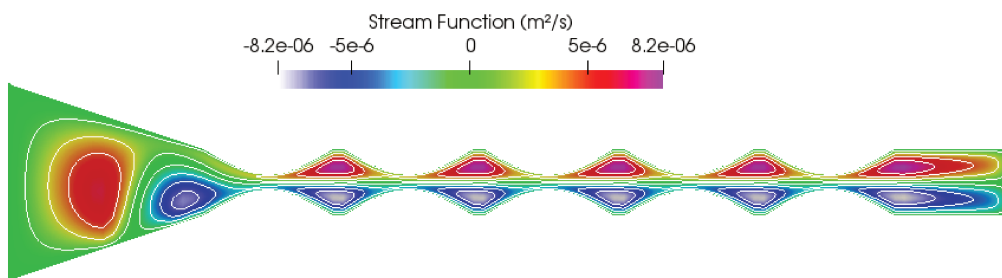
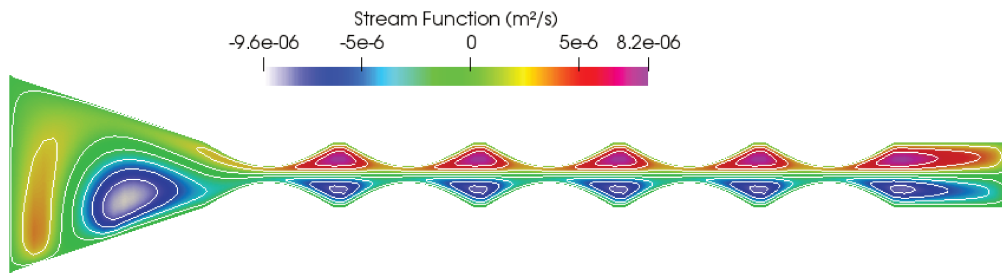
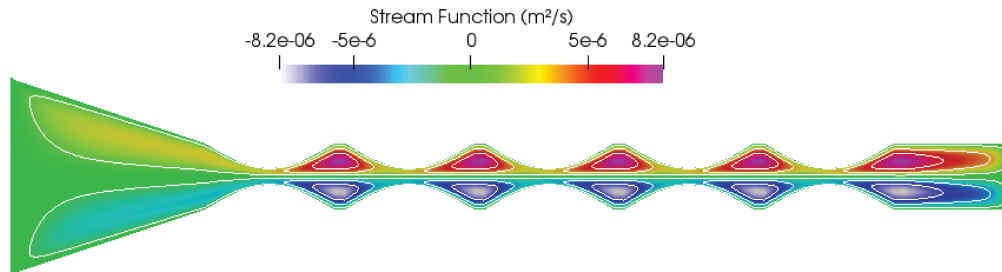
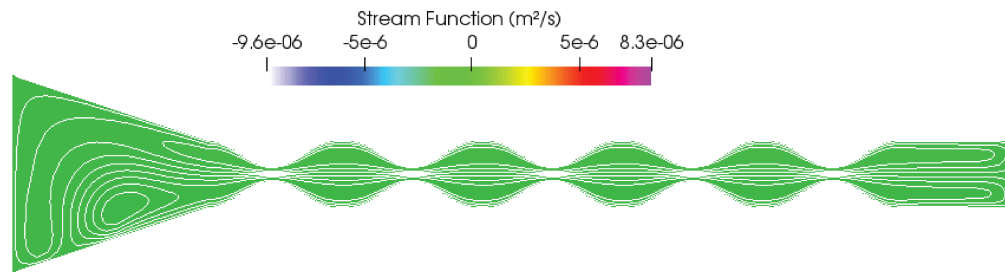
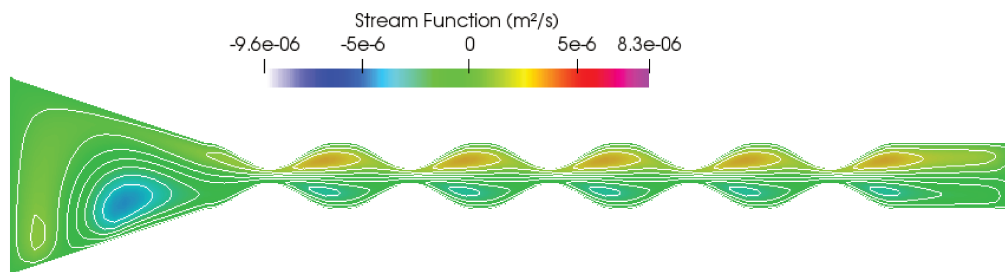


Figure C.60: Stream function with its contours along the microdevice in terms of the feed position where $d=200 \mu m$, $\alpha = 1$ and $Re = 40$ (These figures do not have the same data range).

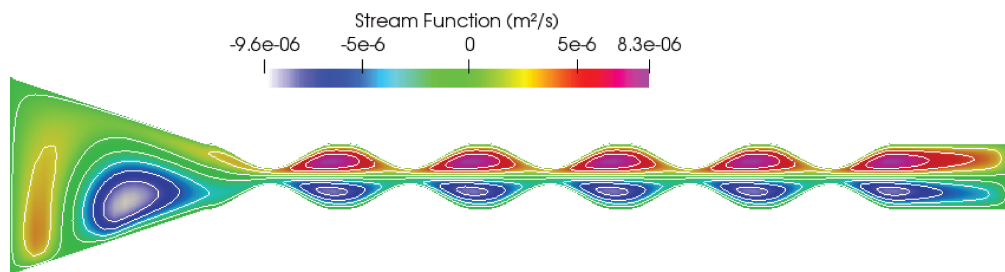
C.6.2.5 Curvature of bumps $\alpha = 2, s = 100 \mu\text{m}$



(a) $Re=1$.



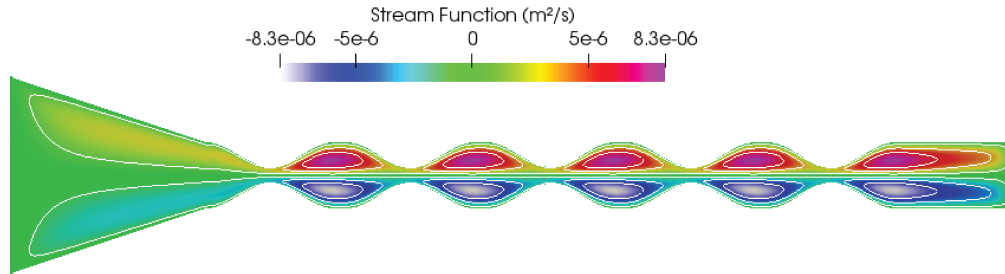
(b) $Re=20$.



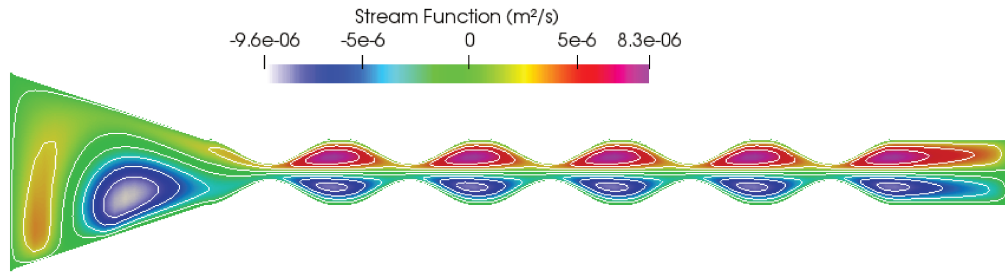
(c) $Re=40$.

Figure C.61: Stream function with its contours along the microdevice regarding Reynolds number where $d=200 \mu\text{m}$, $s = 100 \mu\text{m}$ and $\alpha = 2$.

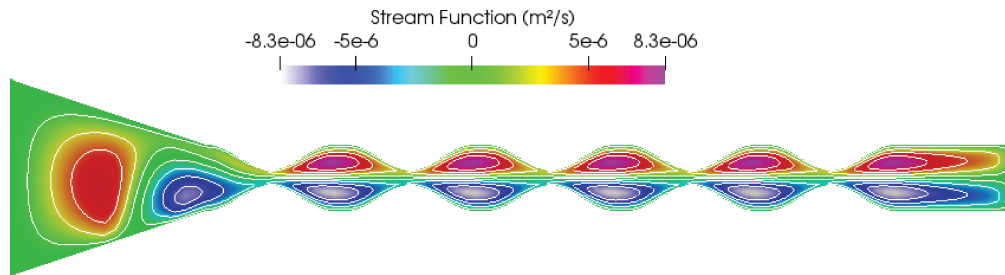
C.6.2.6 Curvature of bumps $\alpha = 2$, $Re = 40$



(a) $s=0 \mu m$.



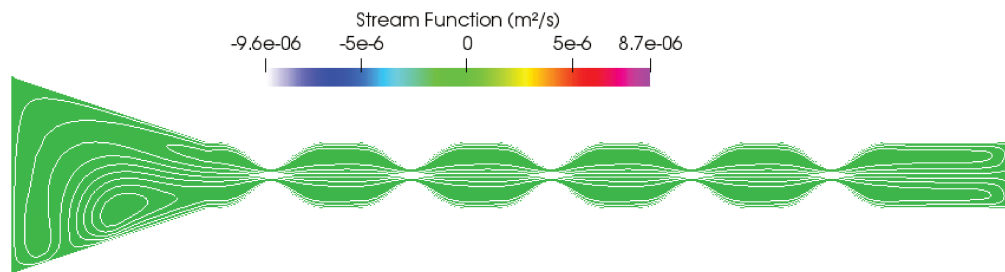
(b) $s=100 \mu m$.



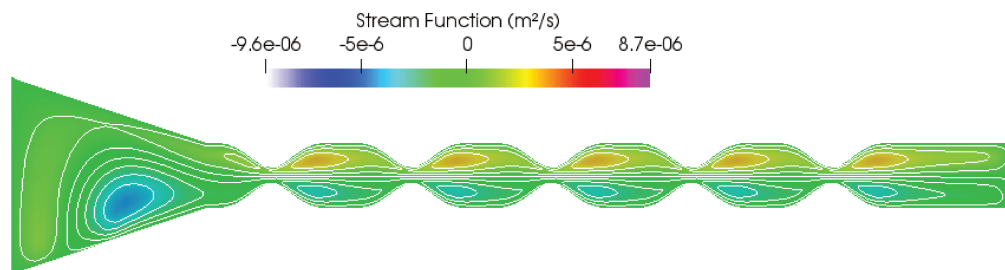
(c) $s=300 \mu m$.

Figure C.62: Stream function with its contours along the microdevice in terms of the feed position where $d=200 \mu m$, $\alpha = 2$ and $Re = 40$ (These figures do not have the same data range).

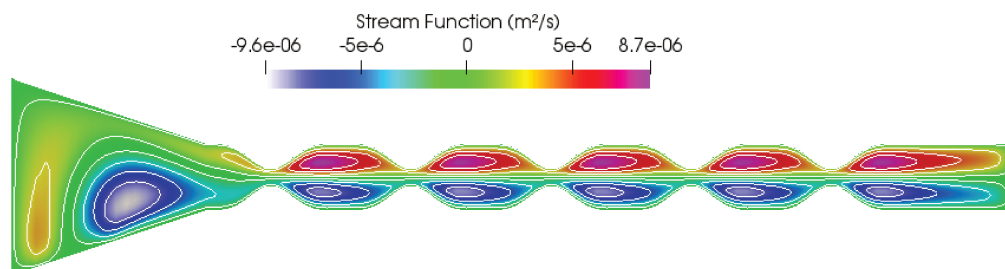
C.6.2.7 Curvature of bumps $\alpha = 4, s = 100 \mu\text{m}$



(a) $Re=1$.



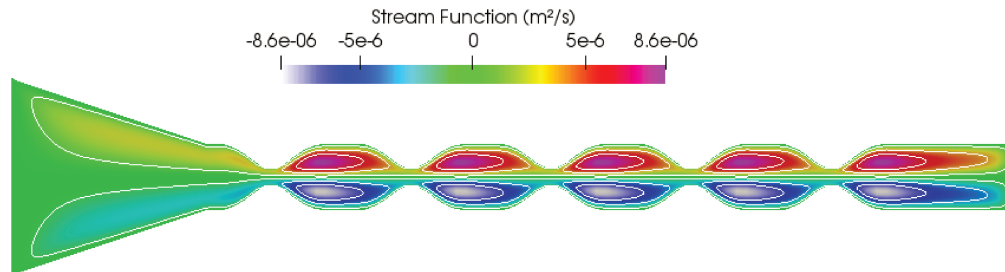
(b) $Re=20$.



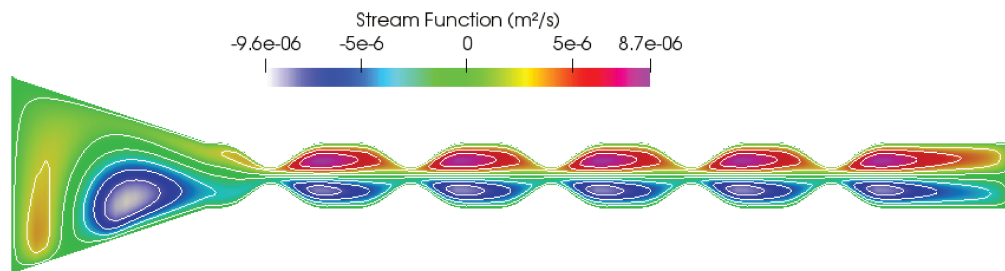
(c) $Re=40$.

Figure C.63: Stream function with its contours along the microdevice regarding Reynolds number where $d=200 \mu\text{m}$, $s = 100 \mu\text{m}$ and $\alpha = 4$.

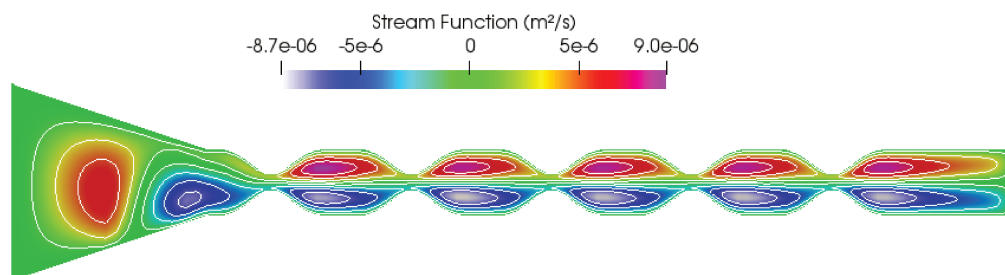
C.6.2.8 Curvature of bumps $\alpha=4$, $Re = 40$



(a) $s=0 \mu m$.



(b) $s=100 \mu m$.



(c) $s=300 \mu m$.

Figure C.64: Stream function with its contours along the microdevice in terms of the feed position where $d=200 \mu m$, $\alpha = 4$ and $Re = 40$ (These figures do not have the same data range).